NASA Contractor Report 4052

Flowfield Measurements in a Separated and Reattached Flat Plate Turbulent Boundary Layer

William P. Patrick

NASA

Flowfield Measurements in a Separated and Reattached Flat Plate Turbulent Boundary Layer

William P. Patrick

United Technologies Research Center
East Hartford, Connecticut

NASA

TABLE OF CONTENTS

TABLE OF CONTENTS (Cont'd)

NOMENCLATURE

B	Bias
C_f	Skin friction coefficient, $2\,U_\tau^2/U_{ref}^2$
C_f'	Local skin friction coefficient, $2\,U_\tau^2/U_e^2$ or eq. (5-34) in backflow boundary layer
C_p	Pressure coefficient, eq. (4-2)
d_f	Fringe spacing
d_m	Minor axis of measurement ellipsoid (i.e., diameter of LV probe volume)
f	Frequency
H	Boundary layer shape factor, $\delta*/\theta$
h	Boundary layer shape parameter, $(H-1)/H$; Height of backward-facing step; maximum thickness of separation bubble
k	Turbulence kinetic energy per unit mass, eqs. (4-4) and (4-5)
l_m	Major axis of measurement ellipsoid
M	Distance from wall to peak in transverse turbulence profile (current study); distance from wall to peak in axial turbulence profile (Simpson et al. data, ref. 1)
N	Distance from wall to location of maximum backflow velocity
n	Coordinate normal to streamwise direction
P	Total pressure
p	Static pressure
Q	Dynamic head pressure
$\sqrt{\overline{q^2}}$	RMS streamwise turbulence component

R — Non-dimensional pressure gradient strength, $\delta/U_e(\partial U_e/\partial x)$

$Re_{x'}$ — Reynolds number in backflow boundary layer, $U_N x'/\nu$

Re_{δ^*} — Reynolds number based on displacement thickness, $U\delta^*/\nu$

Re_θ — Reynolds number based on momentum thickness, $U\theta/\nu$

S — Precision index

s — Coordinate in streamwise direction

T — Static temperature

t — Time

t_{95} — 95th percentile point for Student's "t" distribution

U — Mean velocity in axial, x-direction; Measurement uncertainty

U_{eff} — Mean effective cooling velocity of hot-film probe

U_i — Axial velocity component of inviscid flowfield

U_N — Maximum backflow velocity

U_τ — Friction velocity, $\sqrt{\overline{\tau_w/\rho}}$

U^+ — Non-dimensional axial velocity component, U/U_τ

u — Fluctuating velocity component in axial, x-direction

u_{eff} — RMS fluctuation of effective cooling velocity of hot-film probe

$\overline{uv}$ — Reynolds shear stress

$\sqrt{\overline{u^2}}$ — RMS axial turbulence component

V — Mean velocity in transverse, y-direction

V_B Non-dimensional wake amplitude, eq. (5-23)

V_T Non-dimensional shear velocity, eq. (5-24)

v Fluctuating velocity component in transverse, y-direction

$\sqrt{\overline{v^2}}$ RMS transverse turbulence component

W Mean velocity in spanwise, z-direction

w Fluctuating velocity component in spanwise, z-direction; universal wake function, eq. (5-13)

$\sqrt{\overline{w^2}}$ RMS spanwise turbulence component

x Axial coordinate relative to test section inlet

x_R Axial location of reattachment

$x_{\delta^*_{max}}$ Axial location of maximum separation bubble thickness

x' Axial distance from reattachment location, $x_R - x$

x^* Non-dimensional axial distance from reattachment, eq. (5-38)

y Transverse coordinate relative to test surface

y^+ Non-dimensional transverse coordinate, yU_τ/ν

z Spanwise coordinate relative to wind tunnel centerline

α Test section divergence angle; angle of rotation of LV optics

$\overline{\alpha\beta}$ Streamwise turbulent shear stress component, eq. (5-39)

β Clauser equilibrium parameter, eq. (5-15)

γ_{p_U} Forward flow fraction (i.e., fraction of time flow moves in downstream direction)

$\gamma_{P_{U_{min}}}$ Minimum value of γ_{P_U} in profile near wall

γ_{P_V} Transverse flow fraction (i.e., fraction of time flow moves away from test surface)

δ Boundary layer thickness (i.e., location at which measured total pressure equals 99 percent of freestream total pressure).

δ_{99} Boundary layer thickness (i.e., location at which $U = 0.99\ U_e$)

δ_{995} Boundary layer thickness (i.e., location at which $U = 0.995\ U_e$)

δ^* Displacement thickness

δ_1^* Classical displacement thickness, $\int_o^\delta \left(1 - \dfrac{U}{U_{iw}}\right)dy$

δ_2^* True displacement thickness, $\int_o^\delta \left(1 - \dfrac{U}{U_{iw}}\right)dy - \int_o^\delta \left(1 - \dfrac{U_i}{U_{iw}}\right)dy$

δ_3^* Pressure-based displacement thickness, $\int_o^\delta \left(1 - \dfrac{U}{U_i}\right)dy$

θ Momentum thickness

θ_1 Classical momentum thickness, $\int_o^\delta \dfrac{U}{U_{iw}} \left(1 - \dfrac{U}{U_{iw}}\right)dy$

θ_2 True momentum thickness, $\int_o^\delta \dfrac{U}{U_{iw}} \left(1 - \dfrac{U}{U_{iw}}\right)dy - \int_o^\delta \dfrac{U_i}{U_{iw}} \left(1 - \dfrac{U_i}{U_{iw}}\right)dy$

θ_3 Pressure-based momentum thickness, $\int_o^\delta \dfrac{U}{U_i} \left(1 - \dfrac{U}{U_i}\right)dy$

κ Half-angle between intersecting laser beams; experimentally determined constant in eq. (5-13)

Λ Boundary layer shape parameter, δ^*/δ; Pohlhausen pressure-gradient parameter, eq. (5-36)

μ Viscosity

ν Kinematic viscosity

ξ LV inclination angle in y-z plane

Π Boundary layer wake parameter

ρ Density

τ_w Shear stress at wall

ϕ Angle of streamline relative to test surface

ψ Stream function, eq. (5-2)

ω Vorticity, $\dfrac{\partial V}{\partial x} - \dfrac{\partial U}{\partial y}$

Subscripts/Superscripts

$-$ Overbar, denotes time average except for LV measurements which are ensemble-averaged

$\sim$ Wavy overbar, denotes magnitude of instantaneous velocity

$\wedge$ Caret overbar, denotes nondimensional parameter

e   Quantity measured at $y = \delta$

ref   Quantity measured at reference location

w   Quantity measured on test surface

FLOWFIELD MEASUREMENTS IN A SEPARATED AND REATTACHED
FLAT PLATE TURBULENT BOUNDARY LAYER

William P. Patrick

SUMMARY

An experimental investigation of turbulent boundary layer separation with reattachment on a flat plate test surface was conducted in the United Technologies Research Center Boundary Layer Wind Tunnel. The objective of the study was to provide a comprehensive set of data for use in assessing the accuracy and assisting the further development of computational procedures for predicting boundary layer separation phenomena. The approach was to conduct a large scale, two-dimensional flow simulation of an airfoil turbulent separation bubble at low subsonic Mach number by imposing a strongly adverse and subsequent favorable pressure gradient. A combination of laser Doppler velocimetry, hot-wire anemometry, pneumatic probing techniques, and flow visualization were used as diagnostics.

The boundary layer separated and reattached over an axial distance of approximately 55 cm. The maximum bubble thickness, measured to the height of the mean dividing streamline, was 17 cm, which was twice the thickness of the inlet boundary layer. A strong backflow region in which the flow moved upstream 100 percent of the time was measured near the test surface over the central 35 percent of the axial extent of the bubble. A laminar backflow boundary layer having pseudo-turbulent characteristics including a log-linear velocity profile was generated under the highly turbulent backflow. Velocity profile shapes in the reversed flow region only matched Simpson's universal backflow profile at the upstream edge of the separation region where the backflow was intermittent. A smoke flow visualization movie and hot-film measurements revealed low frequency nonperiodic flapping at reattachment. However, forward flow fraction data at reattachment and mean velocity profiles in the redeveloping boundary layer downstream of reattachment correlated with backward-facing step data when the axial dimension was scaled by the distance from the maximum bubble thickness to reattachment.

Other principal observations concerning the separation bubble flowfield were that an outer inviscid rotational flow can be defined which essentially convects over the blockage associated with the inner, viscously dominated bubble recirculation region. In the outer flow region, velocity profiles were similar over the axial extent of the bubble while significant profile alteration occurred within the inner flow region, including the development of the reversed flow boundary layer at the base of the recirculation zone. The identification of this three-tiered structure is believed to have important implications relative to the numerical modeling of the flowfield.

1

CHAPTER 1

INTRODUCTION

Development of reliable numerical procedures for predicting compressor and turbine airfoil boundary layer separation is important to the gas turbine design process since the potential for occurrence of separation is high, when it occurs its effects are usually large, and present empirically based prediction methods have significant shortcomings.

The adverse pressure gradient responsible for boundary layer detachment can arise from local surface curvature effects or be imposed on the boundary layer by the outer flow (flow deceleration or incident shock waves). Depending on the strength of the adverse pressure gradient and the boundary layer characteristics (whether laminar or turbulent and the boundary layer shape factor) separation can occur on either the airfoil pressure or suction surface and at various axial positions. The boundary layer may remain deattached or reattach after a short or long distance (as a percent of chord) and it may undergo transition to turbulence if initially laminar.

A schematic of a turbomachinery blade showing several of the possible separations in terms of location, source and downstream development is given in figure 1-1. A closed leading edge bubble (termed a transitional bubble) is shown on the suction surface where typically deceleration of a laminar boundary layer causes separation, and transition to turbulence in the bubble shear layer fosters reattachment. Under a sufficiently adverse pressure gradient imposed by the outer flow, reattachment may not occur and the phenomenon of massive stall will result. A second form of suction surface separation encountered in the outboard regions of supersonic fan blades is shown further aft. This shock-induced phenomenon usually involves separation of a turbulent boundary layer and arises from interaction of the boundary layer with a bow shock from a neighboring blade. Depending primarily on shock strength and the degree of downstream diffusion, reattachment may or may not occur. Another region of surface separation is the airfoil trailing edge where the thick, blunt geometries required for structural and durability reasons invariably result in a surface curvature-induced separation. A fourth separation phenomenon is shown on the pressure side where surface curvature can induce a turbulent boundary layer ("cove") separation which subsequently reattaches under the influence of a favorable pressure gradient. Complicating these isolated phenomena is the possibility of interaction where, for example, a boundary layer weakened by negotiating the pressure rise of a shock may separate upstream of the trailing edge under the influence of diffusion and hence alter the trailing edge separation.

It is therefore clear that the potential for occurrence of separation is high and that once separated, the subsequent downstream development can have a significant impact on the aerodynamic performance (and for the turbine application, also the surface heat transfer). While the prediction of the inception of separation is important, and in some cases reasonably well treated by existing methods, the ability to predict the subsequent downstream flow development is equally important. Existing airfoil design procedures typically rely upon an inviscid transonic cascade calculation to predict the overall flowfield and a coupled boundary layer calculation to account for near surface viscous effects. In the absence of separation the procedures are generally satisfactory for design purposes. When separation occurs, however, lack of a reliable calculation method requires the use of approximate methods derived from test data and past experience. This empirical approach, while successful in many applications, not only limits the designer to interpolation within the experience base but also presents problems in the application of the available codes. For example, in treating either a closed leading edge or shock-induced separation bubble, it may be possible to use correlations to define the approximate extent of the separation region. Uncertainty exists, however, in boundary layer characteristics aft of the bubble. Since these are required to initiate an attached boundary layer calculation over the remainder of the airfoil surface, the accuracy of the overall airfoil calculation procedure is impacted.

The focus of the present study was the pressure side "cove" separation depicted in figure 1-1. The approach was to conduct a large-scale, two-dimensional flow, low Mach number simulation on a flat plate test surface. The flat plate geometry was selected since it provided the simplest test case for code assessment purposes. There have been no previous investigations of this turbulent separation bubble geometry using non-intrusive laser velocimetry although Simpson (refs. 1-4) has performed extensive research relative to flat plate turbulent boundary layer separation without downstream reattachment. Simpson's work has provided significant information regarding both the mean and turbulent velocity fields within the separated flow region and some of his results apply directly to the leading edge region of the bubble investigated in this study. Although a number of other investigators have conducted closed separation bubble studies which have indirect relevance to the problem considered here, test geometries invariably involved rapid surface curvature and salient edges which produced fixed separation points and also affected the development of the reversed flow region within the bubble. Only Perry and Fairlie (ref. 5) and Cutler and Johnston (ref. 6) have reported investigations of flowfields comparable to the current study. Their studies, described in Chapter 2, used pitot and hot-wire traverses to obtain data within the separation bubble and, in addition, Cutler and Johnston used thermal tufts at the wall.

4

For the near future, computer codes providing numerical solutions of the Reynolds-averaged equations will continue to be the most useful engineering approach for the solution of flowfields having turbulent separation bubbles (ref. 7). Such codes use numerical correlations and zonal modeling to divide the flowfield into several regions, each dominated by a particular type of flow, and to analyze each region by the computationally optimum numerical technique for that region (ref. 8). Current codes use flow models which have been derived from open separation bubble data for the separation region and, primarily, from backward-facing step data for the flow at and downstream from reattachment. Within the separation bubble Gosman (ref. 9) noted that insufficient reliable data exists to define the structure of the backflow region. He suggested that future experiments should be on large-scale models using laser anemometry or other quantitative directionally sensitive techniques. The present study was undertaken to provide such detailed data for the entire flowfield of a separated flow configuration relevant to gas turbine airfoil design. The overall objective was to provide a comprehensive data base from which the accuracy of existing models could be assessed and improved models could be developed.
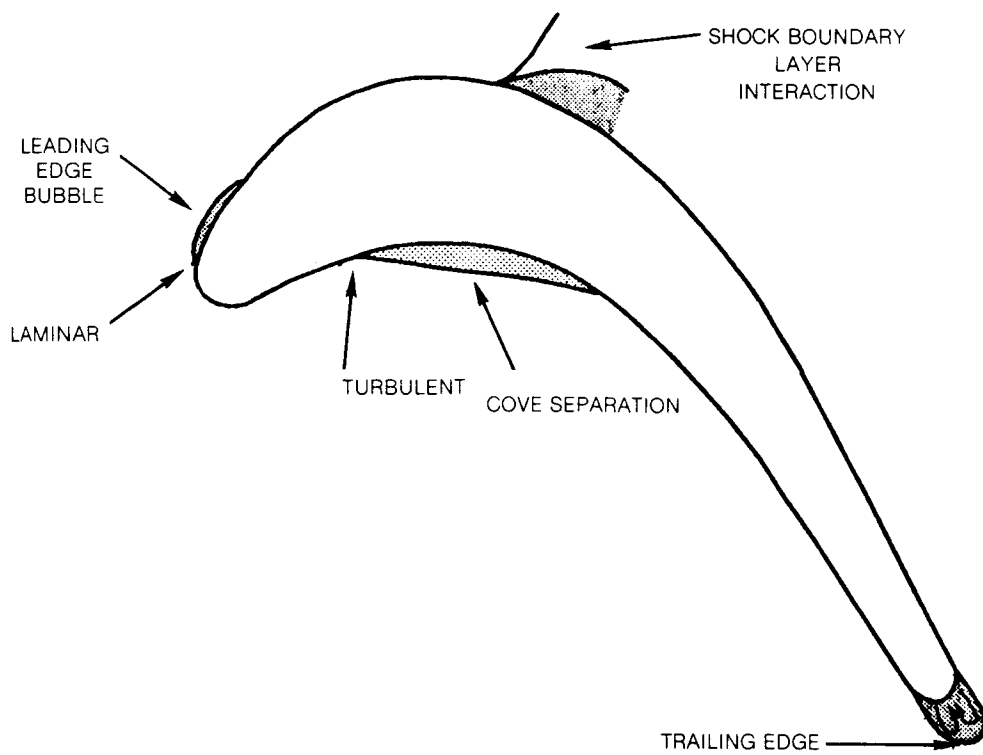
Figure 1-1 Airfoil Surface Separation

CHAPTER 2

REVIEW OF PREVIOUS INVESTIGATIONS

Detailed measurements of turbulent boundary layer separation and reattachment on a rotating compressor or turbine blade are unavailable because of the obvious difficulties of obtaining high resolution measurements in an operating engine environment. As noted in the previous chapter, only two experimental studies of the more tractible problem of turbulent boundary layer separation and reattachment on a stationary flat plate at low subsonic speed have been reported in the literature (refs. 5 and 6). Each of these studies, which yielded partial data bases, will be described below. To date, flow modelers have had to rely on the extensive body of literature which exists for both reattaching and separating turbulent flows.

Subsonic turbulent flow reattachment has been reviewed by Mueller (ref. 10), Bradshaw and Wong (ref. 11), and more recently by Eaton and Johnston (ref. 12). Eaton and Johnston noted that at the time of Bradshaw and Wong's review in 1972 very few reliable data for reattaching flows were available. Although details of reattachment length and mean flow profile development downstream of reattachment were known with good accuracy, turbulent stress data required to develop turbulence models were sparse. Since that time the development of laser velocimetry and pulsed-wire anemometry has enabled several investigators (refs. 13-17) to obtain reliable, quantitative reattachment data. Details of these investigations will not be reviewed in this section although pertinent studies such as those by Chandrsuda and Bradshaw (ref. 18), Driver and Seegmiller (ref. 14), and Westphal, et al. (ref. 17) will be discussed in Chapter 5, "Analysis and Discussion".

Ota and his colleagues (refs. 19-21) have studied separation bubbles having turbulent reattachment which form at the leading edge of blunt flat plates and circular cylinders aligned with the flow. These flows have a negligible boundary layer thickness at separation and therefore are unaffected by upstream boundary layer history as can be the case for backward-facing step flows. Ota, et al. studied the redeveloping boundary layer downstream of reattachment and found strong similarities between their data and the backward facing step data of Bradshaw and Wong (ref. 11), Mueller, et al. (ref. 22), and others.

Between the pioneering efforts of Sandborn and Kline (ref. 23) in defining turbulent separation criteria and the recent definitive experimental studies of Simpson and his colleagues (refs. 2-4), numerous studies of turbulent boundary layer separation have been reported in the literature. These studies have been reviewed by Simpson (refs. 8 and 24) and except for the

studies of Simpson and his colleagues (refs. 1-4) and a later study by Smith, et al. (ref. 25) will not be discussed in this section. However, as noted above for the turbulent reattachment data, pertinent studies will be included in the data comparisons presented in Chapter 5, "Analysis and Discussion".

Little reliable quantitative data was obtained within turbulent separated boundary layers prior to 1974 due to a lack of proper instrumentation. Simpson, et als. (ref. 1) pioneering effort in applying a one-component directionally sensitive laser velocimeter to the study of separating turbulent airfoil-type boundary layers revealed several new features of these flows including the following:

(1) Law-of-the-wall velocity profile scaling is valid up to intermittent separation.

(2) Intermittent separation occurs when the wall static pressure gradient begins to diminish.

(3) Normal stress terms in the momentum and the kinetic energy equations are important near separation.

(4) The separated flowfield shows some similarity of the streamwise mean velocity, the streamwise turbulence component, and the forward flow fraction.

Later studies by Simpson and his colleagues using a two-component LV system culminated in a series of three papers (refs. 2-4) which presented fundamental mean flow and turbulence structure data from which improved models of the backflow region could be developed. Several significant conclusions resulted from these studies including the following.

(1) The backflow velocity profiles are not consistent with law-of-the-wall type scaling. Simpson (ref. 26) postulated a universal mean backflow velocity profile scaled on the maximum negative mean velocity U_N and the distance, N, of the maximum negative mean velocity from the wall.

(2) Within the backflow the turbulent velocities are comparable to the mean flow velocities although the turbulent shearing stresses are low.

(3) Mixing length and eddy viscosity models are physically meaningless in the backflow and have reduced values in the outer region of the separated flow. Reynolds shearing stress must be modeled by relating it to the turbulence structure and not the mean flow

gradients because the mean backfow velocities are obtained by time-averaging large turbulent fluctuations and are not related to the source of the turbulence.

(4) A three-tiered structure was apparent in the backflow. It consisted of a viscous layer closest to the wall, a wider flat intermediate layer, and an outer backflow region which was part of the large-scaled outer region flow.

Later work by Simpson has been directed toward obtaining an understanding of unsteady separating turbulent boundary layers (ref. 27).

Smith, Hastings, and Williams (ref. 25) studied the structure of an equilibrium separated boundary layer on a flat plate with a single component LV system. The boundary layer was first accelerated and then decelerated such that the boundary layer edge velocity varied with distance according to a negative power law (i.e., $U = Cx^{-m}$). Mean axial velocity and turbulence intensity profiles were measured at several axial stations and one pair of profiles of the mean transverse velocity and turbulence intensity were measured in the separated region. Static pressures were measured on the test surface centerline. Forward flow fraction and shear stress profiles were not measured.

Equilibrium separated flow was maintained for 1.1 m before the boundary layer on the test surface and tunnel ceiling merged. Some flow asymmetry was noted and measurements indicated that the flow was not in strict two-dimensional equilibrium. However, boundary layer displacement and momentum thickness grew linearly as expected for equilibrium flow.

Limited measurements of backflow velocity profiles were presented. Data scatter appeared to be considerable near the test surface although no estimate of measurement error was presented. Smith, et al. corroborated Simpson's finding that the backflow velocity profile could not be modeled using the universal law-of-the-wall. They also concluded that normal Reynolds stresses were considerably more important in the momentum integral equation than would be expected on the basis of equilibrium attached flow.

In addition to the separated turbulent boundary layer studies of Simpson and his colleagues and Smith, et al., only two experimental studies of turbulent boundary layer separation with reattachment on a flat plate have been reported in the open literature. These studies were conducted as Ph.D. dissertations by B. D. Fairlie under A. E. Perry at the University of Melbourne in 1973 (ref. 5) and by A. D. Cutler under J. P. Johnston at Stanford University in 1984 (ref. 6).

Perry and Fairlie (ref. 5) separated an equilibrium turbulent boundary layer to generate a large separation bubble (41 cm long x 8 cm thick at the maximum height of the dividing streamline) on the floor of a low speed open-return wind tunnel. The test section had a rectangular cross section measuring 61 cm long x 11 cm high at the inlet. It was 2.5 m long with a specially constructed flexible roof, allowing any desired streamwise pressure gradient to be obtained. The variable tunnel outlet height was set at approximately 60 cm for the two test cases reported in ref. (5). A false roof mounted below the flexible roof was used to provide a starting point for a new roof boundary layer thereby inducing the flow to preferentially separate from the flat test surface. Smoke, tufts and surface flow visualization indicated moderate three-dimensionality in the flowfield.

Mean velocity, flow angle, and surface static pressures were measured throughout the flowfield. Neither forward flow fraction, turbulence, nor shear stress data were reported. The surface static pressures obtained on the floor centerline showed a pressure plateau over a 37 cm long region under the bubble with pressure maxima at the separation and reattachment points. Velocity traverses were made normal to the plate on the duct centerline throughout the flowfield. Data was obtained with flattened pitot probes upstream of separation. Near separation and within the separation bubble a twin hot-wire probe was used to obtain mean-velocity and flow angle measurements. Flow angles were obtained by traversing a temperature sensitive wire through the wake of the velocity sensitive wire. As reported by Perry and Fairlie, this intrusive hot-wire probing technique is inaccurate in highly unsteady flows or regions having intermittent flow reversals due to signal rectification by the velocity sensitive wire. Reported velocity profiles showed discontinuities at the edge of the backflow region. The velocity profiles indicated strong backflow within the separation bubble. However, the strength of the backflow could not be quantified without forward flow fraction data.

Cutler and Johnston (ref. 6) studied the effect of the state of equilibrium or disequilibrium of the inlet turbulent boundary layer on separation and reattachment on a flat plate. Tests were conducted in a low speed closed-return wind tunnel having a 30.48 cm wide rectangular tests section which diverged over a 1 m length from an inlet height of 10.16 cm to an outlet height of approximately 40 cm. Boundary layer bleed slots on the upper diverging wall caused the flow to preferentially separate from the lower wall flat plate test surface. Measurements were made of wall static pressure distributions, forward flow fraction at the wall using a thermal tuft, total pressure profiles with pitot probes, and mean velocity and turbulence parameters using normal and crossed hot-wire probes.

Complete detachment of the boundary layer was not achieved in the Cutler and Johnston test cases. The test surface boundary layer passed through incipient detachment, closely approached detachment, and then fully reattached. The minimum value of the forward flow fraction measured at the wall was 0.59. Careful conditioning of the flow ensured excellent flow two-dimensionality in the inlet flow. Nevertheless nonnegligible three-dimensional effects were evident near detachment and reattachment when the terms in the two-dimensional momentum integral equation were evaluated using exerimental data.

Cutler and Johnston drew several significant conclusions from their study including the following:

(1) A tripped boundary layer which had not recovered to an equilibrium profile separated further downstream than a boundary layer having an equilibrium profile at the same operating conditions.

(2) Since mean streamline angles to the wall are not small near the separation region even though the wall is flat it becomes important to model flow quantities, particularly turbulent shear stress, in coordinates locally orthogonal to the streamline.

(3) Mean streamline convex curvature becomes significant between the detachment and reattachment locations, even though the wall is flat. The effect of the streamline curvature is to reduce the shear stress and the entrainment of the freestream fluid into the boundary layer and to induce nonnegligible static pressure gradients normal to the flat wall.

(4) To calculate flows downstream of a reattachment, the development of mean-velocity-profile quantities and of turbulence quantities must be modeled separately because there is no unique relationship between these quantities.

CHAPTER 3

DESCRIPTION OF THE EXPERIMENT

3.1 Experimental Arrangement

3.1.1 Wind Tunnel Arrangement

The experiment was conducted in the UTRC Boundary Layer Wind Tunnel which
is shown schematically in figure 3-1. It is a low speed wind tunnel of recir-
culating design and consists of a blower, settling chamber/plenum, contraction
nozzle, boundary layer bleed scoop, boundary layer test surface, downstream
diffuser, coarse air filter, temperature control heat exchanger, and return
duct. This tunnel has been designed to produce large scale two-dimensional
boundary layers with Reynolds numbers, freestream turbulence levels and pres-
sure coefficient distributions typical of turbomachinery blades. A thorough
calibration of the flow characteristics of the tunnel (ref. 28) has shown the
flow to be highly two-dimensional and steady. The freestream turbulence level
can be varied between 0.25 percent and 10 percent with the addition of turbu-
lence generating grids.

For this test program several modifications were made to the tunnel as
shown in figure 3-2. The major modification was the installation of a new
test section, described below, which was designed to produce a large two-
dimensional turbulent separation bubble. Another major modification was the
addition of a submicron filtration system downstream of the diffuser section
to permit LV seeding in the test section without contamination of the fine
mesh screening in the settling chamber.

The 1.83 m x 1.83 m cross-section submicron filtration system consisted
of nine filtration modules arranged in parallel in a 3 x 3 matrix. Each
0.61 m x 0.61 m cross-section filtration module consisted of a prefilter, a
bag filter, and an absolute HEPA filter. Tests of a single filter module
indicated that the filtration system was extremely efficient. Under condi-
tions of heavy LV seeding the air in the return duct was found to be two
orders of magnitude cleaner than the ambient unseeded air circulating in the
unmodified tunnel. The filtration system had a nominal 3 cm H_2O pressure drop
at the 283 SCMM (10,000 SCFM) tunnel operating condition used in the test
program.

Several other modifications were made downstream of the contraction noz-
zle. The leading edge bleed scoop was covered by a contoured wall section
(see inset in fig. 3-2) and the original boundary layer test surface was used
as a boundary layer development section. The downstream horizontal variable
angle diffuser was then replaced by the new diffusing test section. An

0.64 cm square bar was installed downstream of the contraction nozzle to pro-
vide a two-dimensional boundary layer transition process. The axial location
of the trip was 245 cm upstream of the test section inlet (i.e., x = 0).

3.1.2 Test Section Arrangement

The test section consisted of a constant area approach section which
functioned as a continuation of the boundary layer development section, a
diverging section to produce the large adverse pressure gradient required
to separate the turbulent boundary layer from the test plate, a converging
section to force its reattachment and a constant area exit duct. The fixed
dimensions of the test section were: length, 152 cm (60 in.); width, 86.4 cm
(34 in.); inlet height, 21.3 cm (8.38 in.); exit height, 15.2 cm (6 in).

The upper wall test surface was fabricated from 1.27 cm thick aluminum
tooling stock. The plate was machine ground and hand buffed with steel wool
to ensure surface smoothness. The lower wall was fabricated from 1.27 cm
thick aluminum plates joined by flexures. The joints between the flexures and
the aluminum plates were fabricated to eliminate steps in the surface contour.
The lower wall was moveable by means of jack screws. During shakedown testing
the lower wall geometry was adjusted over a wide range until a large separa-
tion bubble having a minimum amount of three-dimensionality and unsteadiness
was achieved on the test surface. Photographs of the final test section con-
figuration selected for the experiment are shown in figures 3-3 and 3-4.

3.1.2.1 Boundary Layer Bleed System

Boundary layer bleed on the test section diverging wall was used to pre-
vent the preferential separation of the turbulent boundary on this surface.
Test surface corner bleed was also used to improve two-dimensionality of the
test section flowfield. The bleed system was driven by natural suction caused
by a static pressure differential between the test section and the inlet to
the submicron filtration system. A 22.9 cm H_2O pressure differential was
created by installing two 40 percent open perforated plates in series just
upstream of the turning vanes ahead of the vertical diffuser section to raise
the static pressure in the test section.

The diverging lower wall was equipped with two bleed scoops which spanned
the width of the test section as shown in the photograph in figure 3-3. The
scoops were designed to force the lower wall boundary layer to remain attached
throughout the strong adverse pressure gradient field required to produce
two-dimensional separation on the test surface. The first scoop, which had a
fixed height of 2.87 cm, could be moved axially, parallel to the lower wall,
over a 22.9 cm. range. The second scoop which could be moved axially and
vertically as well as rotated was found to be unnecessary and remained closed

14

during the experimental program. Approximately 30 percent of the flow entering the test section was removed by the operational lower wall bleed scoop.

The upper wall bleed system consisted of two .32 cm wide, 152 cm long, suction slots on either side of the test surface at the corner between the test plate and side wall. The purpose of these bleed slots was to improve the two-dimensionality of the flow near the test surface by removing low momentum fluid caused by the sidewall boundary layers. Each bleed slot was connected to a plenum located above the test section (fig. 3-5) by fifteen 2.54 cm dia. holes drilled through the test plate support structure. Partitions in the bleed slots and the plenums divided each suction slot into three axial segments each having independent control of suction strength by means of valving. Bleed flow was ducted from the plenums to the filter inlet by a 10 cm dia PVC pipe. Less than one percent of the flow entering the test section was removed by the upper wall bleed system. Prior to installing the corner bleed slots, sidewall fences were used in an attempt to improve flow two-dimensionality in the test section. The fences, made of 20 cm x 70 cm float glass, were mounted approximately 3 cm from the sidewalls on standoffs which permitted adjustment during rig operation. The fences were found to be only moderately successful in reducing flow three-dimensionality.

3.1.2.2 Test Section Instrumentation

The test section instrumentation consisted of 140 wall static pressure taps and 75 0.63 cm dia. probing ports. Of these 120 of the wall static taps and 55 of the probing ports were located on the test surface. As shown in figure 3-5, the static taps were arranged in three rows of forty located on the test section centerline and 15.2 cm to either side of the centerline. In addition 35 of the probing ports were located on the centerline and 10 on either side of the centerline (figs. 3-6 and 3-7). The remaining 20 wall static taps and 20 probing ports were located along the centerline on the lower wall of the test section. The probing ports on the test surface were used for traversing total pressure probes and hot-film probes normal to the test surface to obtain flowfield data. Specific locations of the ports, which were machined into the test surface after the position of the separation bubble was established during shakedown testing, are described in detail below. Probing ports on the lower wall were used for traversing total pressure probes normal to the surface. These data permit calculation of the displacement thickness development and hence define the lower bounding streamline for CFD codes. Additionally, one sidewall of the test section was fabricated from float glass to facilitate LV measurements.

15

3.2 Test Program Definition

3.2.1 Selection of Measured Variables

Directly measured and derived variables were selected based upon code assessment requirements. A viscous-inviscid calculational procedure for predicting two-dimensional boundary layer separation and reattachment on a flat plate requires input data to permit calculation of both the potential flow-field within the test section and the viscous flow along the test plate. The freestream velocity at the test section inlet and the location of the bounding streamline along the lower wall opposite the test surface were required as boundary conditions for use in the potential flow solution. The integral boundary layer parameters (displacement thickness and momentum thickness) and the Reynolds number based on momentum thickness at the test section inlet were required to define the initial station for the viscous calculation. Depending on the complexity of the turbulence model used, the Reynolds stress distribution at the test section inlet may also be needed to initialize the model. The desired output of the calculational procedure is a complete specification of the mean velocity field and static pressure distribution throughout the test section, and depending on the turbulence model used, some turbulence field properties.

Based on these and experimental considerations, axial and vertical mean velocity components, total pressure, wall static pressures, and inlet total temperature were selected as the mean variables to be measured directly. Turbulence quantities measured directly were: the axial component of turbulence intensity, $\sqrt{\overline{u^2}}$; the vertical component of turbulence intensity, $\sqrt{\overline{v^2}}$; and the Reynolds stress, $\overline{uv}$. Turbulence spectra were taken to document the unsteady nature of the separation bubble. In addition, the forward flow fraction, γ_{P_U}, the fraction of the time the flow moves downstream, and the transverse flow fraction, γ_{P_V}, the fraction of the time the flow moves away from the test surface, were selected for measurement to define the zones of separation and reattachment and to delineate the regions where hot-film and total pressure measurements would be reliable.

3.2.2 Tunnel Operating Conditions

The test conditions for the experiment were selected based upon two criteria: the turbulent separation bubble should be large enough to provide high resolution of bubble details and the Reynolds number of the turbulent boundary layer on the test surface at the test section inlet should be in the range applicable to gas turbine airfoils. Establishment of a large separation bubble was achieved by providing a diverging-converging test section of 150 cm axial extent and a suitably scaled test section height. Reynolds number simulation was established by producing a turbulent boundary layer having a Reynolds number based on momentum thickness of 15,000 at the test section

16

inlet at the inlet velocity of 27 m/sec. This value is typical for aircraft turbine blades at the onset of cove separation.

Separation bubble reproducibility (stationarity) throughout the duration of the test program was ensured by adjusting the operating conditions to achieve the same Reynolds number for each test run. This was achieved by adjusting the tunnel dynamic head, Q, to compensate for changes in barometric pressure and tunnel temperature. The dynamic head was determined from the difference between the total pressure measured with a kielhead probe located in the core flow of the boundary layer development section and a wall static pressure measured at the same axial location. Tunnel air temperature was measured with a Cr-Al sheathed thermocouple inserted through an insulated plug in the tunnel sidewall. The tunnel dynamic head was adjusted mainly for changes in barometric pressure and to a lesser extent for tunnel temperatures. The tunnel temperature varied from 22 to 27 deg C between winter and summer testing but on any given day the tunnel temperature could be maintained constant to within ± 0.5 deg C.

3.2.3 Selection of Measurement Locations

To meet the code assessment objectives, a "benchmark" study of two-dimensional turbulent boundary layer separation and reattachment on a flat plate must, as a minimum, provide the input data required to perform the computation and sufficient flowfield data at relevant locations to determine prediction accuracy. Supplementary data should also be obtained to assess experimental accuracy and to document flow two-dimensionality.

To perform the calculation, data must be obtained at an initial measurement plane to start the computation and at a sufficient number of stations to define a bounding streamline. A plane normal to the upper wall, located in the boundary layer development section 24 cm upstream of the test section inlet, was selected as the initial measurement plane. The wall static pressure on the test surface and a 70-point total pressure traverse normal to the test surface were used to define the one-dimensional mean velocity profile at this location. A 34-point hot-film traverse was also used to determine the axial turbulence intensity profile. To determine the coordinates of a bounding streamline, wall static pressures and total pressure profiles normal to the wall were measured at 20 stations along the lower wall on the tunnel centerline (fig. 3-6). The measurement increment normal to the wall was chosen to yield a minimum of 20 points in each total pressure traverse.

To assess the accuracy of the code predictions and to acquire a detailed understanding of the flowfield upstream, within, and downstream of the separation bubble, a dense array of static pressure taps and traverse locations was provided on the test plate as shown in figure 3-7. Wall static pressure taps

extended the length of the test plate from the upstream zero-pressure gradient region to the corresponding region downstream of separation. Thirty-six traverse stations were located on the tunnel centerline (Table 1). Twelve stations were located upstream of separation, five within the intermittent separation zone, eight within the reversed flow region, five within the intermittent reattachment zone, and six downstream of separation. Ten additional traverse stations were located on a line 15.2 cm to either side of the tunnel centerline to document flowfield two-dimensionality. Two of the off-centerline traverse stations were located in each of the five distinct flow regions on the test plate.

On the tunnel centerline, total pressure traverses were made at each of the 36 measurement stations, single-element hot-film probe traverses were made at 30 stations, and LV traverses to measure axial and vertical velocity components were made at 16 stations, as shown in figure 3-7. Along the line located 15.2 cm to either side of the tunnel centerline, total pressure traverses were made at each of the 10 measurement stations, single-element hot-film probe traverses were made at 8 stations, and LV traverses were made at four stations. Except for off-centerline LV data taken at the $x = 26.7$ cm ($x = 10.5$ in) station, each LV traverse station coincided with a hot-film traverse station, and each hot-film traverse station coincided with a total pressure traverse station. An additional 20 LV traverses were made at 14 centerline stations and six off-centerline stations, as shown in figure 3-7, to measure Reynolds stress.

The measurement increment normal to the test surface was varied based on resolution requirements. Fine resolution was necessary for defining the velocity field in the near-wall region since this is critical for code assessment. Additional detail was considered desirable to demarcate the edge of the reversed flow region. Since more than 300 traverses were planned in this experiment, regular, fine, and extra fine increment schedules were defined to limit the number of data points required to produce the desired resolution. The regular increment schedule was sufficiently dense to provide a minimum of 10 LV and 20 hot-film or pitot measurements per traverse. It was used for all hot-film measurements and LV Reynolds stress measurements and for pitot and LV velocity measurements at off-centerline locations to document flow two-dimensionality. The fine increment schedule, which provided sufficient detail in the near-wall region to produce a 30- to 40-point traverse, was used for all LDV velocity measurements on the tunnel centerline and most off-centerline pitot measurements. The finest increment schedule, which produced a 50- to 80-point traverse, was used for pitot traverses to define the boundary layer throughout the test section along the test plate centerline and at off-centerline locations near the test section inlet.

In selecting the measurement matrix described above, it was recognized that pitot and hot-film measurements could be inaccurate in regions of high turbulence intensity and would not be meaningful in regions having intermittent flow reversal more than a few percent of the time. The LV measurement locations were selected to define such regions and therefore permit the pitot and hot-film measurements to be interpreted correctly. In regions where the pitot measurements were valid, finer resolution of the near-wall velocity field was obtained. In conjunction with the LV mean velocity measurements, pitot data provided a means to estimate the static pressure field within the flow. In regions where the hot-film measurements were valid, turbulence spectra were acquired to contribute to an understanding of the unsteady nature of the turbulent separation bubble. In addition, the measured components of mean velocity and rms turbulence intensity provided a redundant set of data to check the LV measurements.

3.2.4 Flow Two-Dimensionality and Steadiness Criteria

Objectives were identified at the outset of the experiment regarding spanwise uniformity of the flow at the initial measurement plane and at three measurement planes in the test section: at the test section inlet, just upstream of separation, and within the reversed flow region. The spanwise uniformity criterion at the initial measurement plane was defined as deviation of less than one percent in the measured pitot pressure at tunnel midheight during a traverse across the tunnel (excluding a 7.6 cm region at each sidewall). Within the test section the criterion for spanwise uniformity of the flow at each measurement plane was agreement to within five percent of the boundary layer integral properties measured on the test plate centerline and at stations 15.2 cm to either side of the centerline.

Criteria were also defined relative to the two-dimensionality of the separation line and for steadiness of the flow in the test section. A satisfactory two-dimensional separation was defined as a separation line deviating from a straight line by less than 5 percent of the test section span excluding a 7.6 cm region at each sidewall. The criterion for flow steadiness in the test section was defined as the absence of intermittent flow reversal on the contoured wall opposite the test plate and on the test plate outside the separated flow region as indicated by surface mounted tufts.

3.3 Instrumentation

3.3.1 Laser Velocimeter System

The LV system (fig. 3-8) is described in detail in Appendix A. The system consisted of a 2W argon-ion laser, backscatter optical system, counter-

type signal processor, computer for on-line data reduction, and a hard disk storage device for subsequent off-line data reduction. All system components are commercially available.

The LDV was operated in a dual beam or "fringe" mode in which light from the intersection of two incident beams having a wavelength of 0.5145 μm is heterodyned to detect the Doppler shift from an injected seed particle, at the local, instantaneous fluid velocity. In this mode, the LV measures the velocity component in the plane of the incident beams that is perpendicular to the bisector of the beams. The effective shape of the resultant measurement volume is an ellipsoid with major axis in the direction of the bisector of the beams. Sketch A below shows these features and the theoretical measurement volume dimensions assuming that the ellipsoidal surface is defined by the locus of points where Doppler signal amplitude is $1/e^2$ of its centerline value. No direct measurements of the effective measurement volume dimensions were made; they can be affected by signal amplitude and the signal processor threshold level setting. To obtain maximum resolution, the major axis was aligned in the spanwise direction. Resolution of the LV system was high when compared to the relevant dimensions of the experiment. The minor axis of the measuring ellipsoid, d_m, was 1/850 of the inlet boundary layer thickness and the major axis, l_m, was 1/560 of the test section width.

The optical system used a 3.75X beam expander, a relatively wide angle lens (κ = 4.9 deg), and 152 mm dia. optics to produce a sufficiently high signal/noise ratio (SNR) to permit measurements to be made in the backscatter mode. A Bragg cell was used to eliminate directional ambiguity and to provide a 360 deg acceptance angle.

The counter-type signal processor featured user selectable measurement mode, fringe count, validation accuracy, input gain, threshold level setting, and large amplitude signal rejection level. The processor was operated in the continuous (CONT) mode in which a measurement is made each time the minimum number of fringes is counted. The CONT mode was chosen to counter the effects of individual realization biasing (see discussion in Appendix C). Optimal histograms and fast data rates were achieved with the fringe count selector set at 32 and the accuracy limit for data validation set a 2%. The signal gain and large amplitude signal rejection level were adjusted to reject 10 to 25% of the Doppler bursts to ensure that particle lag biasing (which could be caused by large seed particles in the tail of the seed particle size distribution) was eliminated. Data rates of validated signals ranged from 20/sec to more than 2000/sec depending on the region of the flow being measured. Based upon the uncertainty analysis in Appendix C and the large turbulence levels generated by the separation bubble, 2000 samples were acquired per data point to generate velocity histograms for mean velocity and turbulence intensity measurements. For Reynolds stress measurements the previously measured local

20

INCIDENT BEAMS

2𝑥

V

MEASUREMENT VOLUME

d_f

d_m

ℓ_m

MEASURED VELOCITY COMPONENT

N_f(UNSHIFTED) = 44

x = 4.9 deg

d_m = 133 μm
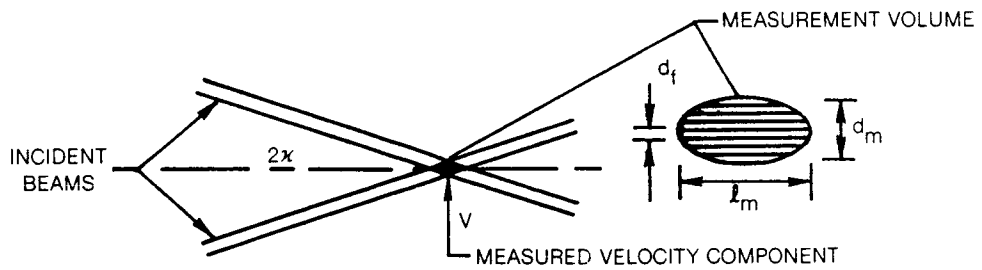
ℓ_m = 1.6 mm

d_f = 3 μm

Sketch A — LDV Beam Arrangement

turbulence intensity was used to determine whether 2000, 4000, or 8000 samples per data point were required to obtain the desired accuracy. Additional details concerning LV data processing are given in Appendix A.

Titanium dioxide powder having a nominal particle size of 1.0 μm dia was dispersed into the tunnel airstream to provide highly reflective light scattering centers for LV measurements using the seeding system described in Appendix A. A mixture of titanium dioxide powder and Cab-O-Sil, a silica deaglomerating agent was fluidized in a low pressure seeder and injected into the tunnel just downstream of the aftermost turbulence suppression screen using a seeder probe designed to minimize the disturbance to the tunnel airstream. Particle lag calculations and LV velocity measurements across a normal shock using similar seeding material (see Appendix C) indicated the 1.0 μm dia titanium seed particles would follow the mean flowfield variations with a lag of less than 0.3 percent throughout the test section. Less than 1 percent error in turbulence intensity was anticipated for turbulence fluctuations below 2.9 KHz.

3.3.2 Total Pressure Instrumentation

The total pressure measurement system, shown in figure 3-9, consisted of total pressure probes described below, a probe traverse system, pressure transducers, signal conditioners and amplifiers, averaging voltmeters, a data logger, an on-line computer, and a micromanometer. The probe traverse system, described in reference 28, consisted of an ball/screw traverse drive suspended on a linear ball bearing track above the test section. Three 0-0.5 psid pressure transducers were used to measure total pressure, test section wall static pressure, and the tunnel dynamic pressure. Transducers were calibrated each day with the micromanometer. The measured pressures were averaged for 100 sec using averaging voltmeters and were recorded together with the tunnel temperature on a data logger.

Two sets of specially designed pitot probes, shown in figure 3-10, were used for total pressure traverses. The two sets, which differed only in the offset distance (1.27 cm or 1.91 cm) from the sensing face to the probe shaft centerline, each consisted of a boundary layer probe for near wall measurement and a kielhead probe for midstream measurements. The boundary layer probe was constructed from .081 cm dia stainless steel tubing flattened to an oval cross-section at the probe face having major and minor axes of 0.122 cm and 0.043 cm respectively. A 0.64 cm dia. brass sleeve plugged the probing port during near wall traversing and was pushed out by and locked into the probe shaft for the remainder of the traverse. The kielhead probe was fabricated from a 0.159 cm dia. aspirated kielhead tube soldered into a 0.064 cm dia. probe shaft. The aspirated kielhead tube contained four 0.038 cm dia. holes equally spaced around its periphery at a distance of 0.191 cm downstream from

22

the probe face and a concentric inner sensing tube (0.038 cm ID). The four aspiration holes functioned in the same manner as the open back end of a conventional kielhead probe by permitting a through flow of air past the sensing tube. The kielhead tube was bent into alignment with the midrange of the mean flow directions anticipated during a traverse to ensure that the flow direction relative to the probe face was within the ± 30 deg acceptance angle determined during probe calibration.

3.3.3 Hot-Film Instrumentation

The hot-film measurement system consisted of a single element hot-film probe, a commercially available constant temperature anemometer system (including a fourth-order polynomial linearizer and a signal conditioner containing high- and low-pass filters), two rms voltmeters to time average the mean and fluctuating output signals, and a spectrum analyzer. The single-element hot-film probes (fig. 3-11) each used an 0.051 cm dia. cylindrical sensor to measure the streamwise mean velocity and turbulence components. Frequency response of the anemometer system was measured to be 65 KHz in a 27.5 m/sec airstream at the 1.5 overheat ratio used in the test program. The unique design of the probe was necessitated by the desire to insert the probe through the same wall on which boundary layer velocity profiles were to be measured. A pin through the probe stem set the minimum stand-off distance at 0.127 cm In the unbraced configuration supplied by the vendor severe "ringing" caused by vibration of support needles was noted during probe calibration. Nonmetallic braces were used to stiffen the support to eliminate ringing.

3.3.4 Flow Visualization

Flow visualization was accomplished during shakedown testing with surface-mounted tufts, "tuft trees", surface flow visualization, and smoke. Tufts were mounted on the test surface in a dense 10 x 14 array to monitor the size and two-dimensionality of the separation bubble, on the diverging wall opposite the test plate to check that the flow remained attached, and on the tunnel sidewalls. A 3 x 3 array of "tuft trees" was mounted vertically between the lower tunnel wall and static pressure taps in the test plate. The "tuft trees" were constructed from stiff 0.089 cm OD stainless steel tubing over which swivel-mounted tufts were slipped and secured in place by short lengths of shrink-fit tubing. Approximately 10 tufts were positioned on each "tree" to visualize the flow in the vicinity of the separation bubble and to estimate the bubble thickness. Surface flow visualization was achieved by injecting red low-viscosity fluid through static pressure taps in the test plate. The smoke flow visualization system, described in reference 29, used a traversible probe upstream of the test section inlet to produce ammonium sulfite smoke by impinging gaseous jets of anhydrous ammonia and sulfur dioxide within the tunnel airstream.

3.4 Measurement Approach

3.4.1 Total Pressure and Hot-Film

Total pressure and hot-film traverses were aligned normal to the test plate. The total pressure traverses were conducted using boundary layer probes over the range 0.025 cm to 5.08 cm from the test plate and kielhead probes were used from 2.54 cm from the plate to the vicinity of the opposite wall. During the total pressure traversing phase, which was conducted before the flowfield had been defined by LV measurements, the flow direction near the reversed flow region was not known a priori at each point in space. There-fore, two sets of traverses were conducted to obtain a complete set of data at each measurement plane. One set of traverses was made with probes facing upstream and the second set made from the adjacent upstream traversing port with the probes facing downstream. Using probes with either 1.27 cm or 1.91 cm offsets to match the 2.54 cm or 3.81 cm probe port separation distance ensured probe face coincidence in the measurement plane. Hot-film traversing was conducted in a similar manner in the vicinity of the separation bubble.

After the hot-film anemometers were checked at the start of each day an additional linearizer adjustment was made to offset the effects of hot-film aging. The hot-film sensor was positioned at the x = 7.6 cm, y = 10.2 cm location in the tunnel where the streamwise velocity was known to equal 0.9925 of the freestream velocity calculated from rig operating conditions. After the linearizer output gain was adjusted to yield the desired velocity, the probe was moved to the next scheduled traverse location.

3.4.2 Laser Velocimeter

The four LV beam orientations, designated 0, 90, and ± 45 deg, used to measure U, V, $\sqrt{\overline{u^2}}$, $\sqrt{\overline{v^2}}$ and $\overline{uv}$ are shown in figure 3-12. The direction of motion of the Bragg-shifted fringes is also indicated in the figure. In the 0 deg orientation the vertical fringes measure only the horizontal, U, velocity component. In the 90 deg orientation the horizontal fringes measure only the vertical, V, component. In the ± 45 deg orientations, $\sqrt{2}$ (U ± V), is measured from which $\overline{uv}$ can be obtained using the equations derived in Appendix B.

Because of the 9.8 deg included angle between the laser beams, the optical axis was inclined 5 deg relative to the horizontal test plate surface for measurements of V, $\sqrt{\overline{v^2}}$ and $\overline{uv}$ near the test surface (y ≤ 2.54 cm). The inclination of the fringes relative to horizontal introduced a negligibly small uncertainty in the acquired velocity measurement due to the component of the transverse velocity. The 90 deg orientation measured V cos 5° + W sin 5°. The ± 45 deg orientations measured $\sqrt{2}$ (U ± V cos 5° ± W sin 5°). The data reduction equations required to extract V, $\sqrt{\overline{v^2}}$ and $\overline{uv}$ from these measured quantities are derived in Appendix B.

24
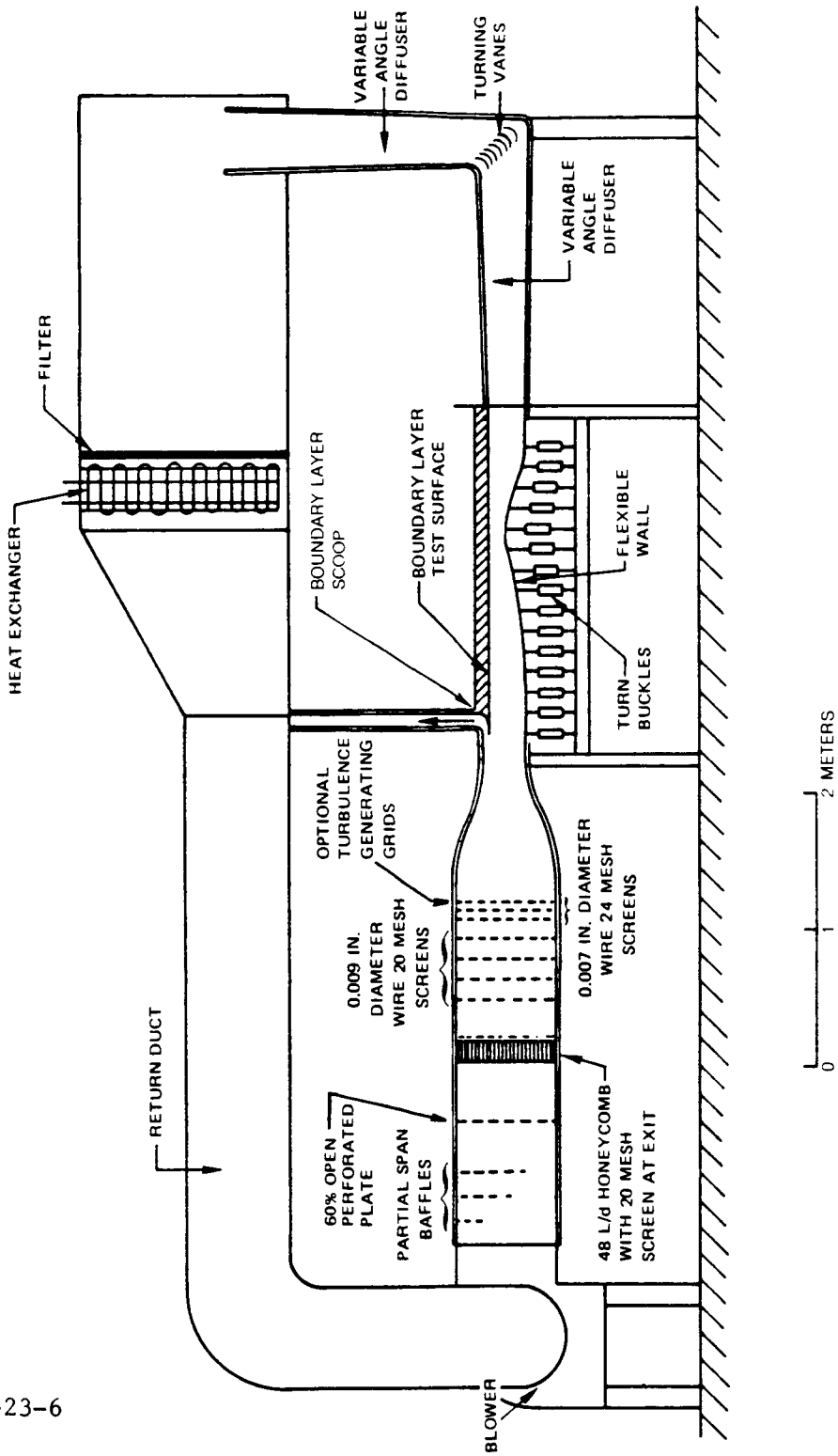
Figure 3-1   United Technologies Research Center Boundary Layer Wind Tunnel

85-2-23-6

25
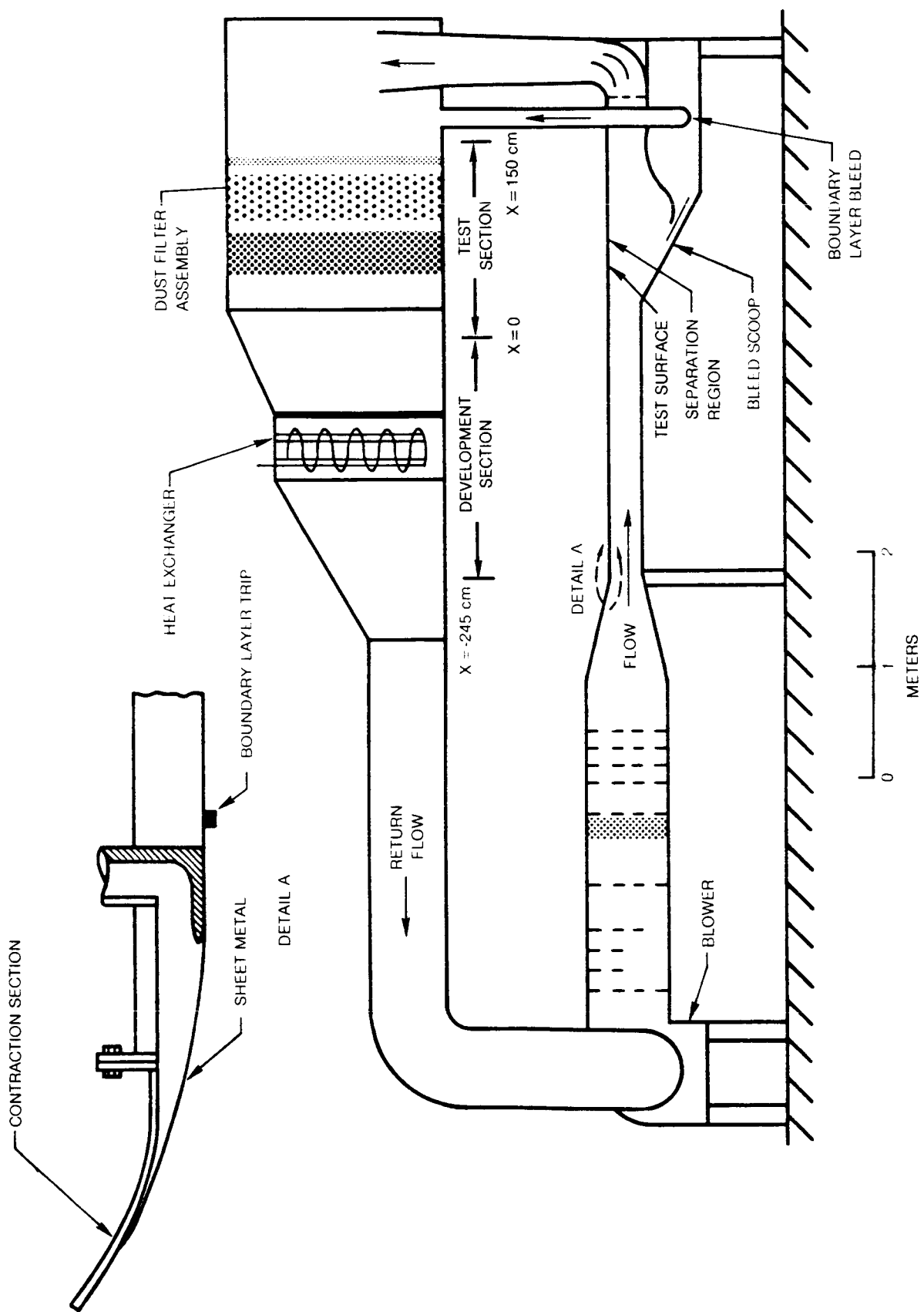
Figure 3-2 Modified Boundary Layer Wind Tunnel
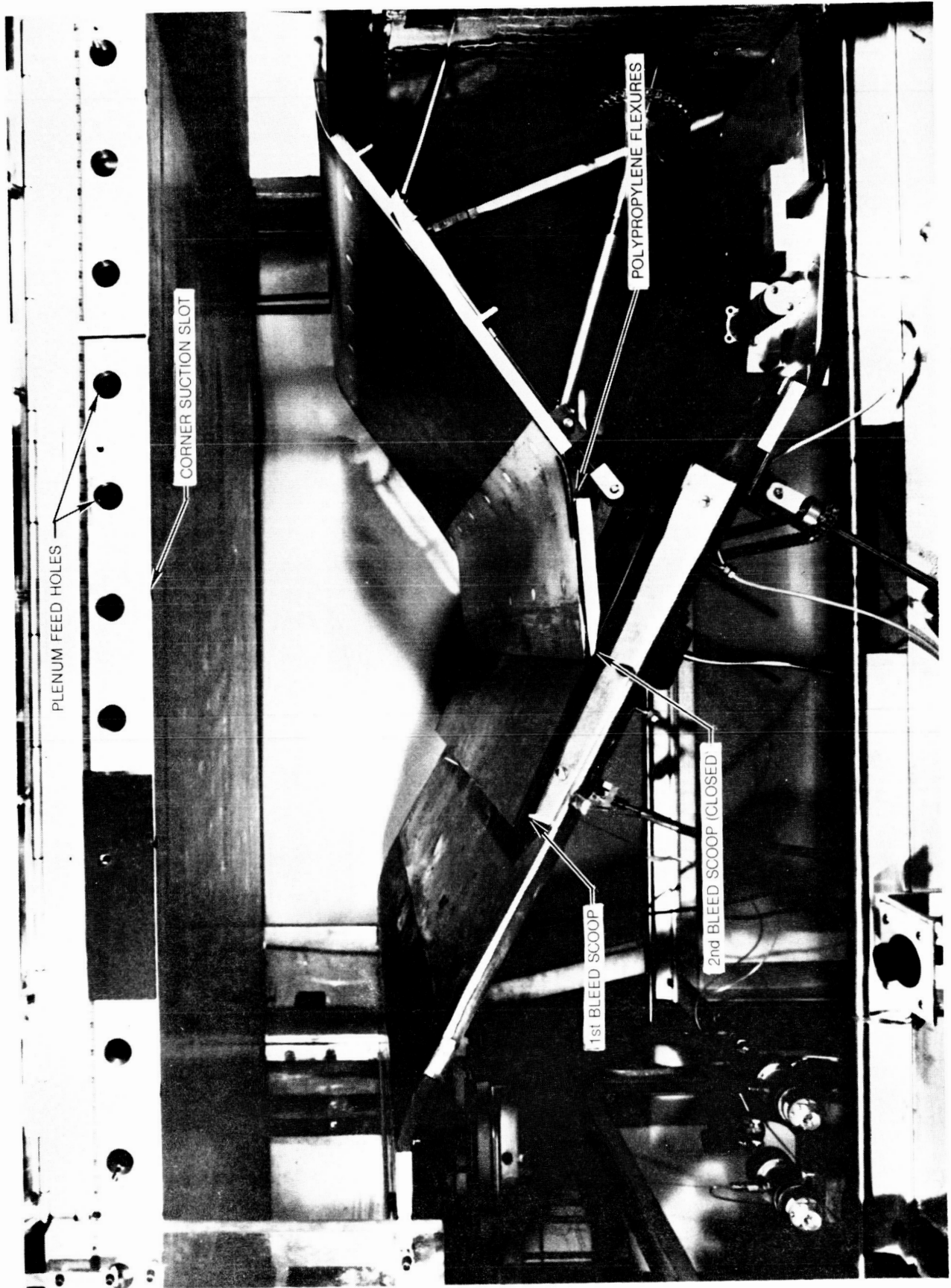
Figure 3-3 Turbulent Boundary Layer Separation Test Section

27

SUBMICRON
FILTER HOUSING

SIDEWALL
BLEED SYSTEM

LOWER WALL
SUCTION SYSTEM
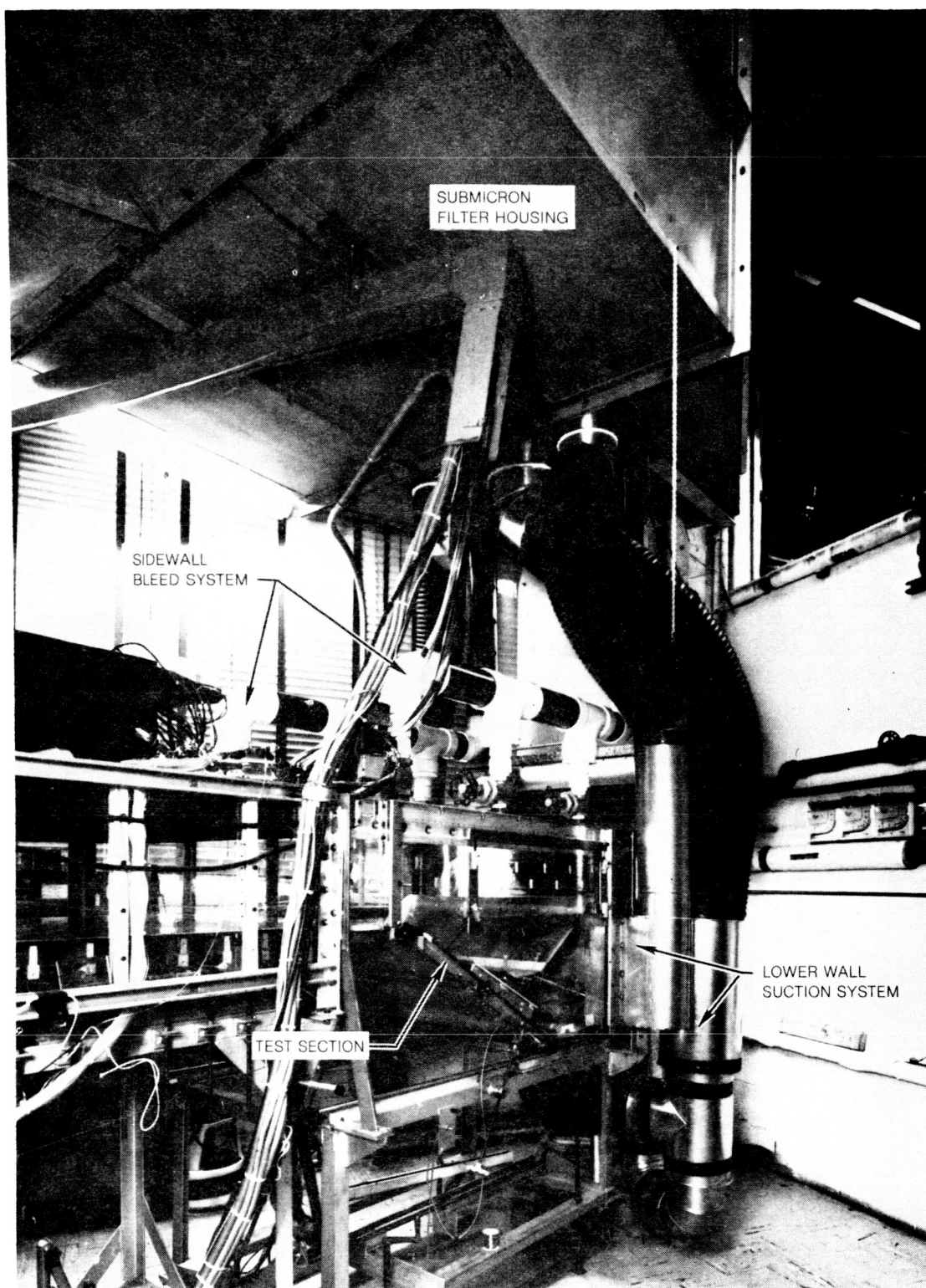
TEST SECTION

Figure 3-4 Turbulent Separation Bubble Test Section Installed in UTRC Boundary
Layer Wind Tunnel

82-10-80-1

28

DUCTING FOR
LOWER WALL
BLEED SYSTEM

SIDEWALL
BLEED
SYSTEM

PLENUM
CHAMBERS

STATIC PRESSURE TAPS
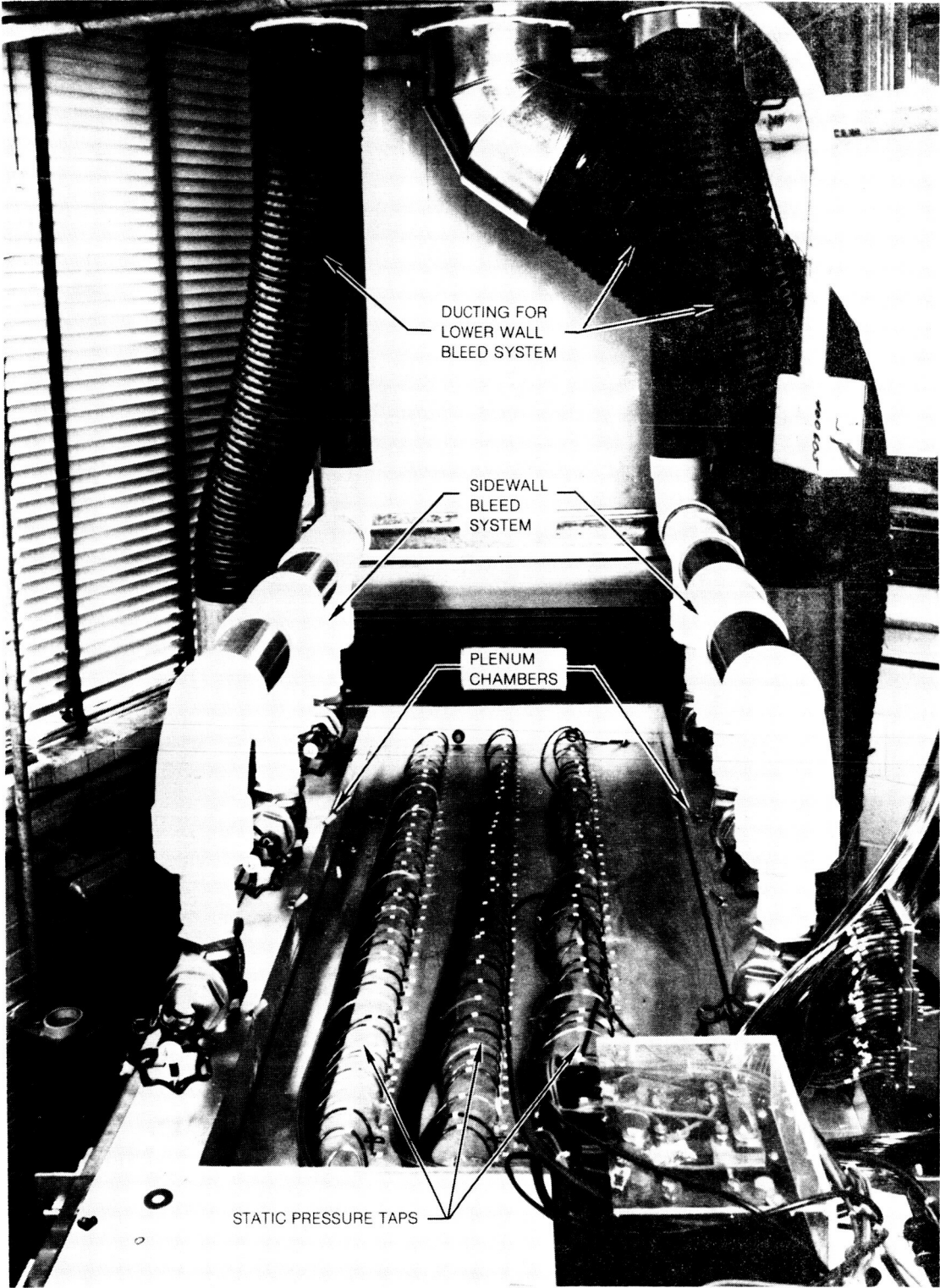
Figure 3-5   Top of Test Section

82-10-80-3

29
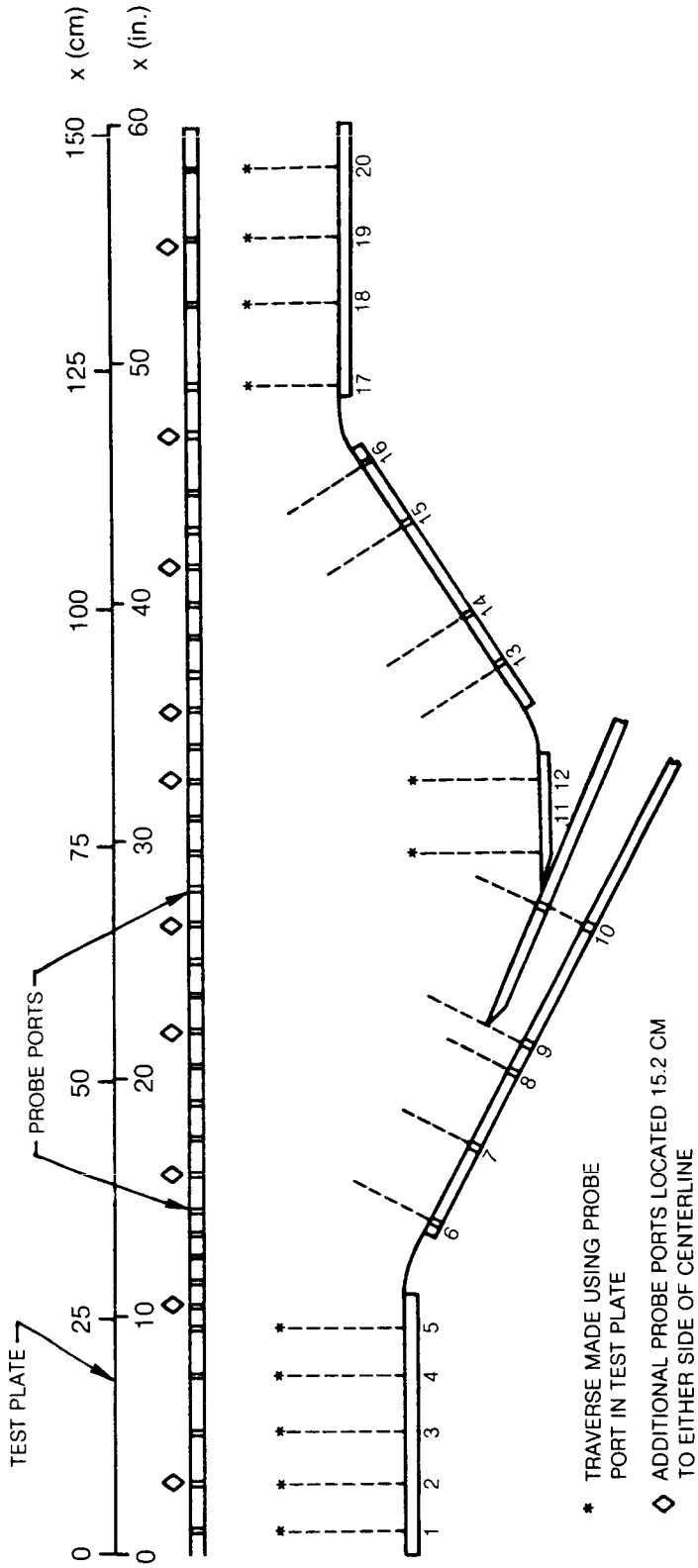
Figure 3-6   Probe Port and Lower Wall Traverse Locations (Test Section Centerline)

* TRAVERSE MADE USING PROBE
  PORT IN TEST PLATE

◇ ADDITIONAL PROBE PORTS LOCATED 15.2 CM
  TO EITHER SIDE OF CENTERLINE
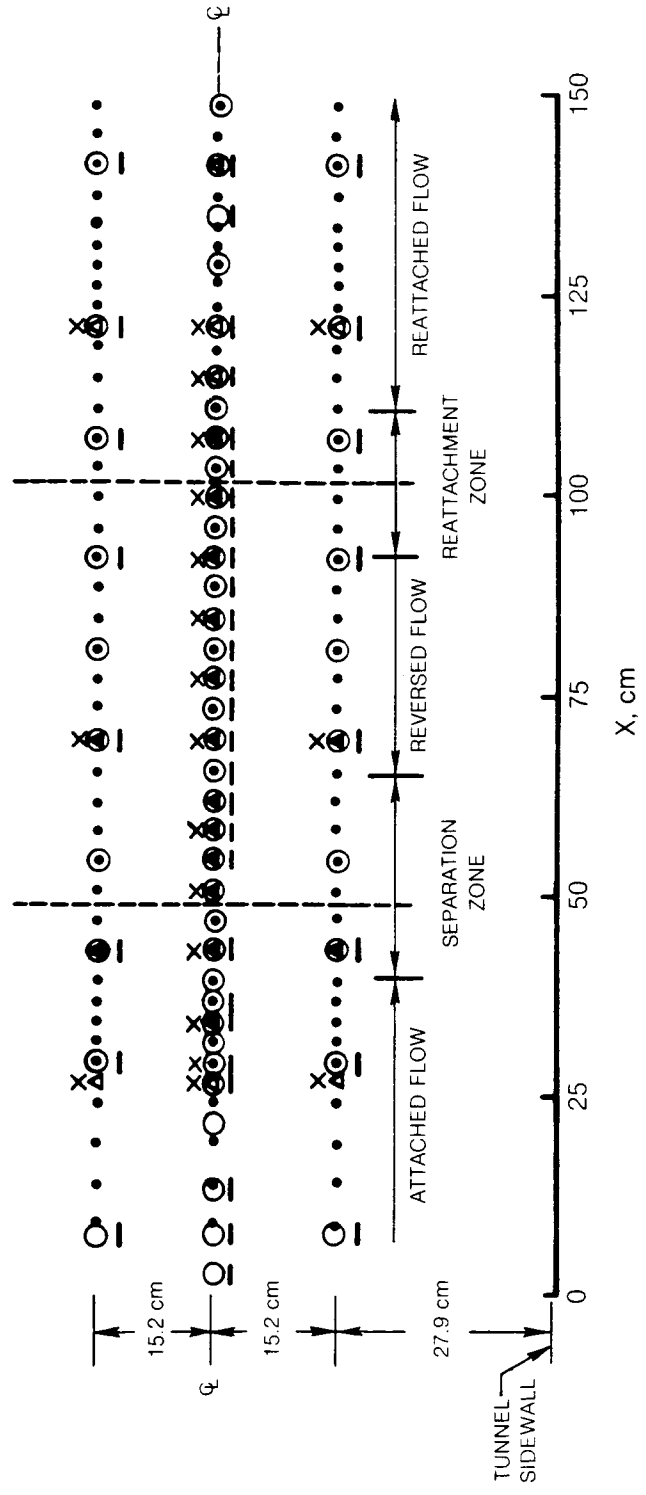
Figure 3-7 Measurement Locations on Test Plate

84-8-1-2

31
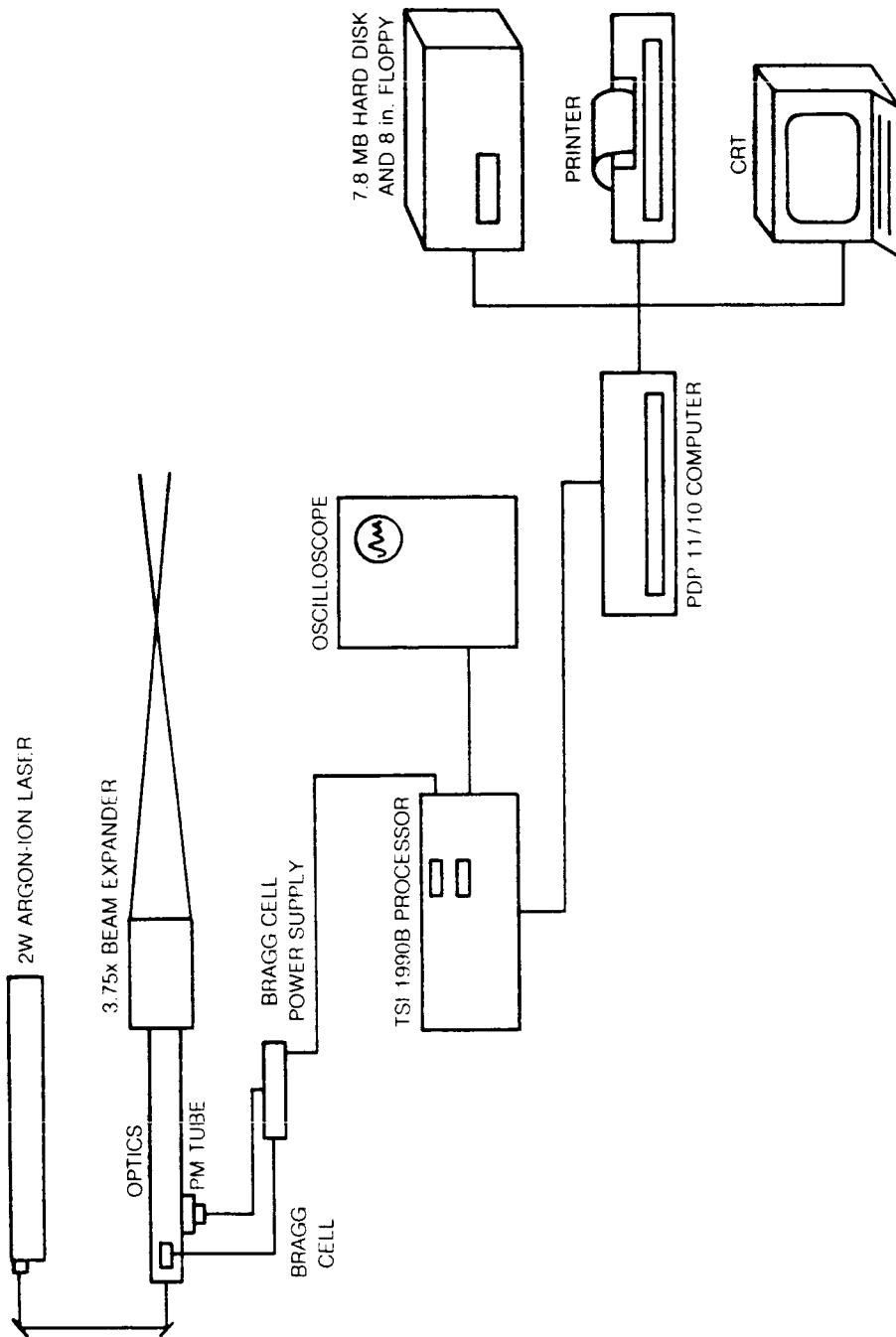
Figure 3-8 Laser Velocimeter Data Acquisition System
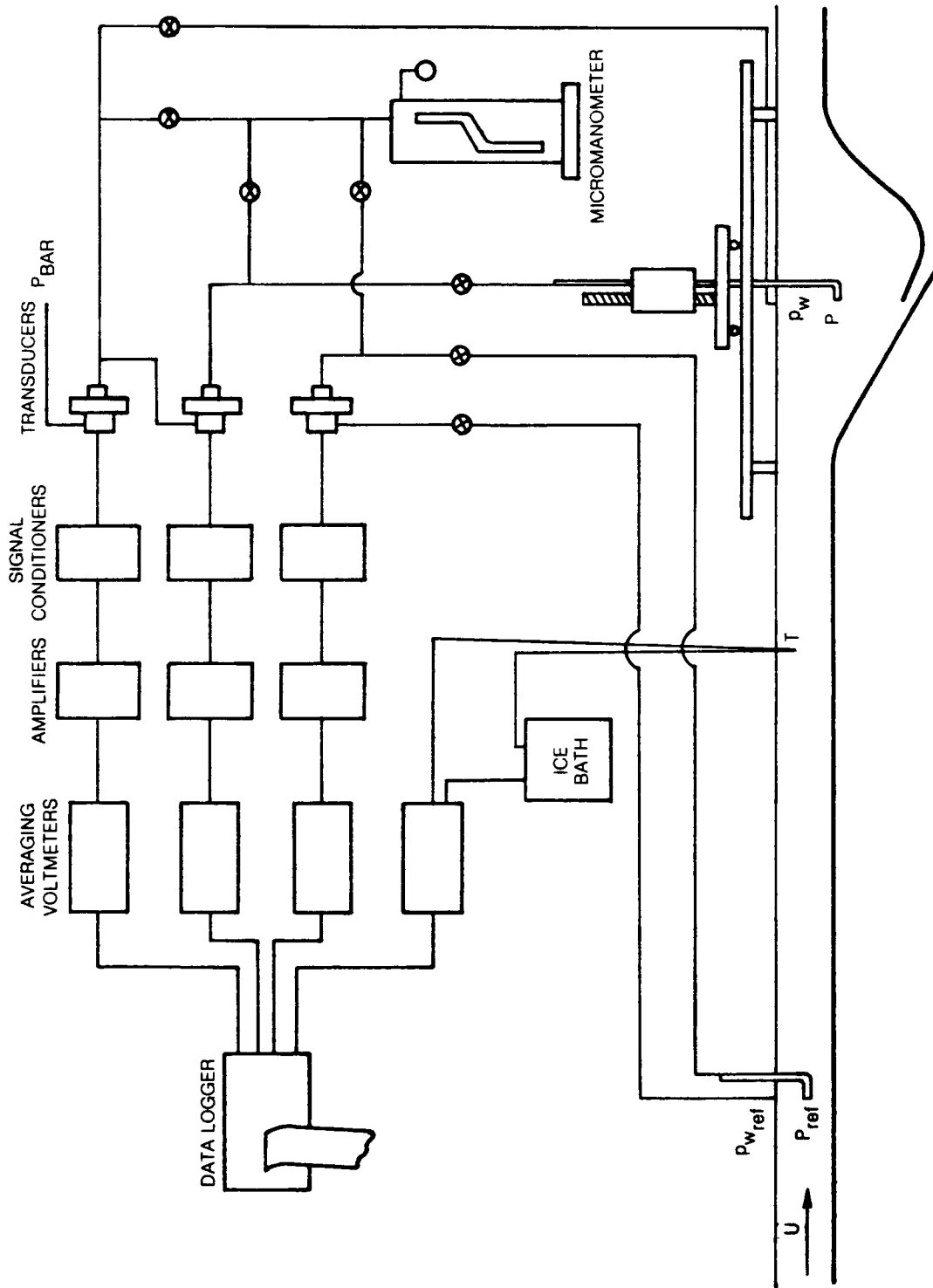
Figure 3-9 Total Pressure Measurement System
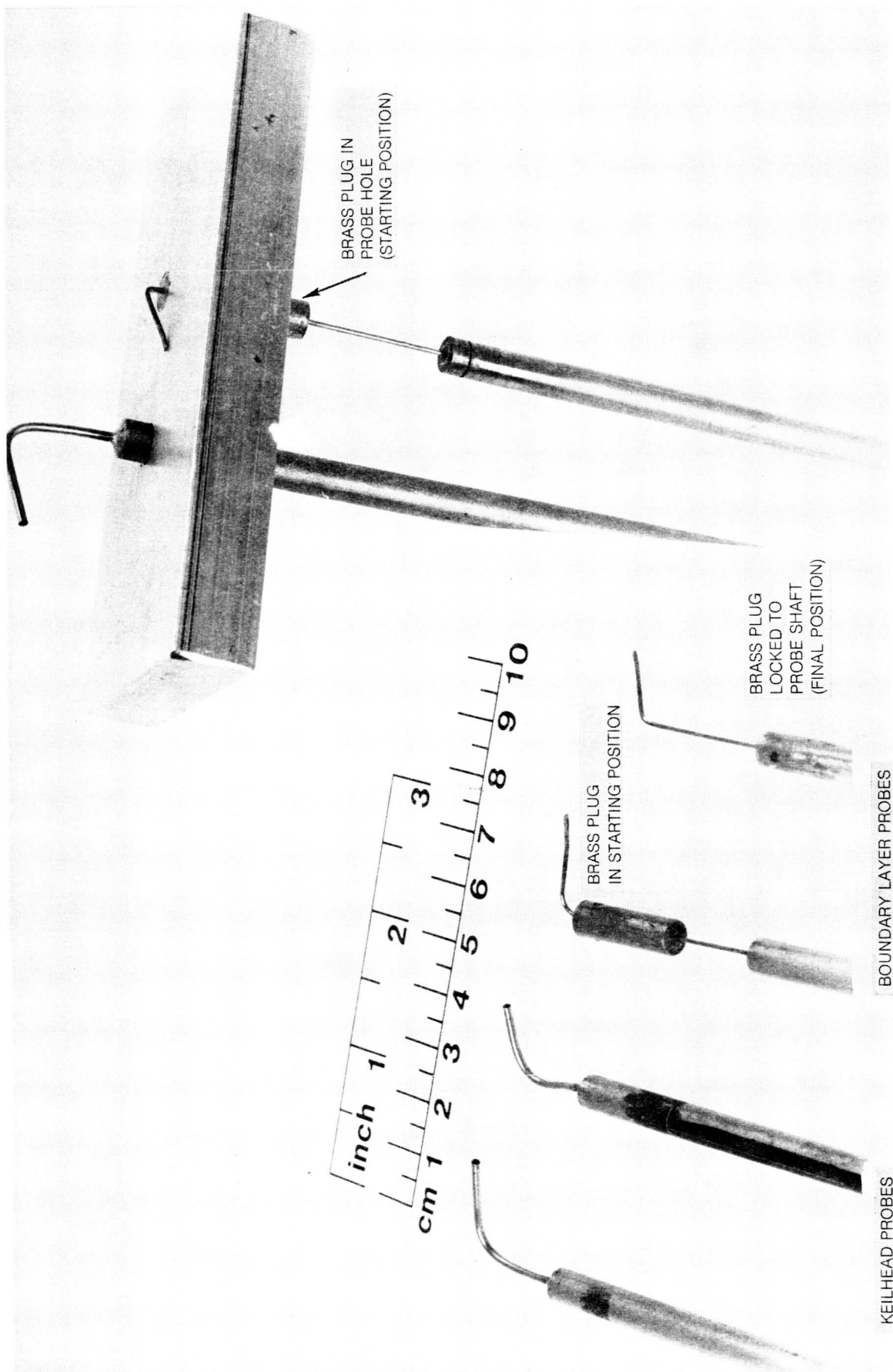
Figure 3-10 Total Pressure Probes

BRASS PLUG IN
PROBE HOLE
(STARTING POSITION)

BRASS PLUG
LOCKED TO
PROBE SHAFT
(FINAL POSITION)

BRASS PLUG
IN STARTING POSITION

BOUNDARY LAYER PROBES

KEILHEAD PROBES

84—8—1—49

NONMETALLIC
BRACES

BRACED CONFIGURATION

UNBRACED CONFIGURATION
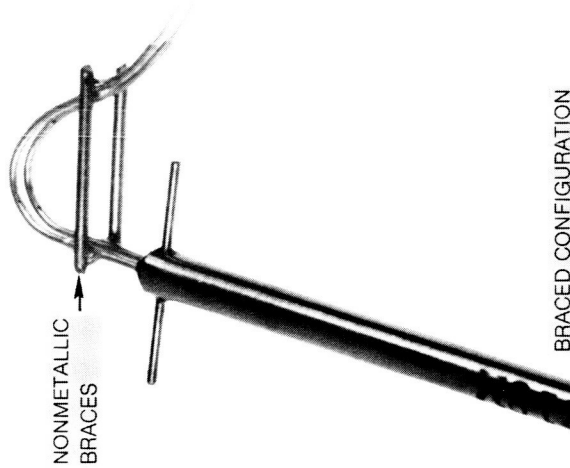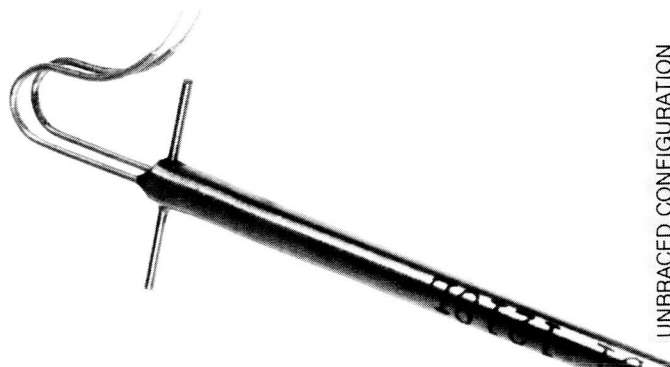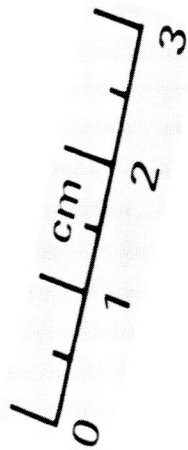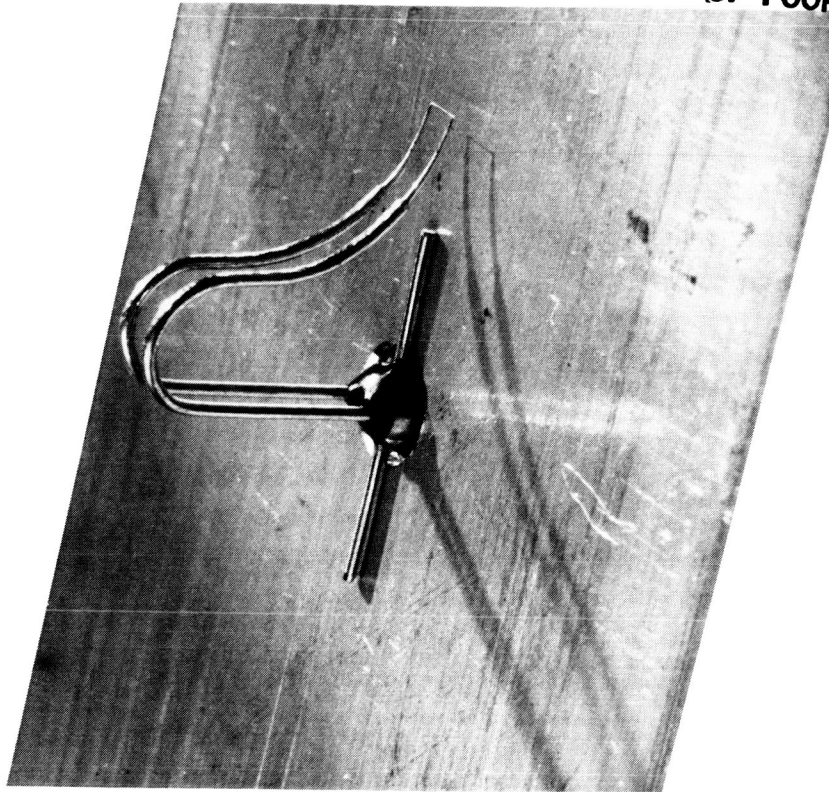
Figure 3-11 Hot-Film Probes
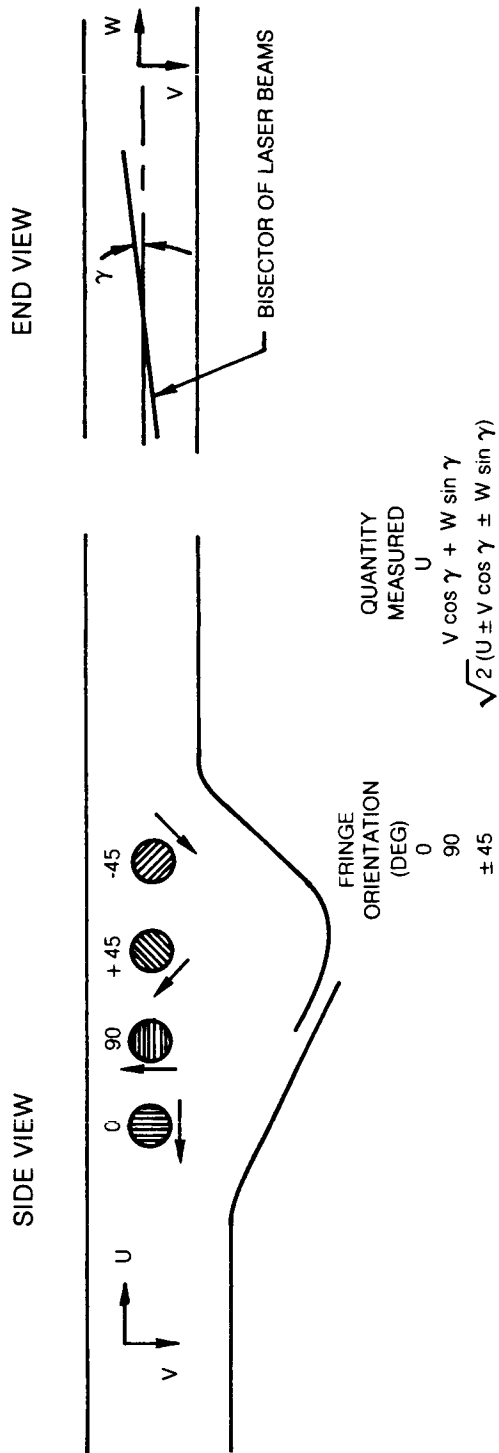
Figure 3-12 LV Measurement Orientations

END VIEW

BISECTOR OF LASER BEAMS

SIDE VIEW

FRINGE ORIENTATION (DEG)	QUANTITY MEASURED
0	U
90	$V \cos \gamma + W \sin \gamma$
±45	$\sqrt{2} (U \pm V \cos \gamma \pm W \sin \gamma)$

CHAPTER 4

RESULTS

4.1 Data Presentation

Velocity and pressure data obtained in this study are presented in both tabular and graphical format. Velocity data have been normalized by the free-stream velocity, U_{ref}, at the tunnel reference location ($x = -156$ cm) in the constant velocity approach section upstream of the test section. U_{ref} equaled 27.05 m/sec (88.75 ft/sec) at nominal tunnel operating conditions ($T_{ref} = 22.2°C$, 72°F and $p_{ref} = 780$ mm Hg, 15.06 psia where p_{ref} was the sum of the tunnel static pressure relative to ambient (18 mm Hg, 10 in H_2O) and the barometric pressure (762 mm Hg)). U_{ref} was adjusted to maintain constant unit Reynolds number at the reference location when tunnel conditions deviated from nominal. Static pressures are referenced to the tunnel static pressure at the reference location. Total pressures were normalized by the freestream dynamic pressure, Q_{ref}, at the reference location. The coordinates used for presentation of results are x, distance downstream from the start of the test section (see figure 3-6), y, transverse distance from the test plate, and z, spanwise position relative to the wind tunnel centerline.

Presentation of the results in the following sections starts with a description of the flow conditions at the initial measurement plane. Then, the results of smoke, tuft, and surface flow visualization are presented to provide an overall understanding of the test section flowfield. Detailed presentations are then made of the test surface static pressure distribution, the mean velocity field, turbulence velocity field, Reynolds stresses, and total pressures throughout the test section.

4.2 Initial Plane Boundary Conditions

To provide data required to start computational codes, an initial measurement plane was chosen well upstream of the region of influence of the adverse pressure gradient and the resulting separated boundary layer. Although such codes should be capable of proceeding downstream from an arbitrary initial profile, the approach geometry for the present study produced a boundary layer having characteristics generally similar to an equilibrium turbulent boundary layer, as discussed below. The initial measurement plane was located in the boundary layer development section 24.1 cm (9.5 in) upstream of the test section inlet. This location, which was 2.5 duct heights upstream of the start of the diverging section, was chosen because test surface static pressure measurements, described subsequently,

showed that the adverse pressure gradient extended less than 1.5 duct heights
upstream of the divergence. Pitot probe traverses, both transverse and span-
wise, were taken to define the flow uniformity in the initial measurement
plane. Hot-film anemometry was used to define profiles of the mean velocity
and the axial turbulence component in the test surface boundary layer.

The measured total pressure distribution is shown in figure 4-1. The
spanwise pitot traverse taken at the tunnel mid-heighth showed the total
pressure variation to be less than ± 0.5 percent of the dynamic head over the
central 90 percent of the span which was outside the sidewall boundary layers.
A transverse (vertical) pitot pressure traverse at mid-span was used to define
the boundary layers on the test (upper) surface and the lower surface. The
boundary layer edge was defined as the location at which the measured total
pressure equaled 99 percent of the freestream total pressure (equivalent to
δ_{995} determined from velocity measurements). The boundary layer on the test
surface, which was tripped at the start of the boundary layer development
section (fig. 3-2), measured 7.67 cm (3.02 in) whereas the untripped lower
wall boundary layer had a thickness of 3.56 cm (1.4 in), leaving a 9.9 cm
(3.9 in) thick inviscid core. Integral properties calculated for the boundary
layer on the test surface at the initial measurement plane are tabulated
below:

Displacement thickness, $\delta^* = .799$ cm
Momentum thickness, $\theta = .631$ cm
Shape factor, H = 1.27
Momentum thickness Reynolds no. = 11,100

The measured shape factor of 1.27 was somewhat less than the value of
1.32 quoted by Coles (ref. 30) for a constant pressure turbulent boundary
layer at the measured momentum thickness Reynolds number of 11,100. The
velocity profile of the test surface boundary layer was found to be in good
agreement with the "law-of-the-wall." In figure 4-2a the profile is plotted
in "law-of-the-wall" (U^+ vs. y^+) coordinates. To obtain figure 4-2a the fric-
tion velocity, U_τ, was chosen to minimize the least squares fit to the
equation

$$U^+ = \frac{U}{U_\tau} = \frac{1}{0.41} \ln y^+ + 5.0 \qquad (4-1)$$

where $y^+ = \frac{yU_\tau}{\nu}$ as recommended by Coles (ref. 30) over the log-linear region of
the profile (50 < y+ < 500). Then the skin friction coefficient could be
calculated from the equation $C_f = 2U_\tau^2/U_{ref}^2$ since $U_\tau^2 = \tau_w/\rho$. Data in the outer
region of the boundary layer deviated from the logarithmic portion as

expected. The maximum deviation, ΔU^+, referred to as the "strength of the wake component" was approximately 1.4. This was less than the value of 2.7 quoted by Coles for an equilibrium turbulent boundary layer having the same momentum thickness Reynolds number.

The measured streamwise turbulence intensity (normalized by boundary layer edge velocity and plotted versus y/δ_{99}) is shown in figure 4-2b to be in good agreement with the turbulence profile presented by Klebanoff (ref. 31) for a flat plate equilibrium turbulent boundary layer. In addition to overall rms measurements, spectra (0-20 KHz) were taken routinely at each hot-film measurement point to ensure that the hot-film signal was free of discrete frequency spikes associated with sensing element vibration.

4.3 Flow Visualization

To optimize the two-dimensionality of the separation bubble, during initial flow visualization testing, surface-mounted tufts and tuft trees (installed in the test section and described previously in Section 3.2) were monitored while adjustments were made to the divergence angle of the lower wall, the boundary layer bleed scoops, and the axial distribution of suction in the test surface sidewall bleed slots. It became apparent that two-dimensionality could only be achieved using a large divergence angle and suction in both the lower wall bleed scoop and the corner bleed slots. This configuration resulted in a long, thick separation bubble having minimal three-dimensionality.

Since the technique of achieving the bubble configurations employed in this experiment may be of interest, some initial exploratory studies will be described. By varying lower wall divergence angle and suction arrangements for the two lower wall slots, a range of bubble configurations could be produced. While the overall bubble length was effectively set by the axial separation of the lower wall divergence and convergence points, bubble thickness could be reduced by decreasing the divergence angle. This tended, however, to produce a more unsteady flow and greater spanwise variation in the separation line. This does not imply that thinner bubbles are inherently more unsteady, rather that a smaller adverse gradient will increase the axial length over which the random process of intermittent separation can occur. The configuration producing the highest degree of bubble two-dimensionality in the present experiment was found to be one in which the divergence angle was increased to the maximum value ($\alpha = 28$ deg) for which slot suction could hold the boundary layer attached to the lower surface. Although the resulting thick bubble caused significant streamline curvature in the x-y plane with resultant transverse static pressure gradients, the strong-adverse-pressure-gradient, strong-suction configuration was considered superior for providing

39

benchmark quality data for code verification and development compared to a configuration producing a shorter, thinner bubble having unknown three-dimensional contamination.

Tuft flow visualization of the test surface is shown in figure 4-3. The five zones of the separation and reattachment process (attached flow, intermittent separation, reversed flow, the reattachment zone, and reattached flow) are clearly evident to the eye but are obscured somewhat in the photography. The inset, taken from a movie made during flow visualization testing, shows a closeup view of the tufts within the reversed flow region to illustrate the strong reversed flow across the entire tunnel span within the separation bubble. The maximum thickness of the reversed flow region within the separation bubble as indicated by the direction of the tufts on the "tuft trees" which extended from the upper to the lower surface was estimated to be 8 cm (3.1 in). Also indicated by the "tuft trees" is the curvature of the free-stream flow convecting over the separation bubble. Surface mounted tufts on the lower wall confirmed that the boundary layer along the lower wall remained attached throughout the test section.

In figure 4-4 the five zones of separation are depicted more clearly. In the attached flow region all the tufts were steady and pointed downstream. Within the intermittent separation zone, tufts fluctuated in direction between upstream and downstream. In the reversed flow region, tufts in the central 60 percent of the span were steady and pointed upstream. In the reattachment zone, the tufts fluctuated in direction between upstream and downstream as the reattachment point shifted in a random, intermittent manner. In the reattached flow the tufts again pointed downstream but jittered due to high turbulence levels in the wake of the separation bubble.

Photographs of the smoke flow visualization obtained while traversing the single-headed smoke probe vertically at inlet station 0 (x = -24.1 cm, -9.5 in) are shown in figure 4-5. For the first photograph (fig. 4-5a) the smoke probe was positioned 10 cm below the test surface (y_o = 10 cm) just outside of the 7.67 cm thick boundary layer at the initial measurement plane. The smoke filament flowed smoothly through the test section but was displaced downward by the separation bubble on the test surface. Note that the axial extent of the separation bubble as indicated by tufts mounted on the test surface is marked on the photographs. At y_o = 7.6 cm (a location corresponding to the edge of the boundary layer at the initial measurement plane where the smoke was injected) the filament continued to flow smoothly around the bubble (fig. 4-5b), indicating that it was in the low turbulence, inviscid freestream. However, at y_o = 6.4 cm (fig. 4-5c) the upper edge of the smoke filament became entrained in the turbulent shear layer surrounding the separation bubble. Near reattachment the smoke filament appears diffuse due to unsteady flapping of the filament lines in that region. When the smoke filament

impinged upon the test surface it was observed that the filament would alternately be ingested into the recirculation region at the aft end of the bubble or be convected downstream. With the smoke probe positioned near the upper wall (y_o = 5.1 cm, fig. 4-5d) the smoke filament became more entrained in the separation bubble. Much of the entrainment occurred in the free shear layer surrounding the bubble as shown in the photograph where a large eddy is being entrained into the bubble in addition to the flow being ingested into the bubble near reattachment. Once within the bubble, the smoke dispersed rapidly causing the smoke density within the bubble to be too low to be seen in the photograph although the smoke was visible as a diffuse haze to the eye.

Flow directions determined from tuft trees, surface tufts, and smoke flow visualization were used to map the streamline pattern throughout the test section (fig. 4-6). The reversed flow region was quite large, being approximately 50 cm long with a maximum thickness of 8 cm. Streamlines upstream of the separation zone were steady and parallel. Near reattachment the streamline pattern for the mean flowfield could only be approximated because of unsteady flapping of the flow-field.

To determine the degree to which a two-dimensional separation had been achieved, tufts were removed from the test section and a low-viscosity red dye was injected through static pressure taps on the test surface (fig. 3-7 shows tap locations). The measurements confirmed the straightness of the separation line indicated by the surface mounted tufts earlier. However, the determination of a quantitative measure of the straightness of the separation line was difficult because the low wall shear in the vicinity of separation barely moved the injected dye. After testing, a sheet of exposed blueprint paper was rolled over the test surface to lift off the dye streaks for permanent storage and subsequent analysis. The dye patterns were interpreted later with the aid of LV measurements of the forward flow fraction (see Section 4.6.1 "Forward Flow Fraction Measurements") at centerline and off-centerline locations near the test surface. Good correlation between a forward flow fraction of 0.5 and lack of motion of the injected dye was obtained. The separation line (i.e. location of transitory detachment) was determined from the dye patterns and interpolation of forward flow fraction data to be straight. The angle of inclination of the straight separation line was 7 degrees with respect to the perpendicular to the tunnel centerline with separation occurring further upstream on the west side of the span ($z > 0$) than the east side ($z < 0$). This 7 degree inclination angle corresponds to a deviation from the line perpendicular to centerline of ±6 percent of the span which is reasonably close to the ±5 percent objective.

4.4 Test Surface Static Pressure Distribution

The static pressure distribution on the test surface measured along the tunnel centerline is shown in figure 4-7. The results are presented in the form of a non-dimensional pressure coefficient defined as

$$C_p = \frac{p_w(x) - p_{w_1}}{Q_{ref}} \qquad (4-2)$$

where $p_w(x)$ is the wall static pressure at any x location, p_{w_1} is the wall static pressure measured by the first static pressure tap in the test section (x = 6.35 cm) and Q_{ref} is the dynamic pressure. Also shown in the figure are streamlines determined from flow visualization testing and curves estimating the C_p distribution at separation and reattachment based on an analysis by Perry and Fairlie (ref. 5).

The static pressure on the test surface began to rise downstream of the test section inlet (x > 10 cm) due to the upstream influence of the 28 deg lower wall divergence which began at x = 30 cm and created a strong adverse pressure gradient. At x = 40 cm C_p reached a value of 0.36 and the boundary layer separated. The wall static pressure remained constant under the separation bubble except near reattachment where the impingement and partial stagnation of the reattaching flow caused C_p to increase to 0.50 on the test surface. Downstream of reattachment C_p decreased rapidly as the flow accelerated in the converging test section leading to the outlet duct. Near the test section exit C_p approached a constant value of 0.22 due to the net diffusion which occurred in the flow between the inlet and outlet of the test section. As shown in the streamline patterns drawn in figure 4-7, when the flow which was removed from the test section via the lower wall bleed scoop is excluded from consideration, the effective inlet height, h_{in}, of the test section was less than the outlet height, h_{out}, resulting in a net flow diffusion within the test section.

Perry and Fairlie noted that the C_p distribution near separation and reattachment could be approximated by parabolae which were defined by the separation (or reattachment) angle, ϕ, and the nondimensional vorticity, $\hat{\omega}$

$$\tan \phi = \pm 2 \left(-\frac{\partial^2 C_p}{\partial x^2} \right)^{1/2} \Big/ \hat{\omega} \qquad (4\text{-}3)$$

The parabolae shown in figure 4-7 were estimated using measured values of the C_p distribution and separation and reattachment angles estimated from the streamline patterns calculated below from LV data (fig. 5-3). The vorticity was assumed to be constant along the mean dividing streamline and was estimated to be the value which resulted in the best parabolic fit to the measured C_p distribution at reattachment.

Test surface static pressure distributions were also measured at off-centerline locations as one of the diagnostics for establishing the degree of flow two-dimensionality. Results of the off-centerline are tabulated in Table IV beginning on page 192.

4.5 Mean Velocity Field

The velocity field within the test section was measured with a laser velocimeter (LV) and a single-component hot-film probe. The LV measured axial and transverse velocity components separately whereas the hot-film probe measured the magnitude of the velocity vector in the x-y plane. Hot-film measurements were made to provide a degree of redundancy in the measurement of the velocity field and to provide information about the unsteady nature of the flowfield. Additional hot-film measurements were made at stations upstream and downstream of the separation bubble where optical inaccessibility pre-vented LV measurements. All hot-film data, including data obtained in regions of intermittent flow reversal where the measurements are known to be inaccur-ate, are presented in Table V. The hot-film velocity data is presented nondimensionally as U_{eff}/U_{ref} and u_{eff}/U_{ref} where U_{eff} and u_{eff} are the mean and rms values of the effective cooling velocity measured by the hot-film probe which was aligned such that the sensor axis was parallel to the z-axis. Comparison of these data to the more accurate LV data could prove useful in evaluating separation bubble data obtained by other investigators using the hot-wire/film technique. A comparison between hot-film and LV data obtained at selected stations during this test program is presented in Appendix D. Error bounds for the LV measurements determined using the error analysis developed in Appendix C are presented in Table C-5. The complete set of LV data including mean velocity components, turbulence components, forward and transverse flow fractions, and Reynolds stress measurements are presented in Tables II and III. Error bounds for pitot and hot-film measurements are given in Appendix D. The velocity data presented below will consist almost entirely

of LV data except for hot-film data obtained at stations where LV measurements could not be made due to optical inaccessibility.

Velocity vectors determined from LV measurements taken on the wind tunnel centerline have been plotted in figure 4-8 to show the mean flowfield in the test section. Several features of the flowfield are notable. First, the size and location of the separation bubble are in agreement with the flow visualization results. Separation (i.e., U < 0 near the wall) occurred at approximately x = 45 cm with reattachment (i.e. U > 0 at y > 0) at x = 100 cm resulting in a 55 cm long separation bubble. The strong recirculation within the separation bubble is readily apparent. The maximum thickness of the reversed flow region is almost 9 cm (i.e., slightly larger than the 8 cm thickness indicated from flow visualization) causing a significant displacement and curvature of the freestream flow. Second, near the leading edge of the bubble at 45 cm < x < 60 cm, a strong free shear layer is evident between the reversed flow near the surface and the displaced boundary layer. Finally, at 90 cm < x < 100 cm, the flow vectors impinge nearly vertically onto the test surface. This impingement caused the peak in the surface static pressure at reattachment which has been discussed in the previous section.

4.5.1 Axial Velocity Measurements

Axial velocity profiles nondimensionalized by U_{ref} are presented in figure 4-9. All data were obtained from LV measurements except the data at Station 1 (x = 2.54 cm) which are streamwise velocity components measured with a hot-film probe.

The general mean flow characteristics of the separation-reattachment process are evident in this figure. Retardation of flow near the wall is evident downstream of Station 6 with detachment occurring at Station 13. Within the reversed flow region, shown bounded by a dashed line, peak velocities are observed near the wall although retardation of the reversed flow at the surface is evident in the forward half of the region. Outside of this reversed flow region significant (apparent) profile adjustments are observed over the axial extent of the reversed flow zone. Downstream of Station 26 reattachment occurs with the development of a new boundary layer downstream suggested by the near-wall data points.

More detailed axial velocity profiles are presented in figures 4-10 a-d. In these figures the axial velocity profiles are plotted in the non-dimensional form U/U_e vs. y/δ where U_e is the local boundary layer edge velocity at $y = \delta$ determined from laser velocimeter measurements and δ is the local boundary layer thickness determined from total pressure traverses as described below in Section 4.9. The data are plotted using semilogarithmic coordinates near the wall ($y/\delta < 0.1$) and linear coordinates outside the near-wall region to permit the closely spaced data points in the near-wall region

to be presented clearly. The profiles are also displaced for clarity.
Symbols adjacent to left and right borders show individual profile ordinates
of zero and 1.0, respectively. By comparing the profiles in part (a) to the
zero values the retardation of the near wall layer between Stations 0 and 11
is evident. Part (b) of the figure shows that at Station 13 a maximum
reversed flow velocity of 0.10 U_e (0.075 U_{ref}) has been measured. The maximum
reversed flow velocity at each station increases monotonically with distance
downstream until Station 22 (located approximately 2/3 of the bubble length
aft of the detachment location) where a value of 0.397 U_e (0.202 U_{ref}) is
reached. As shown in part (d) of the figure, reattachment and the resumption
of downstream flow occurs between Stations 26 and 28. At Stations 15 through
24 values of U/U_e greater than unity were measured within the boundary layer
($y/\delta < 1$). These results, caused by normal static pressure gradients produced
by flow curvature in the test section, are analyzed in Sec. 5.3.2.

4.5.2 Transverse Velocity Measurements

Nondimensional transverse velocity profiles, y/δ vs V/U_{ref}, obtained
from LV measurements are presented in figures 4-11 a-c. Positive transverse
velocities correspond to flow away from the test surface. Figures 4-11a and
4-11b show that at Stations 6 through 16 in the upstream half of the test
section, the transverse velocity, V, increases monotonically with y/δ as the
flow moves away from the test surface. Positive transverse velocities within
the reversed flow region are consistent with the expected counter clockwise
bubble recirculation pattern. Downstream of Station 16 the transverse
velocity component decreases to a value near zero at Station 20. Downstream
of Station 20 negative transverse velocity components are measured indicating
flow toward the test surface. As shown in figure 4-11b and 4-11c the compo-
nents exceed 40 percent of U_{ref} in the reattachment zone located in the vicin-
ity of Stations 28 and 30. At Station 34 in the exit duct the transverse
component magnitude has decreased to the 0-5 percent range.

In summary, the measurements show that significant transverse velocity
component magnitudes occur within the boundary layer regions defined by total
pressure measurements. As in the case of the axial velocity measurements,
profile alterations with increasing axial distance are observed to be signifi-
cant.

4.6 Intermittency Measurements

The directionally sensitive laser velocimeter was used to measure the
fraction of the time the flow was moving in the downstream direction ($U > 0$)
and the fraction of the time the flow was moving away from the test surface
($V > 0$). Simpson et al (ref. 1) have referred to the former measurement as

the intermittency and/or the forward flow fraction. In this report the latter terminology will be adopted and "transverse flow fraction" will be used to denote the fraction of the time the flow moved away from the test surface. In practice these quantities were determined from the ratio of the number of valid samples having positive velocities to the total number of valid samples comprising each LV measurement.

4.6.1 Forward Flow Fraction Measurements

Figure 4-12 shows the distribution of the forward flow fraction throughout the test section. Corresponding tabular information is provided in Table 2. Upsteam of separation (Stations 5 and 8) the flow fraction was unity across the entire profile indicating that the flow was moving in the downstream direction 100 percent of the time. The first indication of intermittent reversed flow occurred near the test surface at Station 11 where γ_{P_U} first deviated from 1.0. Further downstream the backflow region intensified and spread outwards from the test surface. At Stations 18 through 22, a strong steady reversed flow ($\gamma_{P_U} = 0$) extended several centimeters from the test surface. The region of the flow in which reversed flow existed for some fraction of time ($\gamma_{P_U} < 1$) extended more than 17 cm from the test surface. Notice also that the locus of points at which $\gamma_{P_U} = 0.50$ corresponded closely to the boundary of the reversed flow region. The correspondence would be exact if the LV probability distributions where symmetric with respect to $U = 0$. However, near the edge of the reversed flow region, the velocity histograms were skewed because of the nature of the flow. Since the maximum backflow velocity was much less than the freestream velocity, the probability of a turbulent fluctuation having a large positive velocity was greater than the probability of it having a large negative velocity causing a skewed histogram.

More details of the development of the separated flow can be seen in figure 4-13 in which the forward flow fraction is plotted versus y/δ in log-linear coordinates for stations within and adjacent to the separation bubble. As noted above, occurrences of reversed flow appeared initially at Station 11 near the test surface. Downstream of Station 11 these occurrences became more frequent (γ_{P_U} decreased) and penetrated further into the viscous layer as defined by the local boundary layer thickness, δ. At Stations 15 and 16 the forward flow fraction distribution formed a trough near the wall with the more intense regions of reversed flow located slightly away from the test surface (0.01 < y/δ < 0.05).

Downstream of Station 16 the trough-shape disappeared as strong, steady reversed flow was measured adjacent to the test surface at Stations 18 through 22 over almost 10 percent of the boundary layer thickness. These data are

consistent with the velocity profile data shown in figure 4-10 which showed the most intense reversed flow which exceeded 30 percent of the local boundary layer edge velocity occurred at Stations 18, 20 and 22.

Near reattachment, trough-shaped patterns reappeared as the reverse flow weakened. The first reoccurrence of forward flow near the test surface at the reference near-wall measurement location (i.e. y = 0.10 cm) appeared at Station 24 where γ_{P_U} = 0.012 at y/δ = 0.0034. The near-wall forward flow fraction increased to 0.144 at y/δ = 0.0042 and 0.714 at y/δ = 0.0050 at Stations 26 and 28, respectively. At Station 30 the reattachment process was completed and a steady flow profile was reestablished. The axial extent of the reattachment zone from the occurrence of forward flow (γ_{P_U} > 0) to γ_{P_U} = 0.50 near the wall (i.e. $C_f \simeq$ 0) has been determined by data interpolation to be approximately 12 cm. The complete reattachment zone extended from Station 24 to Station 30, a distance of 22.8 cm. For comparison, the boundary layer thickness at Station 8 just upstream of separation was 11 cm. A final point which should be noted in figure 4-13 is the absence of occurrences of reversed flow in the outer 40 percent of the boundary layer at any measurement station.

The trough-shaped pattern noted near separation was similar to the flow fraction distribution measured by Simpson et al (ref. 2) at the downstream stations in their turbulent separation experiment. They did not achieve steady reversed flow (γ_{P_U} = 0) anywhere in their test section. The minimum forward flow fraction which they measured, γ_{P_U} = 0.05, occurred at y/δ = 0.023 at their final measurement station. Thus, the open separation bubble data of Simpson et al. would not be expected to correlate well with closed separation bubble data obtained downstream of the leading edge of the bubble.

4.6.2 Transverse Flow Fraction Measurements

The distribution of the transverse flow fraction throughout the test section is shown in figure 4-14. The transverse flow fraction data are consistent with the mean LV flow directions presented above (fig. 4-8). Near the test surface $\gamma_{P_V} \simeq$ 0.50 except at Stations 28 through 31 where the mean flow impinged strongly onto the test surface. The transverse flow fraction value of 0.5 occurs when the mean flow vector is approximately parallel to the test surface since transverse turbulence fluctuations cause the flow to have an equal probability of moving toward or away from the test surface.

The direction of the freestream flow as indicated by the transverse flow fraction is also consistent with the LV velocity data. In the upstream half of the test section (Stations 6-18) the freestream flow moved away from

the test surface 100 percent of the time ($\gamma_{p_V} = 1$). In the downstream half of the test section (Stations 22-31) the freestream flow moved toward the test surface 100 percent of the time ($\gamma_{p_V} = 0$).

4.7 Unsteady Flowfield

Flow visualization had shown the flowfield in and around the separation bubble to be unsteady. Much of the unsteadiness, such as the streamline flapping at reattachment and the oscillation of the separation line, seemed to be of large scale and occurred at low frequency. It was not clear from flow visualization whether such large scale fluctuations were random (i.e. low frequency turbulence) or ordered (i.e. periodic unsteadiness). In addition, to random versus periodic considerations, the question of whether fluctuations should be considered "turbulence" or "flow unsteadiness" is important to developers of computational procedures. This arises because measured unsteadiness levels can be interpreted in terms of turbulence level (and hence effect turbulence modeling) or interpreted as an unsteady flow with lower levels of imbedded turbulence.

To obtain some information regarding the nature of the unsteadiness in the flowfield, the frequency content of the flow was measured with a hot-film probe during traverses at three critical regions of the flowfield. Frequency data were obtained at Station 13 in the intermittent separation zone, at Station 18 within the reversed flow region, and at Station 28 in the reattachment zone. Typical spectra of the hot-film signal taken over the 0-500 Hz range are shown in figure 4-15. Except for a single discrete frequency spike in the spectrum obtained in the freestream (y = 27 cm) at Station 18, all spectra were broadband indicating random unsteadiness. The single low amplitude spike at 460 Hz was caused by blower noise generated at the blade passing frequency. Additional 0-20 KHz spectra taken during each hot-film measurement to check for probe vibrations revealed no flow periodicity at high frequencies.

4.7.1 Streamwise Turbulence Measurements

The broadband spectra showed considerable strength in the low frequency range (f < 50 Hz). To quantify this low frequency contribution to the turbulence signal, two rms measurements of the linearized hot-film signal were made. For the first rms average, which was performed for each hot-film measurement made in the test program, the prefilters on the rms voltmeter were set to average the signal over the wideband range of 5 Hz-50 KHz. In addition, the voltages obtained at Stations 13, 18, and 28 were averaged on a

second voltmeter to permit determination of the rms contribution in the low frequency 5-50 Hz range.

Turbulence intensity profiles $\left(y \text{ vs. } \sqrt{\overline{u_{eff}^2}}/U_{ref} \right)$ calculated from the rms voltage averaged over the 5 Hz-50 KHz bandwidth are shown in figure 4-16 as solid lines. The mean square turbulence level $\overline{u_{eff}^2}$ can be considered the turbulence level in the x-y plane associated with the local mean flow direction. Note that the turbulence intensities have been normalized by U_{ref} rather than U_e to provide absolute rather than relative turbulence intensities. Upstream of separation the flow had a standard Klebanoff-like turbulence profile as shown previously. High turbulence levels exceeding 20 percent were measured in the free shear layer surrounding the separation bubble. These peak turbulence levels decayed somewhat downstream of reattachment but remained above 10 percent at the test section outlet.

At Stations 13, 18, and 28 the portion of the overall streamwise turbulence level attributed to the low frequency (5 Hz-50 Hz) band has been shaded. This low frequency contribution to the overall turbulence level was substantial across the entire profile. In the free shear layer the low frequency (5 Hz-50 Hz) unsteadiness accounts for approximately 40-45 percent of the overall turbulence level (5 Hz-50 KHz). Uncertainty in these measurements exists within regions of flow reversal.

Turbulence data at Stations 13, 18, and 28 are listed in Table V. Measurement points where flow reversal occurs some fraction of the time ($0 < \gamma_{p_U} < 1$) are indicated in the table. At those points the rms average of the hot-film voltage does not yield an accurate measurement of the turbulence level (see Appendix D). Thus, care should be taken when using the data in Table V.

With regard to the issue raised above regarding interpretation of measured unsteadiness as turbulence or a basically unsteady flow with imbedded turbulence, the above measurements were not definitive. Some form of conditional sampling may be required to address this issue more directly. That large scale turbulence with low frequency content existed within and in the vicinity of the recirculation zone is clear based on the smoke flow visualization movie taken as part of the study. Overall flowfield unsteadiness was also apparent. This was particularly noticeable in the aft end of the bubble where a previously described non-periodic flapping of the reattaching flow occurred. This flapping phenomenon has been reported previously by Eaton and Johnston (ref. 32), for a reattaching backward-facing step flow, Cherry et al. (ref. 33), for a separating and reattaching flow at the leading edge of a two-dimensional rectangular blunt plate, and Mabey (ref. 34) among others. Mabey

showed that reduced shedding frequencies from various experiments correlated well when normalized by the reattachment length. He suggested that a feedback mechanism, whereby the shedding of vorticity from reattachment interacted with the formation of disturbances near separation, controlled the separation process. In the present experiment a characteristic disturbance length can be estimated from the flapping frequency, $f < 50$ Hz, and the average freestream velocity in the vicinity of the bubble, $U_e = 15$ m/sec, to be greater than 0.3 m (i.e. half the length of the separation bubble).

An additional degree of unsteadiness would be expected in the current experiment because of the intermittent nature of turbulent boundary layer separation on a flat plate. The random upstream and downstream wandering of the separation line due to the lack of a salient edge to fix the location of separation presumably added to the downstream unsteadiness. Thus, there is sufficient evidence to conclude that the unsteadiness observed was not an artifact of the wind tunnel test configuration employed here.

4.7.2 LV Turbulence Measurements

Accurate measurements of the turbulence levels throughout the test section, including regions of flow reversal, were made with the laser velocimeter. An overview of the axial and transverse turbulence intensity profiles determined from LV data is shown in figure 4-17. Qualitatively, the axial turbulence intensity profiles are similar to the streamwise turbulence intensity profiles from hot-film measurements presented in figure 4-16. The transverse turbulence intensity profiles have the same general characteristics as the axial turbulence profiles although lower in level. Peak transverse turbulence intensities were approximately 12 percent while the corresponding peak axial turbulence intensities exceeded 20 percent.

4.7.2.1 Axial Component Turbulence Measurements

More detailed axial turbulence intensity profiles are shown in figures 4-18 a-d where the data are plotted in nondimensional coordinates, y/δ vs. $\sqrt{\overline{u^2}}/U_{ref}$. At Station 0, located 24 cm upstream of the test section, the boundary layer had a Klebanoff-like turbulence distribution with maximum turbulence intensity of approximately 8 percent as noted previously. As the flow moved downstream and approached separation, turbulence levels near the test surface increased rapidly. At Station 11, the start of intermittent separation, turbulence reached a level of 17 percent at $y/\delta = 0.10$. Just downstream of the mean separation location (Station 13) peaks in the turbulence intensity profiles grew higher and wider, and moved away from the test surface due to turbulence being generated in the free shear layer and diffusing throughout the boundary layer. The peak turbulence intensity of 21

percent was measured at Station 15 at y/δ = 0.34. Downstream of Station 15 the peaks in the profiles decayed, continued to widen, and shifted outwards to larger values of y/δ. Over the upstream half of the separation bubble the peak turbulence intensity occurred approximately 0.1 δ farther from the test surface than the mean dividing streamline (see Table VI, Streamline No. 1 for coordinates of the mean dividing streamline determined from LV measurements). Over the downstream half of the separation bubble the peak turbulence intensity shifted further outside of the mean dividing streamline.

At all stations the axial turbulence intensity in the freestream approached 2 percent or less except at Station 34 at the test section outlet where upper and lower wall boundary layers began to merge causing the freestream turbulence level to rise to 4 percent. The freestream turbulence level of 2 percent is a quantitative measure of the overall unsteadiness of the freestream flow in the test section.

4.7.2.2 Transverse Component Turbulence Measurements

Detailed nondimensional transverse turbulence profiles are shown in figure 4-19 a-d. At initial measurement Station 6 the turbulence distribution for this component again exhibited a standard Klebanoff-like profile with a maximum intensity of approximately 4 percent. Approaching separation, transverse turbulence levels increased near the test surface. At the leading edge of the separation bubble the transverse turbulence level peaked at 8.2 percent at y/δ = .17. Just downstream of separation at Stations 14 through 16 the peak transverse turbulence level remained constant at approximately 8 percent but widened and diffused outward from the test surface.

The behavior of the transverse turbulence intensity at the next several measurement stations provides insight into the nature of the transverse velocity fluctuations. At Station 18 the transverse turbulence intensity peaked at 12.6 percent. The peak declined to 9.6 percent at Station 20 before increasing to 11.8, 12.6, and 12.7 percent at Stations 22, 24, and 26, respectively. The mean transverse velocity profiles plotted in figure 4-11b indicated positive transverse velocities at Station 18, negligible transverse velocities at Station 20, and negative transverse velocities at Stations 22, 24, and 26. Thus it seems possible that a major contribution to transverse turbulence intensities originate as streamwise velocity fluctuations when the mean streamline had a nonaxial orientation.

The high transverse turbulence levels at Stations 26, 28 and 30 near reattachment also resulted from unsteady streamline flapping. Downstream of reattachment transverse turbulence intensity decreased due to turbulence decay and a more axial orientation of the streamwise flow vector. Transverse

51

turbulence levels in the freestream approached 2 percent or less at all
stations.

4.7.3 Turbulence Kinetic Energy

The turbulence kinetic energy per unit mass, k, is defined as

$$k = (\overline{u^2} + \overline{v^2} + \overline{w^2})/2 \qquad (4\text{-}4)$$

Although the spanwise turbulence component, w, was not measured in this
experimental program, Simpson (ref. 4) has shown that in separated flows
$v \simeq w$. Thus, k can be approximated as

$$k = (\overline{u^2} + 2\,\overline{v^2})/2 \qquad (4\text{-}5)$$

Turbulence kinetic energy profiles calculated using eq. (4-5) are presented in
figure 4-20. The profile shapes are somewhat similar to the axial turbulence
profiles discussed above. The profiles had sharp and growing peaks near
separation (Stations 11-13), remained at nearly constant peak amplitude but
broadened near the maximum bubble thickness (Station 18-22), and decayed
downstream of reattachment. The profile peaks occurred just outside the
location of the mean dividing streamline over the upstream half of the bubble,
whereas downstream of the maximum bubble thickness, they moved outward from
the mean dividing streamline into the bubble wake.

4.8 Reynolds Stress Measurements

Profiles of the Reynolds stress, $\overline{uv}$, were measured with the LV system
at 20 stations. Fourteen of the stations were located on the wind tunnel
centerline and six were located at ± 15.2 cm on either side of the centerline
at three axial locations (upstream of the separation bubble, within the
bubble, and downstream of reattachment). Reynolds stress data from thirteen
centerline locations is listed in Table III. Profiles obtained at twelve
stations along the wind tunnel centerline are plotted in figure 4-21. Five
features of the Reynolds stress profiles should be noted. First, at Station 6
the Reynolds stress has a Klebanoff-like profile (fig. 18.5 in ref. 35).
Second, in the freestream flow around the bubble the Reynolds stress is
negligible as expected. Third, the Reynolds stress peaks near reattachment
and remains high downstream of reattachment. Fourth, the Reynolds stress is
small in the reversed flow region. And fifth, just upstream of separation and

in the shear layer surrounding the bubble no meaningful trend is apparent in
the Reynolds stress data.

The almost random nature of the Reynolds stress profiles in the separated
flow region is not particularly elucidative. However, the Reynolds stress
data in this coordinate system can be used to calculate shear stress profiles
in a coordinate system aligned with the local mean flow direction. This
streamwise shear stress is more meaningful for developing flow structure
models, since the assumptions used in the boundary layer equations which are
used to calculate separating flows are more accurate if applied in streamwise
orthogonal coordinates (ref. 6). It will be shown below in Section 5.7,
"Streamwise Turbulent Shear Stress Measurements" that the large values of
shear stress expected in the shear layer are masked by the effects of flow
curvature and they do not become fully apparent until the streamwise shear
stress is calculated.

4.9   Total Pressure Measurements

Total pressure traverses were made normal to the test surface at 55
stations. Thirty-five stations were located on the wind tunnel centerline and
twenty traverses were made at off-centerline locations as shown in figure 3-7.
The total pressure measurements obtained at each centerline traverse location
and at fourteen off-centerline locations are listed in Table IV.

The total pressure profiles obtained on the wind tunnel centerline are
shown in figure 4-22. For clarity, only 18 of the 34 profiles have been
plotted. The measured total pressure has been normalized by Q_{ref}, the free-
stream dynamic pressure at the inlet station (x = -9.5 in, -24.1 cm). Several
features of the total pressure profiles are apparent.

The inviscid core, defined as the region over which $0.99 < P/Q_{ref} < 1.00$,
which is approximately 10 cm thick upstream of the location of intermittent
separation (x < 40 cm), remained intact as it was convected around the bubble.
In the outlet channel (x > 120 cm) the thickness of the inviscid core
diminished but did not disappear until the last measurement station (x = 148
cm) where the upper and lower wall boundary layers merged.

The deceleration of the test surface boundary layer in the region
0 < x < 40 cm is also apparent. The shape of the boundary layer profile
changed as the flow encountered the adverse pressure gradient until an
inflection point was measured in the profile at the wall at x = 40.6 cm just
upstream of separation.

Within the reversed flow region $\partial P/\partial y \simeq 0$ except very near the test surface where a reversed flow boundary layer developed under the separation bubble. The presence of the reversed flow boundary layer is not apparent in figure 4-22 but it can be discerned in the tabulated data in Table IV and it is discussed in detail below in Section 5.5.1, "Description of the Backflow Boundary Layer".

Downstream of reattachment a new boundary layer began to grow along the test surface beneath the remnants of the upstream boundary layer which had been convected around the separation bubble. Details of the boundary layer downstream of reattachment are discussed in Section 5.6, "Description of the Reattachment Process".

4.9.1 Determination of Bounding Streamline

Total pressure traverses were made normal to the lower wall of the test section at 20 locations on the wind tunnel centerline to determine the location of a free streamline required as a boundary condition for numerical computation codes. Using wall static pressures measured at each of the 20 traverse locations and assuming that no normal static pressure gradients existed between the lower wall and the location of the bounding streamline, mass flow profiles were calculated from the measured total pressure profiles at each of the 20 axial stations. After accounting for the mass flow out of the lower wall boundary layer scoop, points of equal mass flux were connected to define the bounding streamline shown in figure 4-23.

P = TOTAL PRESSURE AT y,z
P_{ref} = FREESTREAM TOTAL PRESSURE
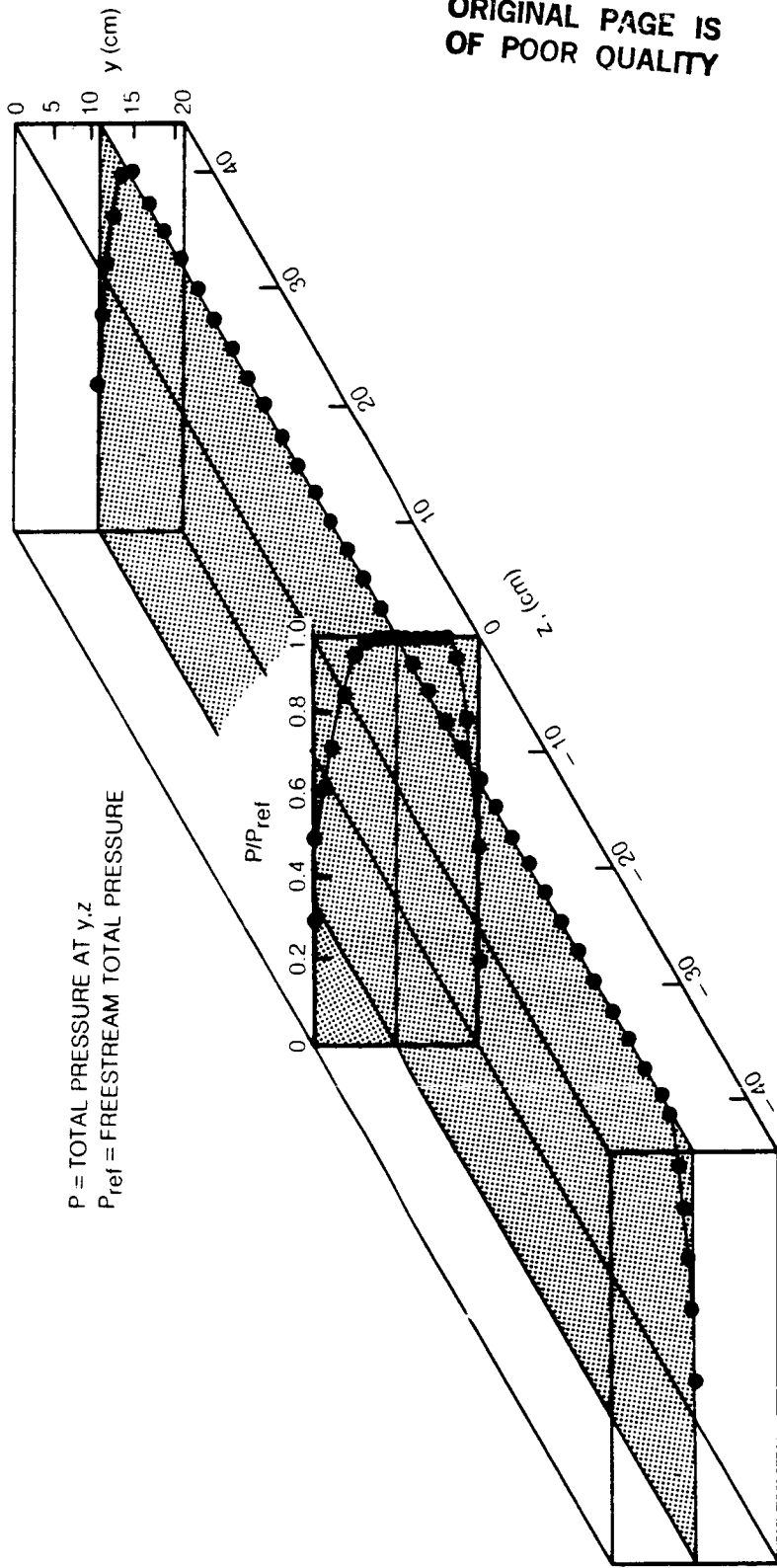
Figure 4-1 Spanwise and Transverse Total Pressure Distributions in Inlet Plane (Station 0, x = −24.1 cm, −9.5 in.)

84—8—1—5

$$U^+ = \frac{1}{0.41}\ \ln y^+ + 5.0$$

	$Re_\theta = 11,100$	
	MEASURED	COLES (REF. 30)
C_f	0.00267	0.00256
$C_f\ Re_\theta$	29.7	28.4
H	1.27	1.32

ΔU^+

U^+

y^+
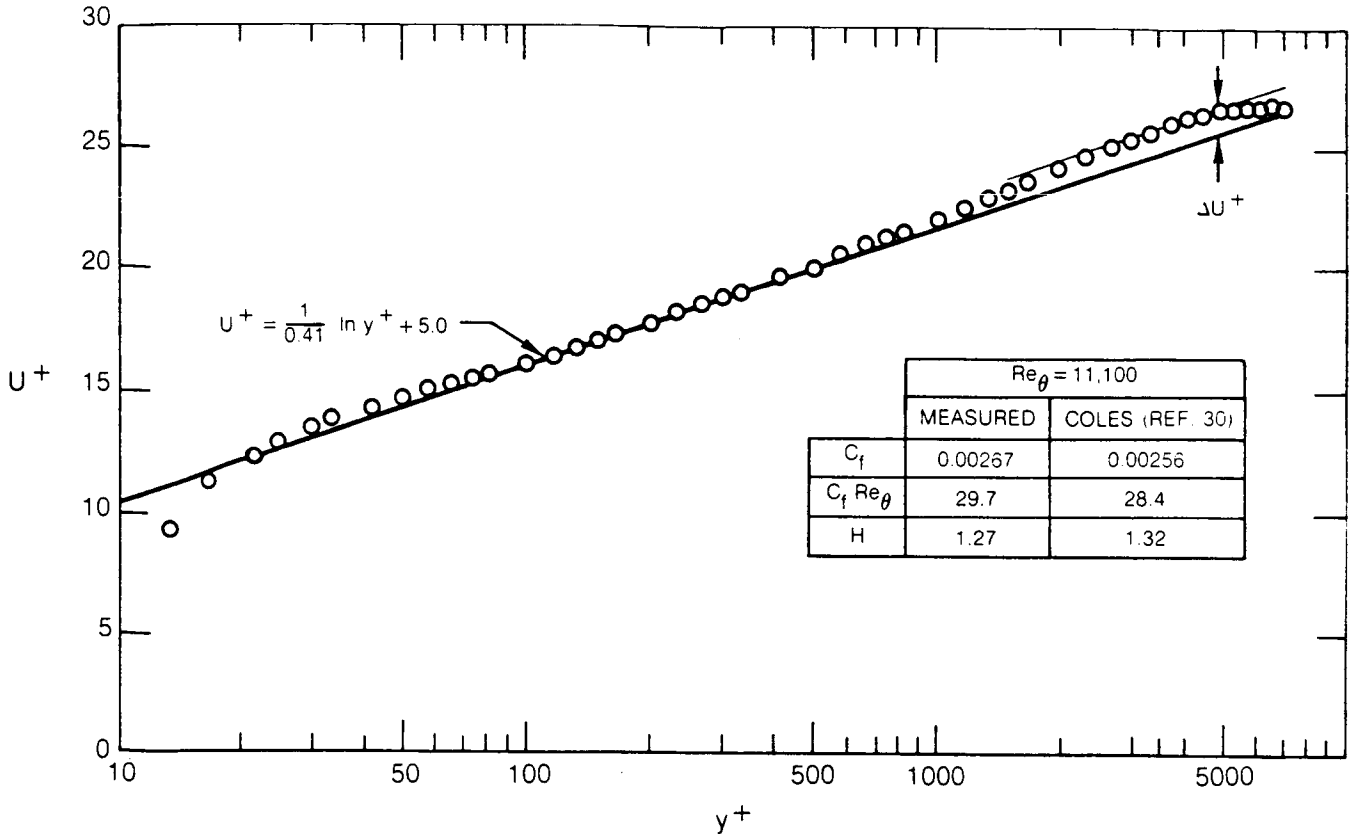
b) STREAMWISE TURBULENCE INTENSITY NORMALIZED BY U_e COMPARED TO KLEBANOFF'S DATA

KLEBANOFF (REF. 31)

$$\sqrt{\frac{\overline{u^2}}{U_e}}$$

y/δ_{99}
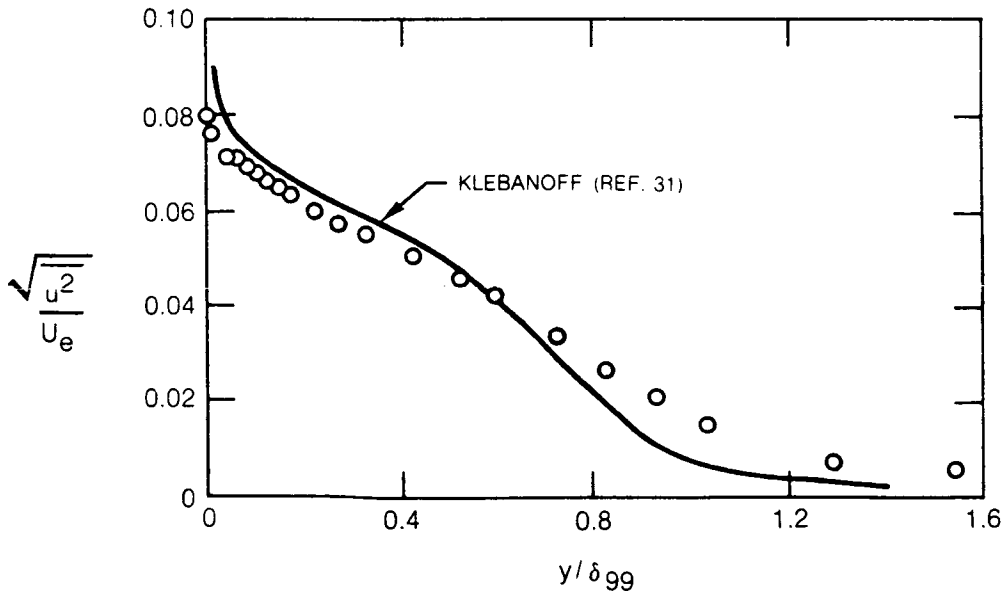
**Figure 4-2 Boundary Layer Characteristics at Initial Measurement Plane
(Station 0, x = −24.1 cm, −9.5 in.)**

DIRECTION OF FREESTREAM FLOW

TUFT
TREES

| ATTACHED FLOW | SEPARATION ZONE | REVERSED FLOW | REATTACHMENT ZONE | ATTACHED FLOW |
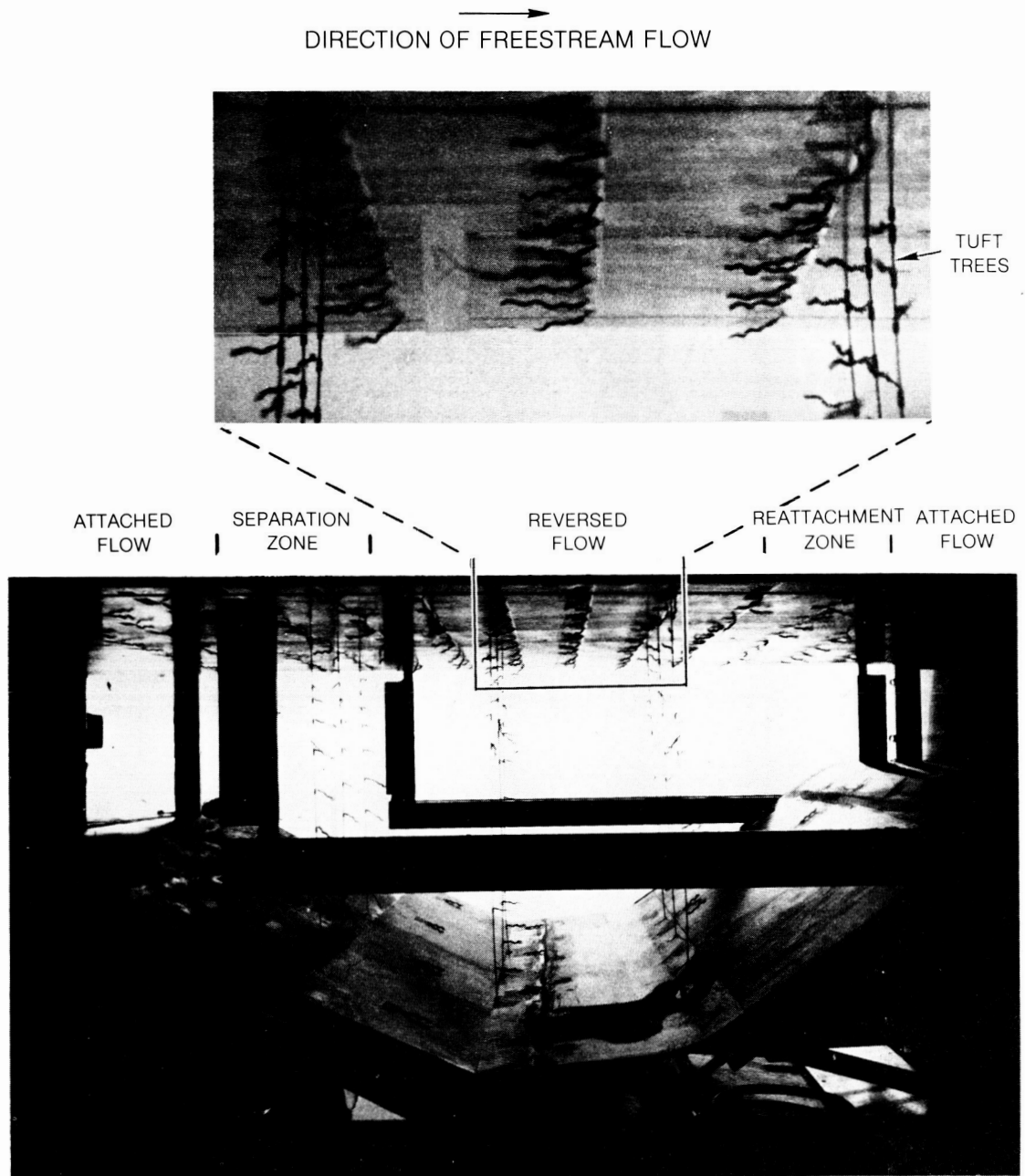
Figure 4-3 Tuft Flow Visualization
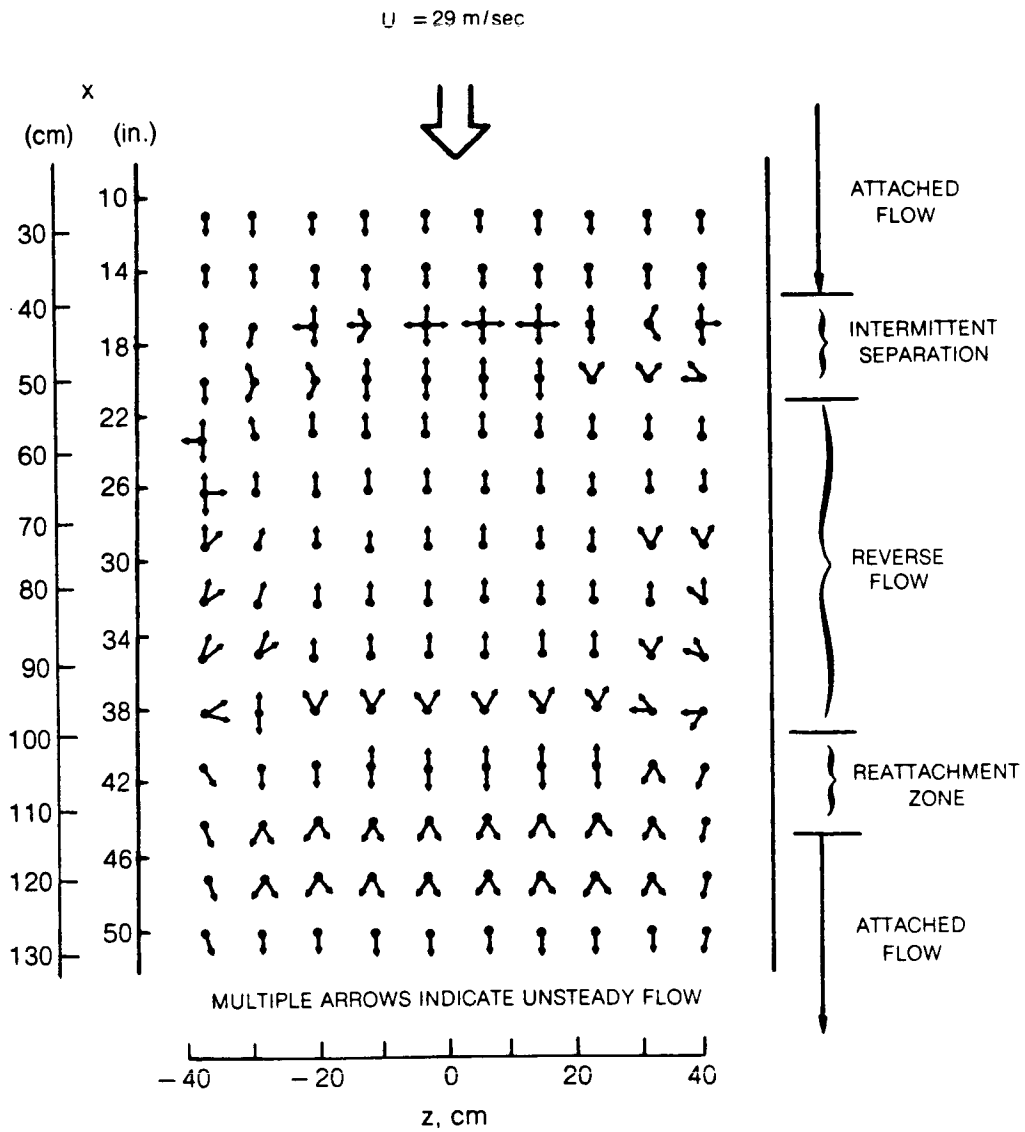
Figure 4-4 Surface Flow Directions on Test Plate as Indicated by Tufts

SEPARATION REGION

REATTACHMENT REGION
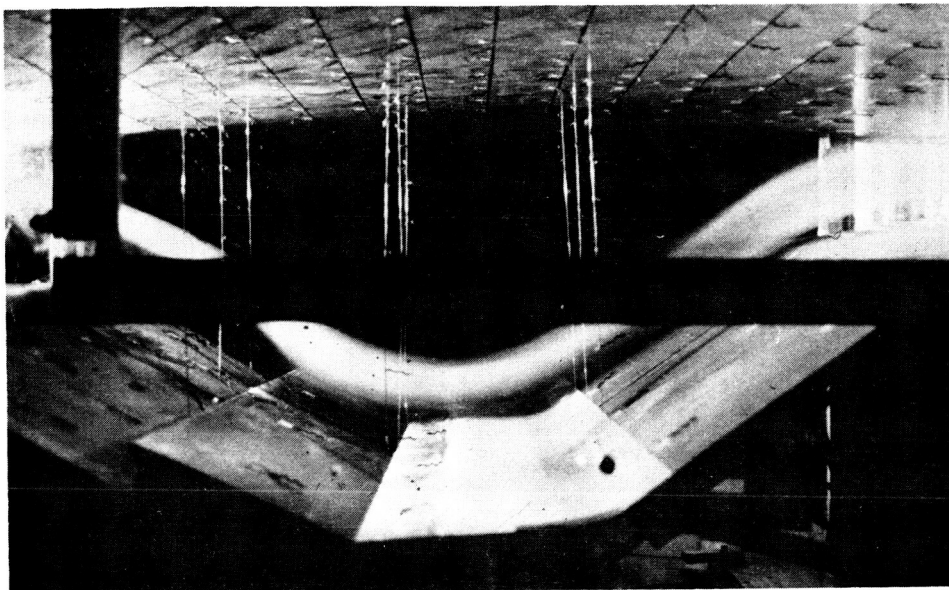
a) $y_{probe} = 10$ cm

SEPARATION REGION

REATTACHMENT REGION
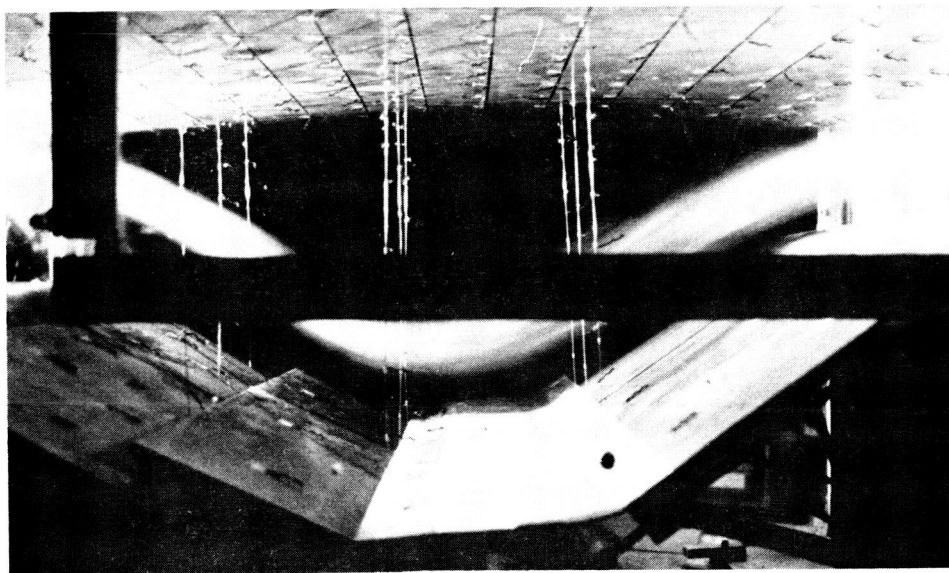
b) $y_{probe} = 7.6$ cm

Figure 4-5 Smoke Flow Visualization of Separation Bubble

SEPARATION REGION

REATTACHMENT REGION
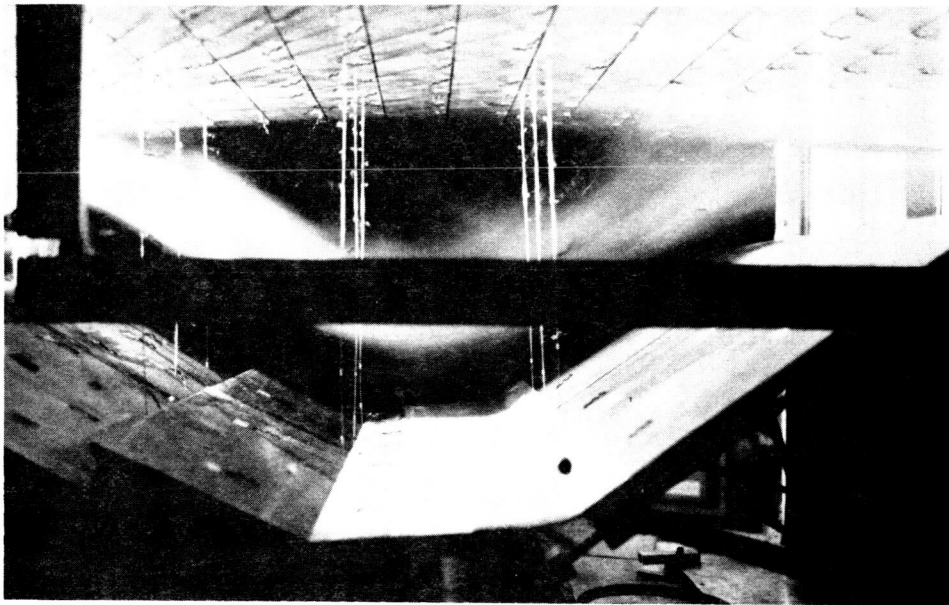
c) $y_{probe} = 6.4$ cm

SEPARATION REGION
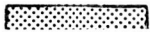
REATTACHMENT REGION
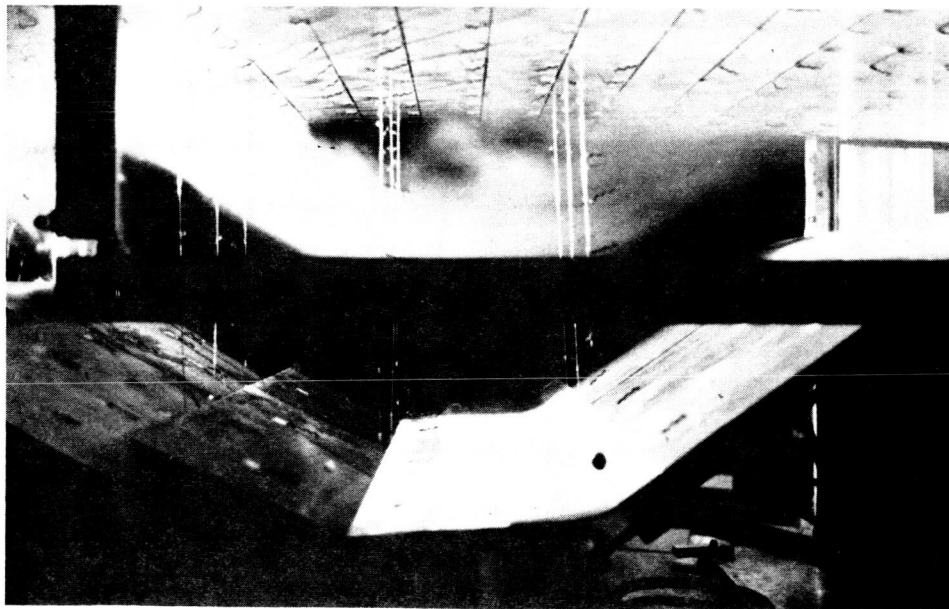
d) $y_{probe} = 5.1$ cm

Figure 4-5 Smoke Flow Visualization of Separation Bubble (Concluded)

84—8—1—73
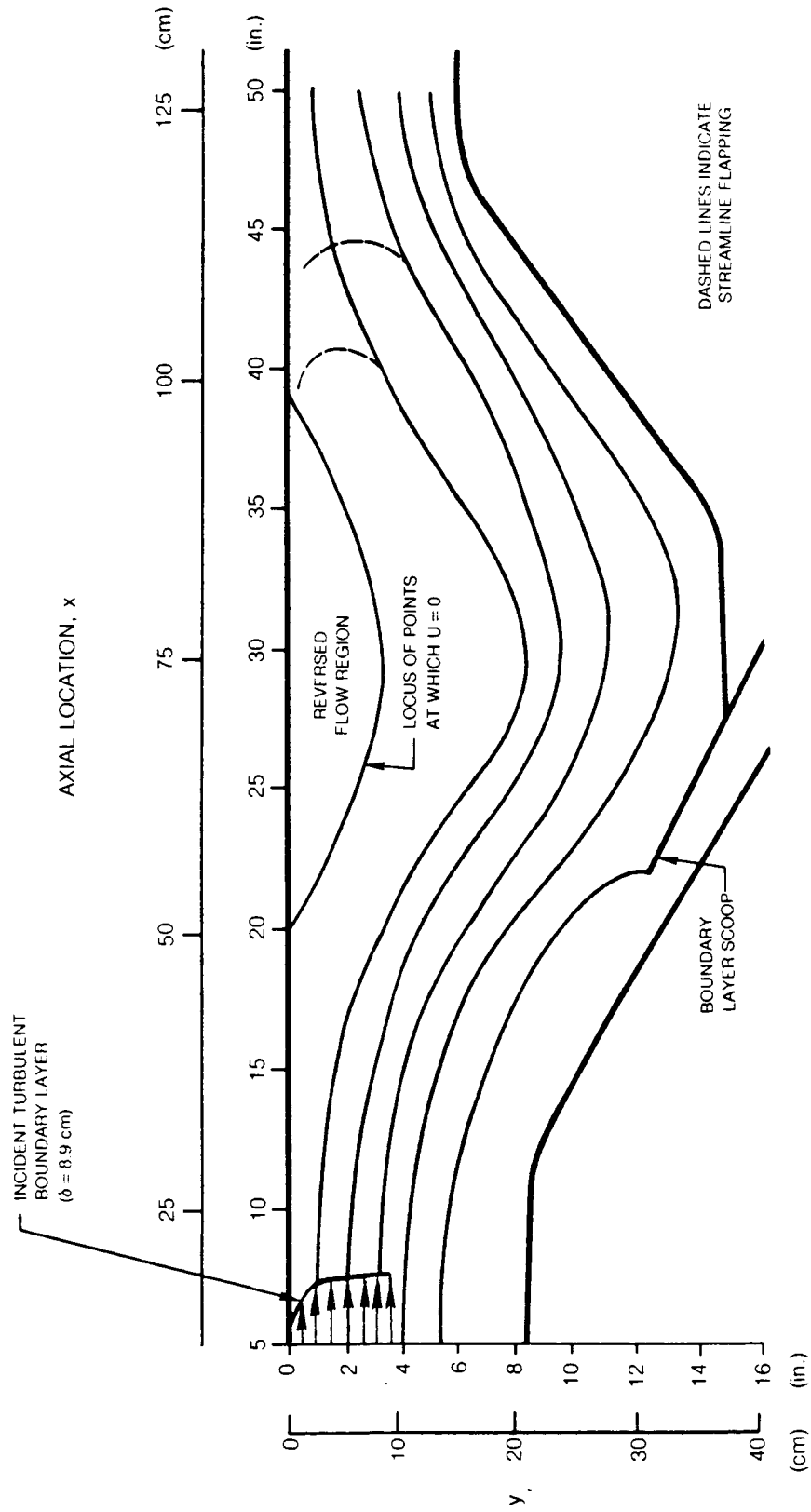
Figure 4-6 Streamlines Determined from Smoke Flow Visualization and Tuft Trees

84-8-1-8

61
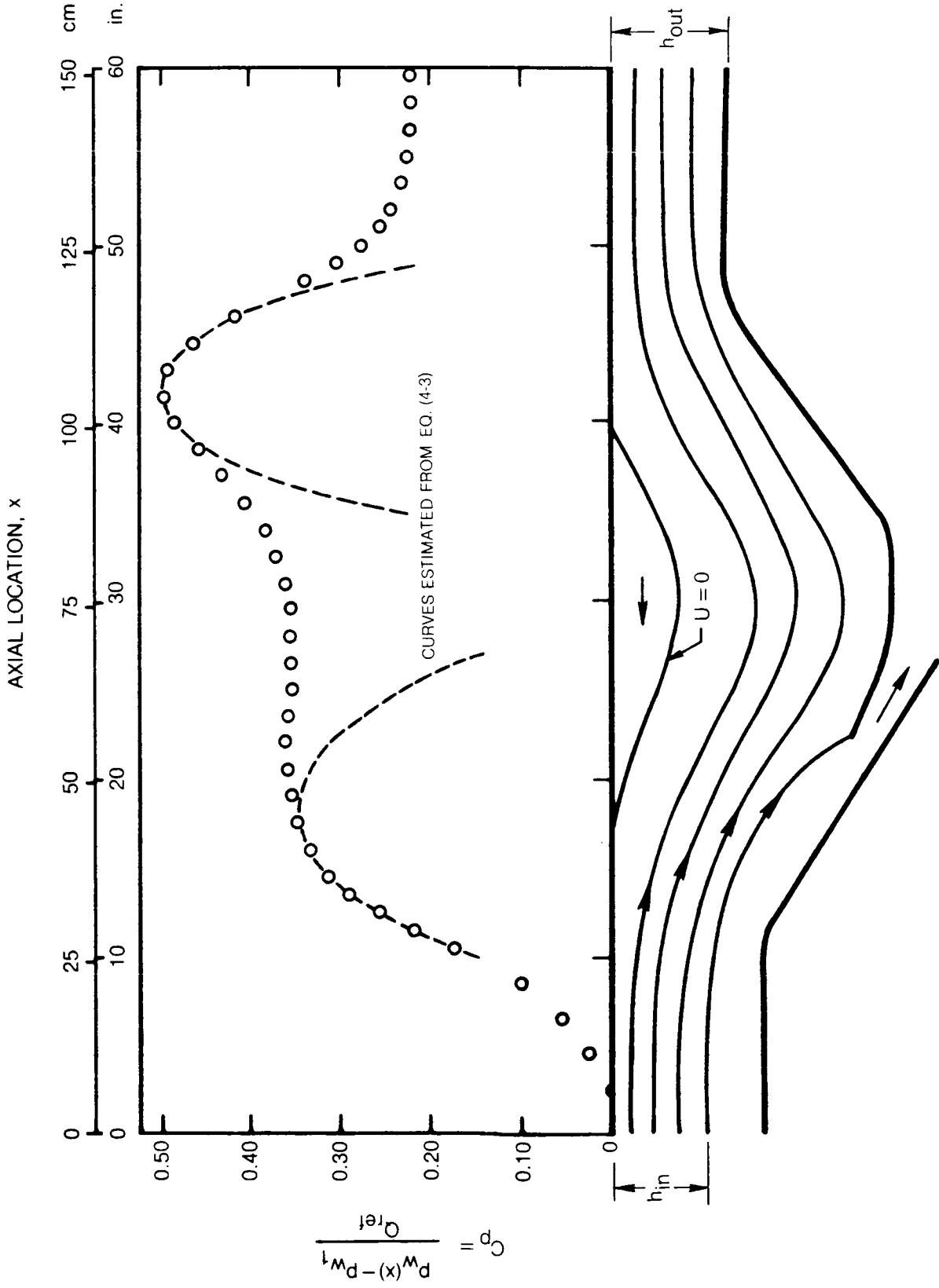
Figure 4.7 Test Surface Static Pressure Distribution on Tunnel Centerline

85-8-36-9

62
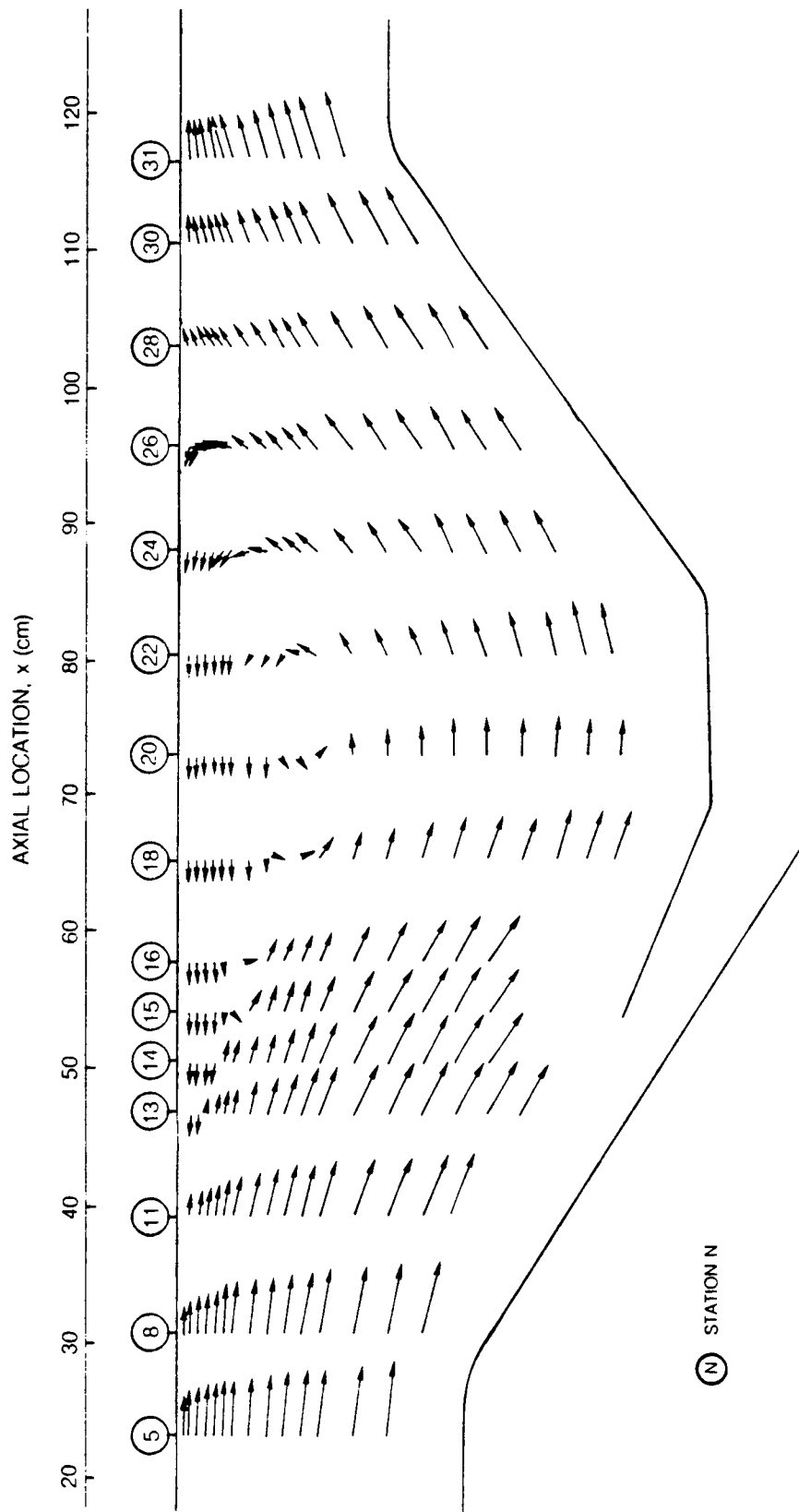
Figure 4-8 LV Mean Velocity Measurements on Wind Tunnel Centerline

84-4-66-2

63
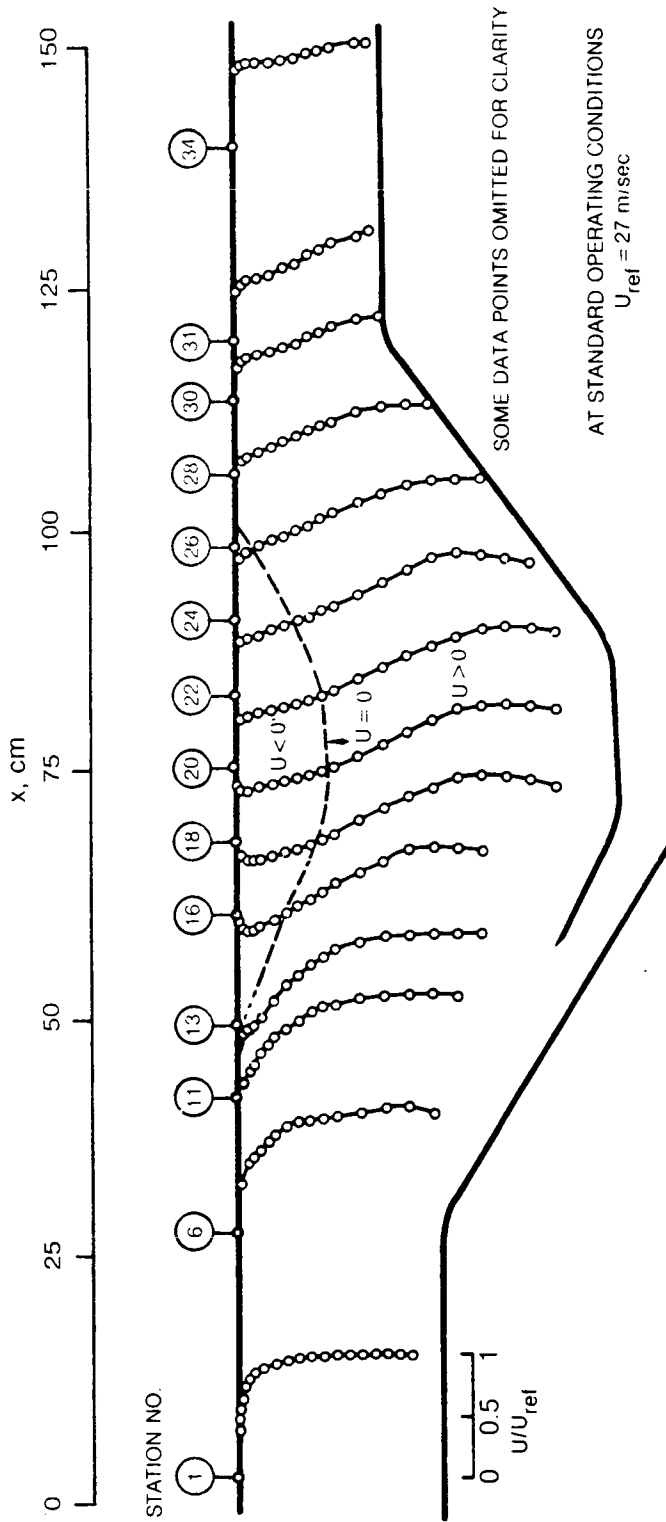
Figure 4-9 Nondimensional Axial Velocity Profiles, y vs $\dfrac{U}{U_{ref}}$

SOME DATA POINTS OMITTED FOR CLARITY

AT STANDARD OPERATING CONDITIONS
$U_{ref} = 27$ m/sec

STATION NO.

x, cm

$U < 0$

$U = 0$

$U > 0$

0   0.5   1
U/U_{ref}

84-8-1-10
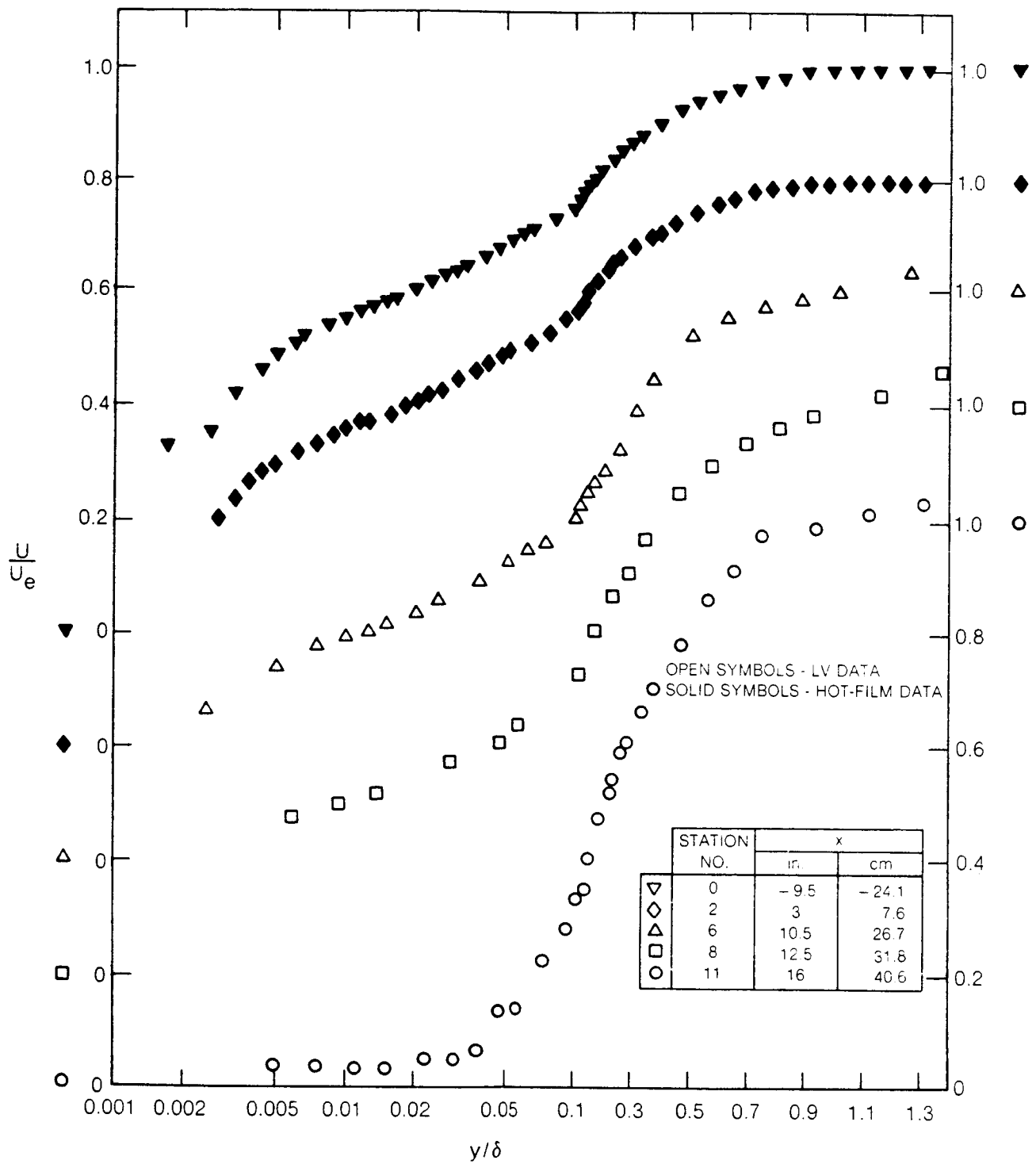
Figure 4-10a Non-Dimensional Axial Velocity Profiles. Note Log-Linear Abscissa and Displaced Ordinates

84-8-5-59
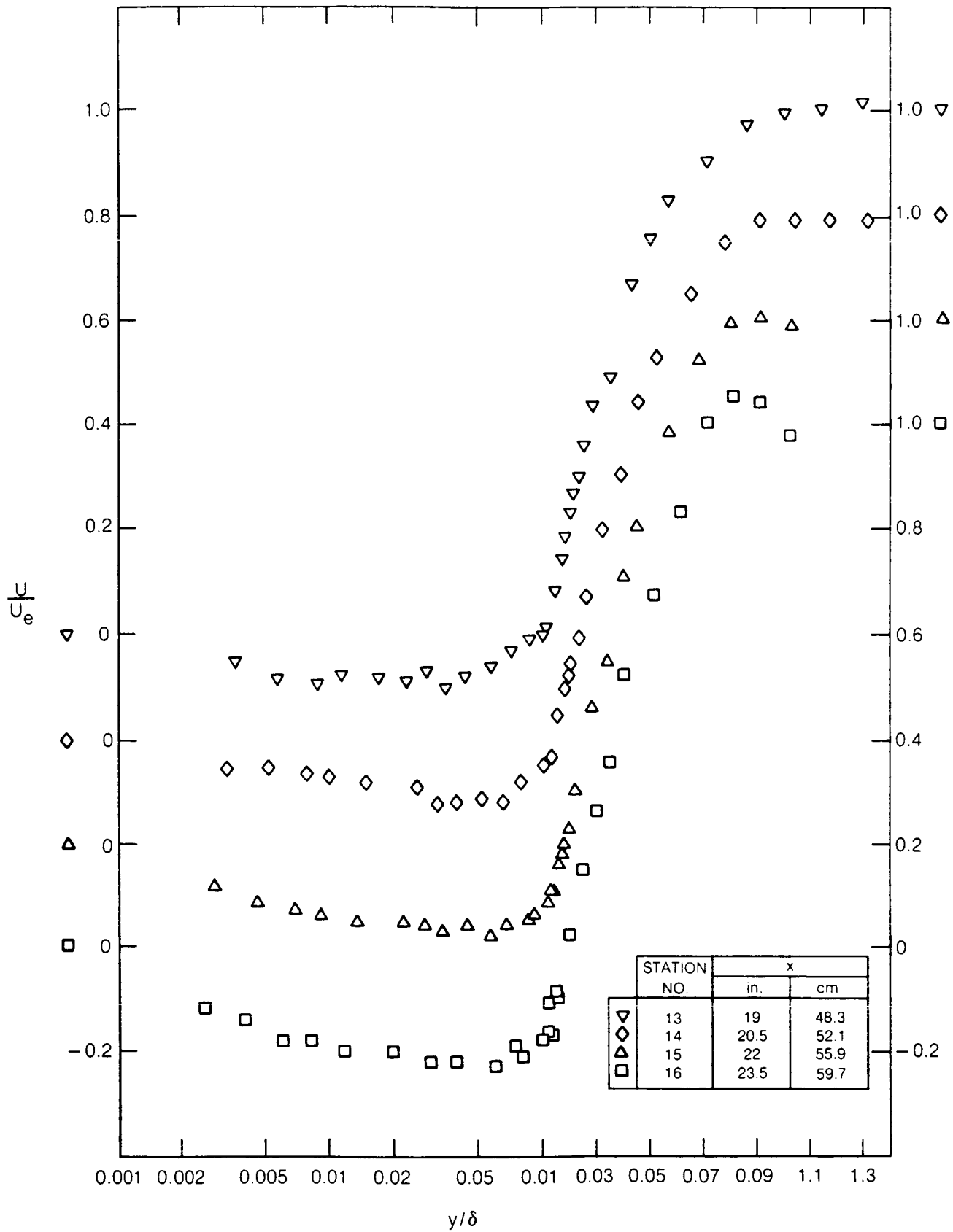
Figure 4-10b Non-Dimensional Axial Velocity Profiles. Note Log-Linear Abscissa and Displaced Ordinates (Continued)

84-8-1-20
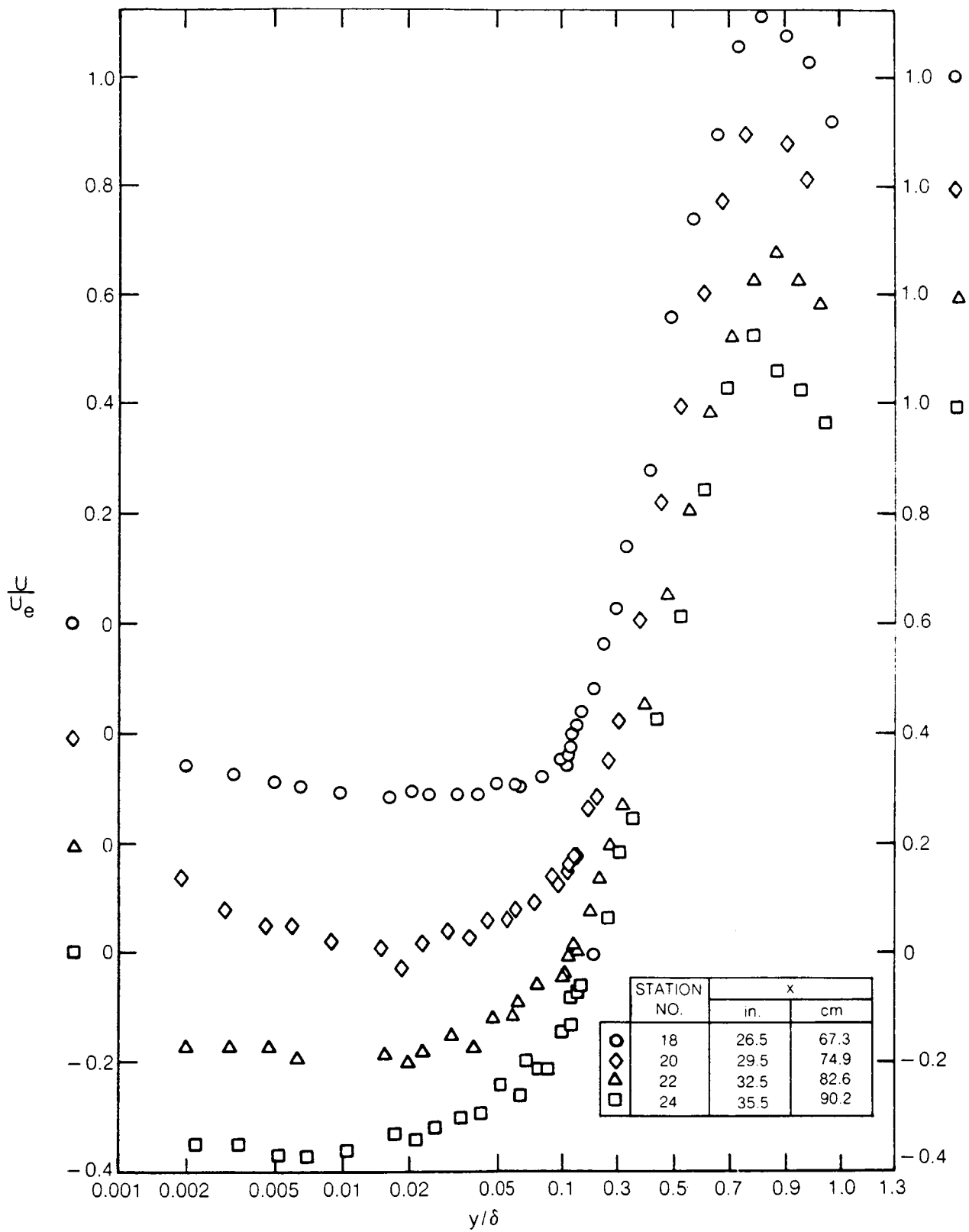
Figure 4-10c Non-Dimensional Axial Velocity Profiles. Note Log-Linear Abscissa and Displaced Ordinates (Continued)
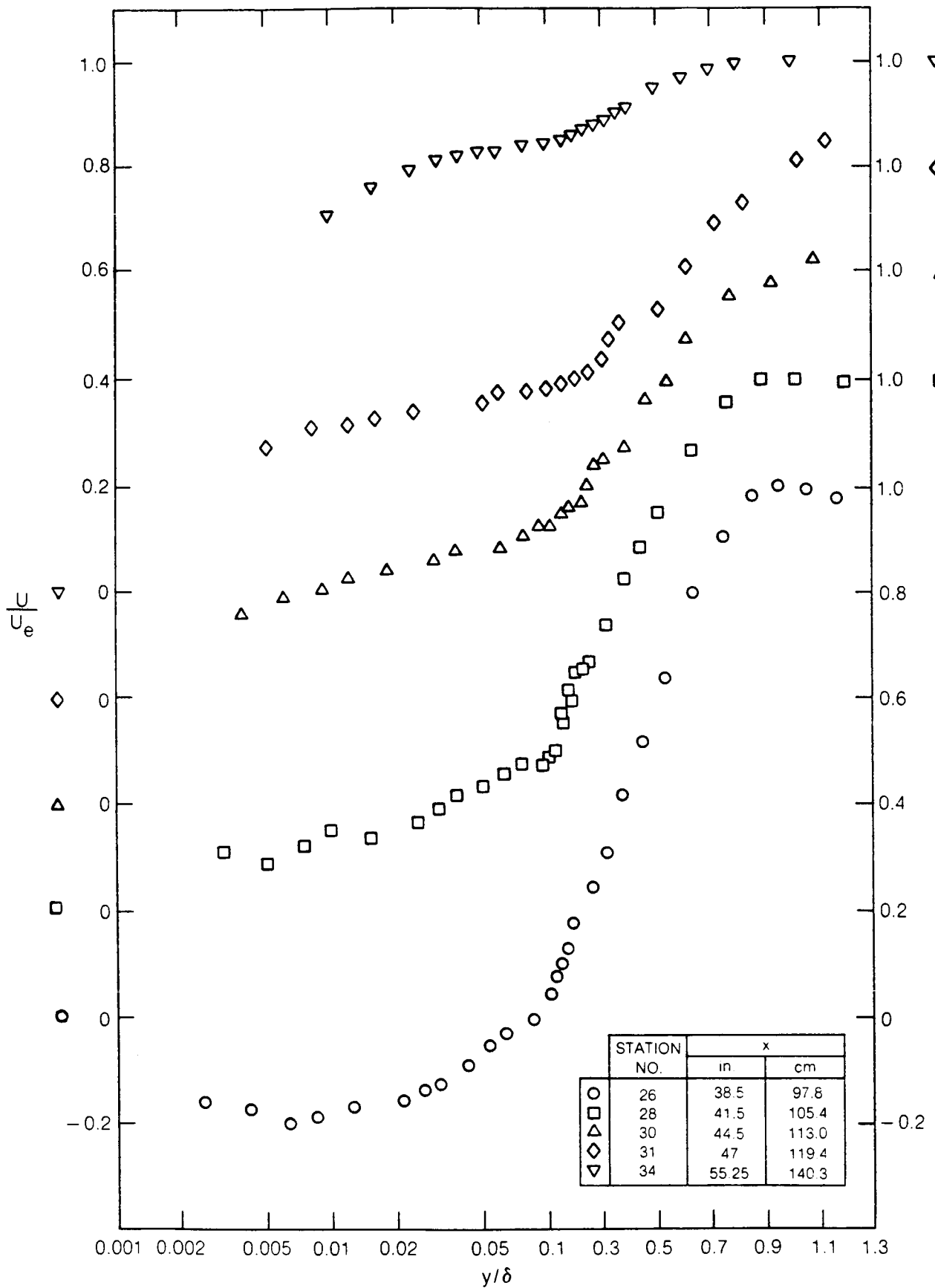
Figure 4-10d Non-Dimensional Axial Velocity Profiles. Note Log-Linear Abscissa and Displaced Ordinates (Concluded)

84—8—1—62
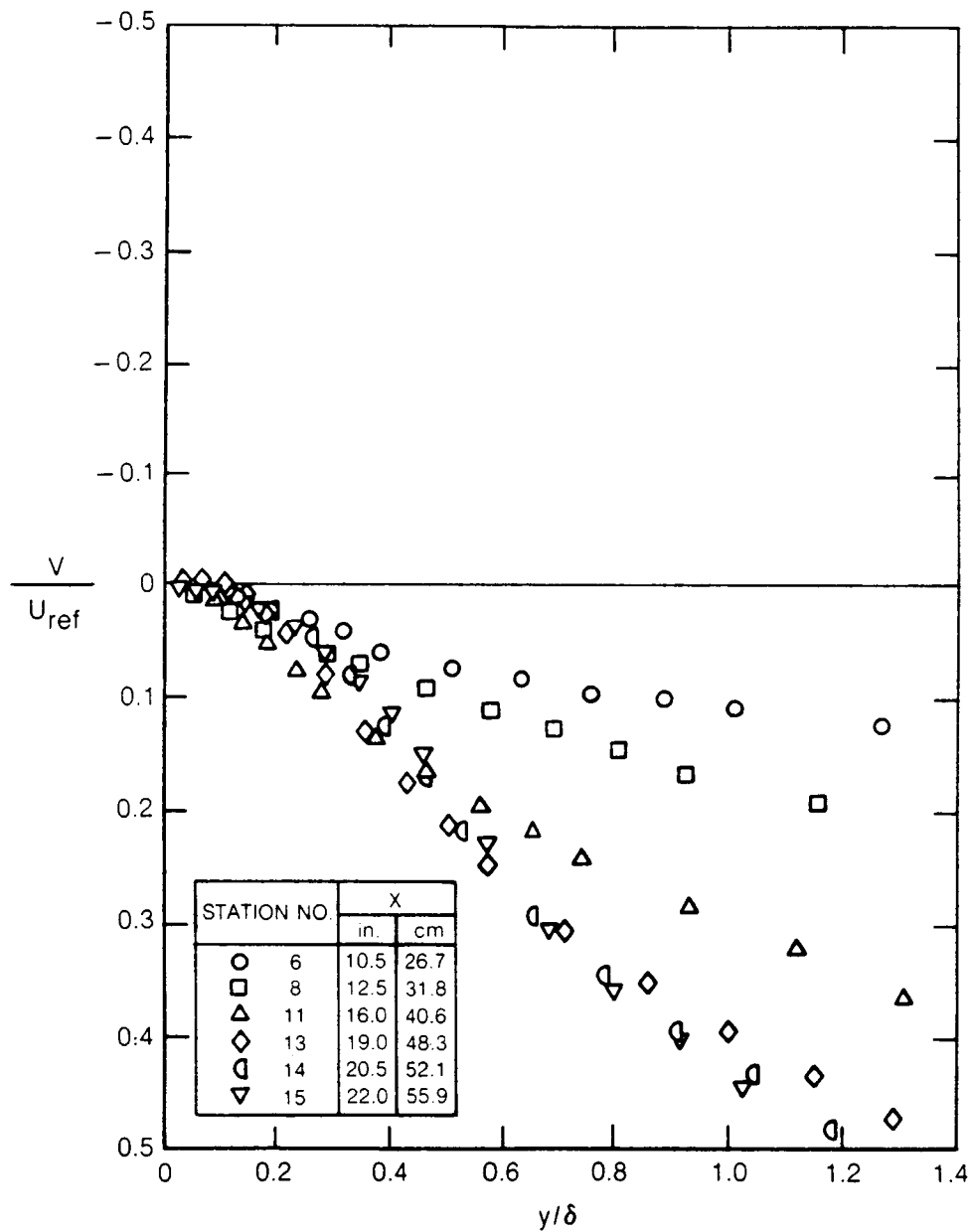
Figure 4-11a LV Measurements of Transverse Velocity Profiles
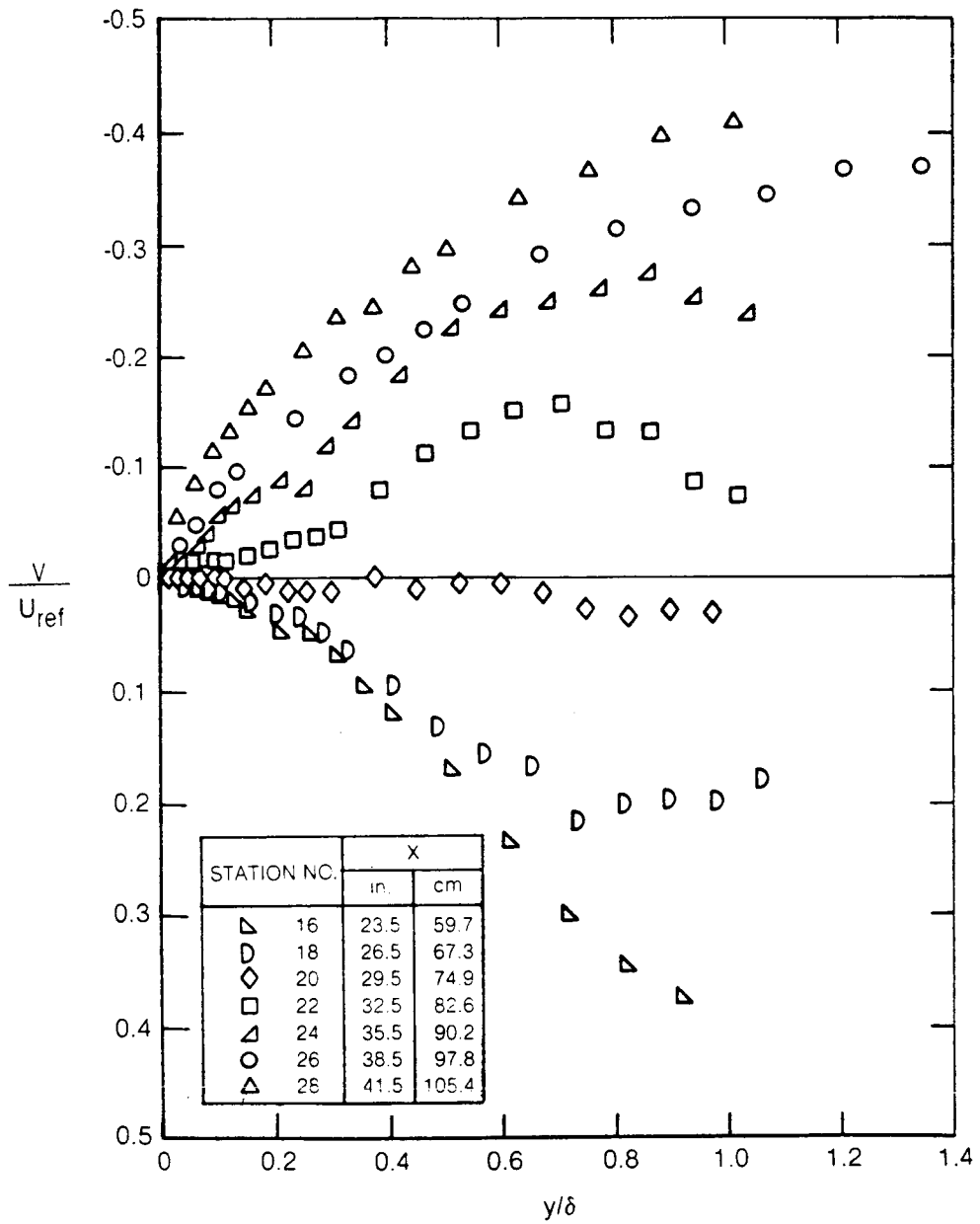
Figure 4-11b LV Measurements of Transverse Velocity Profiles (Continued)

84-8-1-38

STATION NO.		X	
		in.	cm
□	30	44.5	113.0
◁	31	47.0	119.4
▽	34	55.25	140.3
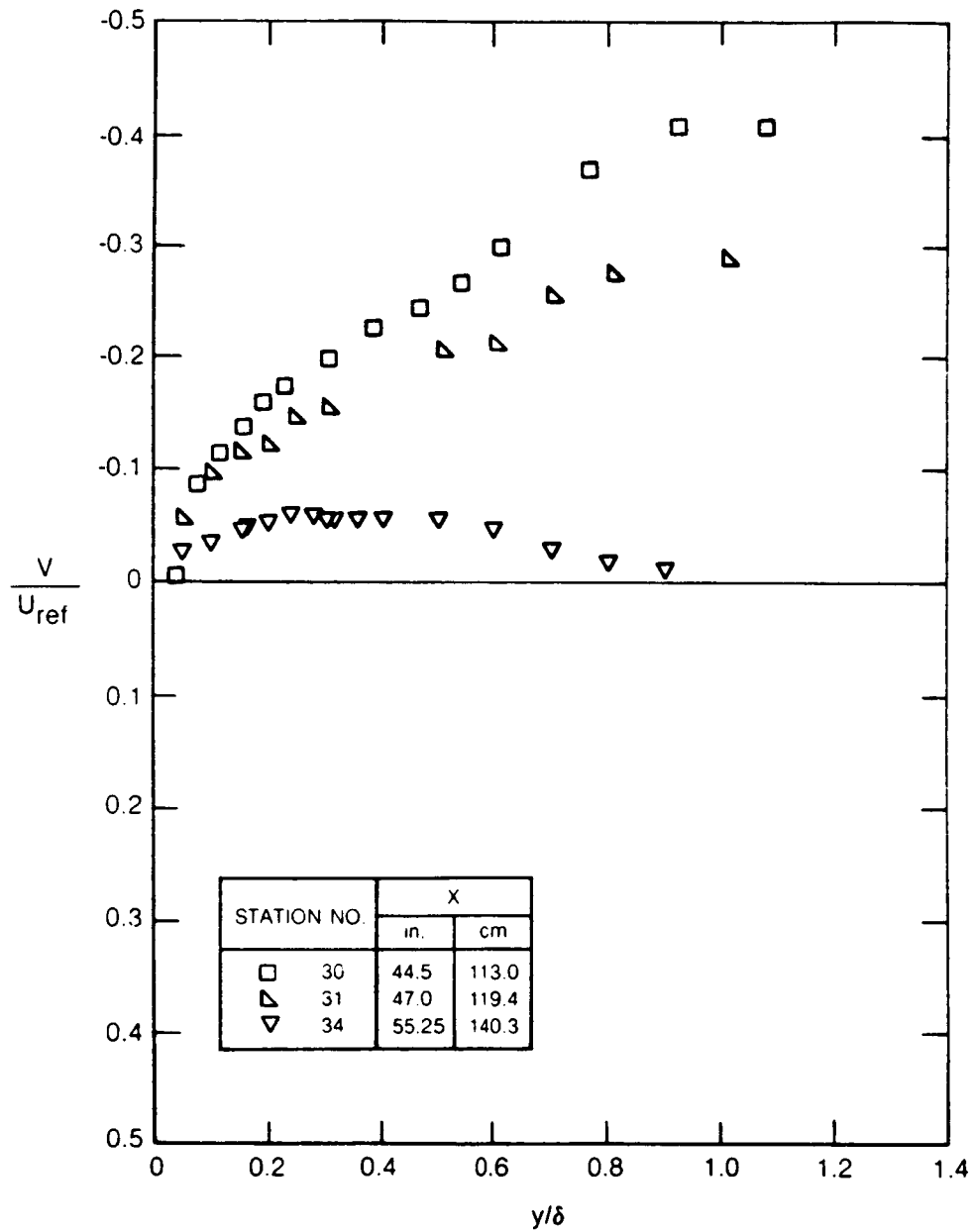
Figure 4-11c LV Measurements of Transverse Velocity Profiles (Concluded)
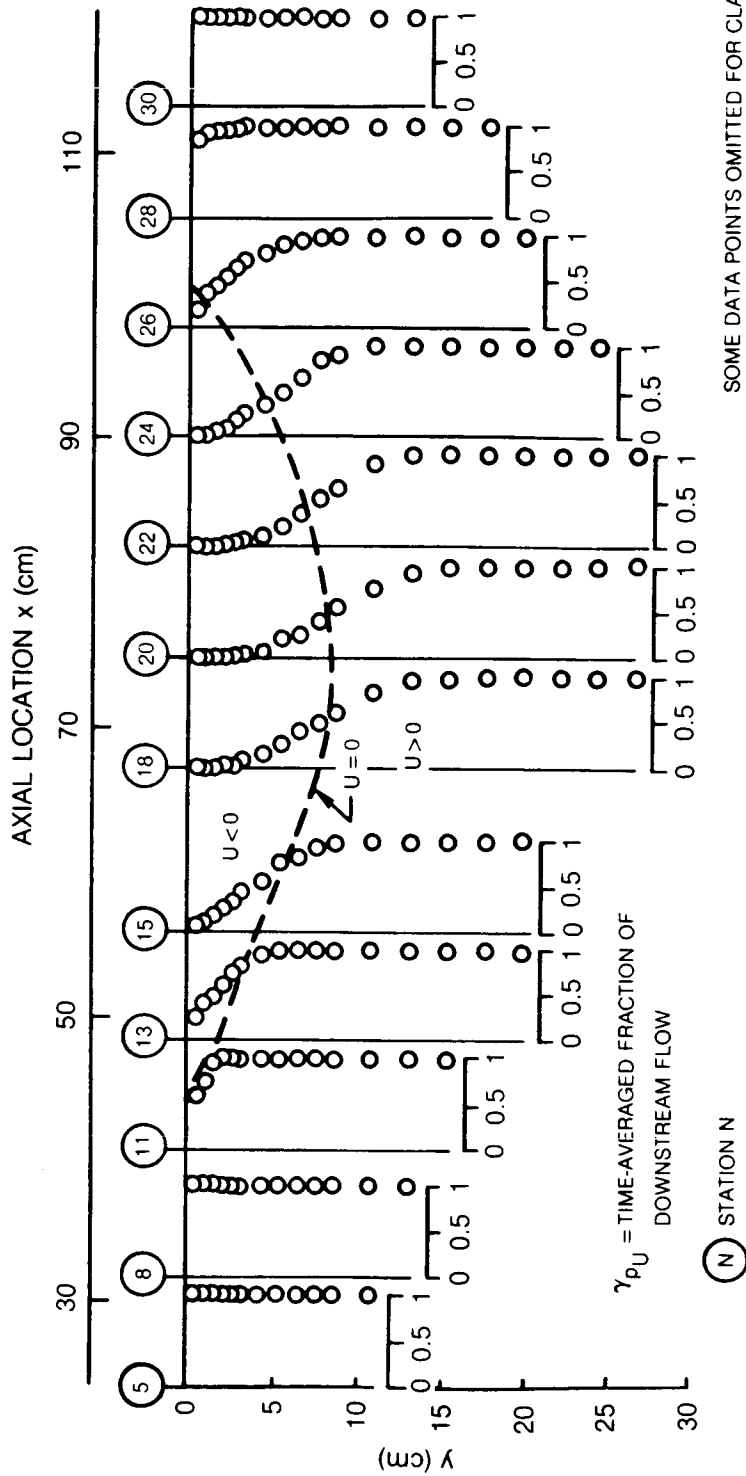
Figure 4-12 Forward Flow Fraction (γ_{p_U}) Profiles Determined from LV Histograms (z = 0)
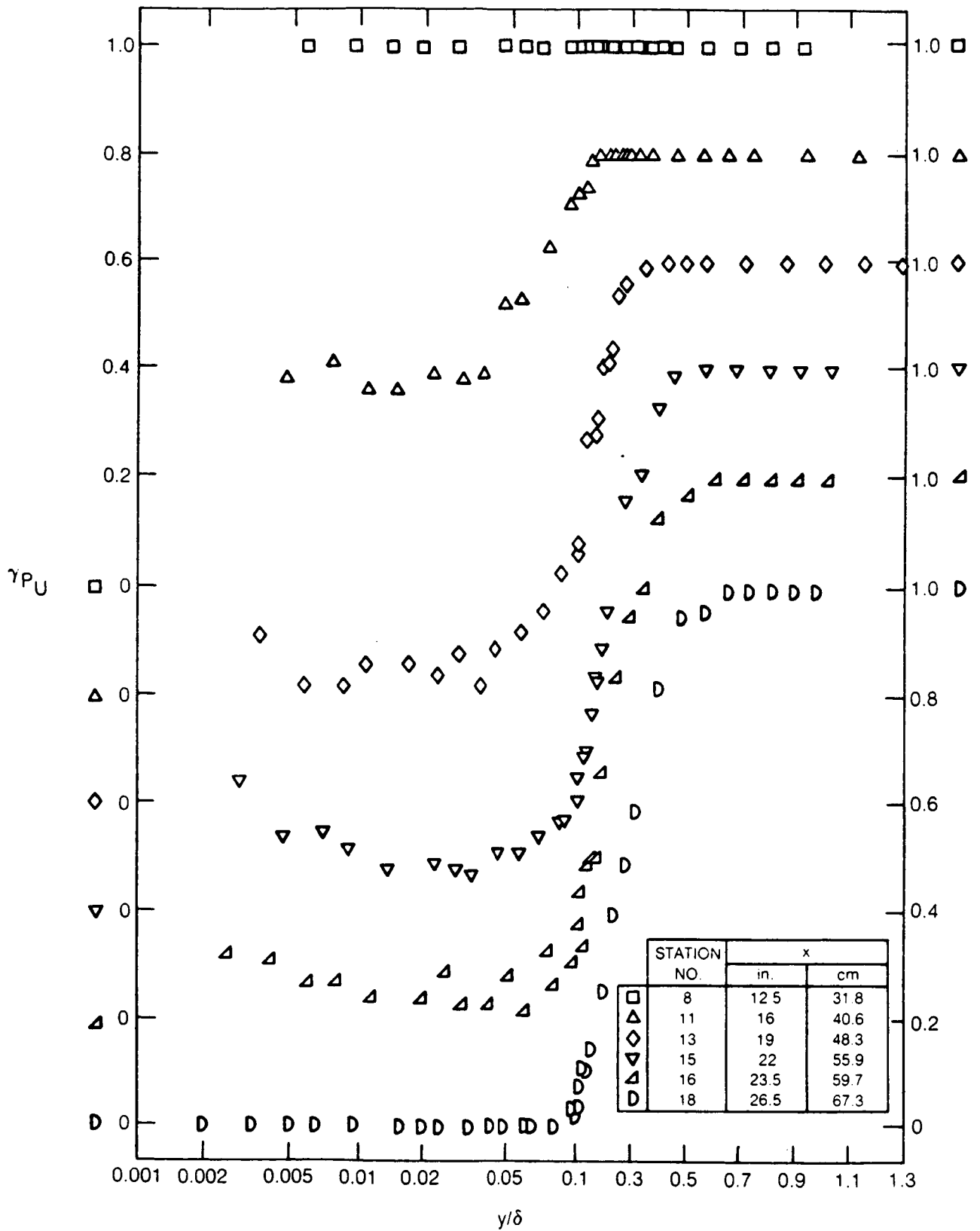
Figure 4-13a Forward Flow Fraction Profiles · Note Log-Linear Abscissa and Displaced Ordinates

84-8-1-66

STATION	x	
NO.	in.	cm
D 20	29.5	74.9
▽ 22	32.5	82.6
◁ 24	35.5	90.2
◇ 26	38.5	97.8
△ 28	41.5	105.4
○ 30	44.5	113.0

γ_{P_U}

y/δ
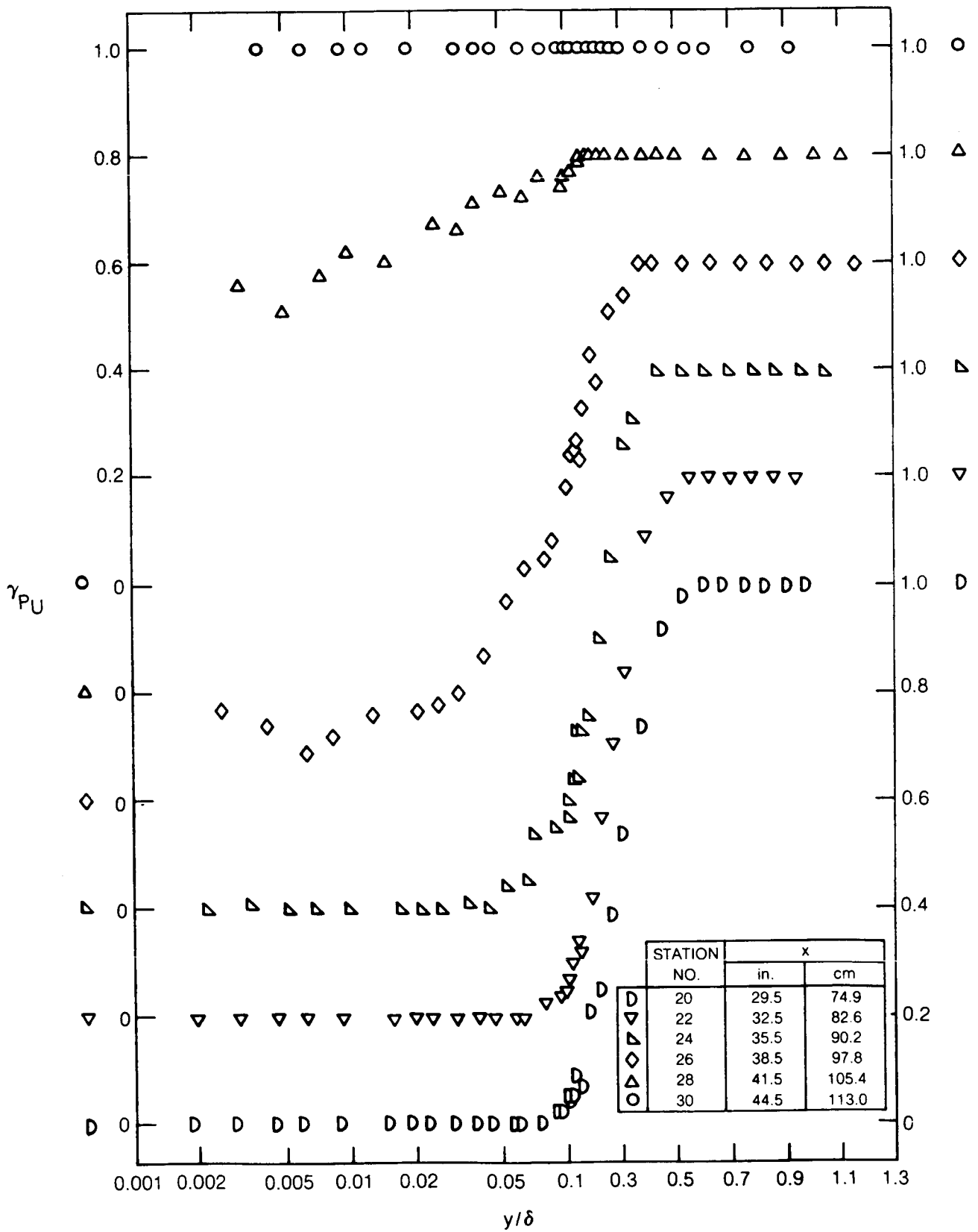
Figure 4-13b Forward Flow Fraction Profiles – Note Log-Linear Abscissa and Displaced Ordinates (Concluded)

84–8–1–65

Figure 4-14 Transverse Flow Fraction (γ_{p_V}) Profiles Determined from LV Histograms (z = 0)
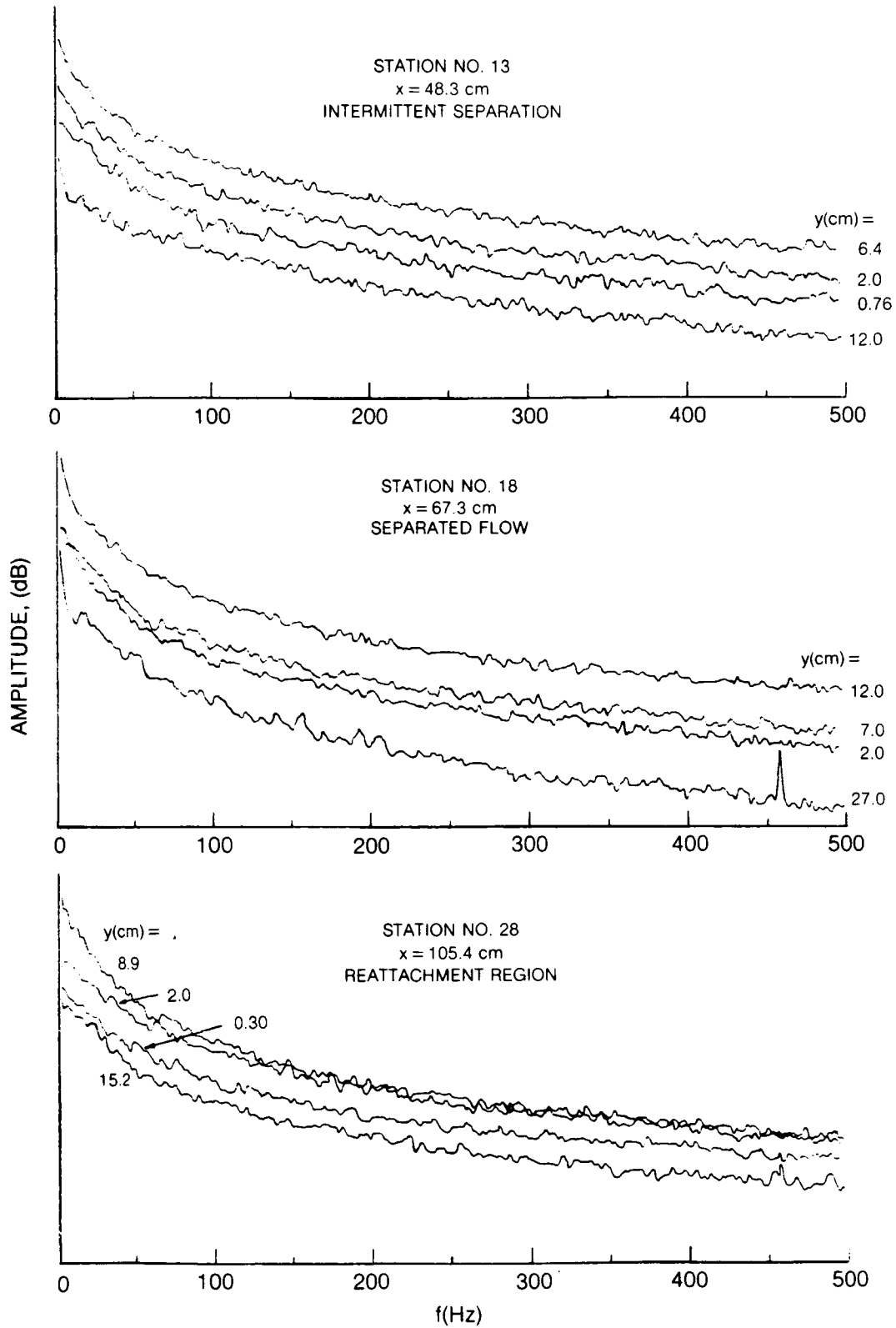
Figure 4-15 Spectra of Streamwise Turbulence Component Measured with Hot-Film

84-8-1-34
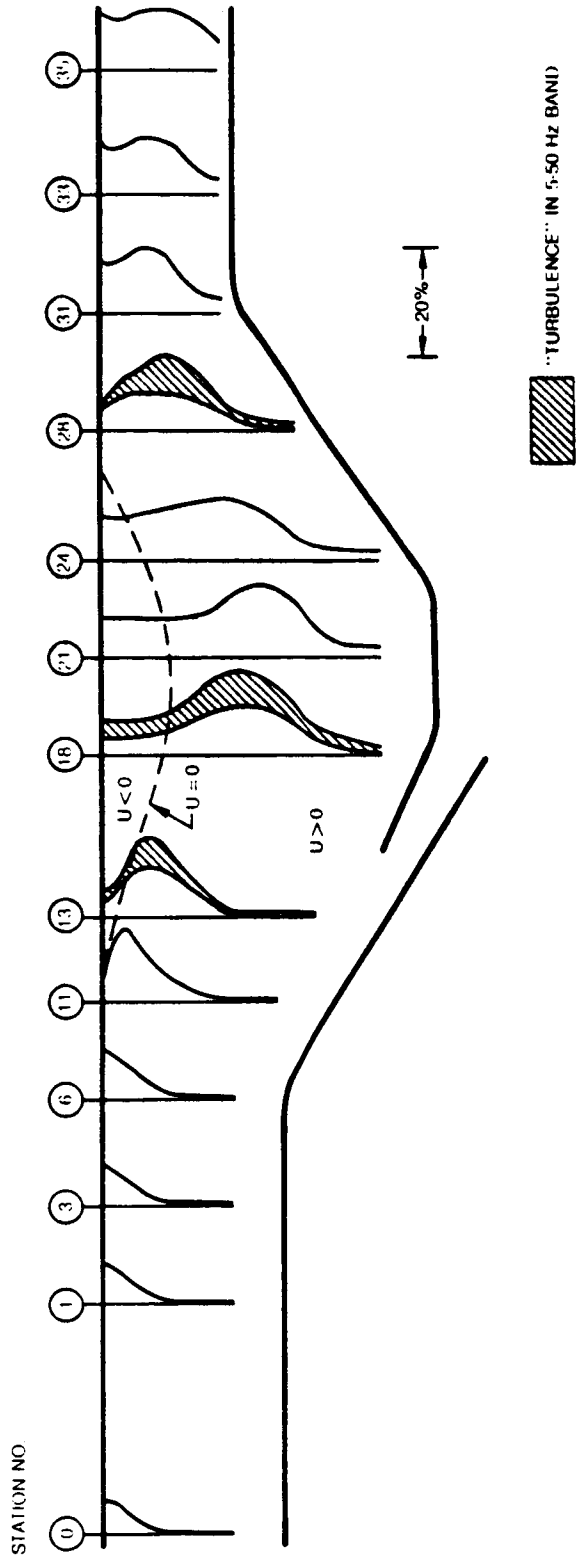
Figure 4-16 Profiles of Streamwise Turbulence Levels, y vs $\sqrt{\dfrac{\overline{q^2}}{U_{ref}}}$, Measured with Hot-Film Showing Flow Unsteadiness

PROFILES OF AXIAL TURBULENCE INTENSITY, y vs $\dfrac{\sqrt{\overline{u^2}}}{U_{ref}}$

PROFILES OF TRANSVERSE TURBULENCE INTENSITY, y vs $\dfrac{\sqrt{\overline{v^2}}}{U_{ref}}$
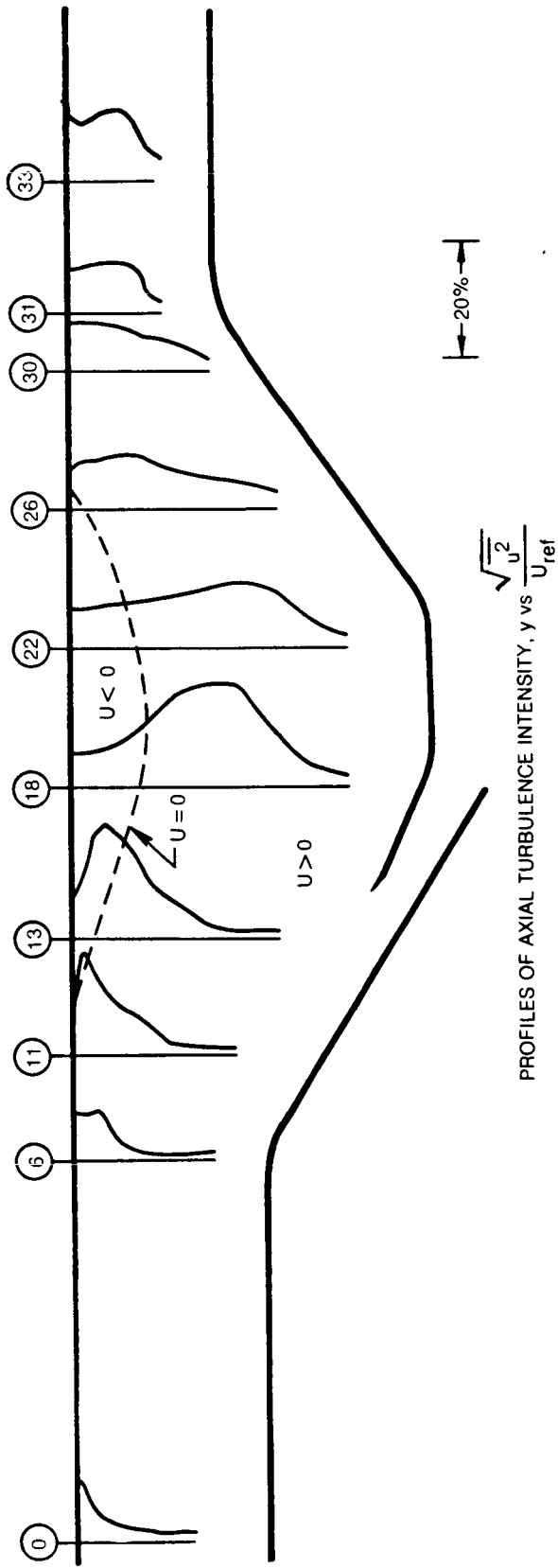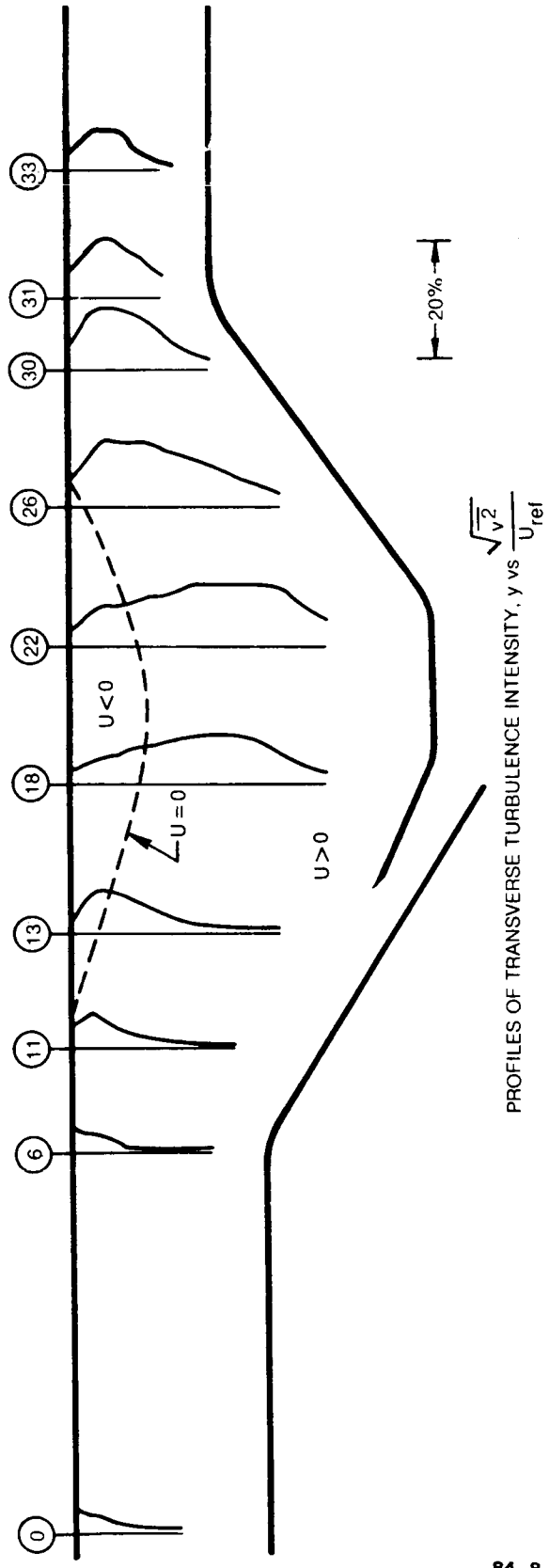
Figure 4-17 Turbulence Profiles Measured by Laser Velocimeter

78

84−8−1−13
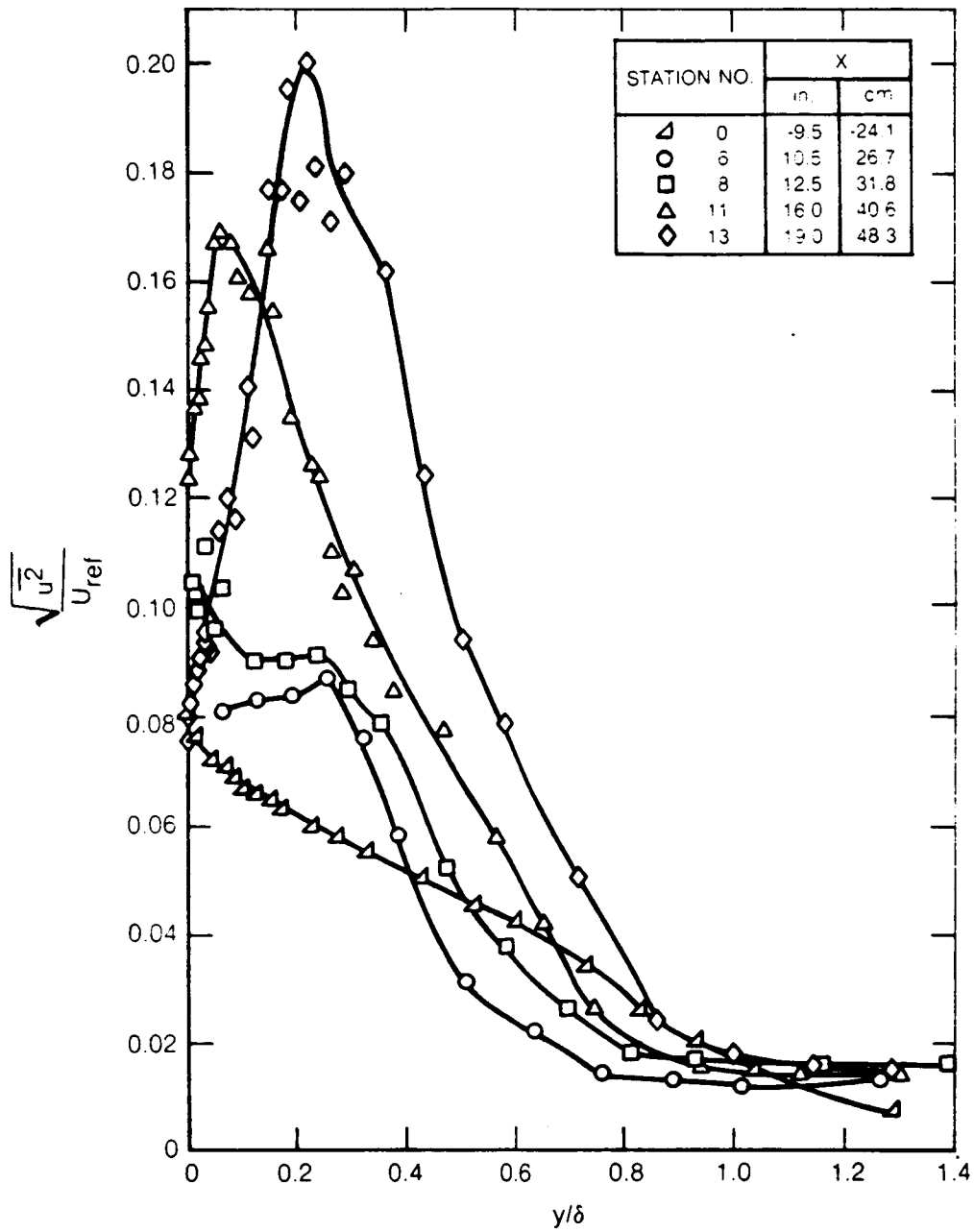
Figure 4-18a Nondimensional Axial Turbulence Profiles (z = 0)
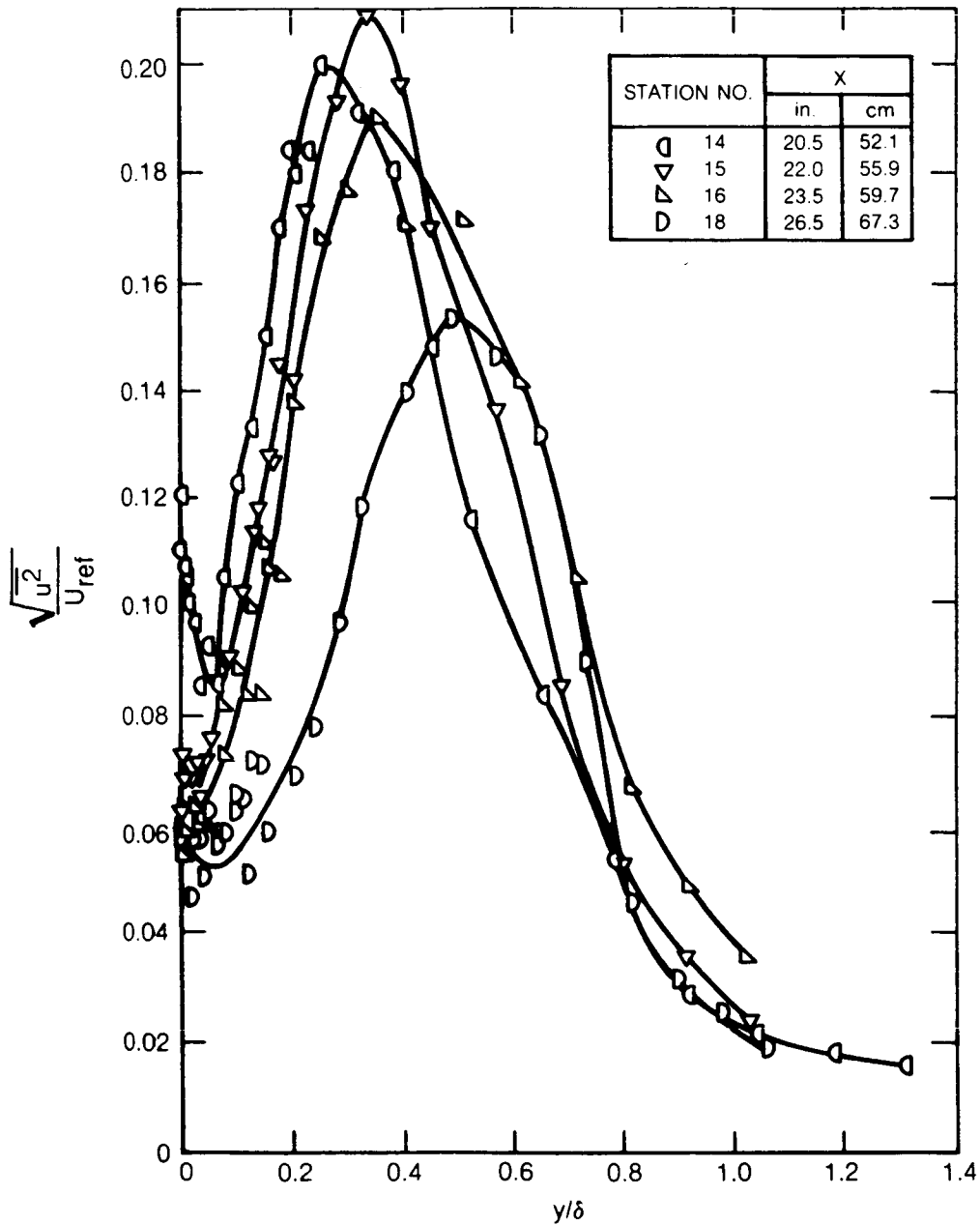
Figure 4-18b Nondimensional Axial Turbulence Profiles (z = 0) (Continued)
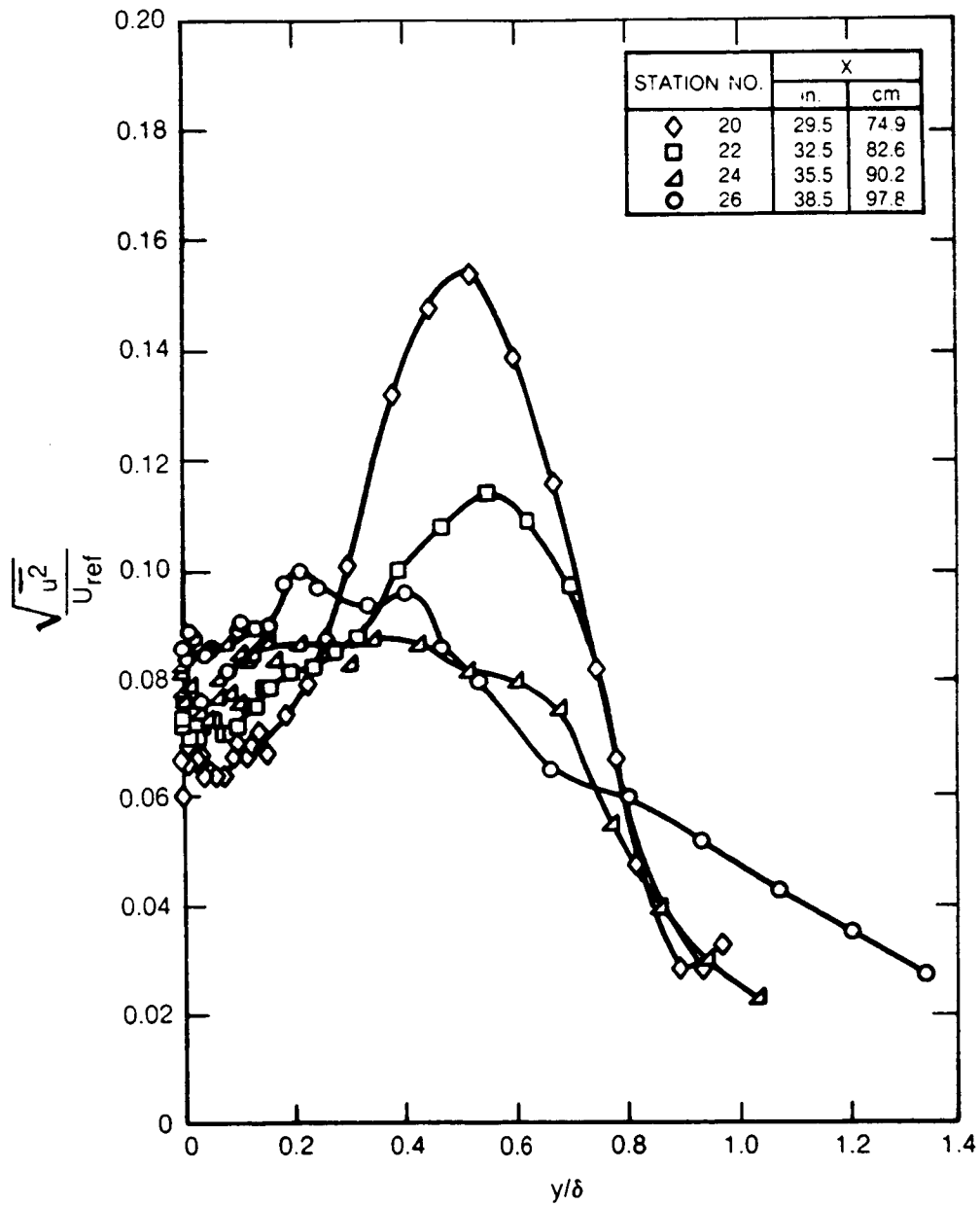
Figure 4-18c Nondimensional Axial Turbulence Profiles (z = 0) (Continued)
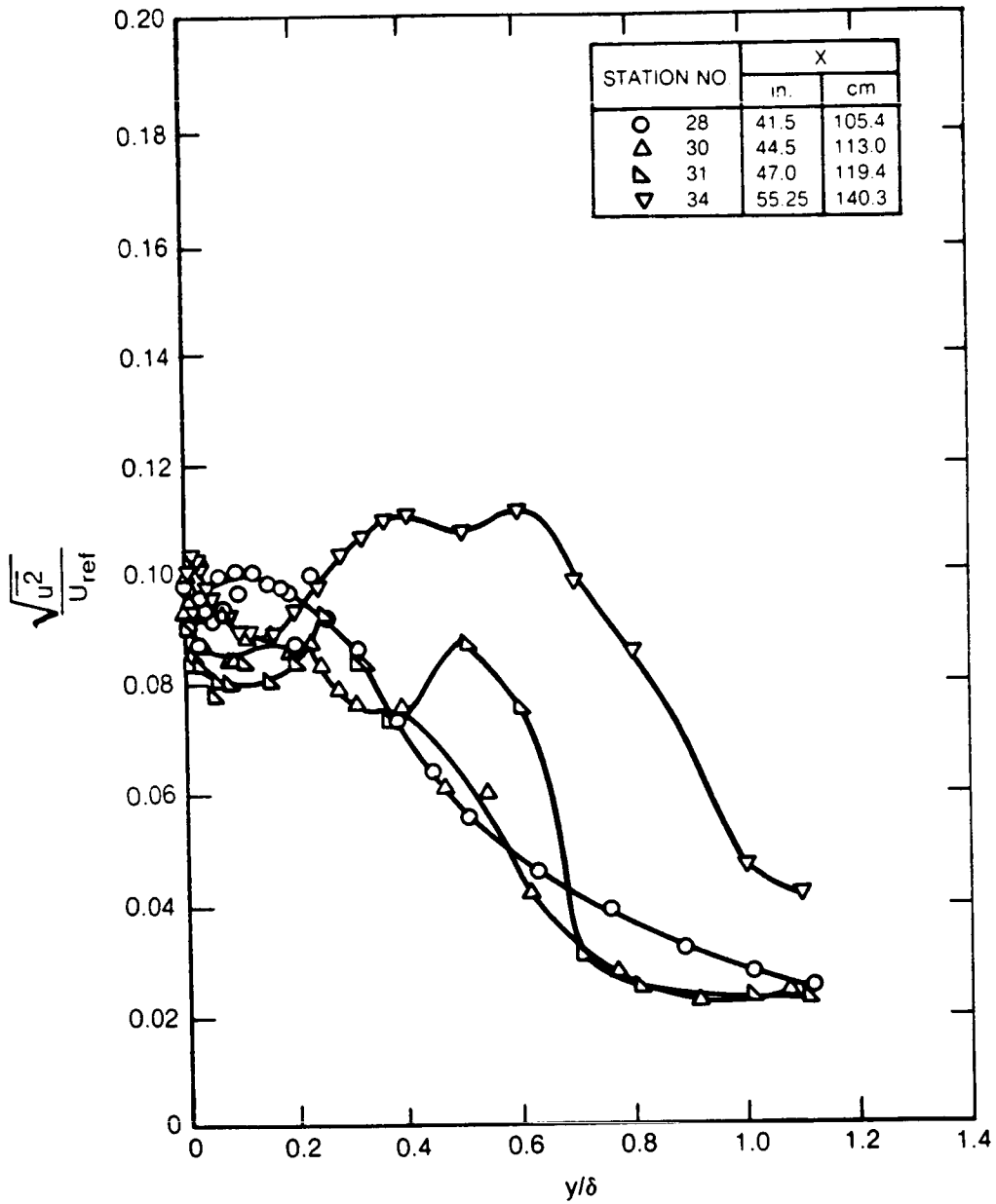
Figure 4-18d Nondimensional Axial Turbulence Profiles (z = 0) (Concluded)

84-8-1-42
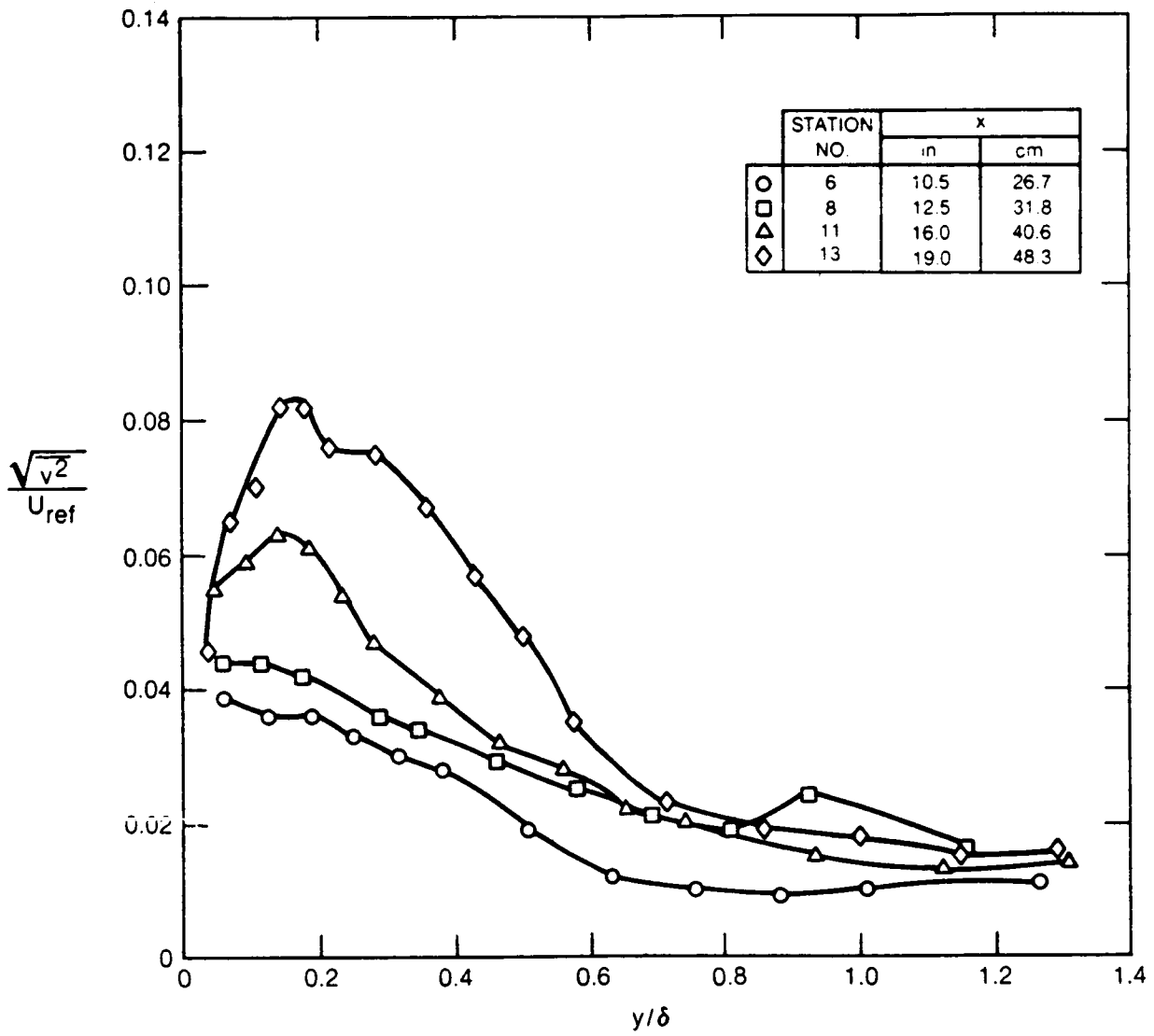
Figure 4-19a Non – Dimensional Transverse Turbulence Profiles
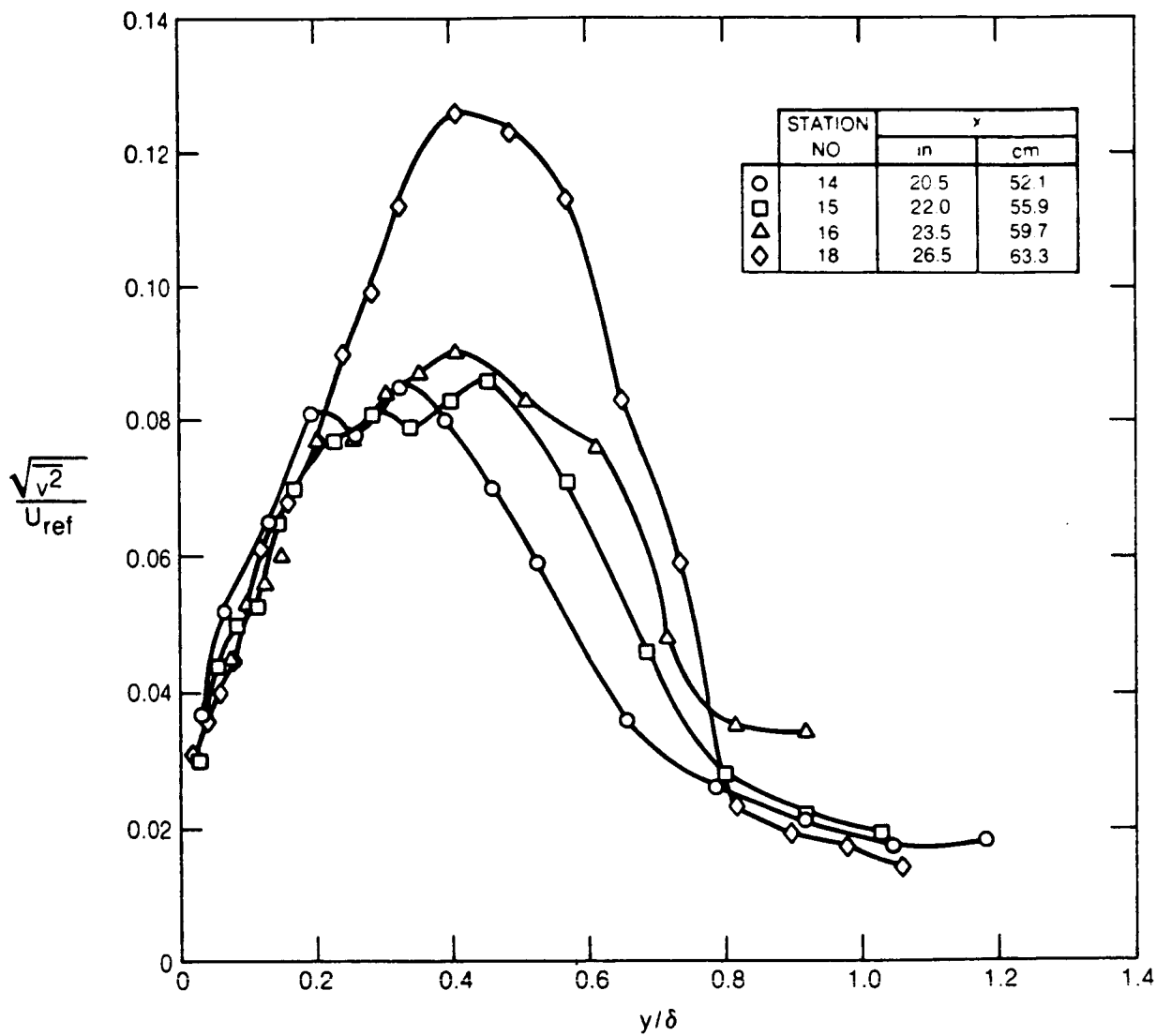
Figure 4·19b Non – Dimensional Transverse Turbulence Profiles (Continued)

84-8-1-68
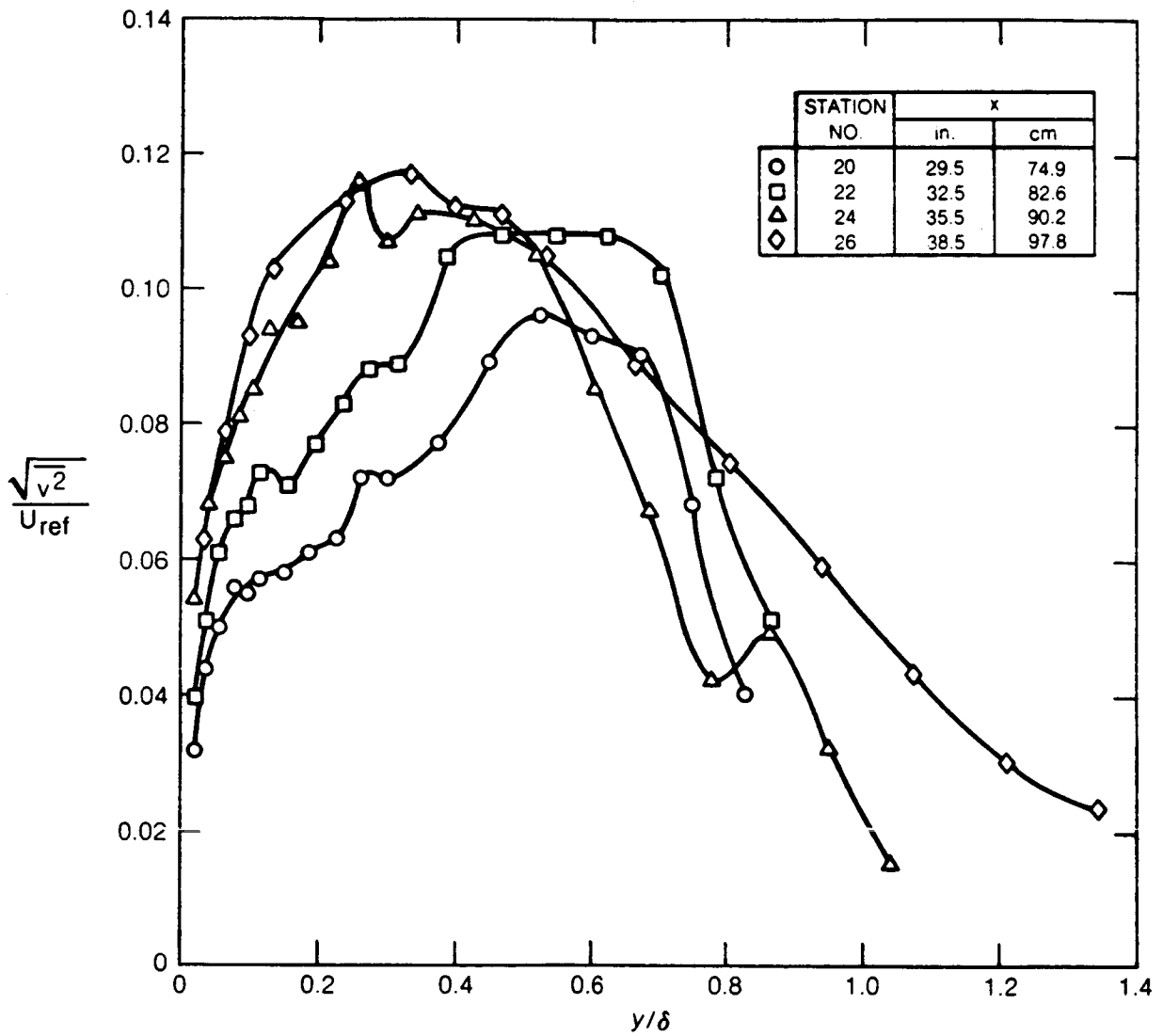
Figure 4-19c Non − Dimensional Transverse Turbulence Profile (Continued)
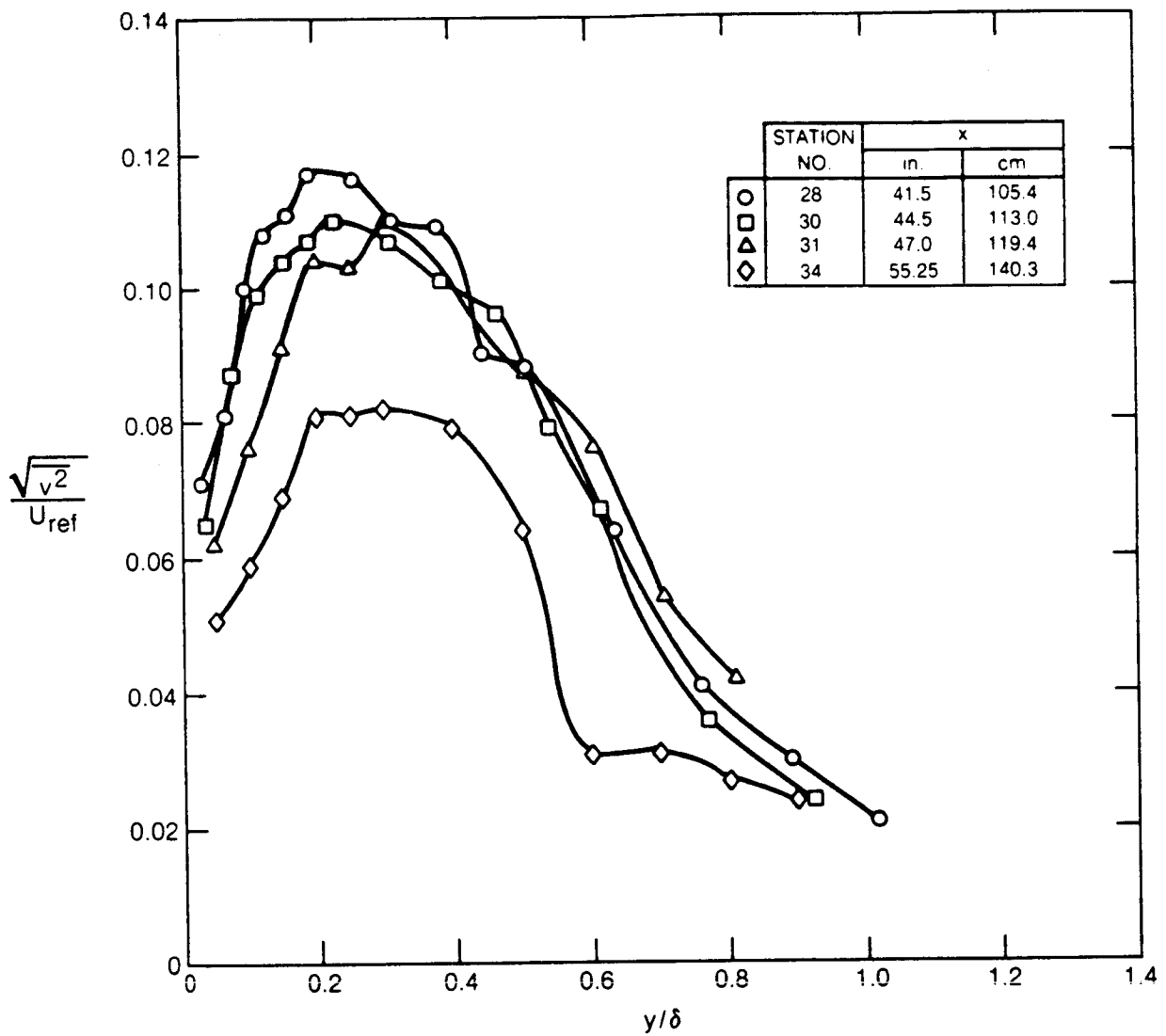
Figure 4·19d Non – Dimensional Transverse Turbulence Profiles (Concluded)

84–8–1–70
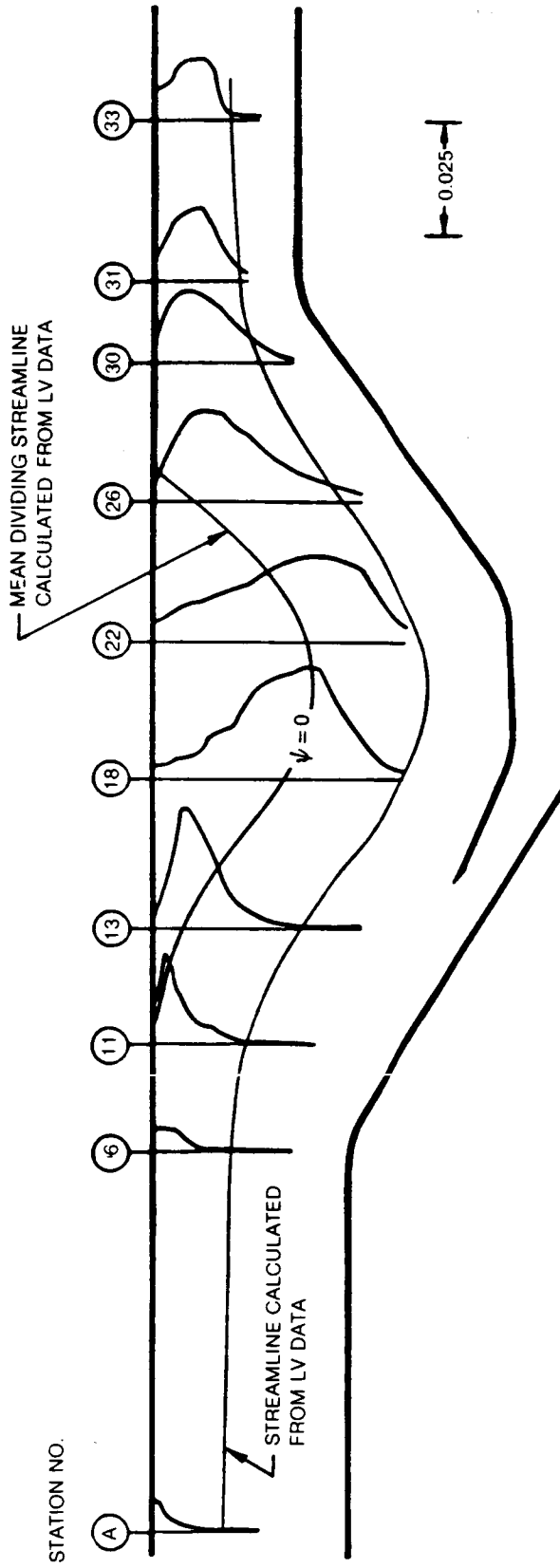
Figure 4-20 Profiles of Non-Dimensional Turbulence Kinetic Energy, y vs $\dfrac{(\overline{u^2} + 2\,\overline{v^2})}{2U^2_{ref}}$

Figure 4-21 Nondimensional Reynolds Stress Profiles Determined with Laser Velocimeter (z = 0)
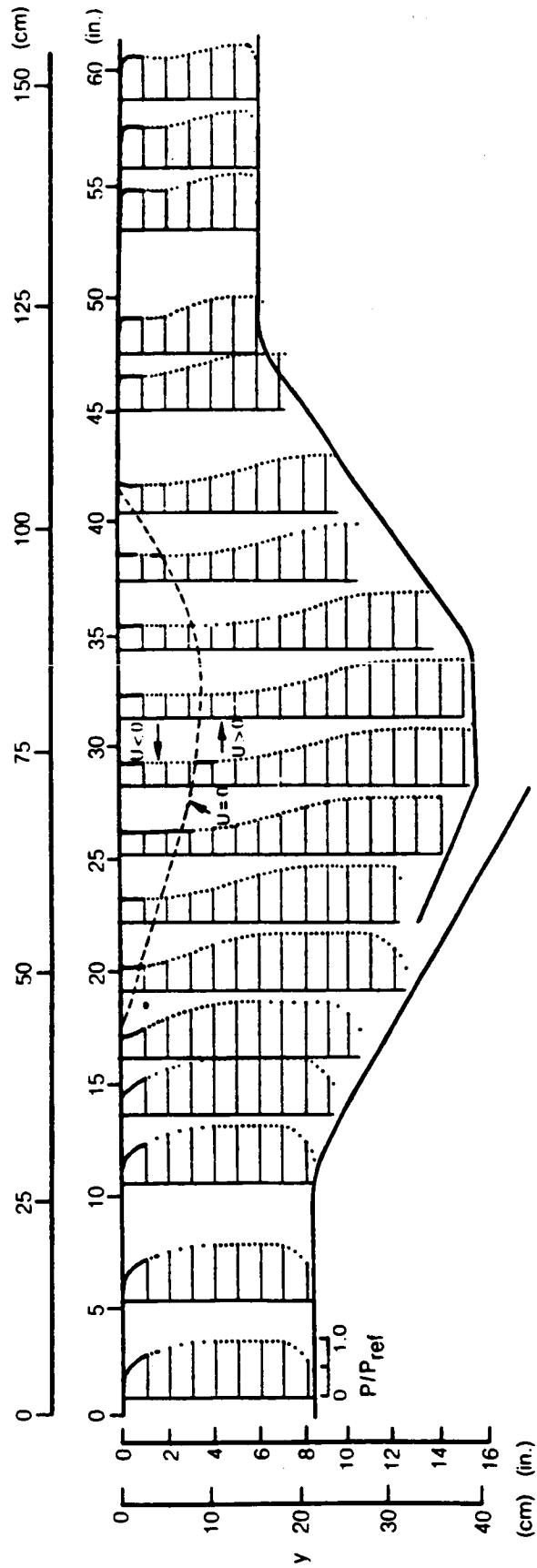
Figure 4-22 Normalized Total Pressure Profiles on Wind Tunnel Centerline

Figure 4-23 Bounding Streamline Determined by Lower Wall Total Pressure Traverses
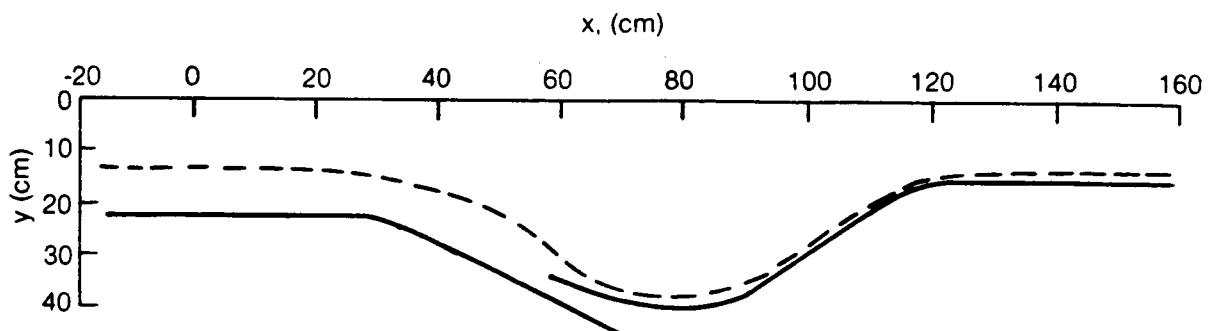
STATION NO.	x (cm)	y (cm)
1L	-22.86	13.08
2L	2.54	13.34
3L	7.62	13.46
4L	13.34	13.56
5L	17.78	13.69
6L	37.62	17.58
7L	47.52	21.95
8L	57.63	28.35
9L	58.85	32.74
10L	69 62	37.57
11L	75 57	38.02
12L	82 55	37.34
13L	92.96	34.06
14L	98.43	30.05
15L	106.40	24.69
16L	111.51	21.54
17L	133.99	14.71
18L	140.97	14.76
19L	146 05	14.76
20L	151.13	14.73

84-8-1-17

$C-2$

90

CHAPTER 5

ANALYSIS AND DISCUSSION

Chapter 4 presented the results from direct measurements along with their discussion. In this chapter, additional quantities derived from the measurements will be analyzed and discussed. These quantities include flowfield streamline coordinates, static pressure, skin friction, and streamwise shear stresses. Boundary layer integral properties and law-of-the-wall plots are also presented. The measured and derived data are then analyzed and compared to the results and correlations developed in previous investigations. In doing this the flowfield has been partitioned into eight regions or zones because the flat plate separated and reattached boundary layer has not been studied previously in its entirety with LV. Data in each flow zone will be compared to available data obtained in other separation and reattachment studies.

5.1 Flow Zones

The flow zones are defined in figure 5-1. Zone I is the attached boundary layer upstream of separation. Boundary layer profiles in Zone I can be compared to studies concerning the development of turbulent boundary layers in adverse pressure gradients. The attached boundary layer flows against the adverse pressure gradient until the kinetic energy in the boundary layer at the wall is converted into potential energy at which point the boundary layer separates from the test surface. Since the boundary layer kinetic energy at any point in a turbulent boundary layer is proportional to the square of the sum of the steady velocity field and the unsteady turbulence velocity field, separation occurs over a zone rather than at a point as occurs in a laminar boundary layer. The intermittent separation zone, Zone II, has been studied extensively for open separation bubbles by Sandborn, Kline, Simpson, and many others. Hence, comparisons can also be made for this region of the flowfield. Zone III, the turbulent separation bubble, is defined as the region between the mean dividing streamline and the test surface. Strong backflows exceeding 30 percent of the local freestream velocity occur within this region. The open separated flow data of Simpson et al. can be used as a basis for comparison in the upstream half of the bubble and the downstream half of the bubble can be compared to separation data obtained downstream of a backward facing step. The strong recirculating flow within the separation bubble causes a backflow boundary layer, Zone IIIA, to originate near the reattachment point and to develop along the test surface. No basis for comparison exists in this zone because details of the backflow boundary layer in a closed separation bubble have not been previously reported.

The reattachment of the separated shear layer is an inherently unsteady process which occurs within Zone IV, the reattachment zone, on the test surface. In this zone the reattaching flow impinges steeply onto the test surface causing a static pressure peak which drives the strong backflow within the separation bubble. The flow is characterized by high turbulence levels and frequent flow reversals. Boundary layer integral properties, skin friction, and forward flow fraction data in the reattachment zone can be compared to the data of Driver and Seegmiller (ref. 14), Westphal et al. (ref. 17), and others for reattaching flows behind a backward facing step.

Downstream of reattachment the flow recovers the structure of a flat-plate turbulent boundary layer. This process occurs in two stages. In Zone V, a new boundary layer begins to grow along the test surface and quickly develops a log-linear velocity profile near the wall. The relaxation of the outer free shear layer in Zone VI occurs much more slowly, however. Through a complicated process of turbulence energy exchange between Zones V and VI the turbulence structure downstream of reattachment gradually obtains the outer wake-like structure of a turbulent boundary layer. Data in Zones V and VI have been correlated with the recovering boundary layer profiles of Chandrsuda and Bradshaw (ref. 18).

When properly normalized the axial velocity profiles in Zone VII, the outer flow region, are found to be invariant throughout the test section. Results in this zone can be compared to separated flow studies of Perry and Fairlie (ref. 5) and Paterson and Weingold (ref. 36).

5.2 Static Pressure Field

The static pressure field within the test section was calculated at 36 stations. Twenty-six of the stations were located on the test plate centerline and five pairs of stations were located at ± 15.2 cm off the centerline. The measured quantities used to determine the static pressure, p, were the total pressure, P, and the mean axial and transverse velocities measured with the LV system

$$\frac{p - p_{w_{ref}}}{Q_{ref}} = \frac{P}{Q_{ref}(P)} - \frac{1}{2}\left[\left(\frac{U}{U_{ref}(U)}\right)^2 + \left(\frac{V}{U_{ref}(V)}\right)^2\right] \qquad (5\text{-}1)$$

where $Q_{ref}(P)$ is the dynamic pressure at the reference location during the measurement of P and $U_{ref}(U)$ and $U_{ref}(V)$ are the freestream velocities at the reference location during the measurement of U and V, respectively. As noted in Section 4.1, U_{ref} was adjusted during testing to maintain constant unit

92

Reynolds number at the reference location. The results are presented in terms of the difference between the local static pressure and the static pressure at the reference location in the boundary layer development section, $P_{w_{ref}}$, normalized by the reference dynamic pressure, Q_{ref}. For these calculations the density, ρ, which varied less than 0.3 percent throughout the test section, was assumed to be constant. Calculated values of the static pressure are listed in Table IV. Static pressure profiles at 15 stations on the test plate centerline are plotted in figure 5-2.

The transverse static pressure gradient, $\partial p/\partial y$, was essentially zero at the inlet and outlet stations. It was negative between Stations 3 and 15 due to streamline curvature. Within the separation bubble (Zone III) the static pressure was nearly constant except at the wall near reattachment (as shown previously in fig. 4-7) where the static pressure increased due to flow impingement onto the test surface. Outside the separation bubble between Stations 18 and 24, $\partial p/\partial y > 0$ due to the concave curvature of the streamlines in the freestream flow associated with flow around the bubble and the converging lower surface. Between Stations 30 and 33 the convex curvature of the lower surface at Station 31 caused $\partial p/\partial y < 0$ as the flow accelerated into the outlet duct.

The normal static pressure gradients within the test section were significant. At some stations the static presure difference between the upper test surface and the lower wall equaled 0.5 Q_{ref}. The static pressure gradients were caused by the streamline curvature in the inviscid flow due to the combined effects of the tunnel geometry and the aerodynamic blockage induced by the large separation bubble. The effect of the transverse static pressure gradients on the calculation of the boundary layer integral properties is assessed below in Section 5.3.3.

Spanwise variations in the static pressure were minimal at most stations. The maximum variation in static pressure between the centerline and the off-centerline traverse stations, which occurred near the boundary layer scoop and at Station 34 downstream of reattachment, was less than .01 Q_{ref}/cm.

5.3 Mean Flowfield Characteristics

5.3.1 Mean Flowfield Streamlines

Axial velocity profiles measured with the laser velocimeter were integrated to determine the value of the streamfunction ψ_i at any point y_i

$$\psi_i = \int_o^{y_i} U dy \qquad (5\text{-}2)$$

The locus of points of equal values of ψ_i, determined by interpolation, were used to define the mean flowfield streamline pattern shown in figure 5-3. Coordinates for the mean dividing streamline and eight additional streamlines located 1.27 cm apart at initial LV measurement Station 6 are listed in Table VI. The bounding streamline (dashed line) determined from lower wall total pressure traverses (see Section 4.9.1) has also been plotted in figure 5-3. Coordinates of the bounding streamline are given in figure 4-23 for use in computing the flowfield. The displacement of the mean flowfield by the separation bubble is quite evident. The maximum thickness of the separation bubble, h, measured from the surface to the $\psi = 0$ mean dividing streamline was 17 cm (6.7 in.) as noted in Table VI. Separation bubble length was 64 cm (25 in.). Significant streamline curvature is evident in the vicinity of the separation bubble.

At most points within the test section the mean flowfield streamlines are tangent to the measured mean velocity vectors as expected in a steady flow. Nontangency between the streamlines and the mean flow vectors near the leading edge of the separation bubble is unexplained but may arise from individual realization bias errors (ref. 37) in the transverse velocity component measurements in regions of the flowfield having spatially non-uniform seed particle distributions. Such non-uniformities are noticeable near the separation bubble where the seed density in the shear layer around the bubble was higher than the density within the bubble. Thus, positive, downward velocity fluctuations would provide relatively fewer valid counts than negative, upward velocity fluctuations because of the lower seed density near the test surface. This individual realization bias would tend to reduce the magnitude of the measured transverse velocity component.

5.3.2 Inviscid Outer Flow

Analysis of mean velocity data acquired in the present experiments has shown a feature of the velocity profile development which appears to have important implications for the numerical modeling of the flow. When static pressure variations associated with streamline curvature are taken into account, congruence of velocity profiles outside of the recirculating region is found over the axial extent of the separation bubble region. This feature will be discussed in this section.

Axial velocity profiles measured on the test section with the laser velocimeter have been shown in figure 4-9. When the profiles from the various axial measurement stations are overlayed, station-to-station similarity is not

evident. Because of the large displacement of the flow streamlines caused by the separation bubble, the axial velocity profiles have been distorted by streamline curvature in addition to viscous effects.

It is possible, however, to separate viscous from streamline curvature effects by normalizing the measured axial velocity component, U, by the inviscid axial velocity component, U_i, at each point on the profile. The inviscid axial velocity component was calculated from the freestream total pressure, P_{ref}, the measured transverse velocity component, $V(y)$, and the local static pressure, $p(y)$, discussed in the previous section.

$$U_i(y) = \frac{2}{\rho} \sqrt{P_{ref} - p(y) - \frac{1}{2} \rho V^2(y)} \qquad (5-3)$$

This procedure for normalizing the axial velocity profiles by the local inviscid velocity has been used previously by others to calculate boundary layer integral properties in flows over curved surfaces and in shock boundary layer induced separations where normal pressure gradients are also significant (see Section 5.3.3.1 "Definition of Integral Properties").

The normalized axial velocity profiles are shown in figure 5-4. These profiles have been overlayed in figure 5-5 using $y-\delta$ as the ordinate where y is the vertical distance from the flat plate test surface and δ is the the local boundary layer thickness. For clarity, profiles at stations 18, 20, 22 and 26 have been omitted from figure 5-5 although their profiles lie within the envelope formed by profiles at stations 16, 24, and 28. Using the boundary layer at station 6 (x = 26.7 cm, 10.5 in.) as reference, it can be seen that as the flow moves downstream the inner part of the initial boundary layer profile is eroded by the viscous processes associated with separation and reattachment. A similar observation has recently been made in a widely different separated flow experiment. As reported by Paterson and Weingold (ref. 36), flow downstream of a simulated compressor airfoil blunt trailing edge displays velocity profile congruence over the axial extent of the trailing edge separation bubble. In that case profile similarity was directly evident in the measured data since streamline curvature and associated static pressure gradients were significantly less than that encountered in the present experiment.

These results suggest that the outer flow can be considered basically an inviscid, rotational flow which convects around the viscously dominated recirculation zone. This is considered to be potentially important in the modeling of separated flow by viscous-inviscid interaction procedures.

5.3.3 Boundary Layer Integral Properties

5.3.3.1 Definitions of Integral Properties

In classical boundary layer theory in which the static pressure is assumed to be constant across the boundary layer, the displacement thickness, δ^*, and the momentum thickness, θ, are defined with the boundary layer edge velocity as the reference velocity

$$\delta_1^* = \int_0^\delta \left(1 - \frac{\rho U}{\rho_e U_e}\right) dy \qquad (5\text{-}4)$$

$$\theta_1 = \int_0^\delta \frac{\rho U}{\rho_e U_e} \left(1 - \frac{\rho U}{\rho_e U_e}\right) dy \qquad (5\text{-}5)$$

As long as the boundary layer thickness to the streamline radius of curvature is less than about 1 percent, the static pressure difference across the boundary layer will be less than 2 percent of the dynamic pressure and these definitions are adequate (ref. 38). However, in the present experiment, as noted above, streamline curvature within the test section was significant. Static pressure changes across the boundary layer exceeding 40 percent of the dynamic head occurred at several measurement stations in the vicinity of the separation bubble.

Kiock (ref. 38) has considered the interpretation of boundary layer data when sizeable transverse pressure gradients exist across the boundary layer. He reviewed five definitions for both the displacement and momentum thickness and compared their calculated values in example flows having prescribed normal static pressure gradients. In the present experiment, boundary layer integral properties have been calculated from data using three of the five definitions reviewed by Kiock.

The displacement thickness is defined as the thickness of the hypothetical layer in which the fictitious inviscid flow is equal to the reduction of the real mass flow due to the boundary layer. Since the mass flux between the displacement surface and the edge of the boundary layer in the fictitious inviscid flow must equal the total mass flow in the real boundary layer, the displacement thickness in the current experiment can be defined by the following equation

$$\int_{\delta^*}^{\delta} U_i \, dy = \int_{0}^{\delta} U \, dy \qquad (5\text{-}6)$$

where U_i is the local inviscid axial velocity defined above in Section 5.3.2.

Kooi (ref. 39) has shown that equation (5-6) can be solved to obtain the true definition of δ^* in the presence of normal static pressure gradients as the sum of the displacement thickness evaluated from classical boundary layer theory, δ_1^*, and a correction term to account for the effects of normal static pressure gradients

$$\delta_2^* = \int_{0}^{\delta} \left(1 - \frac{U}{U_{iw}}\right) dy - \int_{0}^{\delta} \left(1 - \frac{U_i}{U_{iw}}\right) dy \qquad (5\text{-}7)$$

where U_{iw}, the inviscid velocity at the wall calculated from the local wall static pressure and the inlet total pressure, equals U_e when $\partial p / \partial y = 0$.

Another definition of the displacement thickness, referred to by Kiock (ref. 38) as the "pressure-based" displacement thickness,

$$\delta_3^* = \int_{0}^{\delta} \left(1 - \frac{U}{U_i}\right) dy \qquad (5\text{-}8)$$

has been used by So and Mellor (ref. 40), Mayle, et al. (ref. 41), and others to account for normal static pressure gradients due to streamline curvature.

Kooi has shown that the true definition of the momentum thickness can be expressed as the sum of the momentum thickness evaluated from classical boundary layer theory, θ_1, and a correction term to account for the effects of the normal static pressure gradients.

$$\theta_2 = \int_{0}^{\delta} \frac{U}{U_{iw}} \left(1 - \frac{U}{U_{iw}}\right) dy - \int_{0}^{\delta} \frac{U_i}{U_{iw}} \left(1 - \frac{U_i}{U_{iw}}\right) dy \qquad (5\text{-}9)$$

The "pressure-based" momentum thickness for incompressible flow has been defined (ref. 38) as

$$\theta_3 = \int_0^\delta \frac{U}{U_i} \left(1 - \frac{U}{U_i}\right) dy \qquad\qquad (5\text{-}10)$$

The boundary layer shape factor, H, defined as the ratio between the displacement thickness and the momentum thickness can be calculated for each of the three definitions of the integral properties defined above.

Kiock (ref. 38) used examples to show that when U_i increases monotonically across the boundary layer $\delta_2^* > \delta_3^* > \delta_1^*$, $\theta_2 > \theta_3 > \theta_1$, and $H_2 < H_3 < H_1$. When U_i decreases monotonically across the boundary layer $\delta_2^* < \delta_3^* < \delta_1^*$, $\theta_2 < \theta_3 < \theta_1$, and $H_2 > H_3 > H_1$. The equations of classical theory hold when U_i is constant across the boundary layer and $\delta_1^* = \delta_2^* = \delta_3^*$, $\theta_1 = \theta_2 = \theta_3$ and $H_1 = H_2 = H_3$.

5.3.3.2 Calculated Values of Integral Properties

Each of the three values of the displacement thickness, momentum thickness, and the shape factor defined above were calculated at each LV traverse location within the test section. Plotted values of the displacement and momentum thicknesses on the wind tunnel centerline are shown in figure 5-6a. The displacement thickness increased rapidly downstream of the start of the intermittent separation zone (x = 40.6 cm, 16 in) until it peaked at x = 74.9 cm (29.5 in.), the location of the maximum thickness of the separation bubble (see fig. 5-3). The shape of the displacement thickness curve is almost symmetric about the center of the bubble. The momentum thickness increased much more slowly as the boundary layer approached separation. Within the separation bubble the momentum thickness remained relatively constant before decreasing downstream of reattachment.

Values of the shape factor are plotted in figure 5-6b. The true value of the shape factor, H_2, increased from 1.38 at x = 26.7 cm (10.5 in.) to 2.09 at x = 40.6 cm (16.0 in.) near separation, then to a peak value of 16.1 at x = 74.9 cm (29.5 in.) before declining to a value of 1.23 in. the accelerating flow in the outlet duct. Peak values of H_3 and H_1 also occurred at x = 74.9 cm and equaled 11.8 and 7.5 respectively.

The results follow the trends shown in Kiock's example boundary layers. Upstream of separation (x < 48 cm, 19 in.) and downstream of reattachment (x > 113 cm, 44.5 in.), where $\partial U_i/\partial y > 0$ across the boundary layer, $\delta_2^* < \delta_3^* < \delta_1^*$, $\theta_2 < \theta_3 < \theta_1$ and $H_2 > H_3 > H_1$. Near the center of the separation bubble (48 cm < x < 90 cm), $\partial U_i/\partial y < 0$ across the boundary layer and $\delta_2^* < \delta_3^* < \delta_1^*$, $\theta_2 < \theta_3 < \theta_1$, and $H_2 > H_3 > H_1$. At x = 48 cm, 19 in., $\partial U_i/\partial y \simeq 0$ across the boundary layer and $\delta_1^* = \delta_2^* = \delta_3^*$, $\theta_1 = \theta_2 = \theta_3$, and $H_1 = H_2 = H_3$. At the

remaining measurement stations the sign of $\partial U_i/\partial y$ varied across the boundary layer. Although Kiock demonstrated the relationships between classical, true, and pressure-based integral parameters with simple mathematical models of the boundary layer, the agreement shown here demonstrates that these trends hold equally well in complex flowfields of interest.

5.3.4 Skin Friction Coefficient on Test Surface

Law-of-the-wall velocity profiles were calculated from pitot data and LV velocity data in the attached flow upstream of separation and downstream of reattachment. The skin friction coefficient was determined from the friction velocity, U_τ

$$C_f = 2 \frac{U_\tau^2}{U_{ref}^2} \tag{5-11}$$

Within the separation bubble the skin friction coefficient was determined from backward facing pitot data. At all stations within the bubble C_f was evaluated from the normal velocity gradient at the wall estimated from pitot data. Where possible C_f was also calculated from friction velocities obtained from law-of-the-wall plots of the backflow velocity profiles. Details of the calculations are given in Section 5.5.1.

The skin friction coefficients in the test section are presented in terms of the upstream reference velocity (i.e., $C_f = 2\tau_w/\rho U_{ref}^2$) and also in terms of the local freestream velocity (i.e., $C_{f_L} = 2\tau_w/\rho U_e^2$). Values of the skin friction coefficient based upon the upstream reference velocity, C_f, will be used to quantify wall shear stress variations in the test section. C_{f_L}, based on the local freestream velocity, will be used to compare to Swafford's correlation of skin friction in attached and separated turbulent boundary layers (ref. 42).

Values of C_f on the test plate centerline are plotted in figure 5-7a. At the reference station 24 cm upstream of the test section inlet C_f equaled 0.00267, a typical value for a zero-pressure gradient turbulent boundary layer having $Re_\theta = 11,100$. C_f decreased in the decelerating boundary layer upstream of separation until it reached a value of 0.0001 at $x = 40.6$ cm just upstream of detachment. The negative value of C_f calculated from the backflow velocity profiles within the separation bubble indicated that the wall shear stress within the separation bubble was approximately 1/10 as large as the wall shear in the attached flow wall upstream of separation. Down-

stream of reattachment C_f increased rapidly until a value of 0.00282 was reached at the last measurement station in the exit duct.

Swafford (ref. 42) has proposed the following empirical correlation which uses measured values of shape factor, H, and momentum thickness Reynolds number, Re_θ, to estimate C_{f_L} in both attached and separated flows.

$$C_{f_L} = \frac{0.3e^{-1.33H}}{(\log_{10}Re_\theta)^{1.74+.31H}} + (1.1 \times 10^{-4}) \left[\tanh \left(4 - \frac{H}{.875} \right) - 1 \right] \quad (5\text{-}12)$$

The first term in Swafford's correlation is the skin friction correlation given by White (ref. 43) for attached turbulent boundary layers. Swafford added the second term to correlate the negative skin friction coefficients in reversed flows. Experimentally determined values of C_{f_L} on the test plate centerline have been plotted in figure 5-7b together with Swafford's correlation. Experimentally determined values of θ_2 and H_2 were used to evaluate eq. (5-12). The agreement between the correlation and the data is very good up to separation. The correlation correctly predicts the length of the separation bubble but significantly underpredicts the skin friction in the backflow boundary layer. The maximum negative value of skin friction coefficient (i.e., C_{f_L} = -0.00022) which can be obtained from eq. (5-12) limits its ability to correlate the wall shear in energetic backflow boundary layers. Downstream of reattachment the Swafford correlation underpredicts the rapid monotonic increase in skin friction by 20 to 40 percent. Swafford anticipated that his correlation would not be universally applicable to all flow situations since it was developed largely from the open separation bubble data of Simpson et al. (ref. 1) and Alber et al. (ref. 44). The Swafford correlation has not been compared previously to separation bubble data through reattachment.

5.3.5 Demonstration of Flow Two-Dimensionality

The criterion to measure the spanwise uniformity of the flow at the initial measurement plane, test section inlet, just upstream of separation, and within the reversed flow region have been defined in Section 3.2.4 "Flow Two-Dimensionality and Steadiness Criteria". The attainment of the spanwise uniformity criterion at the initial measurement plane, which was defined as deviation of less than one percent in the measured pitot pressure at tunnel midheight, has been described in Section 4.2 "Initial Plane Boundary Conditions". The attainment of a straight separation line which deviated from a line perpendicular to the tunnel centerline by ±6 percent of the test section span excluding the sidewall regions has been described in Section 4.3 "Flow

100

Visualization". This ±6 percent deviation only slightly exceeded the ±5 percent criterion. Satisfaction of the remaining criterion that the boundary layer momentum thickness at each spanwise measurement station (i.e., z = -15.2 cm, 0, +15.2 cm) deviate from the spanwise average by less than 5 percent will be discussed in this section.

First, however, the spanwise uniformity of the total pressure profiles within the test section should be noted. In figure 5-8 nondimensionalized total pressure data are plotted vs. transverse distance from the test plate at three spanwise locations for each of six axial stations: two stations upstream of separation, two stations within the separation bubble, two stations downstream of reattachment. The profiles at Stations 2, 11, 18, and 24, encompassing the region from upstream of separation to the aft end of the bubble, show good spanwise uniformity with the maximum profile difference being on the order of .05 P/Q_{ref}. Downstream of reattachment at Station 31 (fig. 5-8e) the total pressure profile on the centerline has a larger defect at 2.5 cm < y < 7.5 cm than the off-centerline profiles. This difference is almost eliminated at Station 34 (fig. 5-8f) in the exit duct.

The same data have been replotted in figure 5-9 with the ordinate normalized by the boundary layer thickness. Minimal spanwise skewness is evident in the profiles at Stations 18 (fig. 5-9c) and 24 (fig. 5-9d) indicating that the skewness observed in figure 5-8c and 5-8d resulted from small spanwise variations in the boundary layer thickness within the separation bubble. The variation in the boundary layer thicknesses measured at the z = +15.2 cm and z = -15.2 cm locations at stations 18 and 24 were 11.6 percent and 7.0 percent of the boundary layer thicknesses on the centerline, respectively.

The spanwise variations in the momentum thickness at the same six axial stations has been assessed. Values of θ_1, the momentum thickness derived from classical boundary layer theory, and θ_3, the pressure-based momentum thickness (see Section 5.3.3.1 "Definitions of Integral Properties") normalized by the spanwise average are plotted in figure 5-10. At stations 2 and 11 upstream of separation and Stations 18 and 24 within the reversed flow region θ_1 varied less than 5 percent across the span. Downstream of reattachment at stations 31 and 34 the momentum thickness peaked on the wind-tunnel centerline and varied from the spanwise average by 8 and 13 percent, respectively. The pressure-based momentum thickness, θ_3, showed similar trends to θ_1 except at station 18 where θ_3 was 8 percent less than the spanwise average at z = 0. The slight three-dimensionality in the flowfield downstream of reattachment, apparent from the spanwise variations in momentum thickness, is consistent with the inward skewness of the surface tufts shown above in figure 4-4.

5.4 Description of the Separation Process

5.4.1 Nature of the Decelerating Boundary Layer

The streamwise mean-velocity distribution in a turbulent boundary layer can be expressed as a linear combination of wall and wake functions as shown by Coles (ref. 45).

$$u^+ = f(y^+) + \frac{\Pi}{\kappa} w\left(\frac{y}{\delta}\right) \qquad (5\text{-}13)$$

where κ is a constant to be determined from experimental data and $w(y/\delta)$ is a universal wake function. The near wall flow is dominated by viscosity whereas the wake flow represents the cumulative effect of the pressure gradient. When the inner layer (or wall) structure is in equilibrium with the outer layer (or wake) structure the turbulent boundary layer is said to be in equilibrium.

Coles showed that the wake parameter Π could be expressed as

$$\Pi = \kappa \left(\frac{\delta^*}{\delta}\right)\left(\frac{U_e}{U_\tau}\right) - 1 \qquad (5\text{-}14)$$

He further noted that when Π is constant the turbulent boundary layer is in equilibrium and there is a certain balance between the constraints imposed by inertia (i.e. U_e) and viscosity (i.e. U_τ). A balance also exists between the large-scale and small-scale mixing processes (ref. 45). This concept of equilibrium is useful in zero, favorable, and slightly adverse pressure-gradient, turbulent boundary layer flows whose mean-velocity profile and turbulence structure are dominated by the effects of the wall (ref. 6).

Another equilibrium parameter, which characterized the flow in the outer layer, was derived by Clauser (ref. 46).

$$\beta = \frac{\delta^*}{\tau_w} \frac{dp_e}{dx} \qquad (5\text{-}15)$$

Clauser showed that a turbulent boundary layer with variable pressure gradient, but β constant, is in equilibrium.

White (ref. 43) studied 13 near equilibrium flows presented at the 1968 Stanford Conference (ref. 47) and proposed the following empirical relationship between Π and β for equilibrium flows

$$\Pi \approx 0.8 \, (\beta + 0.5)^{0.75} \tag{5-16}$$

To determine the nature of the boundary layer upstream of separation, velocity profiles were plotted in law-of-the-wall coordinates (fig. 5-11). The velocity profiles at Stations 0-5, were determined from pitot traverses with the assumption that transverse static pressure gradients were negligible. At Station 6 ($x = 26.25$ cm) profiles were determined from both pitot and LV data. Only LV data is presented at Station 8 ($x = 31.75$ cm) because of significant transverse static pressure gradients at that station.

Values of skin friction, C_f, and the wake parameter, Π, were calculated at each station from the profiles. The skin friction decreased monotonically from a value of .00267 at Station 0 ($x = -24.1$ cm) to .00077 at Station 8. The wake parameter, Π, equaled 0.33 at Station 0 where the boundary layer was nearly in equilibrium (see Section 4.2). (Coles suggested a value of 0.55 for a flat-plate zero-pressure-gradient boundary layer.) The wake parameter remained relatively constant through Station 3 ($x = 13.34$ cm) before increasing rapidly to a value of 3.4 at Station 8 ($x = 31.75$ cm) as the flow encountered an increasingly adverse pressure gradient as shown previously in figure 4-7.

The Clauser equilibrium parameter, β, was also evaluated at the same measurement stations after eq. (5-15) was transformed into the following form.

$$\beta = \frac{\delta^*}{C_f} \frac{dC_p}{dx} \tag{5-17}$$

The calculated values of β and Π are plotted in figure 5-12 together with the empirical curve, eq. (5-16), defining the relationship between Π and β for equilibrium flows. As shown in the figure, although the boundary layer was nearly in equilibrium at Stations 0, 1 and 2, neither Π nor β remained constant between Sections 3 and 8 as the boundary layer lost its equilibrium structure when it encountered the strong adverse pressure gradient.

Some insight into the reasons for this loss of equilibrium can be obtained by differentiating eq. (5-17) with respect to x

$$\frac{\partial \beta}{\partial x} = \frac{\delta^*}{C_f} \frac{\partial^2 C_p}{\partial x^2} + \frac{1}{C_f} \frac{\partial C_p}{\partial x} \frac{\partial \delta^*}{\partial x} - \frac{\delta^*}{C_f^2} \frac{\partial C_p}{\partial x} \frac{\partial C_f}{\partial x} \qquad (5\text{-}18)$$

Thus, it should not be surprising that given the shape of the measured static pressure distribution upstream of separation (i.e. $\partial^2 C_p/\partial x^2 > 0$) that the decelerating flow was not in equilibrium. Since $\partial \delta^*/\partial x > 0$ and $\partial C_f/\partial x < 0$ upstream of separation, all the terms on the rhs of eq. (5-18) are positive, thereby precluding $\partial \beta/\partial x$ from equaling zero, the condition for equilibrium. In decelerating flows, equilibrium can only be achieved when $\partial^2 C_p/\partial x^2 < 0$.

Cutler and Johnston (ref. 6) have noted that in strongly adverse pressure gradient and detaching flows the concept of equilibrium is not too useful. The boundary layer loses profile and structural self-similarity when the inner layer cannot adjust fast enough to changes imposed on the outer layer by the adverse pressure gradient.

A measure of the strength of the gradient can be obtained from a ratio of the boundary layer thickness, δ, and a characteristic length scale of the adverse gradient, $U_e/(\partial U_e/\partial x)$.

$$R = \frac{\delta}{U_e} \frac{\partial U_e}{\partial x} \qquad (5\text{-}19)$$

This non-dimensional gradient strength, R, usually can be calculated from experimental data when detailed profile information is not available to evaluate the wake parameter, Π. In the following section values of R have been calculated for the experiments of Simpson et al. (ref. 2) and Sandborn and Liu (ref. 49) and are compared to the non-dimensional gradient strengths calculated from data measured in the current study.

5.4.2 Analysis of Data in the Separation Region

In the absence of a salient edge, turbulent boundary layer separation occurs over a region rather than at a single streamwise location as occurs in laminar boundary layer separation. This process of turbulent boundary layer separation on a faired surface has been described by Sandborn and Kline (ref. 23) as follows:

104

"...separations of a turbulent shear layer do not usually begin in a steady or two-dimensional fashion on a faired surface. Instead they more often commence with intermittent streaks of backflow extremely near the surface. At the present time the onset of these streaks of backflow is not well correlated; indeed, the onset apparently depends on the nature of the fluctuations in the free stream. However, this is probably not of crucial importance, since these streaks of backflow are now known to be only an evidence of the existence of islands of hesitation which form a portion of the inherent flow model of the wall layers of the turbulent shear layer described by Kline and Runstadler (ref. 48). In favorable or mild adverse pressure gradients these islands of hesitation merely move more slowly than neighboring fluid layers; backflows are not observed. However, as the adverse pressure gradient is increased, these layers of very small inertia begin, relatively soon, to show upstream motions and to create local intermittent flow separation with streaks of backflow near the surface of a very small length scale. As the adverse pressure gradient is increased still further, these local backflows begin to accumulate slow moving fluid near the wall faster than it can be removed by the through flow. This leads to large transient three-dimensional stall patterns wherein the slow moving fluid is removed by intermittent adjustments in the over-all flow pattern and pressure distribution. Finally, upon still further increase in adverse pressure gradient, this process leads to a complete breakdown of the boundary-layer potential flow pattern and a fully established stall."

The following terminology has been defined (refs. 6 and 8) to quantify the process of turbulent boundary layer separation.

Detachment (D) - the locus of points where the limiting streamline of the time-averaged flow leaves the wall; a location of zero mean skin friction.

Incipient Detachment (ID) - the point upstream of detachment having backflow at the wall 1 percent of the time ($\gamma_{p_U} = 0.99$).

Intermittent Transitory Detachment (ITD) - the point upstream of detachment having 20 percent instantaneous backflow of the wall ($\gamma_{p_U} = 0.80$).
Transitory Detachment (TD) - the point in the region of detachment having 50 percent instantaneous backflow at the wall ($\gamma_{p_U} = 0.50$). This point is usually coincident with or very close to the detachment point (D).

The locations of incipient detachment, intermittent transitory detachment, and transitory detachment for the current study occurred at x = 32, 35.5, and 42 cm, respectively, as shown in figure 5-13. Thus, the axial

extent of the separation region between incipient detachment and detachment was 10 cm which was less than the 11 cm thick boundary layer at Station 8 (x = 31.75 cm) just upstream of incipient detachment. Sandborn and Liu (ref. 49) who studied a turbulent separation bubble on a curved surface also achieved separation over one boundary layer thickness whereas Simpson et al separated the flow more gradually over 4.4 boundary layer thicknesses. Cutler and Johnston (ref. 6) did not achieve detachment and Smith et al (ref. 25) and Perry and Fairlie (ref. 5) did not measure the forward flow fraction.

To compare the forward flow fraction data in the separation region with data obtained by other investigators, γ_{p_U} has been plotted vs. a shape factor, h = $(H_2-1)/H_2$, in figure 5-14. The shaded region represents the range of turbulent boundary layer separation and reattachment data surveyed by Kline et al (ref. 50). All the turbulent separation cases surveyed were near equilibrium. The data obtained upstream of detachment in the current study lies outside and to the left of the envelope of the equilibrium separation data surveyed. Transitory detachment was achieved in the current study at h ≃ 0.55, significantly less than the 0.69 < h < 0.77 range of the surveyed data. This result could have occurred because of the nonequilibrium nature of the decelerating boundary layer in the current study. The strong adverse pressure gradient caused detachment to occur before the profile could adjust to an equilibrium shape.

Correlations have been developed in the H-Λ plane, where Λ = δ*/δ, to demarcate the regions of unseparated flow, intermittent separation, and fully developed separation. Sandborn (ref. 51) defined the line of demarcation between unseparated flow and intermittent separation in a turbulent boundary layer by the following equation

$$H = 1 + \frac{1}{1-\Lambda} \qquad (5-20)$$

Sandborn and Kline (ref. 23) demonstrated that eq. (5-20) correlated all known intermittent separation data available at that time. Sandborn (ref. 51) also defined a line in the H-Λ plane to denote the location of laminar boundary layer separation. Sandborn and Liu (ref. 49) later showed that the laminar separation line could be generalized as a zero wall shear separation line since it also demarcated the regions of intermittent and fully developed turbulent separation.

The correlations of Sandborn, the present experimental data, and the data of Simpson (ref. 1), Perry and Fairlie (ref. 5), Smith et al (ref. 25), and Sandborn and Liu (ref. 49), are shown in figure 5-15. Equations (5-7) and (5-9), which include the effects of normal static pressure gradients within the boundary layer, were used to determine the boundary layer integral

properties from the current experimental data. The Sandborn curves correlate the experimental data of both Simpson and the current experiment very well. In the current experiment, intermittent separation (ITD) commenced just upstream of Station 11 and separation (i.e. detachment (D)) occurred downstream of Station 13. The locus of data points from the present experiment also passes through the range of all experimental separation data surveyed by Sandborn. The location of intermittent and fully developed separation in Simpson's experiment were also predicted by the Sandborn correlation.

The data of Smith et al and Perry and Fairlie generally follow the trends of Simpson's data which lie to the right of the data obtained in the current study. The data of Sandborn and Liu show intermittent and fully developed separations occurring near the boundaries predicted by Sandborn's correlations. However, their data lie significantly to the left and outside the range of data surveyed by Sandborn and Kline.

Values of R, the non-dimensional strength of the deceleration gradient, were calculated at the point of incipient detachment and transitory detachment for the current experiment and for the studies of Simpson et al and Sandborn and Liu. At incipient detachment, R, was calculated using eq. (5-19) to be 0.022, 0.052 and 0.061, for the data of Simpson, the current study, and Sandborn and Liu, respectively. At detachment, the same relationship existed. R equaled 0.026, 0.033, and 0.097 for the data of Simpson, the current study, and Sandborn and Liu, respectively. Thus the deceleration gradient imposed by Sandborn and Liu was larger than the gradient imposed in the current study, which in turn was larger than Simpson's deceleration gradient. These data tend to indicate that increasing R causes the locus of data points in a given experiment to move up and to the left in figure 5-15. A consequence of this movement is that δ^*/δ at separation varies inversely with R.

Kline, Bardina, and Strawn (ref. 50) have developed an improved correlation for detachment for any boundary layer having a velocity profile which satisfies the modified Coles' wall-wake profile (ref. 30).

$$U^+ = \frac{1}{\kappa} \ln y^+ + \frac{\Pi(x)}{\kappa} \left(1 - \cos \frac{\pi y}{\delta} \right) + C \qquad (5-21)$$

where $\Pi(x)$ is the wake amplitude. Equation (5-21) has been extremely effective in correlating the vast majority of turbulent boundary layers. The correlation becomes inadequate only for those boundary layers in which the inner and outer layers are far from equilibrium (ref. 50). Kline et al. cast eq. (5-21) into the following form

$$\frac{U}{U_\infty} = 1 + V_T \ln\left(\frac{y}{\delta}\right) - V_B \cos^2 \frac{\pi y}{2\delta} \tag{5-22}$$

where V_B (the nondimensional wake amplitude) and V_T (the dimensionless shear velocity) are defined as

$$V_B = 2U_\tau \, \Pi(x)/\kappa U_\infty \tag{5-23}$$

$$V_T = U_\tau/\kappa U_\infty \tag{5-24}$$

respectively. The shear velocity, U_τ, is defined to be positive in both attached and separated flows.

Using eqs. (5-4) and (5-5) to define the momentum and displacement thicknesses, eq. (5-22) can be integrated directly to yield

$$\frac{\theta}{\delta} = V_T + 0.5 \, V_B - 2V_T^2 - 1.5895 \, V_T V_B - .375 \, V_B^2 \tag{5-25}$$

$$\frac{\delta^*}{\delta} = V_T + 0.5 \, V_B \tag{5-26}$$

Solving eq. (5-26) for the wake strength, V_B, and substituting the result into eq. (5-25) yields the correlating equation

$$\frac{h}{\Lambda} = 1.5 + 0.179 \frac{V_T}{\Lambda} + 0.321 \frac{V_T}{\Lambda}^2 \tag{5-27}$$

where

$$h = \frac{\delta^* - \theta}{\delta^*} = \frac{H - 1}{H} \tag{5-28}$$

$$\Lambda = \frac{\delta^*}{\delta} \tag{5-29}$$

108

For equilibrium boundary layers the dimensionless shear velocity, V_T, is given implicitly by

$$V_T = \frac{1 - 2\Lambda}{\ln \dfrac{|V_T|}{\Lambda} + \ln (\kappa\ Re_{\delta^*}) + 0.05} \qquad (5\text{-}30)$$

The correlation of Kline et al. (eq. (5-27)) is plotted in figure 5-16 along with the data of Cutler and Johnston, Sandborn and Liu, and the present experiment. The shaded region represents the range of near-equilibrium separation data surveyed by Kline et al. The data obtained in the current study upstream of separation (i.e., Stations 6, 8, and 11) and in the upstream half of the separation bubble (i.e., Stations 13-15) lie near the Cutler and Johnston data above the Kline correlation for equilibrium turbulent boundary layers and near the boundary of the shaded region. The data of Sandborn and Liu, which was obtained in a strong adverse pressure gradient on a convex surface, lie significantly above the correlation line and outside the shaded region. Data obtained in the downstream half of the separation bubble (i.e., Stations 18, 20, 22, 24 and 26) and downstream of reattachment (i.e., Stations 28 and 31) lie on or near the Kline correlation.

Deviation of data obtained by Sandborn and Liu, Cutler and Johnston, and at Stations 6-15 in the current study from the correlation line is not surprising since the Kline correlation is restricted to the special case of equilibrium turbulent boundary layers. As discussed in Section 5.4.1 above, the decelerating boundary layer in the present experiment which was near equilibrium at the test section inlet lost its equilibrium structure when it encountered the strong adverse pressure gradient. To estimate the effect of boundary layer nonequilibrium on the Kline correlation, eq. (5-27) was rederived for a boundary layer having no wake component (i.e., $\Pi = V_B = 0$). For a zero-wake boundary layer eq. (5-27) becomes

$$h = 2\Lambda \qquad (5\text{-}31)$$

As shown in figure 5-16 the data from Stations 6-15 generally lie between the equilibrium correlation (eq. (5-27)) and the zero-wake correlation (eq. (5-31)). As the flow moves downstream the data approaches the equilibrium correlation as the strength of the deceleration gradient diminishes. Note also in figure 5-16 that the Sandborn-Kline correlation not only predicts the

beginning of intermittent separation between Stations 11 and 13 but the reattachment location between Stations 26 and 28 also.

In the fully developed separation region Simpson et al. (ref. 1) demonstrated that a similarity existed in the forward flow fraction profiles by normalizing and plotting

$$\frac{\gamma_{P_U} - \gamma_{P_{U_{min}}}}{1 - \gamma_{P_{U_{min}}}} \quad \text{vs.} \quad \frac{y}{M} \tag{5-32}$$

where $\gamma_{P_{U_{min}}}$ was the minimum value of γ_{P_U} in the profile near the wall and M was the distance from the wall to the peak in the axial turbulence profile. The data in the present experiment were normalized in the same manner and very good profile similarity was obtained. However, better similarity was obtained when the profiles were normalized with M chosen as the distance from the wall to the peak in the transverse turbulence profile. The profiles normalized by the distance from the wall to the peak in the transverse turbulence profile are plotted in figure 5-17. Data scatter is very small, being well within the bounds of Simpson's data which are based on M chosen as the distance from the wall to the peak in the axial turbulence profile.

5.5 Description of the Separation Bubble

Downstream of separation a large separation bubble, defined as Zone III in figure 5-1, having a maximum thickness, h, of 17 cm was formed between the mean dividing streamline and the upper wall test surface. The flow within the bubble was characterized by vigorous recirculation and high turbulence levels. As shown in figure 5-18, Zone III can be partitioned into three transverse subzones: Zone IIIA, the backflow boundary layer in which $U < 0$ and $\partial U/\partial y < 0$; Zone IIIB, the backflow shear layer in which $U < 0$ and $\partial U/\partial y > 0$; and Zone IIIC, the forward flow shear layer, in which $U > 0$ and $\partial U/\partial y > 0$. The backflow in Zones IIIA and IIIB was strong and steady. Mean backflow velocities exceeding 30 percent of the local freestream velocity have been measured within these subzones. Steady backflow (i.e., $\gamma_{P_U} = 0$) was measured over a large portion of zones IIIA and IIIB. As indicated in figures 4-13, 5-13, and Table II, the region throughout which the forward flow fraction was zero extended along the test surface from Station 18 (x = 67.3 cm) to Station 24 (x = 90.2 cm). The maximum thickness of the steady backflow region was 2.5 cm at Station 20 (x = 74.9 cm). Measurements of $\gamma_{P_U} = 0$ in a separated boundary layer have not been reported previously (ref. 24).

110

As a result of the strong steady backflow within the separation bubble a well developed thin backflow boundary layer (Zone IIIA) grew along the test plate. The boundary layer, which had both laminar and turbulent characteristics, will be described in more detail in Section 5.5.1 below.

Zone IIIB, the backflow shear layer, was approximately an order of magnitude thicker than the backflow boundary layer. The backflow shear layer consisted of an inner layer having a relatively flat velocity profile (Zone IIIB1), which connected the viscous near wall region with the outer shear flow, and the outer backflow region (Zone IIIB2) which was part of the outer shear flow. Zones IIIA, IIIB1, and IIIB2 are components of the three-layer backflow model proposed by Simpson (ref. 1). Zone IIIB was characterized by a nearly constant turbulence level approximating 8 percent of the inlet freestream velocity as shown in figure 4-18.

Zone IIIC, the forward flow shear layer, defined as the region between the locus of U=0 points and the dividing streamline (ψ = 0) contained higher normal velocity gradients, $\partial U/\partial y$, and turbulence levels than Zone IIIB. In fact, the largest values of $\partial U/\partial y$ within the reversed flow region between Stations 13 and 26 occurred at the outer edge of Zone IIIC. As discussed below in Section 5.8, "Shear Stress Correlations" the largest values of the streamwise shear stress, $\overline{\alpha\beta}$, also occurred at the outer edge of Zone IIIC near the dividing streamline. As shown in figure 5-19, Zone IIIC was slightly thinner than the combined thicknesses of the backflow zones (Zone IIIA + Zone IIIB) at all stations. The thicknesses of the backflow zones and the forward flow shear layer (Zone IIIC) increased linearly over the upstream half of the separation bubble. The origin of the linear growth region was the point of transitory detachment (i.e., γ_{P_U} = 0.50 at the wall).

5.5.1 Description of the Backflow Boundary Layer

Although the existence of a steady backflow boundary layer was not anticipated at the outset of the test program, the measurement matrix was sufficiently dense to permit a limited analysis of the structure of the backflow boundary layer. Backflow velocity profiles are plotted in figure 5-20. The profiles were calculated from backward-facing pitot data. The limited number of LV measurements made within the backflow boundary layer indicated that the backflow was steady (γ_{P_U} = 0) between Stations 23 and 18 (i.e. over the central 35 percent of the axial extent of the bubble) and only slightly intermittent (γ_{P_U} < 0.12) at all other locations. LV velocity measurements were in good agreement with the pitot data.

The boundary layer appeared to originate near the reattachment point (x_R = 103 cm) just downstream of Station 27. The boundary layer grew until it reached a maximum thickness of approximately 0.76 cm at Station 15 near Zone II, the intermittent separation zone. The pitot data obtained at Station 15 are not presented in figure 5-20 because values of γ_{p_U} as high as 25 percent measured near the wall at Station 15 could make the data unreliable.

With the understanding that the accuracy would be less than desired because of the small number of data points obtained within the backflow boundary layer, boundary layer integral properties were calculated for each profile presented in figure 5-20. Calculated values of the momentum thickness Reynolds number, Re_θ, the shape factor, H, and other backflow boundary layer parameters are listed in Table VII. Boundary layer parameters determined by Coles (ref. 30) for a zero pressure gradient turbulent boundary layer are also listed in Table VII for comparison. Although the maximum calculated value of Re_θ, which was 184, was much lower than the value of 425 required for transition in low-freestream-turbulence, zero-pressure-gradient boundary layers (Table 2 in Appendix A of ref. 30), the calculated value of H was transitional. The shape factor decreased from 1.98 at Station 25 to 1.48 at Station 16. The values are between the shape factor of 2.59 for a laminar boundary layer having a Blasius velocity profile (ref. 35) and the value of 1.47 given by Coles (ref. 30) for a turbulent boundary layer for which Re_θ equals 855.

To gain additional insight into the nature of the backflow boundary layer the local axial turbulence levels, $\sqrt{\overline{u^2}}/U$, measured within Zone IIIA with the LV system were plotted in figure 5-21. The turbulence level was uniformly high across the boundary layer, varying from approximately 50 percent near the wall to 40 percent at the "freestream." The turbulence was dominated by low frequency large scale eddies (see Section 4.6). The turbulence profile measured by Klebanoff (ref. 31) for a flat plate turbulent boundary layer having a low level of freestream turbulence has been shown for comparison. The local turbulence levels in the Klebanoff profile are less than 10 percent over the outer 90 percent of the boundary layer. Because of the low free-stream turbulence level, the Klebanoff boundary layer is dominated by turbulence which is generated near the wall and diffused outward. If such turbulent transport exists in the backflow boundary layer it is masked by the large scale turbulent eddies.

The turbulence levels within the backflow boundary layer exceed the turbulent boundary layer values measured by Klebanoff at all points in the profile. In this respect, the backflow boundary layer is clearly turbulent. However, it could be argued that the LV turbulence measurement resulted from averaging highly unsteady laminar flow at the wall which is driven by the

large scale turbulent eddies in the "freestream." Therefore, the backflow boundary layer can only be referred to as pseudo-turbulent until its exact nature can be determined from more detailed measurements.

Simpson (ref. 26) has proposed that the backflow velocity profile in Zones IIIA and IIIB has a universal shape defined by the equations

$$\frac{U}{|U_N|} = A\left(\frac{y}{N} - \ln\left|\frac{y}{N}\right| - 1\right) - 1 \qquad (5\text{-}33)$$

where N is the value of y at the transverse location of the maximum backflow velocity, U_N. The present LV data are compared to the Simpson correlation in figure 5-22. Setting A = 0.3 as suggested by Simpson, eq. (5-33) correlated only the profile data at Station 15 just downstream of detachment. Setting A = 0.2 provided a better correlation for data in Zone III A (i.e., y/N < 1). Considering the scatter in the profiles in Zone IIIB when plotted in y/N vs. U/U_N coordinates, eq. (5-33) could not correlate the Zone IIIB data for any value of A. Simpson also noted difficulties in using eq. (5-33) to correlate Zone IIIB profiles.

The flow at Station 15 most closely approximated the flow conditions used in the test cases surveyed by Simpson in developing eq. (5-33). The velocity at Station 15 was intermittent having a minimum value of γ_{P_U} of 0.08. All other profiles presented, except the Station 16 data, had steady backflow (i.e., γ_{P_U} = 0) throughout the profile. None of the profiles surveyed by Simpson had steady backflow at any point in the profile.

Because of the highly turbulent nature of the backflow boundary layer, an attempt was made to plot the backflow data in U^+ vs. y^+ law-of-the-wall coordinates. Simpson had suggested (ref. 1) that such a scaling was not possible in the backflow boundary layer because the law-of-the-wall length scale ν/U_τ varies inversely with its velocity scale U_τ which differs from the behavior of N and U_N which both increased in the downstream direction. In the present data, the behavior noted by Simpson occurred over a short region just downstream of detachment (Stations 13-15) where $\gamma_{P_U} > 0$ as shown in figure 5-14. In the steady backflow region (Stations 18-24), however, N increased in the direction of the backflow while U_N remained relatively constant (see Table VII) which is exactly the behavior attributed to boundary layers which can be modeled in law-of-the-wall coordinates.

Backflow boundary layer data plotted in law-of-the-wall coordinates are presented in figure 5-23. The data are characterized by a short log-linear region ($11 < y^+ < 60$) and a negative wake. Data scatter is minimal. The absence of a wake component in the backflow boundary layer is not surprising. Coles has plotted the strength of the wake component in equilibrium turbulent flow vs. Re_θ in figure 12 of reference 30. Coles's plot shows that the magnitude of the wake component is zero at $Re_\theta = 425$ and increases to its equilibrium value at $Re_\theta \simeq 5000$. The maximum value of Re_θ in the backflow boundary layer was 184. Coles also noted in figure 15 of reference 30 that increasing freestream turbulence decreased the strength of the wake component. Kline et al. (ref. 52) showed that the wake component in an equilibrium turbulent boundary layer, which was normal at a freestream turbulence level of 1.8 percent, decreased to zero when the freestream turbulence level increased to 4.5 percent. As shown above in figure 5-21 the backflow boundary layer had a "freestream" turbulence level of 40 percent.

The friction velocity, U_τ, and the skin friction coefficient, $C_f = -2$ $(U_\tau/U_{ref})^2$, were determined from the law-of-the-wall plots. The skin friction values, shown in figure 5-23, were approximately an order of magnitude lower than the values measured in the attached boundary layer upstream of separation. However, when localized by the local maximum backflow velocity, U_N, rather than the inlet reference velocity, the skin friction coefficient, $C_f' = 2 (U_\tau/U_N)^2$, was quite large. C_f' has been plotted vs. $Re_{x'}$, in figure 5-24 where $Re_{x'} = U_N x'/\nu$ and $x' = x_R - x$ where x_R, the axial location of reattachment, equaled 103 cm.

Also plotted in figure 5-24 are values of C_f' estimated from the normal velocity gradient at the wall at each station within Zone III using the following equation

$$C_f' = \frac{\mu \frac{\partial U}{\partial y}\big|_{y=0}}{\rho\, U_N^2/2} + \frac{Re_\theta}{2}\, \frac{\Delta y}{\theta}\, \frac{\partial U_N}{\partial x} \qquad (5\text{-}34)$$

The second term on the rhs of eq. (5-34) is a correction term to be used in flows having axial pressure gradients (ref. 53). The correction term did not exceed 12.5 percent at any station within Zone III.

C_f' calculated from eq. (5-34) decreased from 0.022 at $Re_{x'} = 2.1 \times 10^4$ near reattachment to 0.0074 at $Re_{x'} = 1.1 \times 10^5$ near detachment. Very good agreement was obtained between values of C_f' calculated using eq. (5-34) and the values determined from the law of the wall plots. Values of C_f' correlated reasonably well with the equation

114

$$C_f' = 3.29 \, Re_{x'}^{-1/2} \qquad (5-35)$$

which has the same $Re_{x'}^{-1/2}$ dependence but which is 400 percent higher than zero pressure gradient laminar skin friction coefficients at the same Reynolds number.

Two possible explanations for the high skin friction coefficients measured in the backflow boundary layer could be the favorable pressure gradient and the high turbulence levels impressed upon the backflow boundary layer by the external flow field. The effect of the favorable pressure gradient on the shear at the wall can be estimated using the Pohlhausen parameter, Λ, (ref. 35, p. 245)

$$\tau_w = \mu \left. \frac{\partial U}{\partial y} \right|_{y=0} = \mu \frac{U_N}{N} \left(2 + \frac{\Lambda}{6} \right) \qquad (5-36)$$

where

$$\Lambda = - \frac{dp}{dx'} \frac{N^2}{\mu U_N}$$

The effect of the pressure gradient on the skin friction can be estimated from eq. (5-36) as

$$\frac{C_{f_\Lambda}'}{C_{f_\Lambda}' (\Lambda=0)} = 1 + \frac{\Lambda}{12} \qquad (5-37)$$

The maximum value of Λ within the backflow boundary layer occurred at Station 23 (x = 86.4 cm) where $\Lambda = 13.9$. Thus, the effect of the favorable pressure gradient could account for as much as 100 percent of the 400 percent increase in skin friction at some points in the backflow boundary layer.

The effect of freestream turbulence in reducing the transition Reynolds number and increasing the skin friction coefficient is well known but not well quantified. Dyban et. al. (ref. 54) have measured a 56 percent increase in skin friction in a laminar boundary layer having a 25 percent freestream turbulence. The increase in the backflow boundary layer skin friction coefficients due to the 40 percent "freestream" turbulence within the

115

separation bubble would be expected to be large but cannot be estimated at this time.

5.6 Description of the Reattachment Process

Reattachment of the separated shear layer is an inherently unsteady process which occurs within Zone IV, the Reattachment Zone. Smoke flow visualization movies showed that the Reattachment Zone was characterized by random streamline flapping (shown schematically in figure 4-6) with large scale eddies being convected alternately upstream and downstream from the impingement point on the test surface. The reattaching flow, impinging steeply onto the test surface, caused a static pressure peak which drove the strong backflow within the separation bubble described above.

The flow within Zone IV was characterized by frequent flow reversals and high turbulence levels. The flow reversals have been quantified by the forward flow fraction, which is the fraction of the time the flow is moving in the downstream direction. Values of the forward flow fraction, γ_{P_U}, near the test surface (y = 0.10 cm) at the four LV measurement stations within the reattachment zone have been plotted in figure 5-25 versus x^*, a non-dimensional axial coordinate

$$x^* = \frac{x - x_R}{x - x_{\delta^*_{max}}} \tag{5-38}$$

where x_R is the reattachment location defined as the point on the test surface where $\overline{C}_f = 0$ and $x_{\delta^*_{max}}$ is the axial coordinate at the location of the maximum separation bubble thickness. The definition of the non-dimensional coordinate, x^*, has been chosen to permit direct comparison of data in the reattachment zone to data obtained in backward facing step flows where the x-coordinate has its origin at the step and $x^* = (x-x_R)/x_R$ (ref. 17). Note in figure 5-25 that γ_{P_U} rises from 0.02 at $x^* = -0.44$ to 1.0 at $x^* = +0.40$. If the reattachment zone is defined as the region between $0.01 \leq \gamma_{P_U} \leq 0.99$ and $x - x_{\delta^*_{max}}$ is approximately 1/2 the bubble length, the reattachment zone can be calculated to be 40 percent as long as the separation bubble. A correlation developed by Westphal et al. (ref. 17) for reattaching flow downstream of a backward facing step shows excellent agreement with the forward-flow fraction data obtained in the present study.

The skin friction coefficient measured within the reattachment zone has been plotted vs. the forward flow fraction in figure 5-26. The skin friction increased monotonically with forward flow fraction throughout the reattachment zone. Also plotted in figure 5-26 are data from two cases investigated by Westphal et al. (ref. 17) for reattaching flow behind a backward facing step. The backward facing step data showed similar trends to the data in the present study. In particular, for both cases studied by Westphal et al. and for the present data the location of $C_f = 0$ occurred near the location at which $\gamma_{p_U} = 0.50$.

Downstream of the reattachment location the reattached flow recovers the structure of a flat-plate turbulent boundary layer. This process occurs in two stages. In Zone V, a new boundary layer develops along the test surface and quickly achieves equilibrium conditions. The relaxation of the outer shear layer in Zone VI occurs much more slowly, however.

Streamwise velocity and turbulence profiles downstream of reattachment are plotted in figure 5-27. The two-layer structure of the reattached boundary layer can be seen quite clearly in the figure as the new boundary layer grows rapidly toward equilibrium under the relaxing outer shear layer. The effective "freestream" turbulence level impressed upon the developing boundary layer was quite high. The turbulence level was approximately 10-14 percent of U_{ref} and on the order of 25 percent of the streamwise velocity at the edge of the new boundary layer at all measurement stations downstream of reattachment. Recovery of the two-layer profile to a flat-plate turbulent boundary layer profile was not complete at x = 148 cm, the final measurement station within the test section.

To study the structure of the recovering flat-plate turbulent boundary layer in more detail, axial velocity profiles at these measurement stations downstream of reattachment have been plotted in law-of-the wall coordinates in figure 5-28. At Station 28 ($x^* = 0.09$) at reattachment the boundary layer structure had no log-linear region. The profile was dominated by the wake-like structure of the reattaching outer shear layer. At Station 30 ($x^* = 0.36$) a short log-linear region had become established at $y^+ < 100$ but the profile dipped below the standard log-linear line before reverting to a strong, albeit somewhat diminished from Station 28, wake component at the edge of the boundary layer. At Station 34 ($x^* = 1.36$) the dip below the log-linear line persisted and the wake component had diminished to the extent that the profile had a negative wake component.

The dashed lines in figure 5-28 represent data obtained by Chandrsuda and Bradshaw (ref. 18) in a reattached fully developed turbulent mixing layer downstream of a backward facing step. The profiles obtained by Chandrsuda and

117

Bradshaw show the same characteristics as the profiles obtained in the present study. Chandrsuda and Bradshaw explained that the dip below the log-linear line occurred because the standard logarithmic law is based upon the assumption that the length scale of the turbulence is proportional to y, while at, and just downstream of, reattachment the length scale will be nearly constant, as it was in the separated shear layer, except very near the surface. Bradshaw and Wong (ref. 11) have shown that the dip persists for 50 step heights ($x^* = 7.5$) downstream before equilibrium is reached in the turbulence energy exchange between the small length scale turbulence being generated near the wall and the large length scale turbulence being fed into the developing boundary layer from the reattached mixing layer. In the present study $x^* = 7.5$ would correspond to an axial location approximately 160 cm (i.e., 3.75 bubble lengths) downstream of reattachment.

The displacement thickness, δ^*, the momentum thickness, θ, and the shape factor, H, have been calculated throughout the reattachment region and are plotted in figure 5-29. The open circles represent data calculated using eqs. (5-4) and (5-5) based on classical boundary layer theory and the solid circles represent pressure-based integral properties calculated using eqs. (5-8) and (5-10) (see Section 5.3.3 "Boundary Layer Integral Properties"). Also plotted in figure 5-29 are integral property data obtained by Driver and Seegmiller (ref. 14) in flow reattaching behind a backward facing step within an adverse pressure gradient. The displacement and momentum thicknesses have been non-dimensionalized by h which equaled the maximum separation bubble thickness of 17 cm in the present study and the step height in the Driver and Seegmiller study.

The data obtained by Driver and Seegmiller for their reference case in a nondiverging tunnel having zero pressure gradient in the reattachment zone are plotted as squares in figure 5-29. The trends shown in their data, namely the monotonic decrease in displacement and shape factor, and the generally increasing value of momentum thickness with axial distance are similar to the trends observed by Kim et al. (ref. 13) and Pronchick and Kline (ref. 16) for zero pressure gradient backward facing step flows. For flows reattaching in an adverse pressure gradient (α = 6 deg) Driver and Seegmiller have shown that the displacement thickness decreases less rapidly and the momentum thickness increases more rapidly with axial distance than the zero pressure gradient case while the behavior of the shape factor is relatively unaffected by the pressure gradient. Conversely, in the present study the separated shear layer reattached within a converging channel (α = -38 deg) having a very favorable pressure gradient downstream of reattachment. Thus, the rapidly decreasing displacement and momentum thicknesses downstream of reattachment in the present study follow the trends identified by the Driver and Seegmiller study of backward facing step flows. The behavior of the shape factor calculated from classical boundary layer theory was uninfluenced by the pressure

118

gradient (ref. 14 data), whereas the more accurate pressure-based shape factor calculated in the present study displayed a more rapid decrease with axial distance within the favorable pressure gradient.

5.7 Streamwise Turbulent Shear Stress Measurements

As noted by Cutler and Johnston (ref. 6), when the mean streamlines are inclined at a significant angle to the test surface, turbulent shear stress data are more meaningful when presented in an orthogonal coordinate system comprised of the mean streamline direction and the normal to the streamline than in a coordinate system orthogonal to the test surface. This is because flow history effects are important in boundary-layer flows (except near the wall) and the streamline orthogonal coordinate system can track the flow development along a given streamline. Cutler and Johnston concluded that the behavior of a turbulence quantity is more likely to be modeled in "universal" form if streamline orthogonal coordinates are used. In the current study, flow within the boundary layer was inclined more than 30 degrees relative to the test surface near separation and reattachment, significantly more than the 10 degree inclinations reported by Cutler and Johnston.

The Reynolds stress, $\overline{uv}$, data in the wall orthogonal (x,y) coordinate system can be rotated into the streamwise orthogonal (s,n) coordinate system using the following relation (ref. 6)

$$\overline{\alpha\beta} = \overline{uv} \ (\cos^2\phi - \sin^2\phi) + (\overline{v^2} - \overline{u^2}) \ \sin\phi \ \cos\phi \qquad (5\text{-}39)$$

where $\overline{\alpha\beta}$ is the streamwise turbulent shear stress and $\phi = \tan^{-1} (V/U)$, the angle of the local mean-flow streamline to the wall. The wall orthogonal shear stress data presented in figure 4-21 have been rotated into streamwise orthogonal coordinates. The resulting values of $\overline{\alpha\beta}$ are tabulated in Table III and are plotted in figure 5-30.

Trends are much more evident in the streamwise shear stress profiles than in the $\overline{uv}$ profiles plotted in figure 4-21. At Station 6 upstream of incipient detachment the shear stress peaks near the wall. At Station 11 as the boundary layer approaches detachment the peak increases in amplitude and moves away from the wall. Downstream of detachment, between Stations 13 and 18, the peak grows much more rapidly and is located near the edge of the backflow region (i.e., locus of U = 0 points) indicating strong turbulence generation in this region. Between Stations 22 and 28 aft of the maximum bubble thickness the peaks broaden and decay and move farther away from the U = 0 line into the

wake of the bubble. This decaying trend is reversed as the shear stress begins to grow again as the flow is accelerated into the exit duct at Stations 30 and 31. No data has been presented near reattachement where highly unsteady flow and steep flow angles make the rotated data of questionable value.

Figure 5-1 Separation Bubble Flow Zones
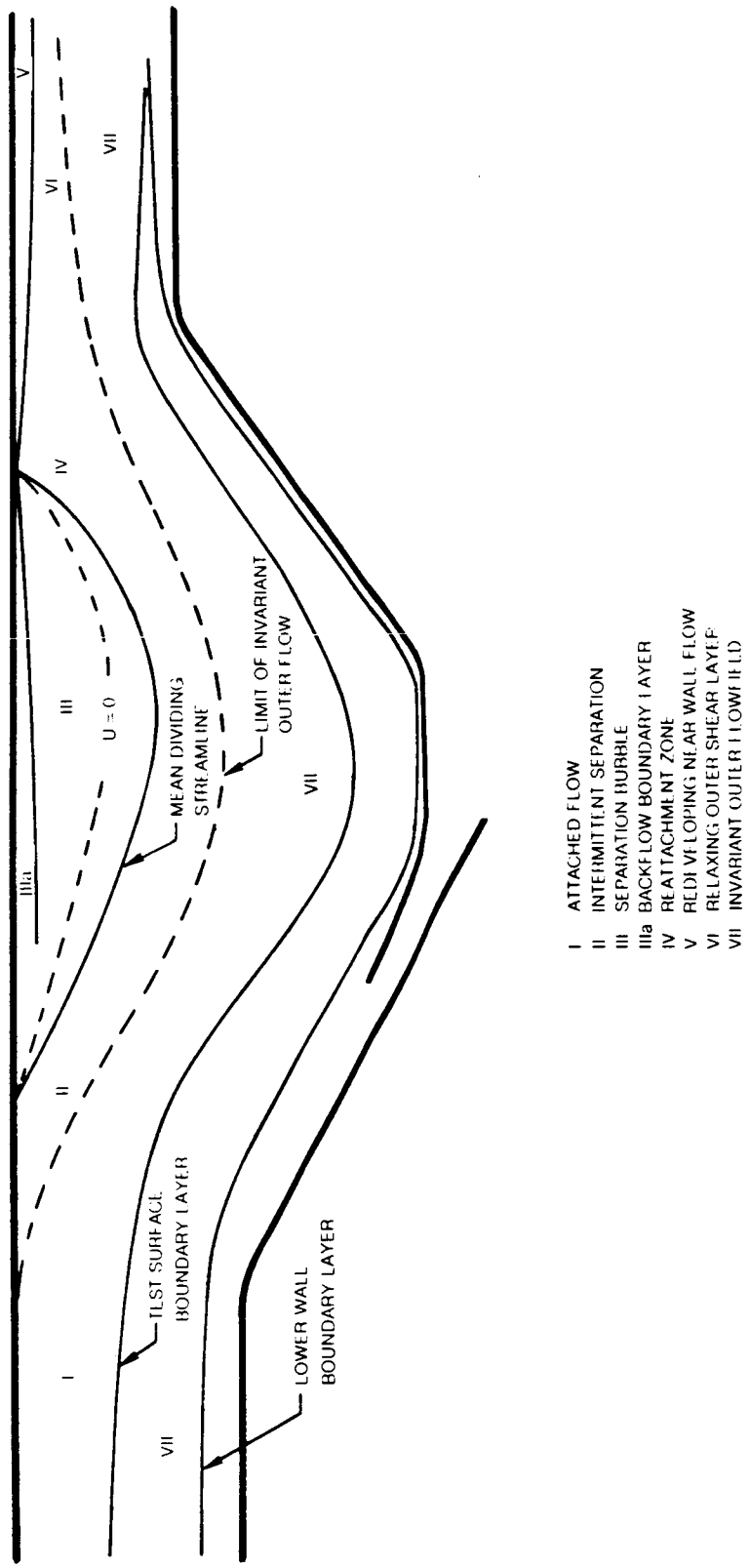
I ATTACHED FLOW
II INTERMITTENT SEPARATION
III SEPARATION BUBBLE
IIIa BACKFLOW BOUNDARY LAYER
IV REATTACHMENT ZONE
V REDEVELOPING NEAR WALL FLOW
VI RELAXING OUTER SHEAR LAYER
VII INVARIANT OUTER FLOWFIELD
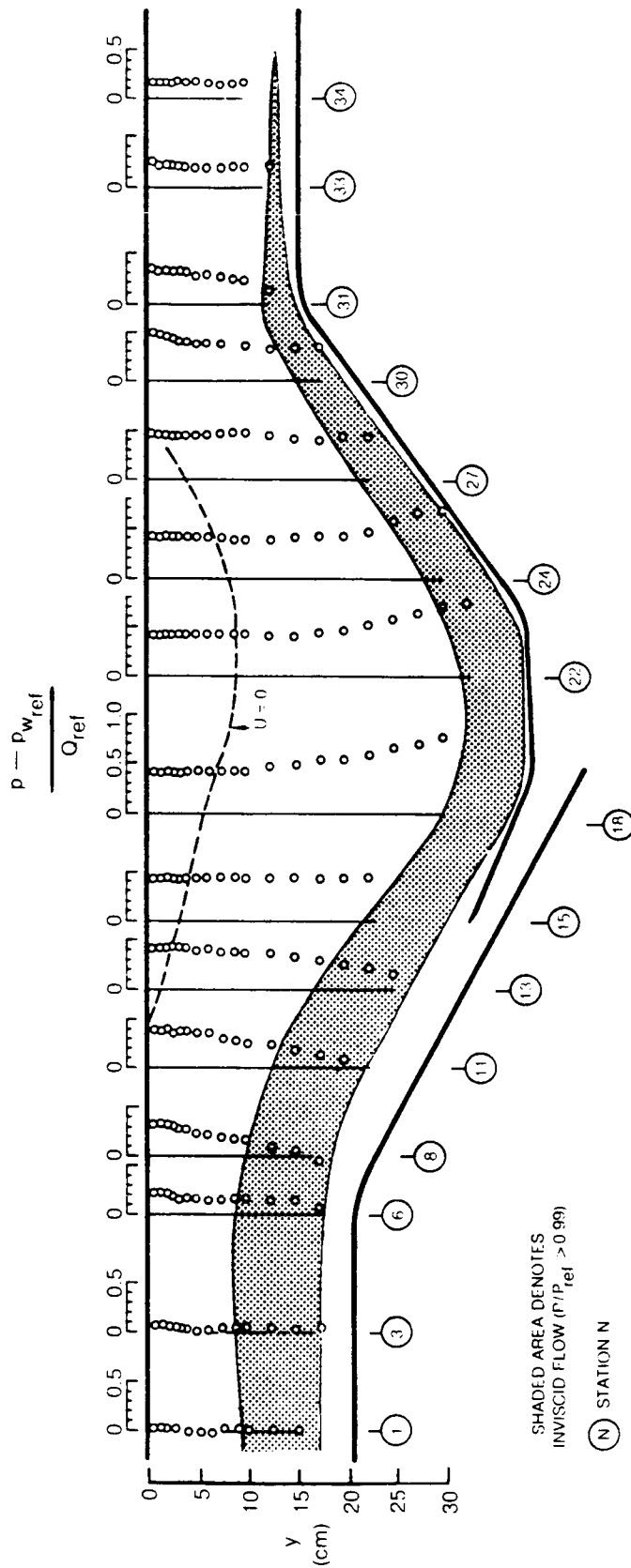
Figure 5-2 Static Pressure Profiles Calculated from Total Pressure and Laser Velocimeter Mean Velocity Measurements (z = 0)
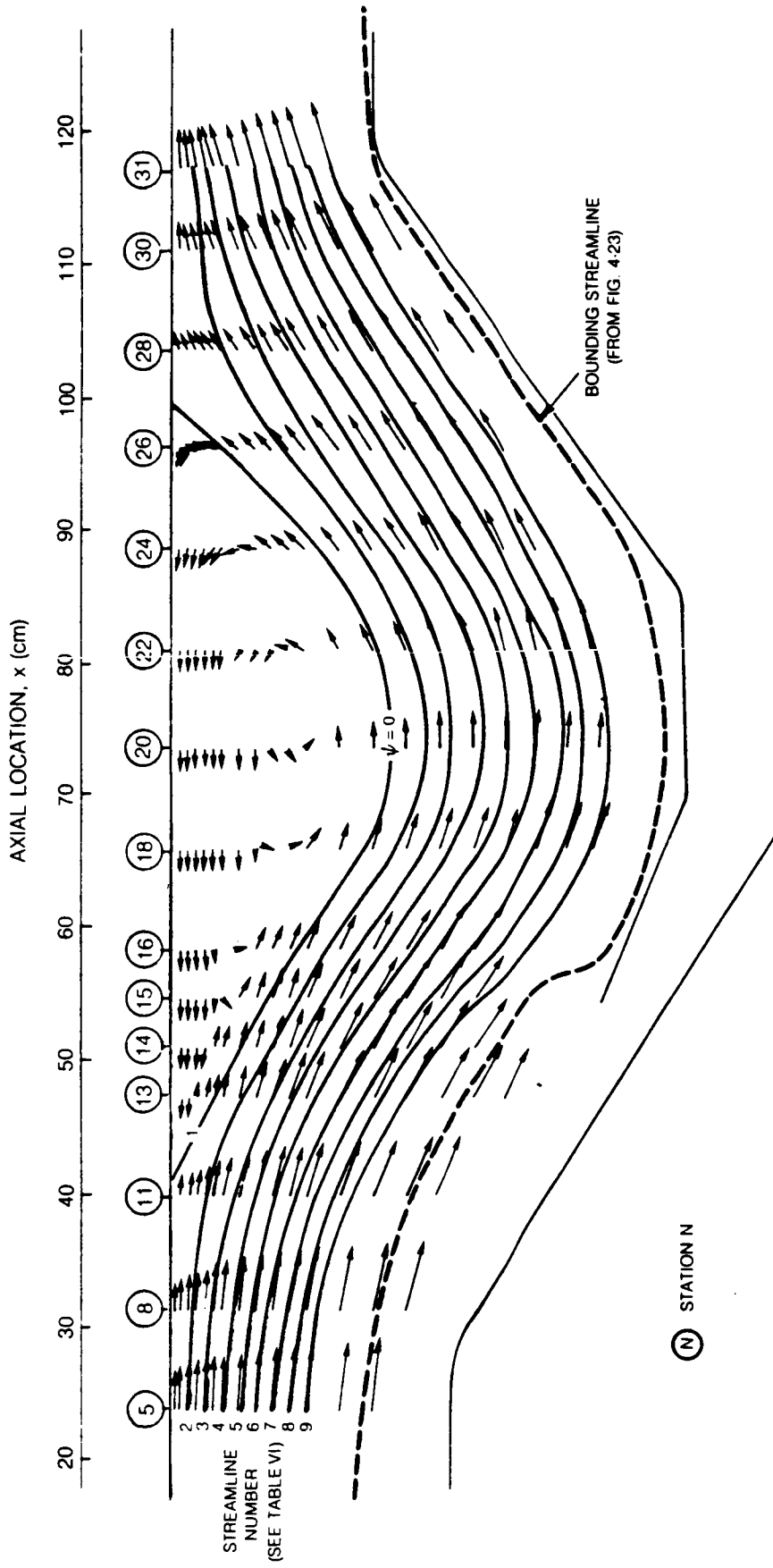
Figure 5-3 Velocity Vectors and Streamlines Determined from LV Mean Velocity Measurements on Wind Tunnel Centerline
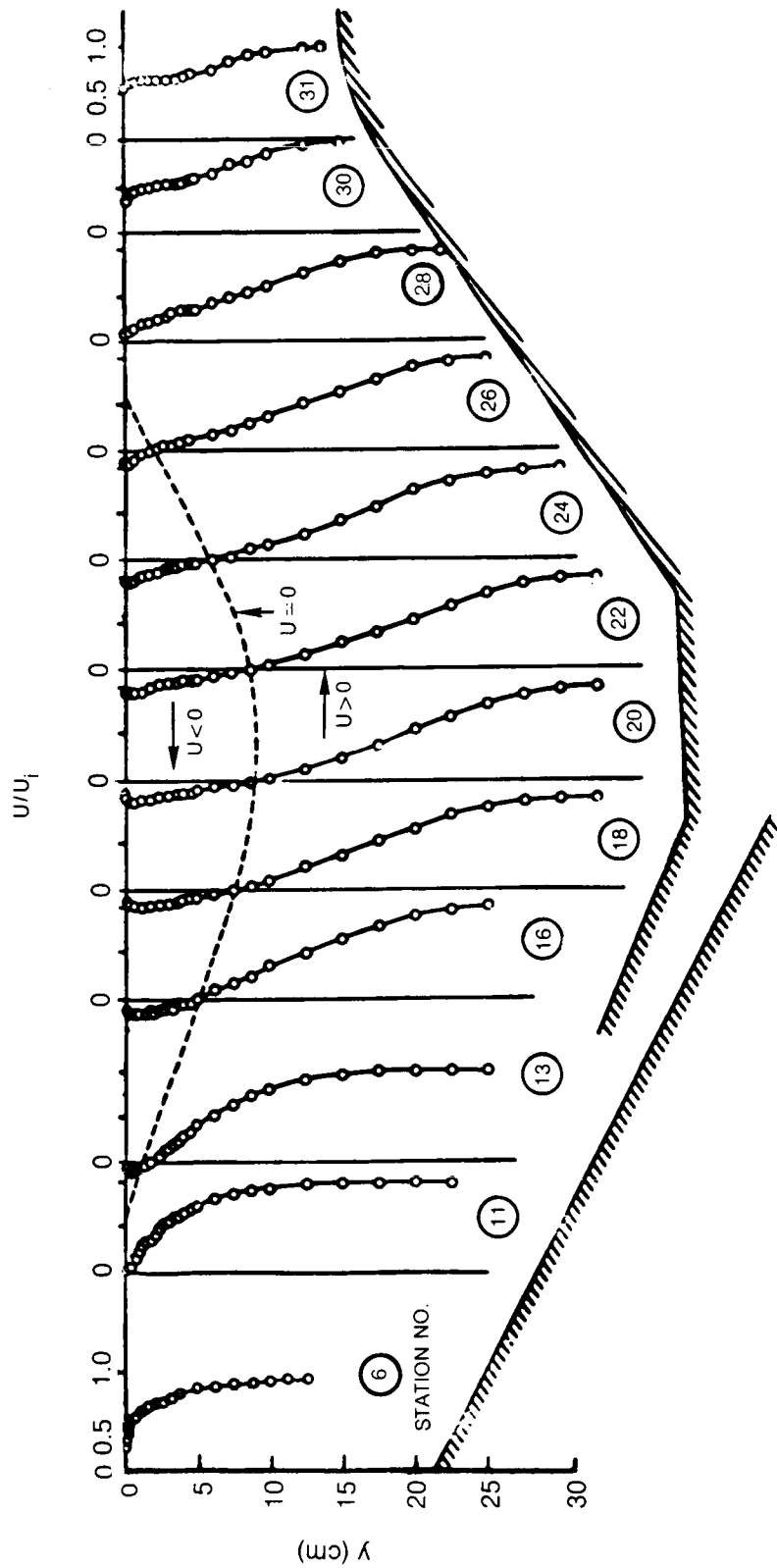
Figure 5-4 Normalized LDV Axial Velocity Measurements on Wind Tunnel Centerline
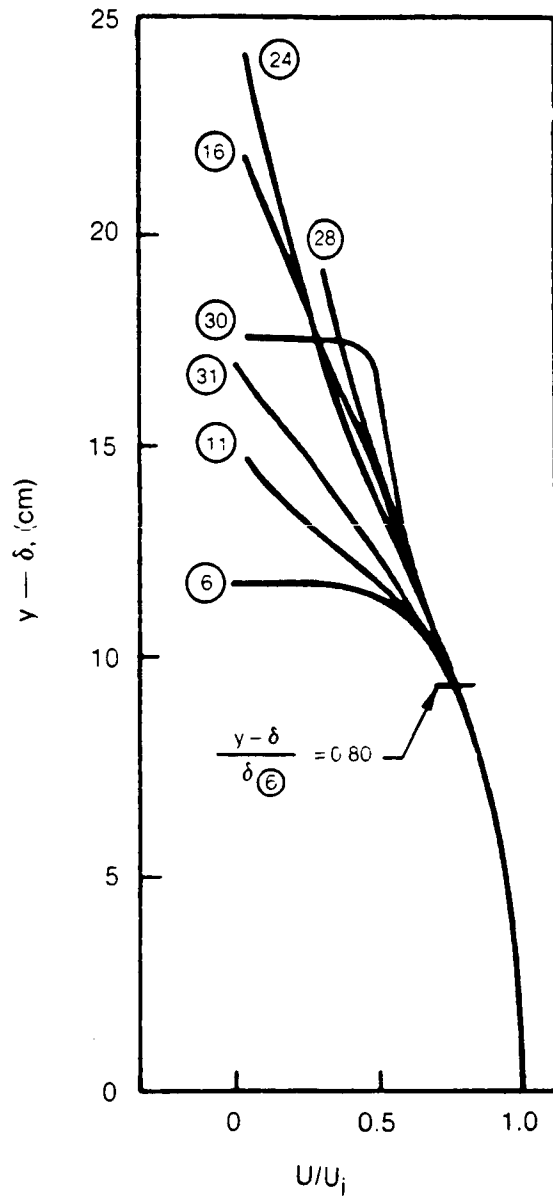
Figure 5-5 Normalized Axial Velocity Profiles Overlayed to Demonstrate Invariant Outer Boundary Layer Profile
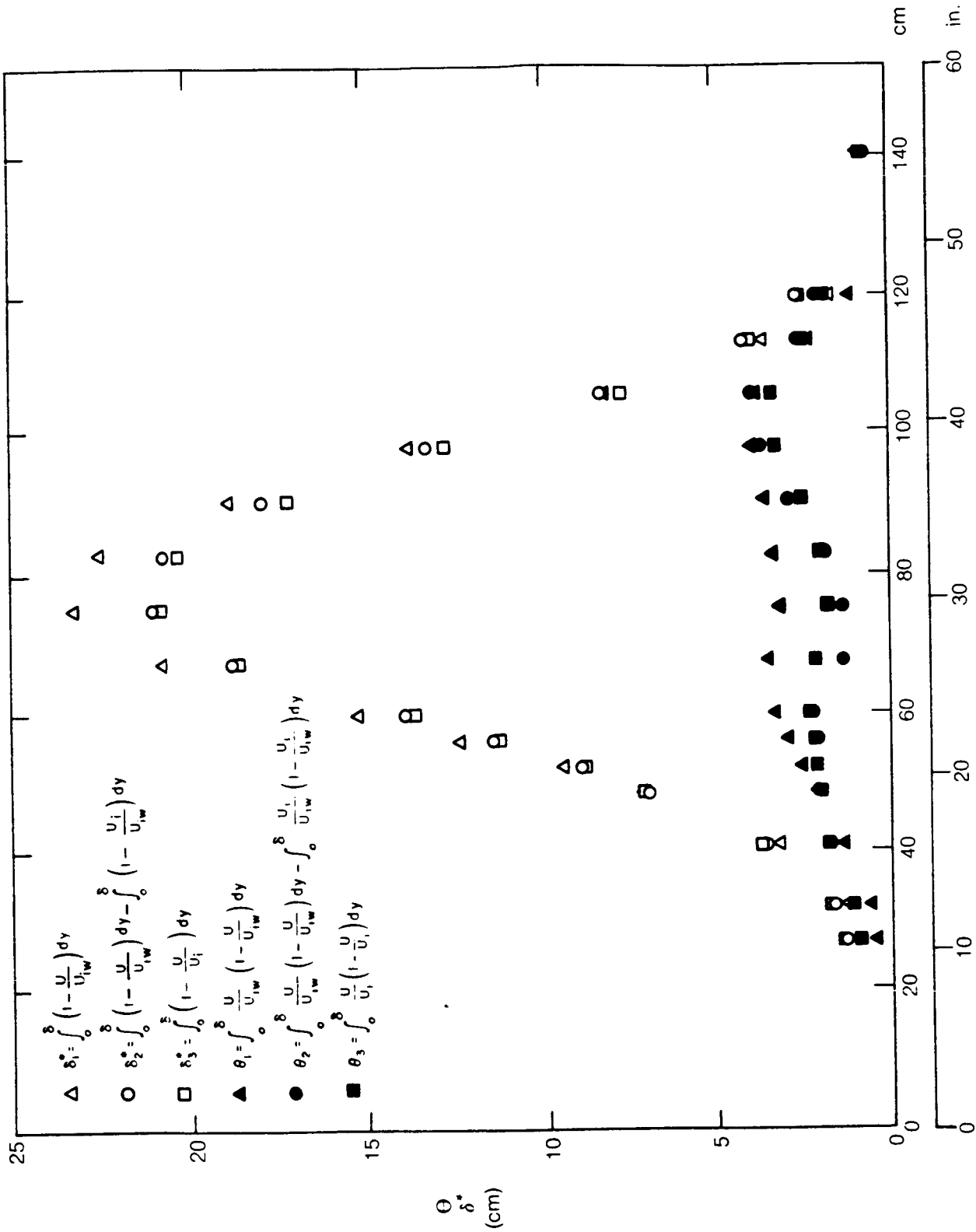
Figure 5-6a Displacement and Momentum Thickness on Wind Tunnel Centerline (z = 0)

126
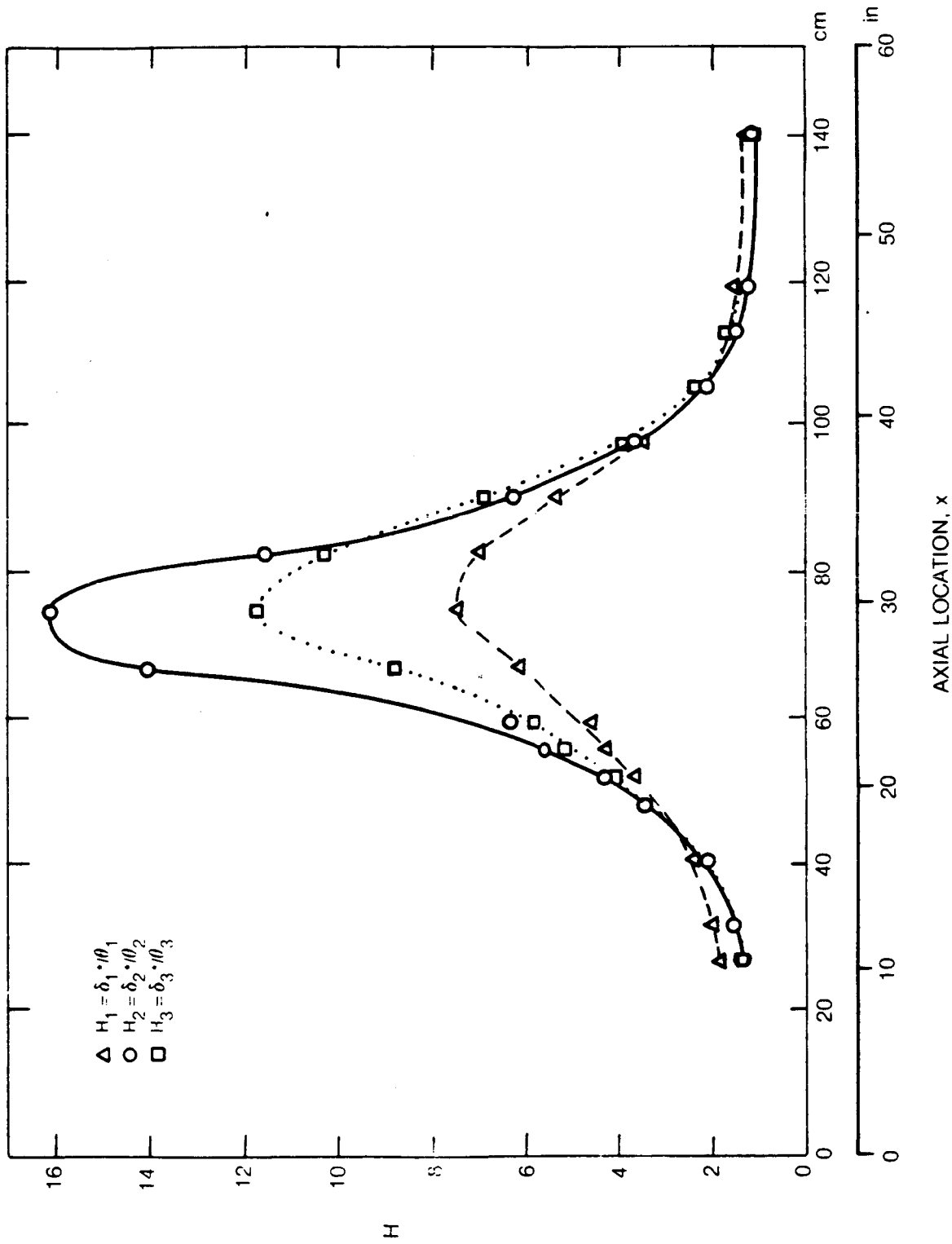
Figure 5-6b Shape Factor Determined from Laser Velocimeter Mean Velocity Measurements (z = 0)

85-2-23-8
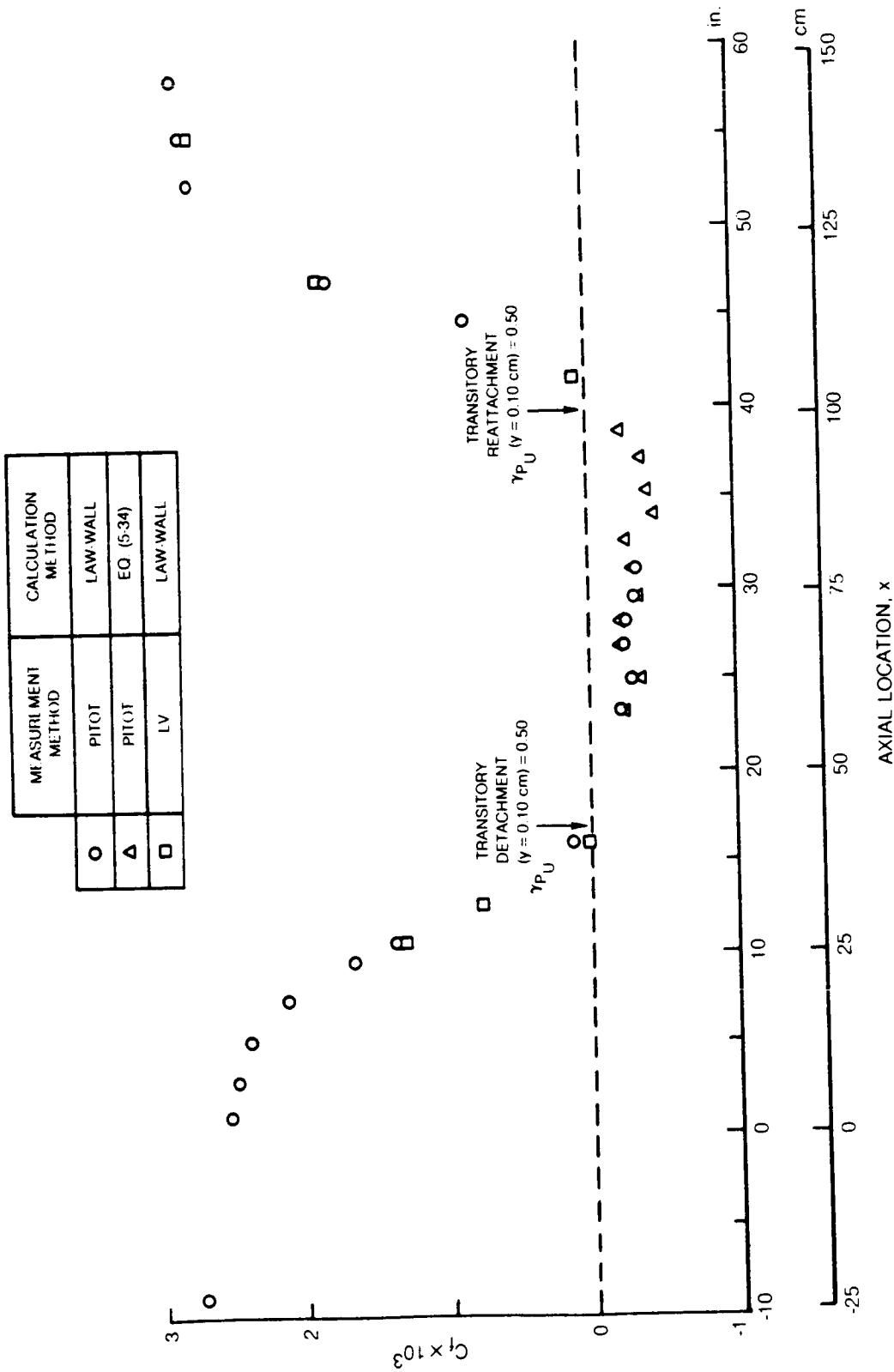
Figure 5-7a Skin Friction Coefficient on Test Surface (z = 0)
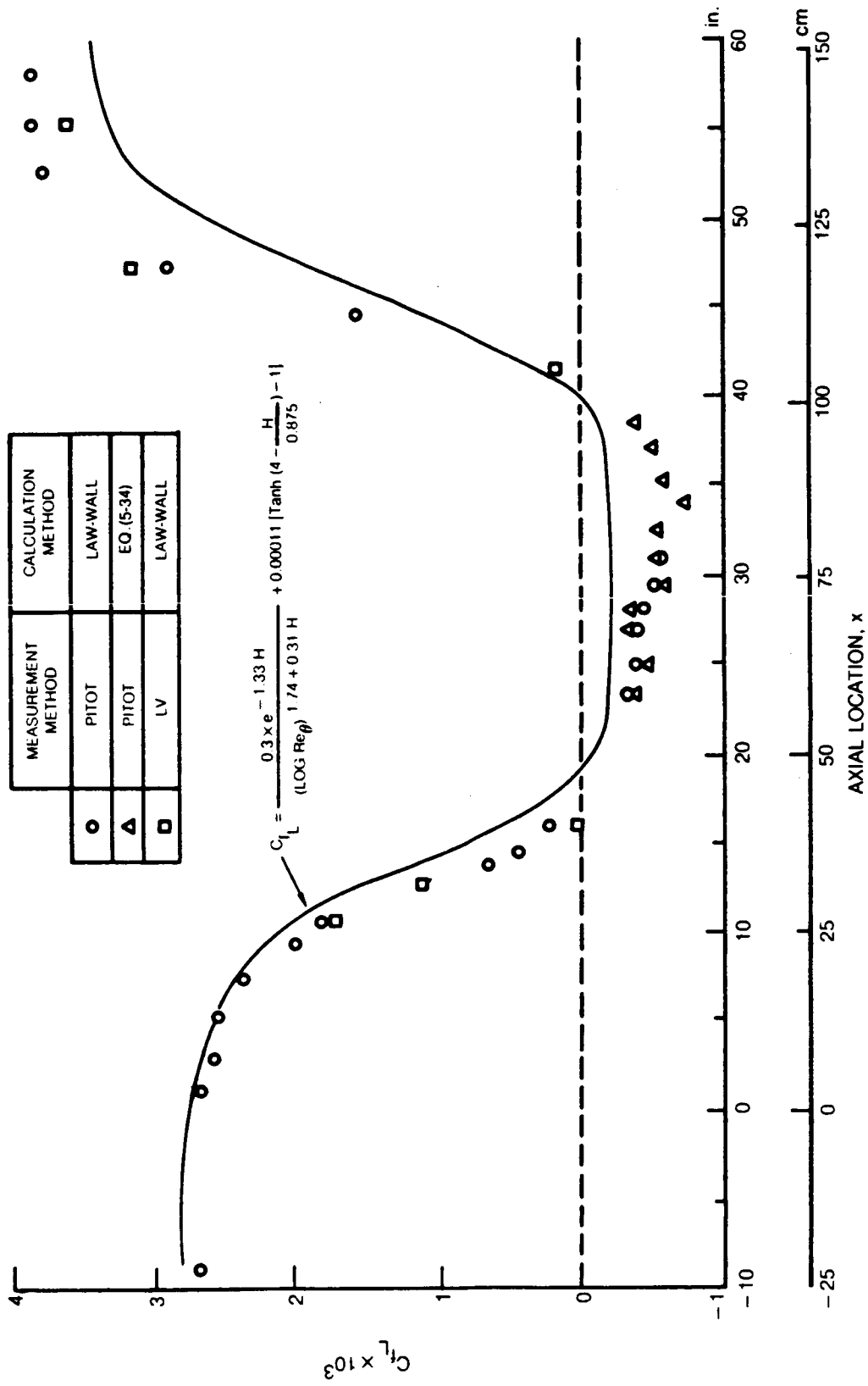
Figure 5-7b Local Skin Friction Coefficient on Test Surface (z = 0)

MEASUREMENT METHOD		CALCULATION METHOD
○	PITOT	LAW-WALL
△	PITOT	EQ.(5-34)
□	LV	LAW-WALL

$$C_{f_L} = \frac{0.3 \times e^{-1.33\,H}}{(LOG\,Re_\theta)^{1.74+0.31\,H}} + 0.00011\,[Tanh\,(4 - \frac{H}{0.875}) - 1]$$

(a) STATION 2, x = 7.62 cm

(b) STATION 11, x = 40.6 cm
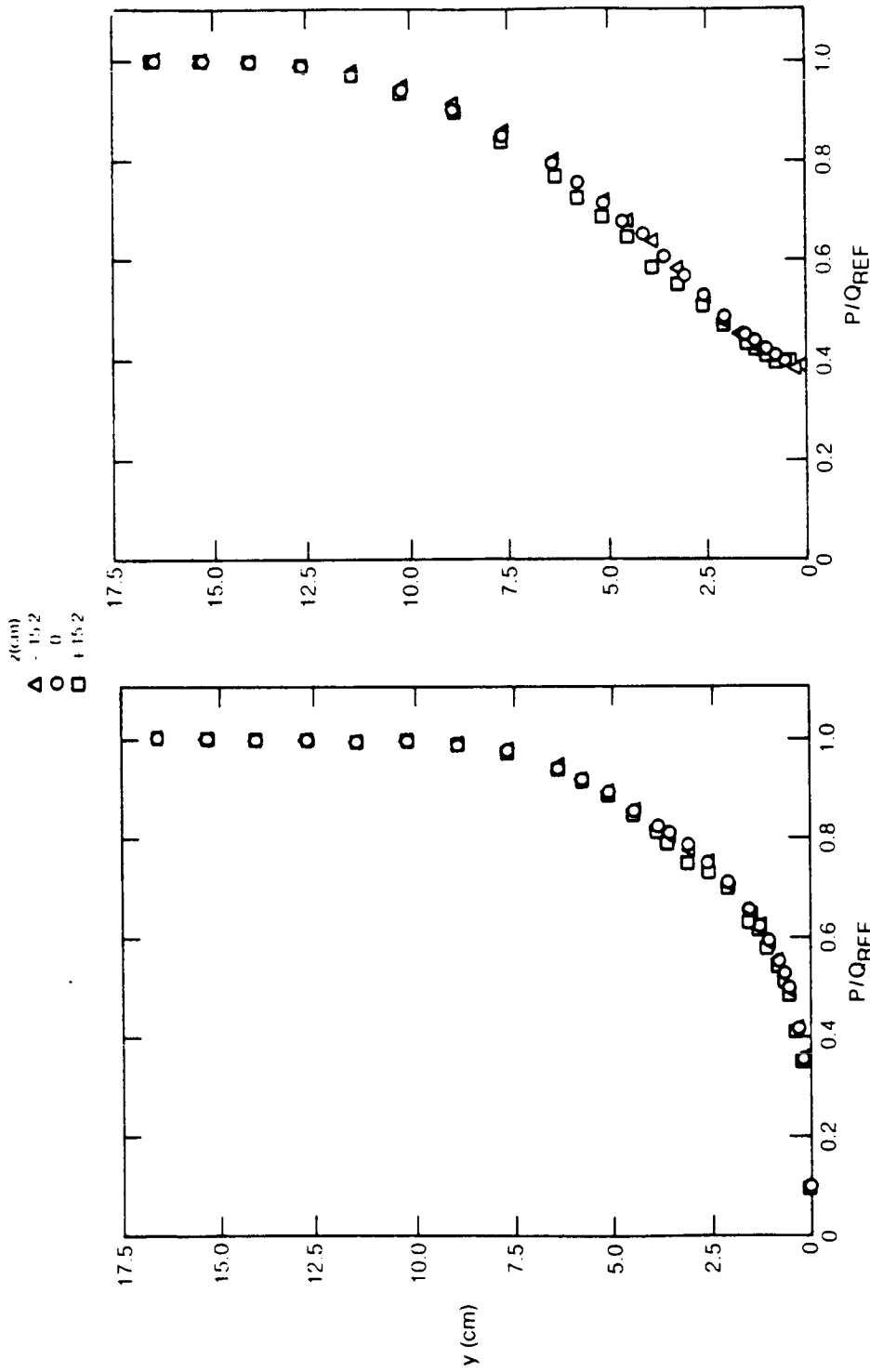
Figure 5-8 Total Pressure Profiles Showing Spanwise Uniformity of Flow
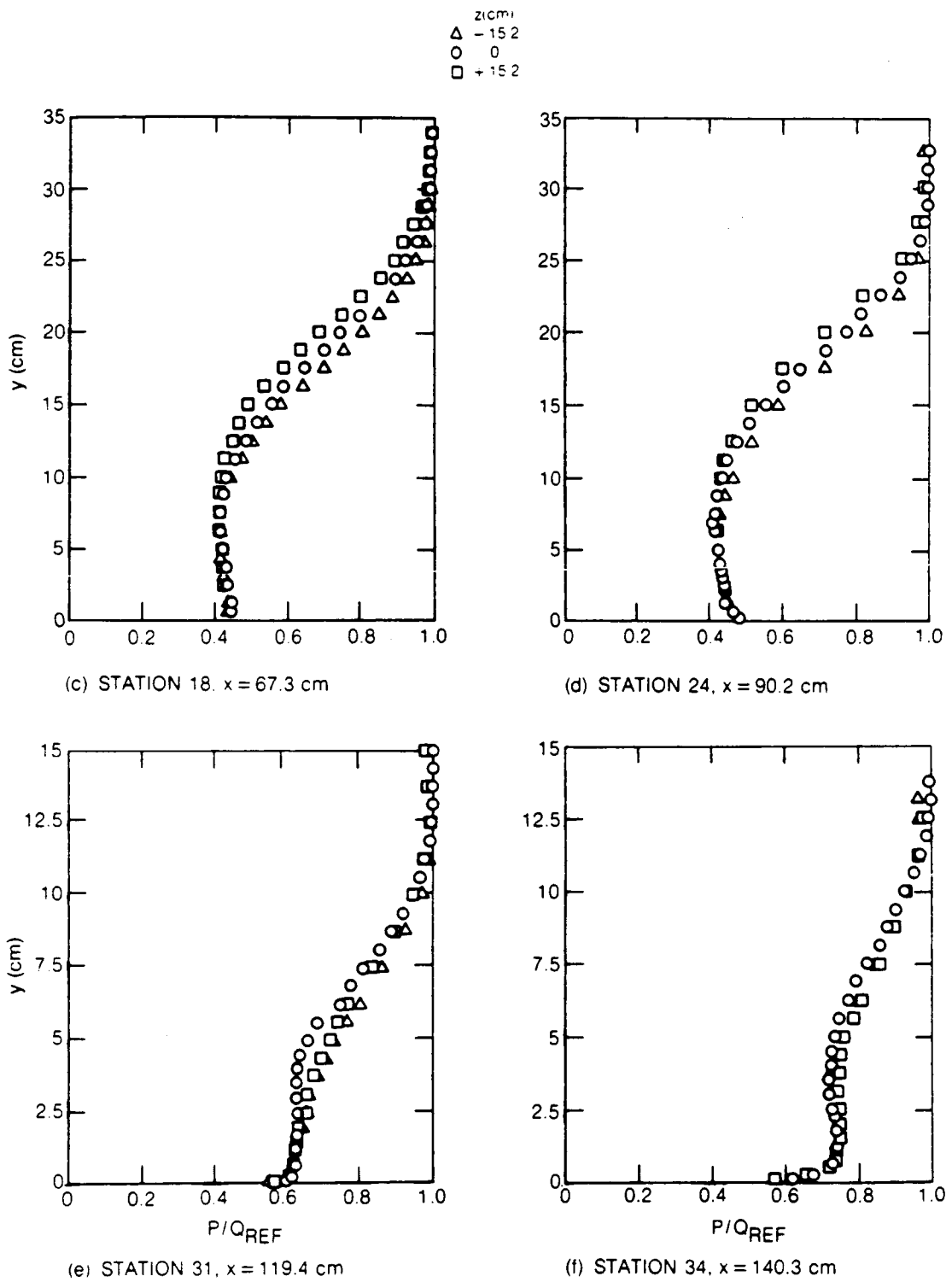
Figure 5-8 Total Pressure Profiles Showing Spanwise Uniformity of Flow (Concluded).
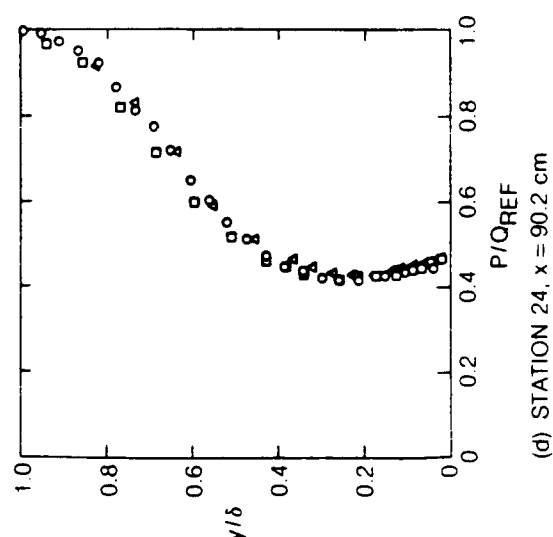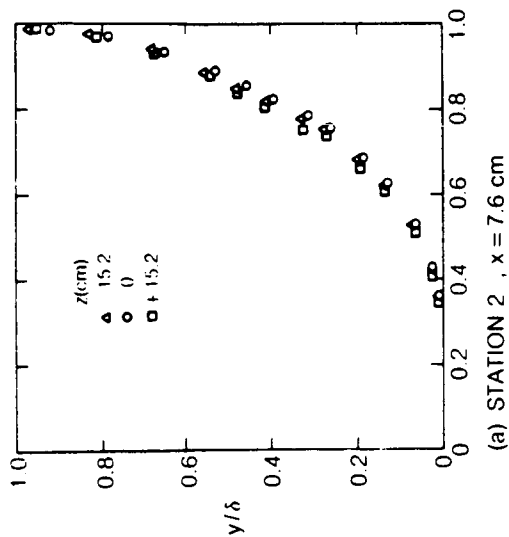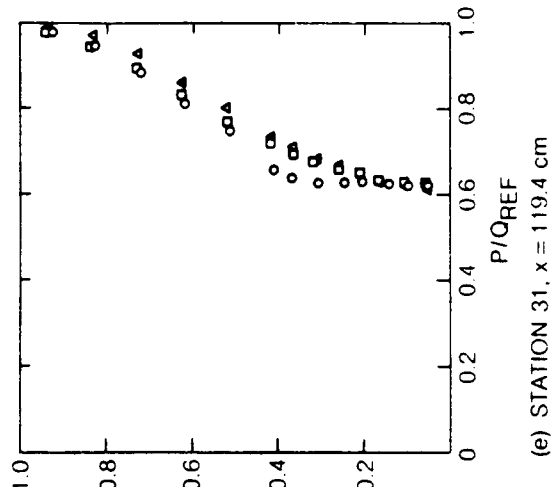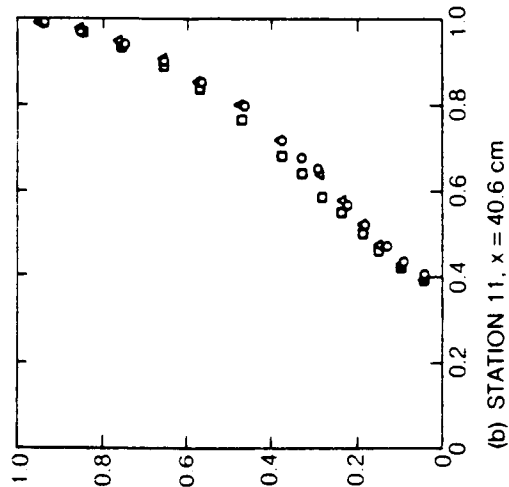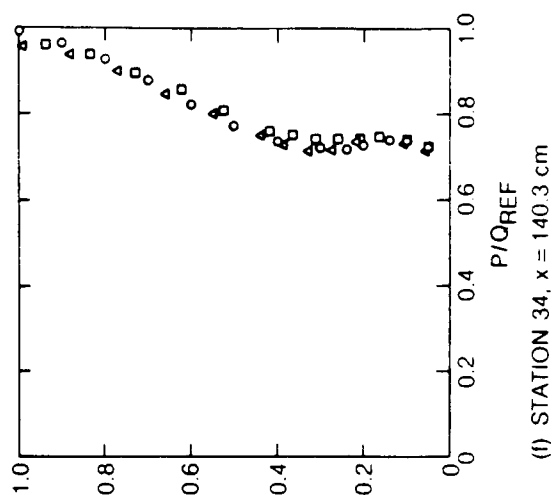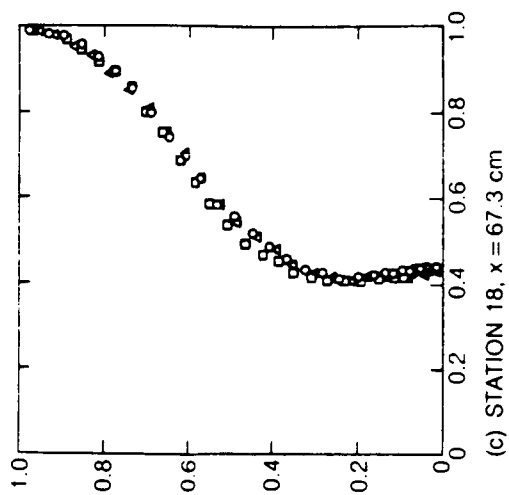
Figure 5-9 Normalized Total Pressure Profiles Showing Spanwise Uniformity of Flow
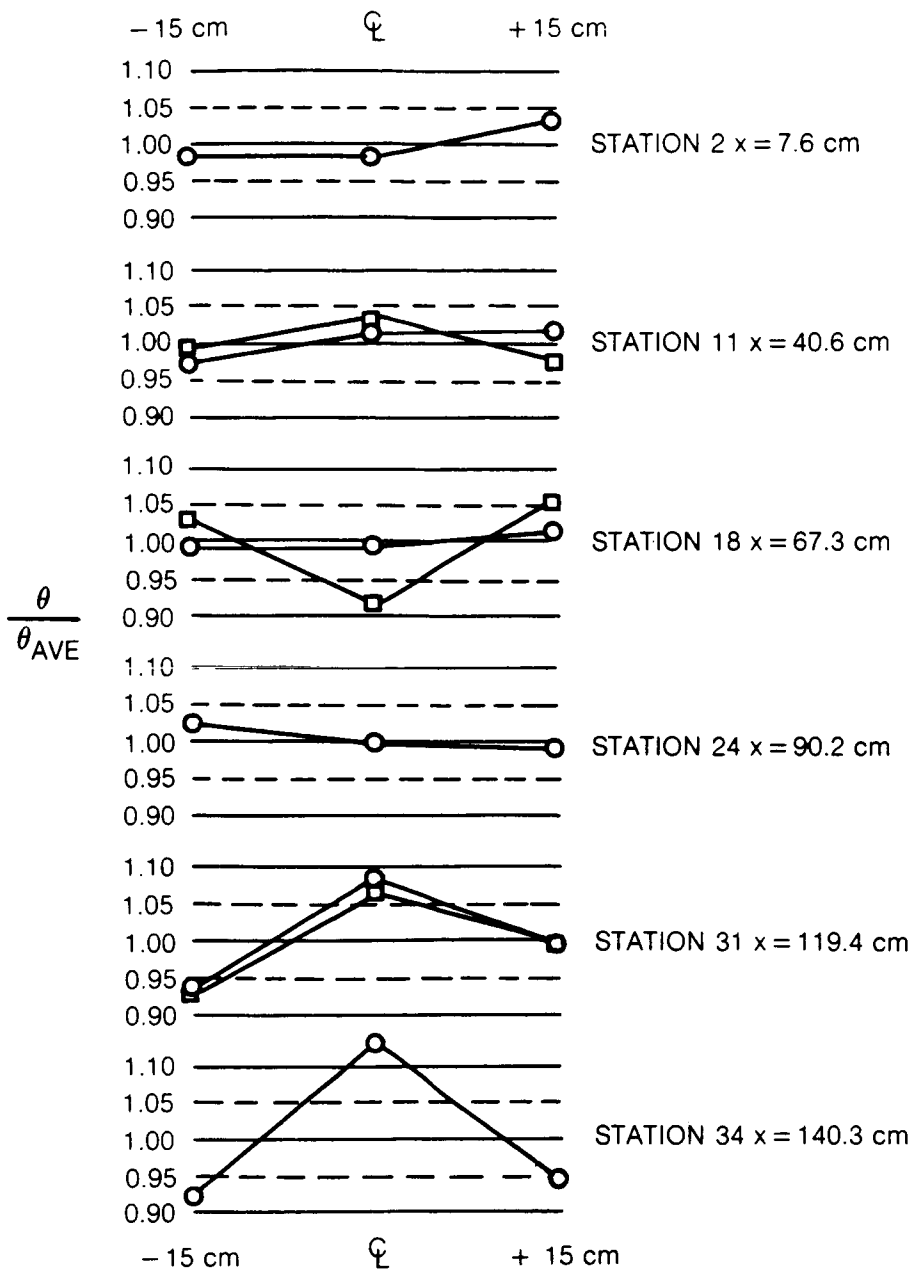
(a) STATION 2 , x = 7.6 cm

(b) STATION 11, x = 40.6 cm

(c) STATION 18, x = 67.3 cm

(d) STATION 24, x = 90.2 cm

(e) STATION 31, x = 119.4 cm

(f) STATION 34, x = 140.3 cm

Figure 5-10 Spanwise Variation in Momentum Thickness

	STATION NO	x (cm)	C_f	Π
O	0	-24.13	0.00267	0.33
□	1	2.54	0.00252	0.42
△	2	7.62	0.00247	0.37
◇	3	13.34	0.00239	0.37
◮	4	19.05	0.00212	0.62
D	5	24.13	0.00165	1.26
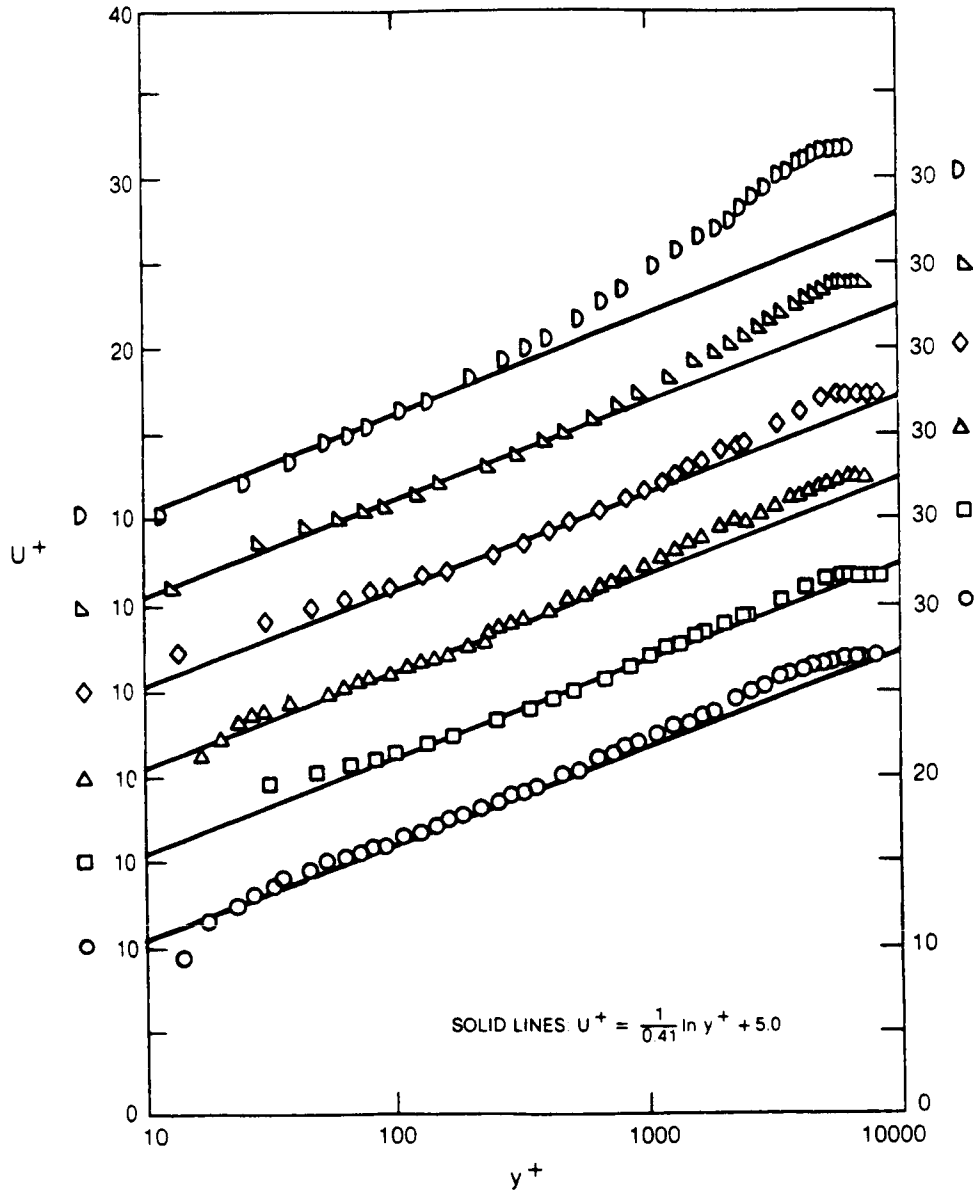
Figure 5-11a Law-of-the-Wall Velocity Profiles Upstream of Separation
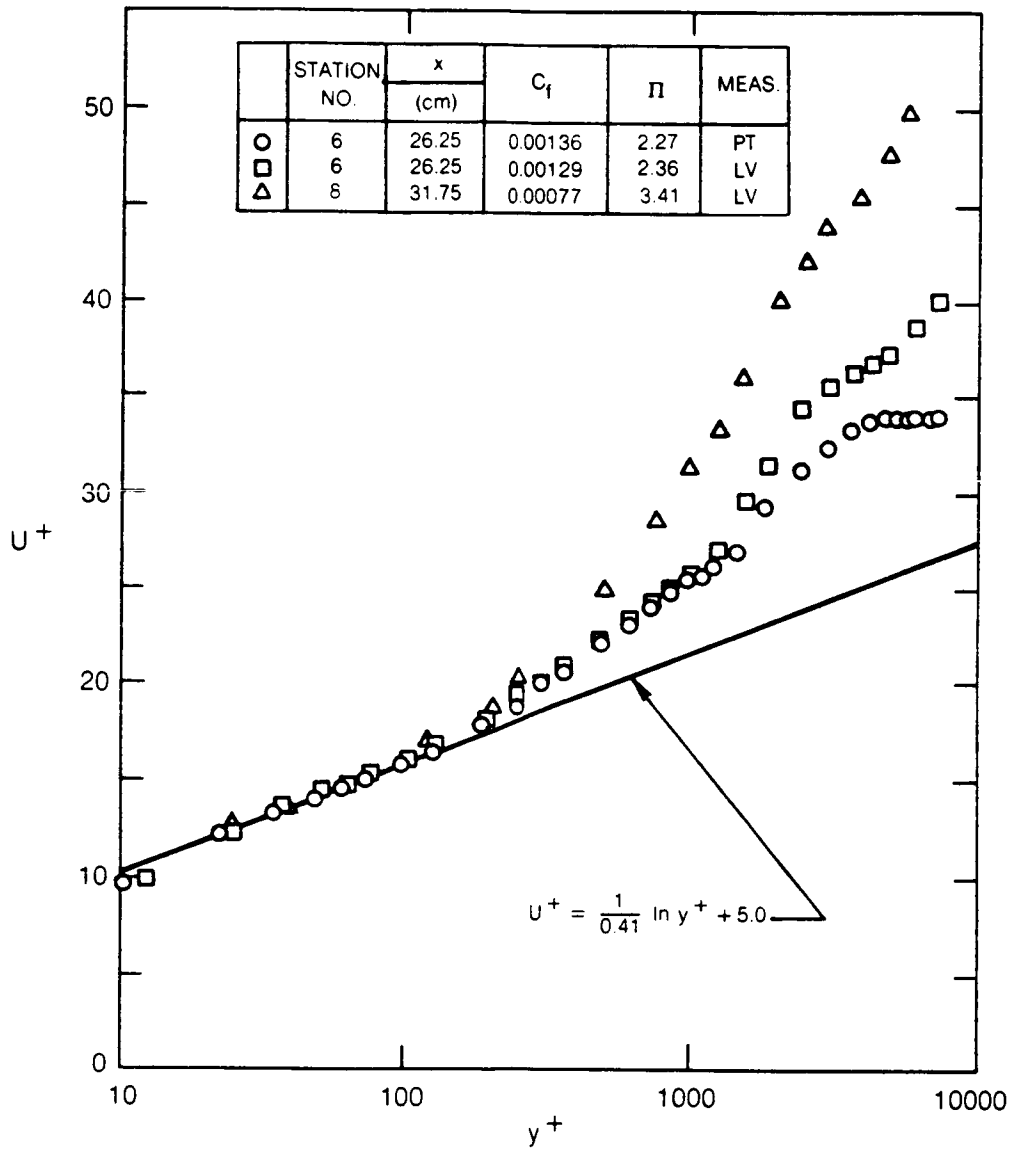
Figure 5-11b Law-of-the-Wall Velocity Profiles Upstream of Separation (Concluded)

The figure contains a data table and plot. Table:

	STATION NO.	x (cm)	C_f	Π	MEAS.
○	6	26.25	0.00136	2.27	PT
□	6	26.25	0.00129	2.36	LV
△	8	31.75	0.00077	3.41	LV

Plot axes: vertical axis U^+, horizontal axis y^+.

Equation shown on plot:
$$U^+ = \frac{1}{0.41}\ \ln y^+ + 5.0$$

84-8-1-22
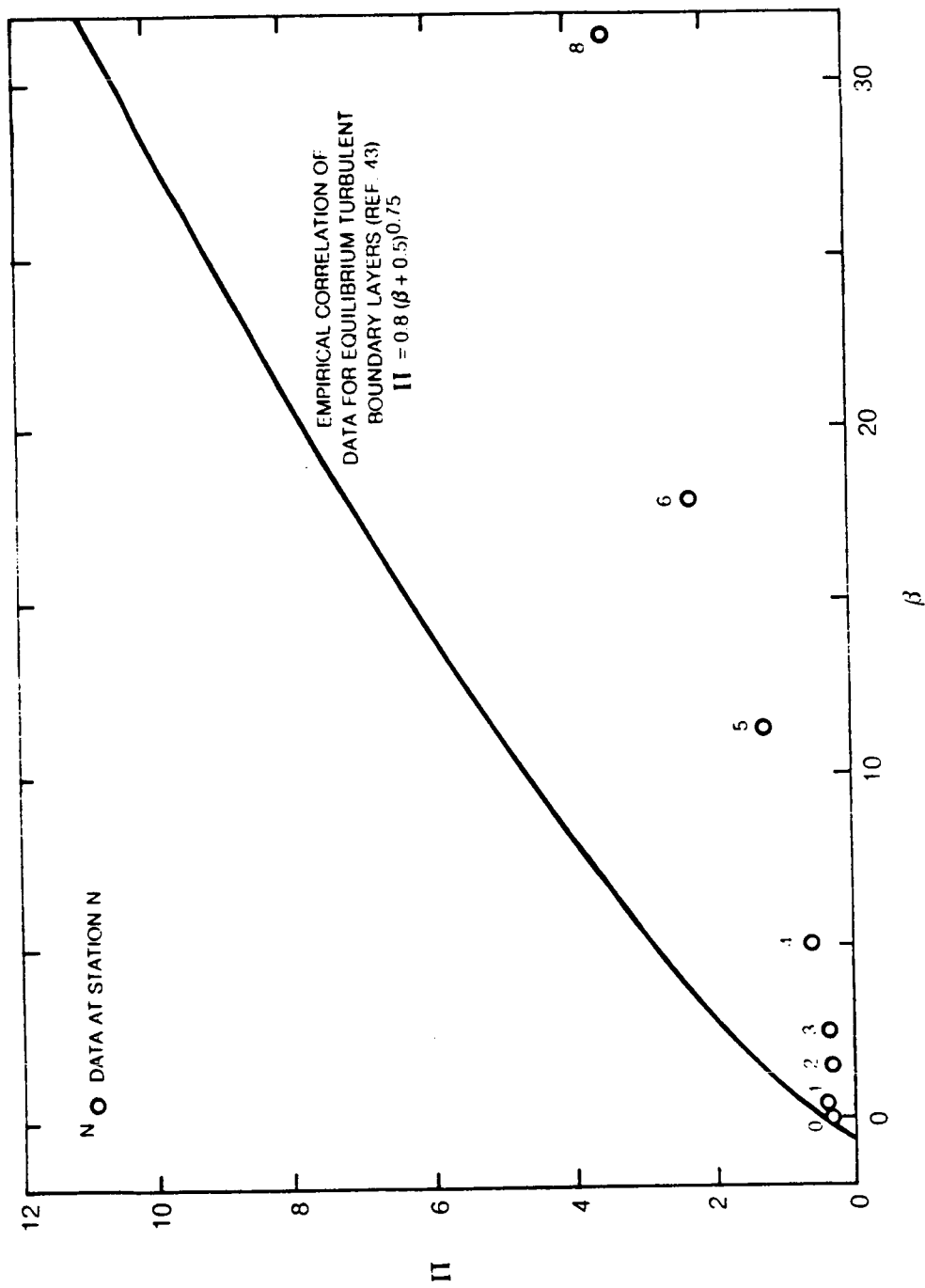
Figure 5-12 Comparison of Law-of-the Wall Wake Parameter, Π, with Clauser Equilibrium Parameter, β, Upstream of Separation

EMPIRICAL CORRELATION OF DATA FOR EQUILIBRIUM TURBULENT BOUNDARY LAYERS (REF. 43)
$$\Pi = 0.8 \, (\beta + 0.5)^{0.75}$$

N O DATA AT STATION N

85—8—36—6
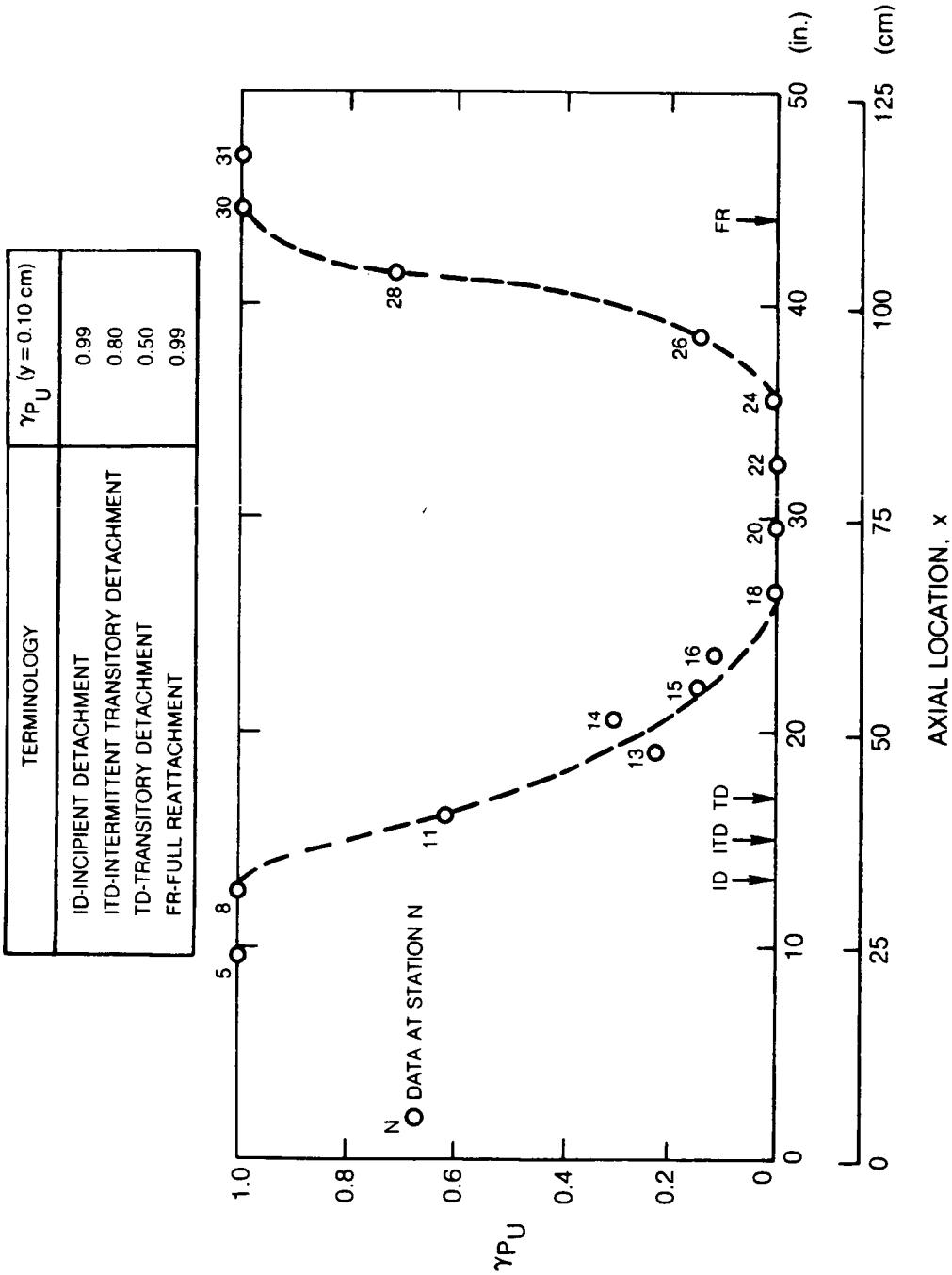
Figure 5-13 Forward Flow Fraction at y = 0.10 cm, z = 0

TERMINOLOGY	γ_{P_U} (y = 0.10 cm)
ID-INCIPIENT DETACHMENT	0.99
ITD-INTERMITTENT TRANSITORY DETACHMENT	0.80
TD-TRANSITORY DETACHMENT	0.50
FR-FULL REATTACHMENT	0.99

N ⃝ DATA AT STATION N

84—8—1—12

137
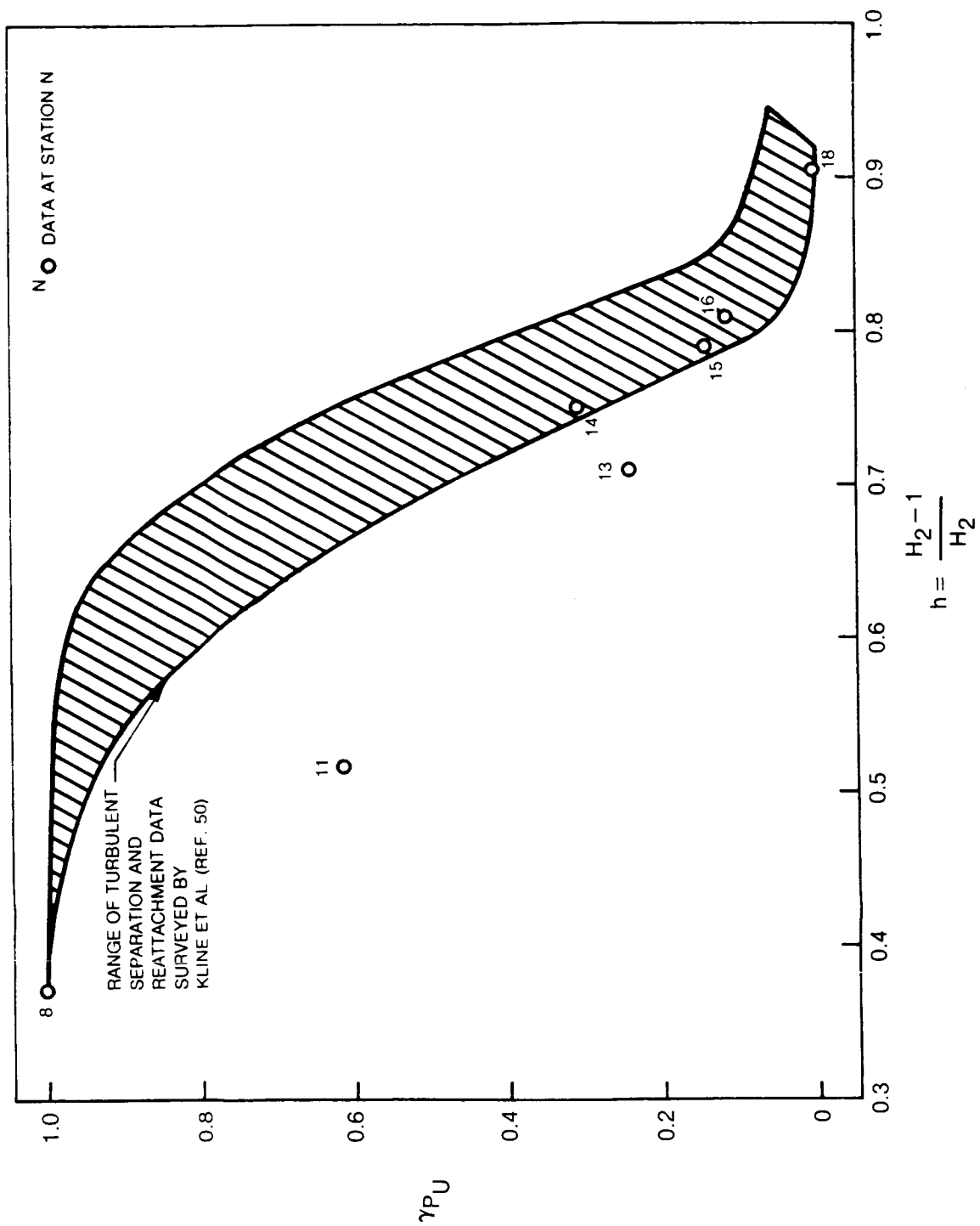
Figure 5-14 Forward Flow Fraction (γ_{P_U}) vs Shape Factor (h) in Separation Region

85-8-36-5
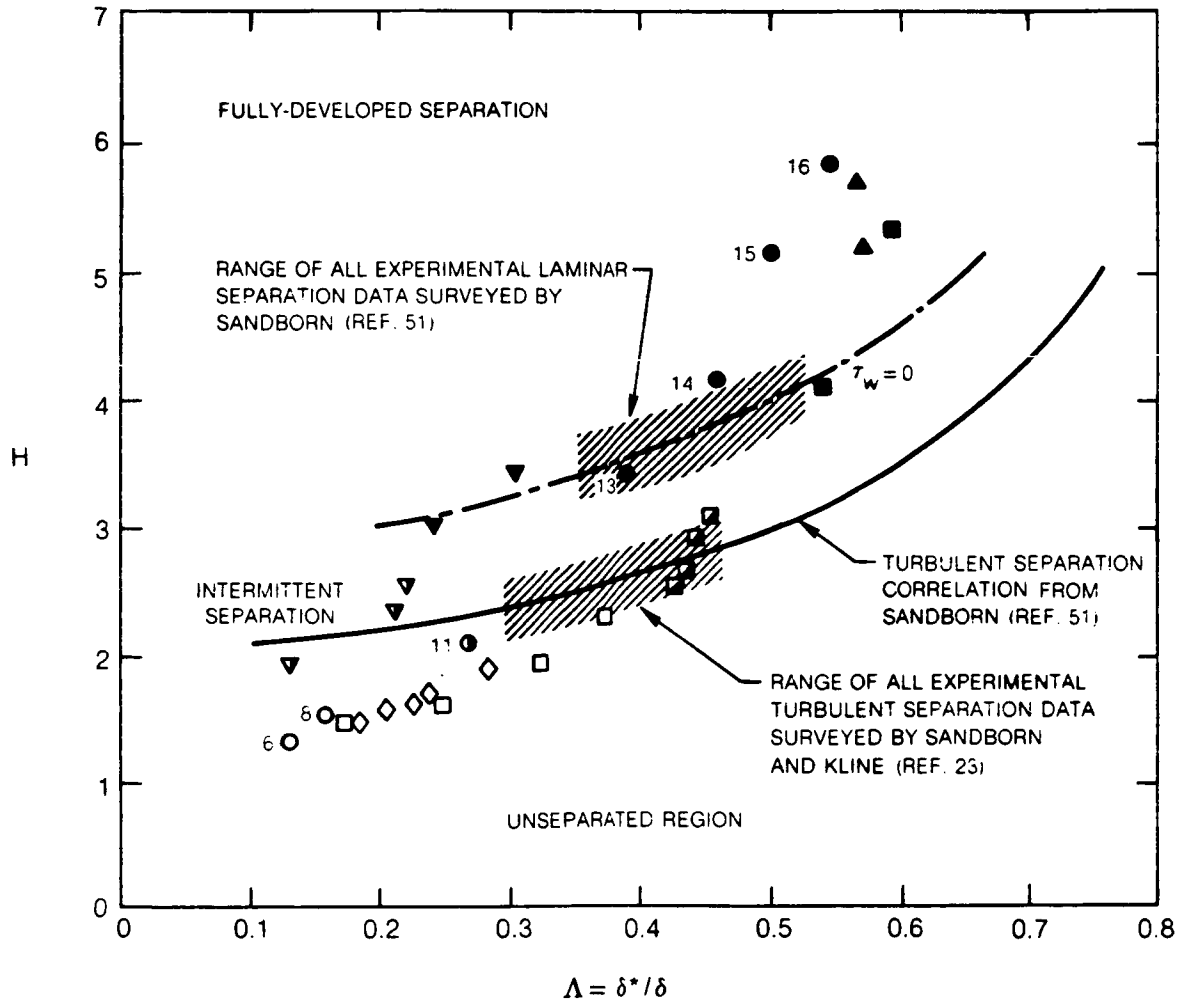
Figure 5-15 Comparison of Mean Velocity Profile Parameters at Separation with Sandborn Correlation
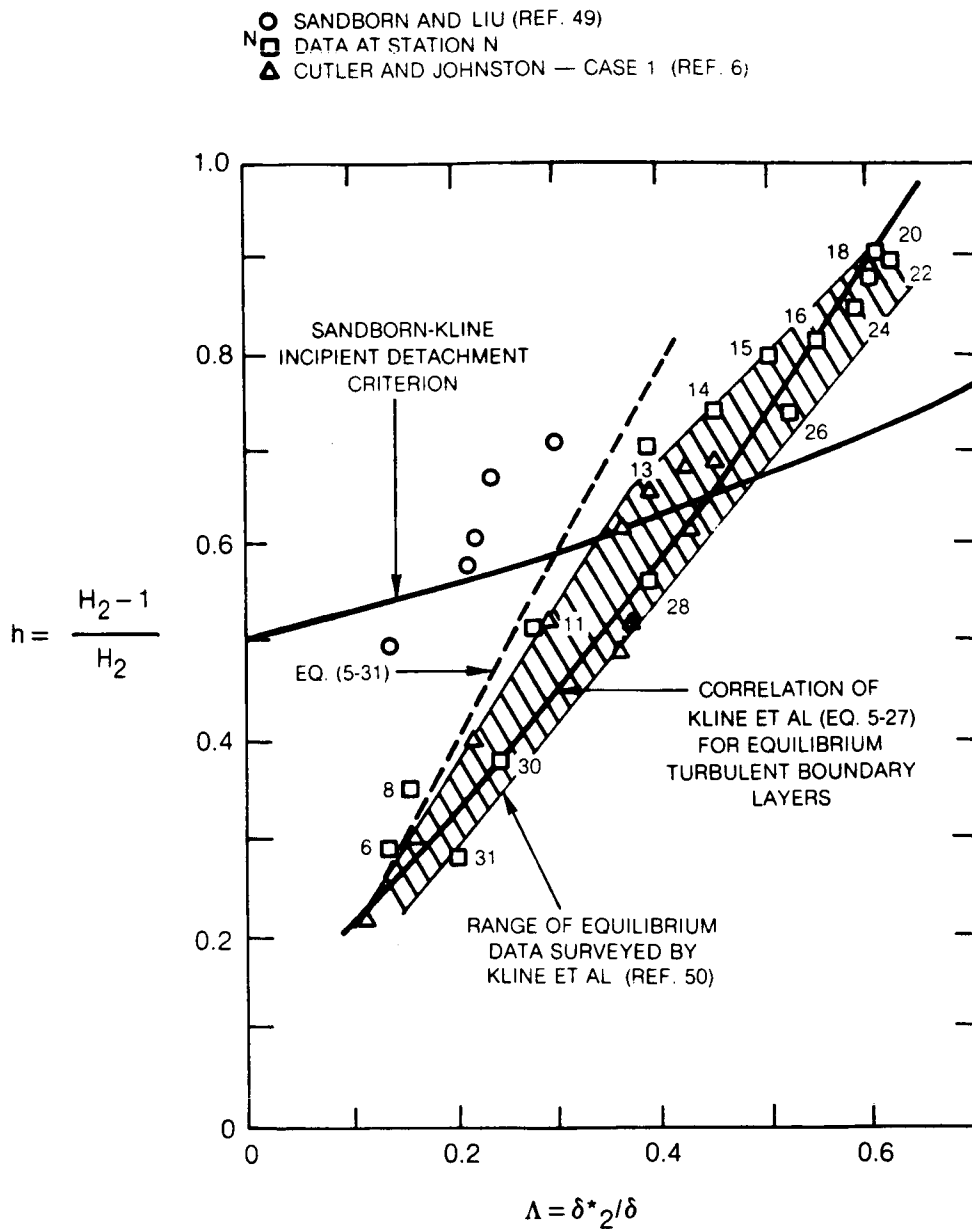
Figure 5-16. Comparison of Experimental Data to Correlation of Kline et al (ref. 50) for Attached and Separated Flows
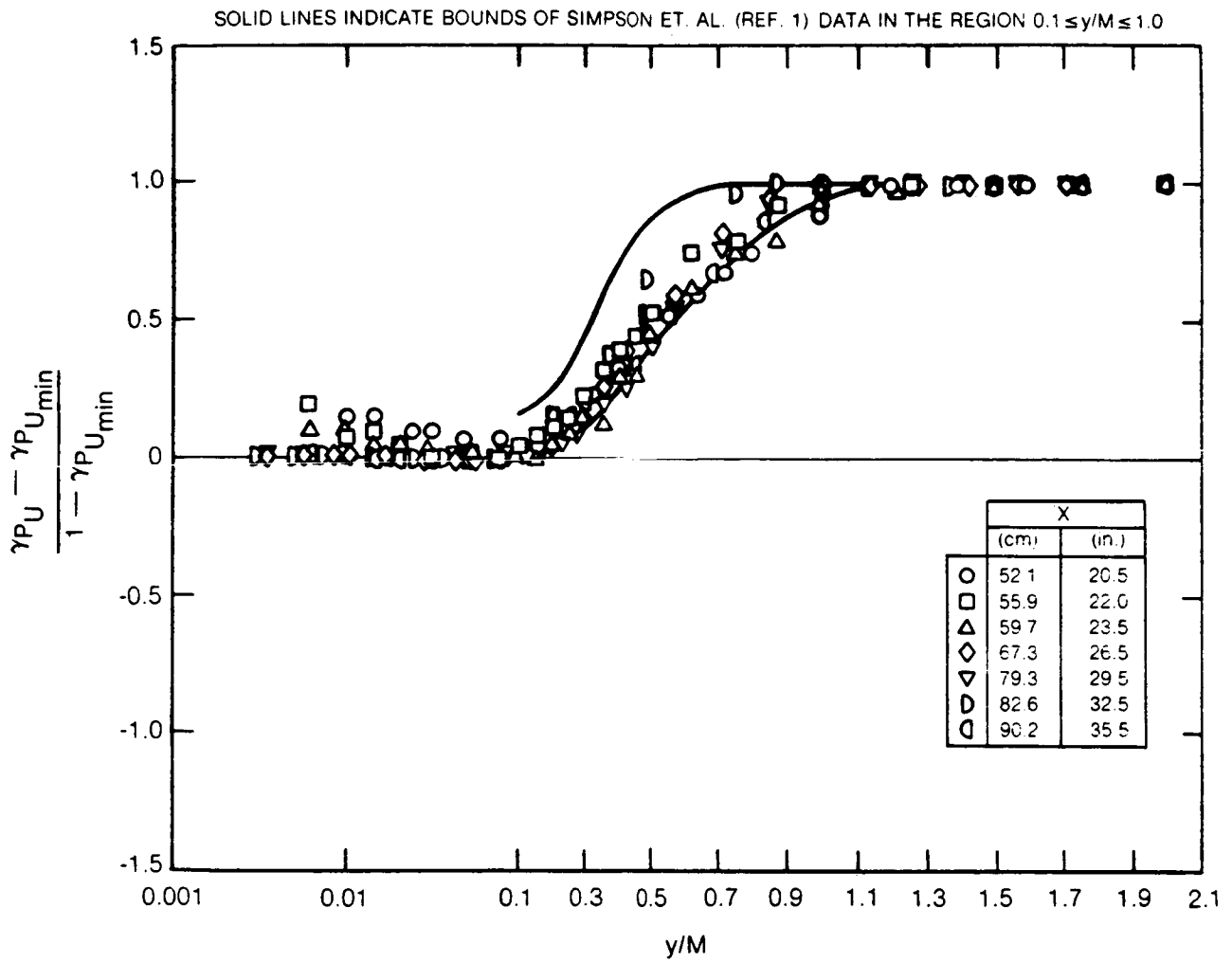
Figure 5-17 Normalized Forward Flow Fraction Profiles in the Separation Region (Note Log-Linear Abscissa)

$U < 0. \quad \dfrac{\partial U}{\partial y} < 0$ ——— ZONE IIIa BACKFLOW BOUNDARY LAYER

ZONE IIIb BACKFLOW SHEAR LAYER

$U < 0. \quad \dfrac{\partial U}{\partial y} > 0$ ——— U = 0 LOCATION

ZONE IIIc FORWARD FLOW SHEAR LAYER

——— LOCATION OF DIVIDING STREAMLINE

ZONE III

$U > 0. \quad \dfrac{\partial U}{\partial y} > 0$

y
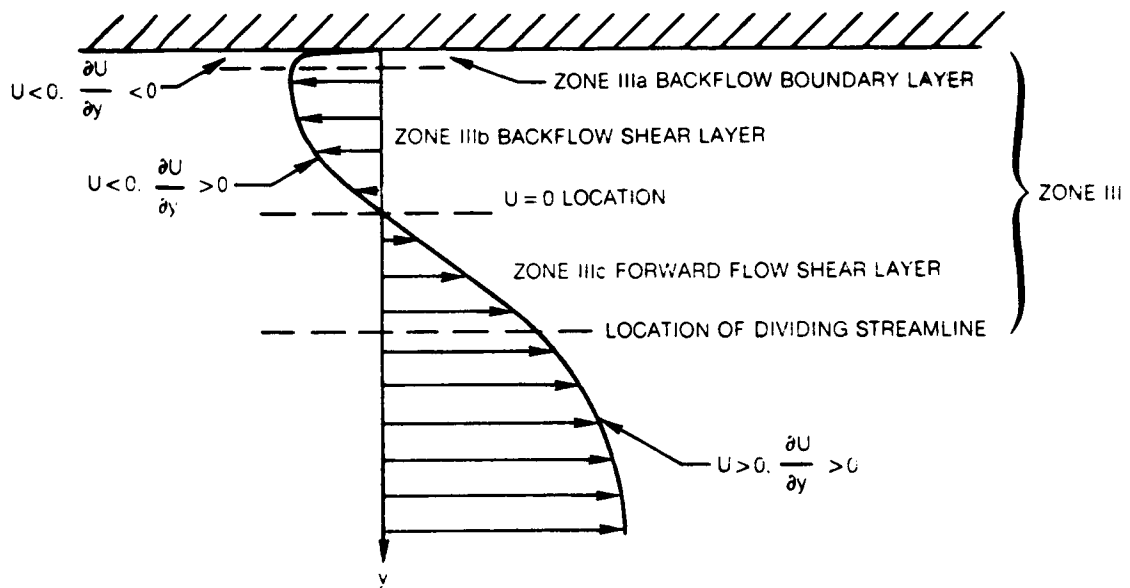
Figure 5-18 Definition of Zone III (Separation Bubble)
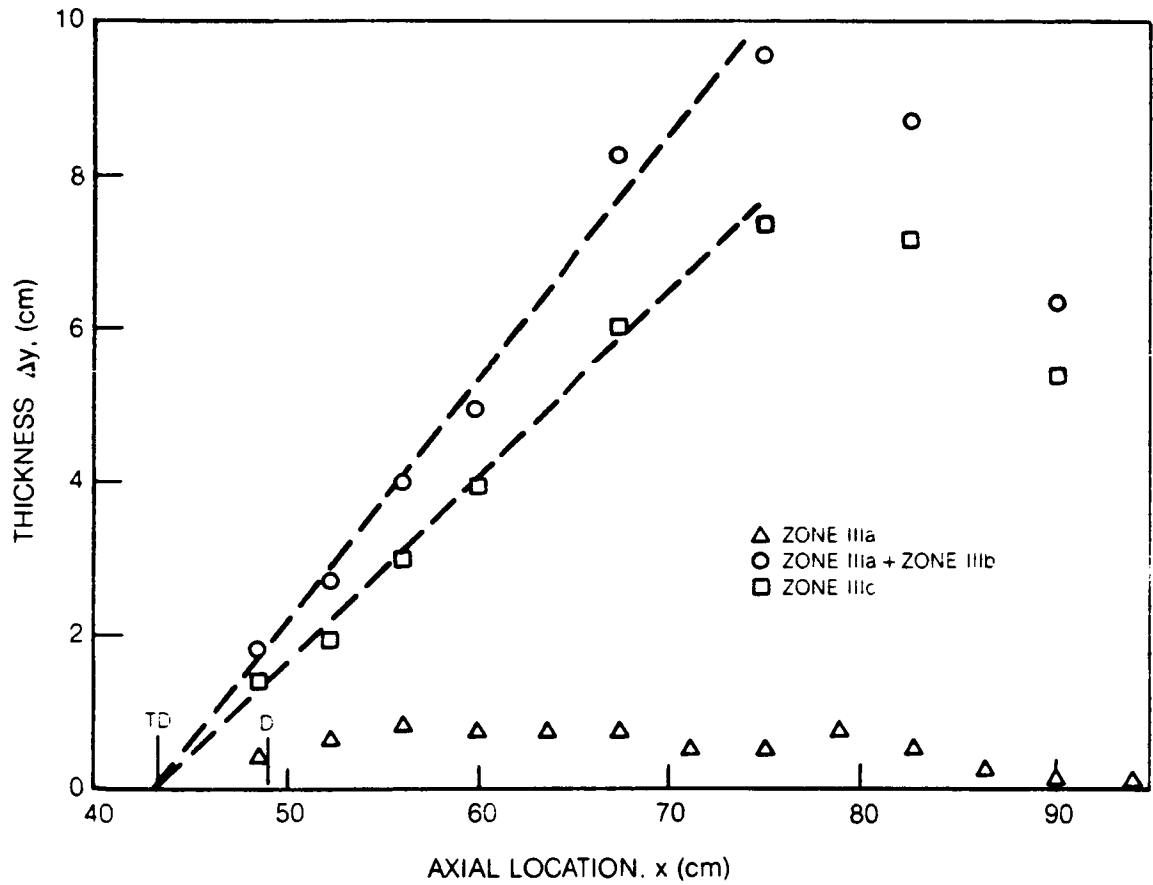
Figure 5-19 Growth of Forward-Flow and Backflow Regions within Separation Bubble
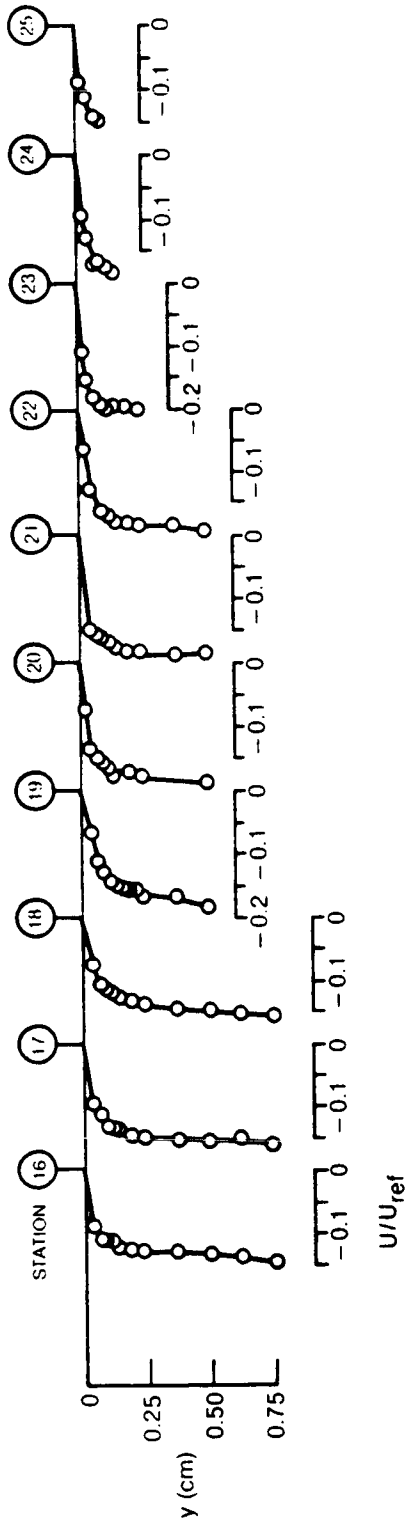
Figure 5-20 Backflow Boundary Layer Velocity Profiles Determined from Pitot Measurements

STATION NO.		x (cm)	N (cm)
O	16	59.7	0.76
□	18	67.3	0.76
◣	20	74.9	0.50
△	22	82.6	0.50
D	24	90.2	0.15

TURBULENCE PROFILE MEASURED BY KLEBANOFF (REF. 31)
FOR FLAT-PLATE TURBULENT BOUNDARY LAYER
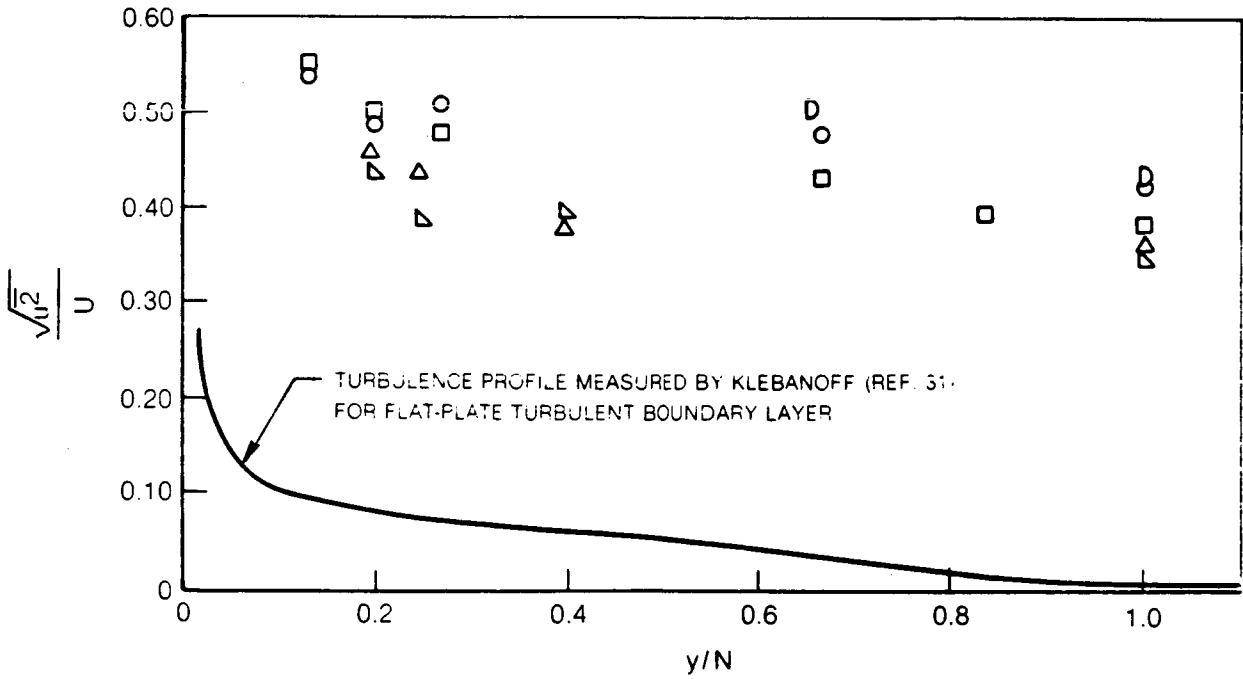
Figure 5-21 Local Axial Turbulence Levels in Backflow Boundary Layer

$$\left|\frac{U}{U_N}\right| = A\left(\frac{Y}{N} - \ln\left|\frac{Y}{N}\right| - 1\right) - 1$$
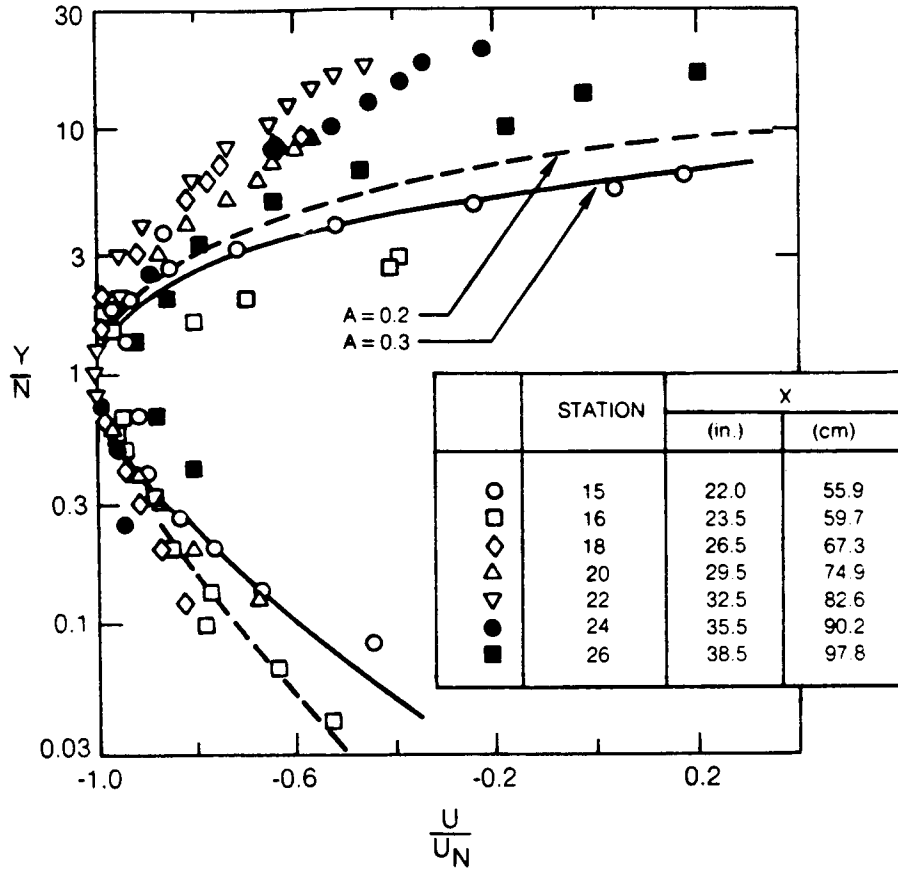
Figure 5·22 Comparison of Mean Backflow Velocity Profiles with Simpson Correlation (ref. 26)
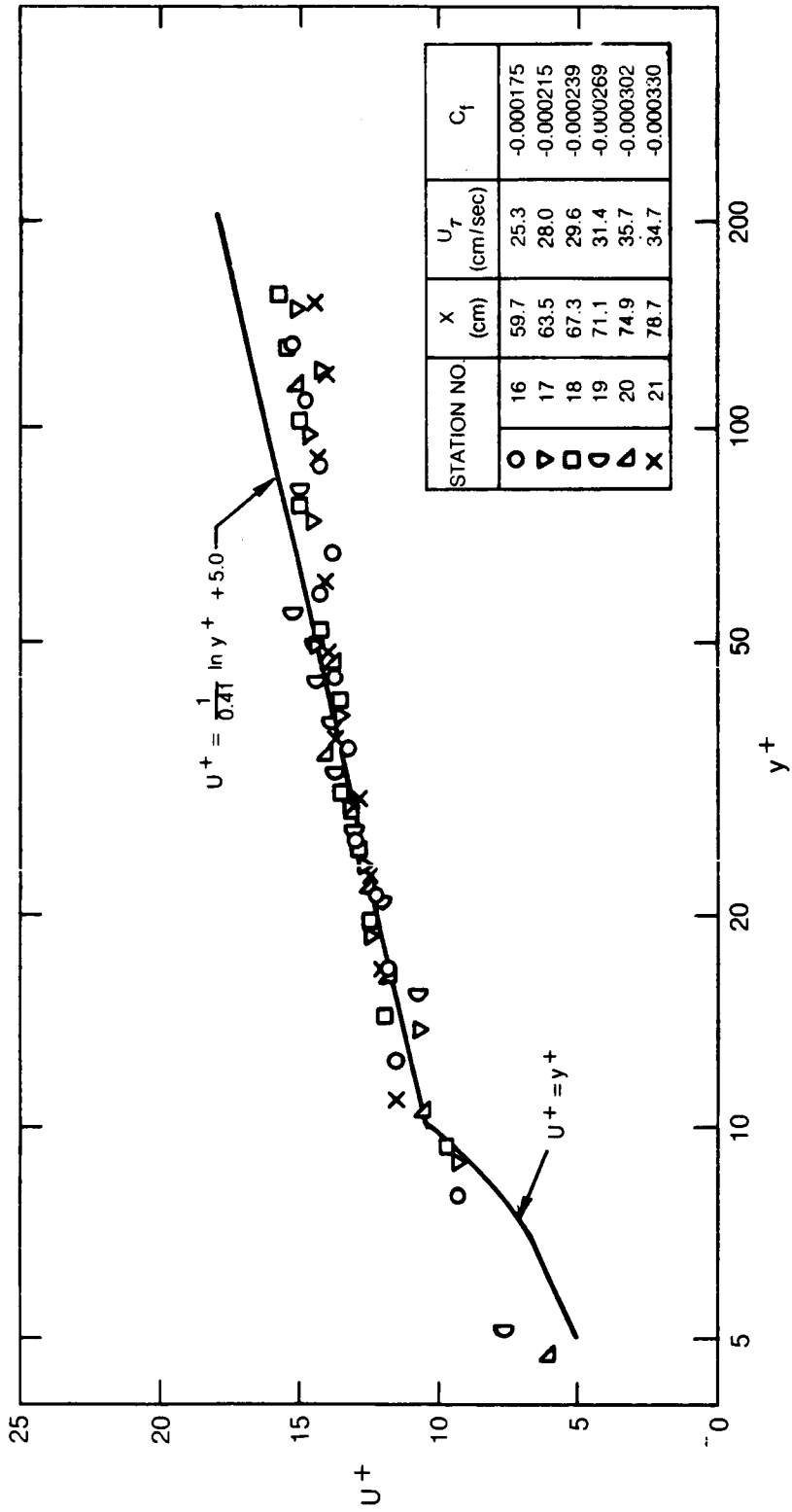
Figure 5-23 Backflow Velocity Profiles Plotted in Law-of-the-Wall Coordinates

STATION NO.		X (cm)	U_τ (cm/sec)	C_f
○	16	59.7	25.3	-0.000175
▷	17	63.5	28.0	-0.000215
□	18	67.3	29.6	-0.000239
◁	19	71.1	31.4	-0.000269
△	20	74.9	35.7	-0.000302
✕	21	78.7	34.7	-0.000330

$U^+ = \frac{1}{0.41} \ln y^+ + 5.0$

$U^+ = y^+$

84-8-1-27
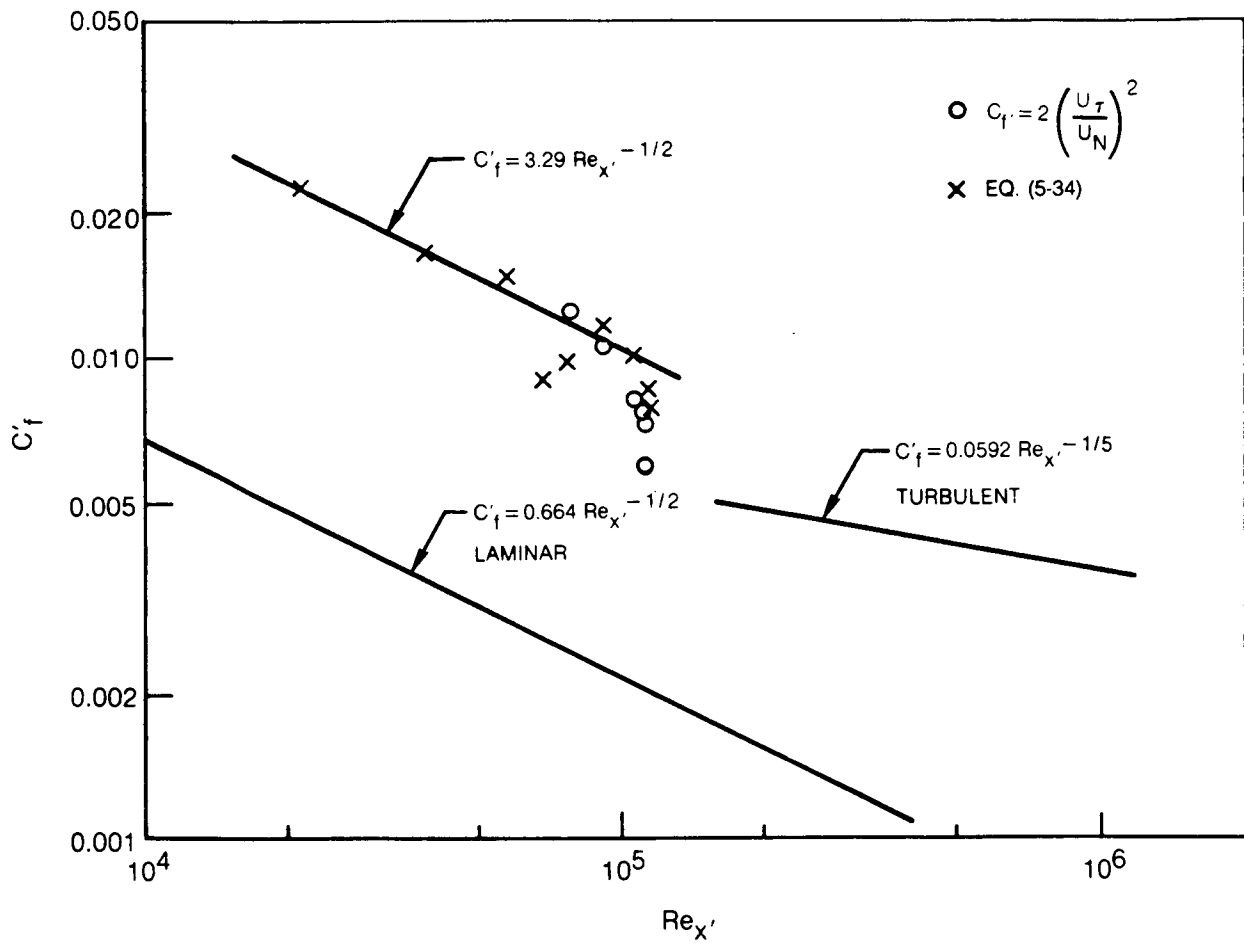
Figure 5-24 Skin Friction Coefficient in Backflow Boundary Layer
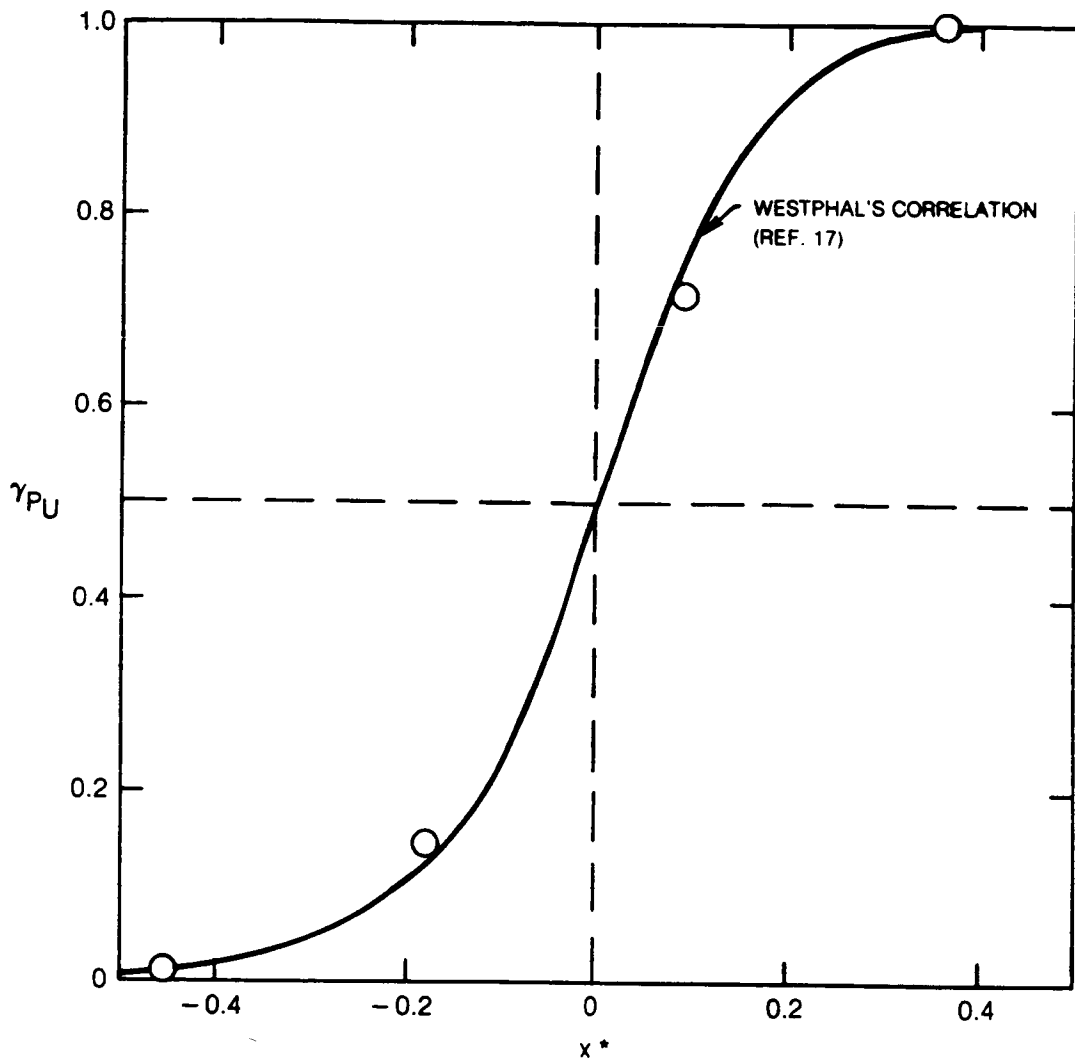
Figure 5-25 Forward Flow Fraction at y = 0.10 cm in Reattachment Region
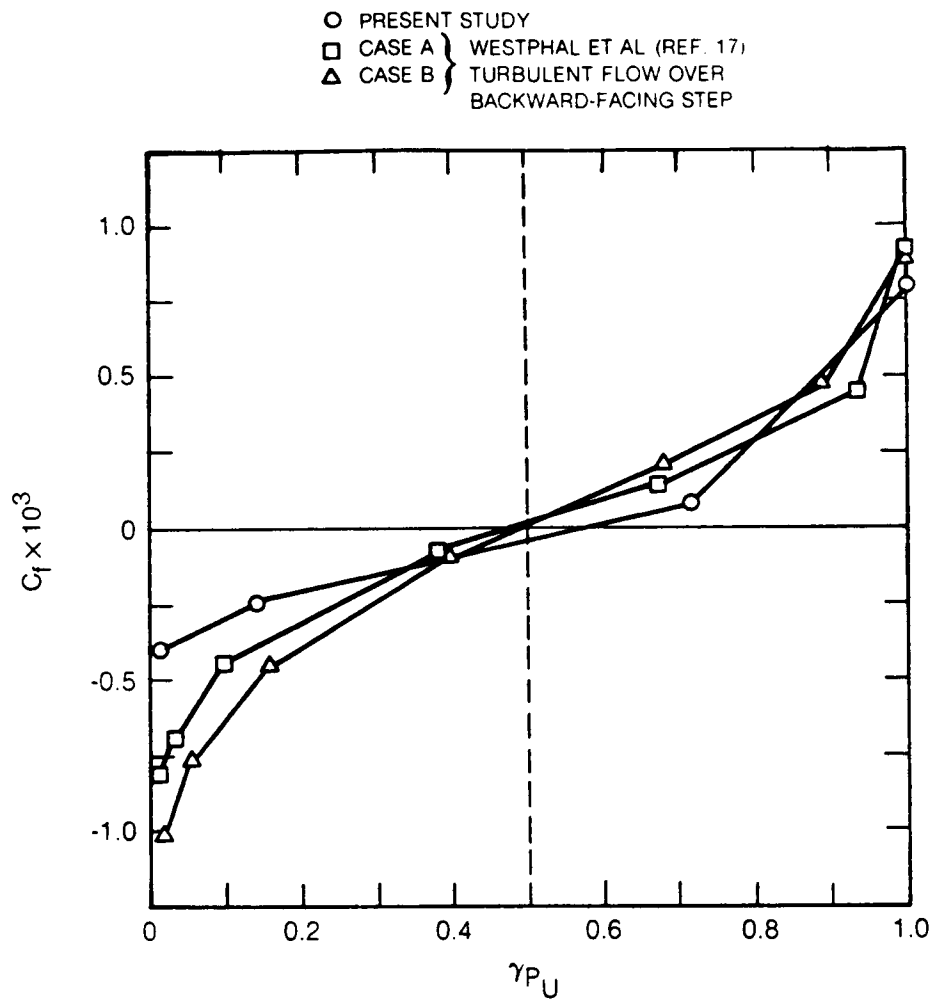
Figure 5-26 Skin Friction Coefficient vs Forward Flow Fraction Near Reattachment
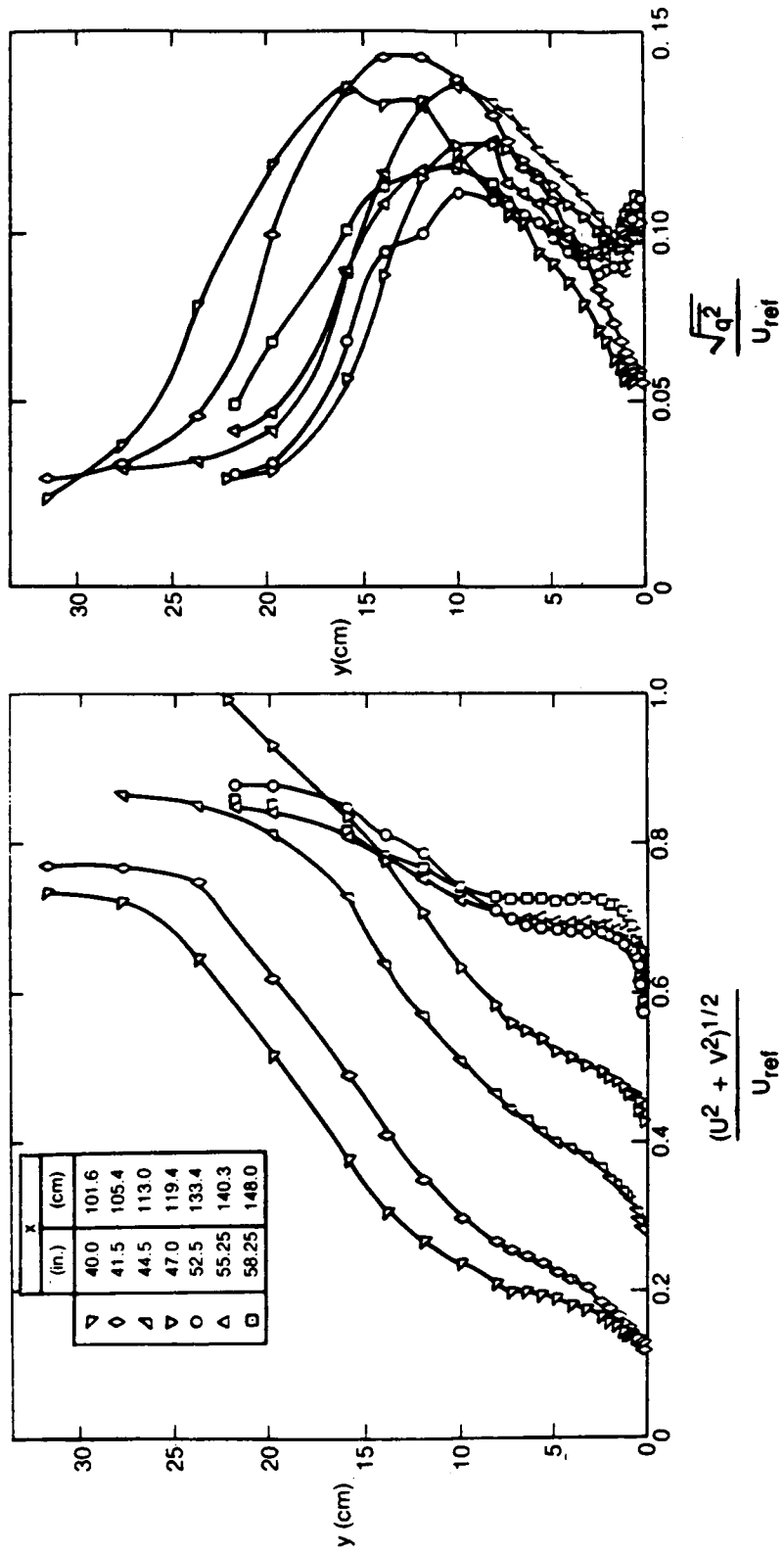
Figure 5-27 Streamwise Velocity and Turbulence Profiles Downstream of Reattachment
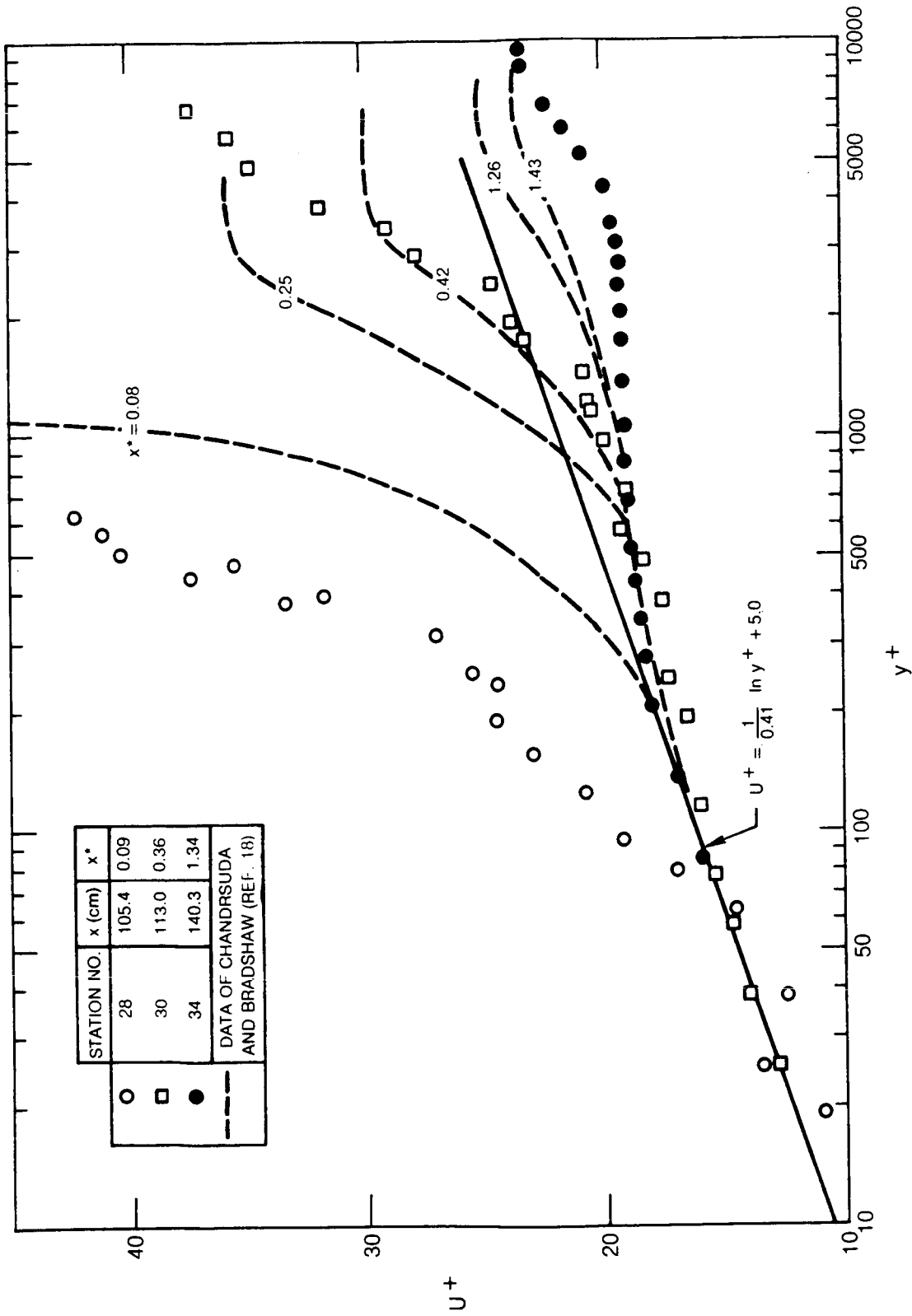
Figure 5-28 Comparison of Law-of-the-Wall Plots in Reattachment and Recovery with Data of Chandrsuda and Bradshaw (ref. 18)

152

a) DISPLACEMENT THICKNESS VARIATION IN REATTACHMENT REGION

b) MOMENTUM THICKNESS VARIATION IN REATTACHMENT REGION

c) SHAPE FACTOR VARIATION IN REATTACHMENT REGION

Figure 5-29 Comparison of Boundary Layer Integral Quantities in Reattachment Region with Data of Driver and Seegmiller (ref. 14)
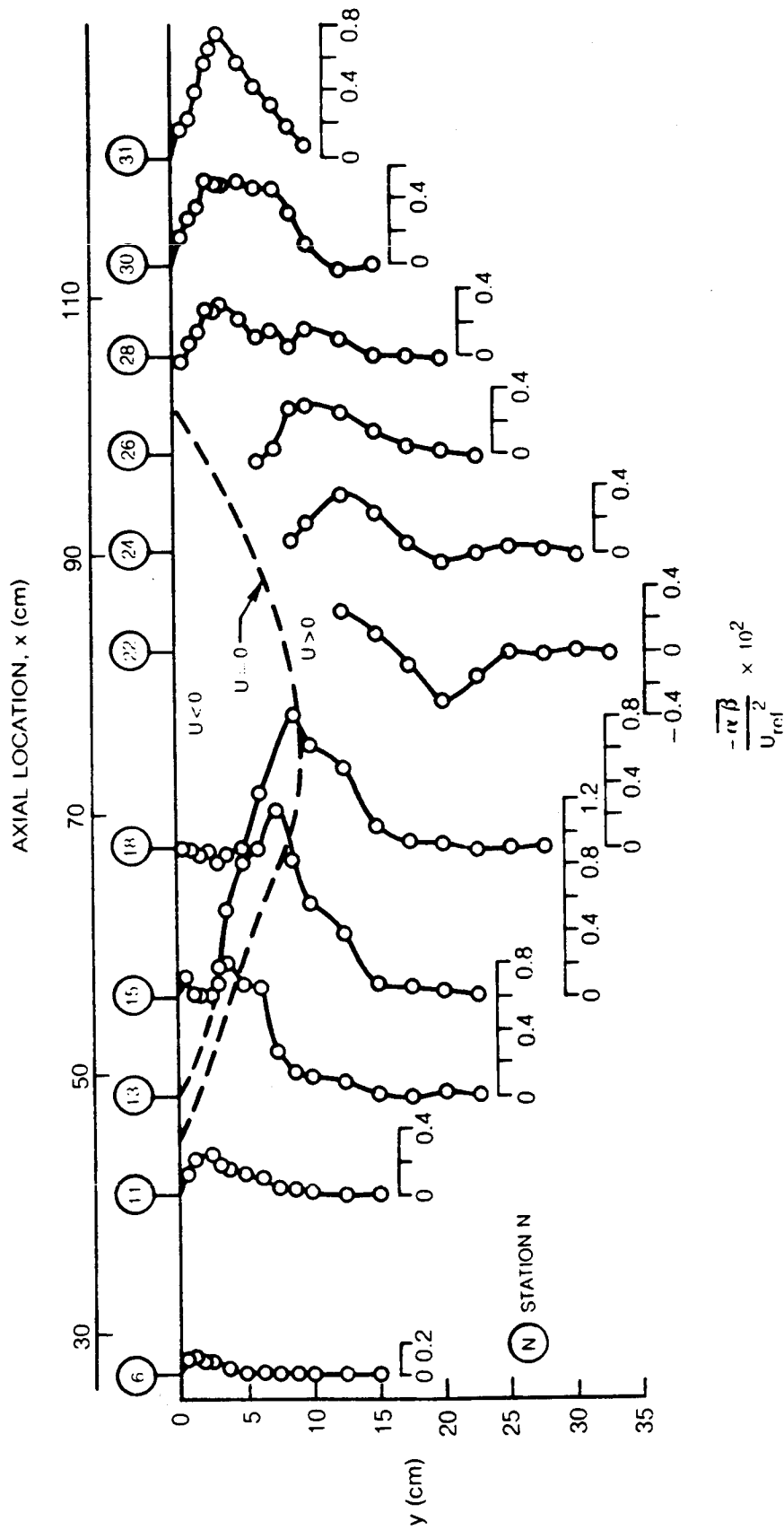
Figure 5-30 Nondimensional Streamwise Shear Stress Profiles Determined from Laser Velocimeter Data (z = 0)

CHAPTER 6

CONCLUSIONS

Overall conclusions and observations regarding the nature of the separated flowfield investigated in the current study are summarized here. Following these general remarks are more specific comments regarding flow in the various zones which comprised the overall flowfield.

The wind tunnel test configuration employed here produced a large scale (55 cm. axial extent, 17 cm. maximum thickness) closed separation bubble on a flat plate test surface with an incident near-equilibrium turbulent boundary layer. Based on flow visualization and spanwise flowfield measurements, the separated flowfield is concluded to be a good approximation to an idealized two-dimensional flow with separation and reattachment and hence a suitable reference case for assessing computational procedures used to predict two-dimensional separated flow phenomena. With regard to flowfield steadiness, an outer inviscid zone was defined in which velocity fluctuation levels were low (approximately two percent of the reference inlet velocity). From this low level it was concluded that the overall wind tunnel test section flow was steady although high levels of unsteadiness were obtained within certain viscously dominated flow zones. Lack of periodicity in the unsteady velocity signal suggests that the intermittent separation and unsteady reattachment process were not linked by a discrete frequency feedback loop mechanism.

As discussed in more detail below, the separated flow region at the forward end of the bubble was found to be generally similar to that obtained in previous open separation studies (turbulent separation without reattachment). While this could be expected, an unanticipated result was that the reattaching flow at the aft end of the bubble bore many similarities to reattaching flows downstream of backward facing steps. In addition to these results regarding the forward and aft end of the separation bubble, important features were identified in the near wall and outer flow regions. A reverse flowing boundary layer was identified at the base of the bubble and the flow around the bubble was found to be basically inviscid and rotational. Congruence of velocity profiles was obtained in this outer flow region supporting a similar observation in a previous separated flow study with a different test geometry.

For the purpose of providing a more detailed analysis of the various flowfield phenomena encountered here it was found that the overall flow could be conveniently divided into eight flow zones. Observations and conclusions for these various zones are given below:

Zone I - Attached Flow Region - Flow in this incident boundary layer region consisted of a near equilibrium turbulent boundary layer which lost its equilibrium structure when it encountered a strong adverse pressure gradient.

Zone II - Intermittent Separation Region - Flow in this region experienced an increasingly adverse pressure gradient causing detachment to occur within a distance equal to one incident boundary layer thickness downstream from incipient detachment. Detachment occurred at a shape factor, H, of 2.2 in line with established separation criterion, although the boundary layer did not track the $(H-1)/H$ vs. δ^*/δ (i.e. displacement thickness/boundary layer thickness) curve established by Kline et. al. (ref. 50) for equilibrium separation.

Zone III - Separation Bubble - This zone, defined as the region between the mean dividing streamline and the test surface, consisted of three sub-regions: a backflow boundary layer (Zone IIIA) at the base of the bubble, a backflow shear layer (Zone IIIB), and a forward flow shear layer (Zone IIIC). The backflow shear layer which is approximately an order of magnitude thicker than Zone IIIA, consists of an inner layer (Zone IIIB1), having a relatively flat velocity profile and a constant turbulence level approximating 8 percent of the inlet freestream velocity, which connected to viscous near wall region to the outer backflow region (Zone IIIB2) which was part of the outer shear flow. The forward flow shear layer, Zone IIIC, defined as the locus of U = 0 points and the dividing streamline, contained higher velocity gradients and turbulence levels than Zone IIIB. Zone IIIC was slightly thinner than the combined thicknesses of the backflow zones (Zones IIIA and Zone IIIB). The thicknesses of the backflow zones and the forward flow shear layer (Zone IIIC) increased linearly over the upstream half of the bubble from the point of transitory detachment.

Although the three-layer backflow structure defined by Zones IIIA, IIIB1, and IIIB2 agrees with the model proposed by Simpson (ref. 1), the backflow velocity profiles only matched his "universal" backflow profile (ref. 26) in the intermittent flow region just downstream of detachment. This lack of correlation can be attributed to the vigorous backflow within the closed separation bubble driven by the static pressure peak at reattachment. A large region of steady backflow, wherein the LV data indicated flow in the upstream direction 100 percent of the time, existed near the test surface over the central 35 percent of the axial extent of the bubble.

Significant normal static pressure gradients existed within the boundary layer in the vicinity of the separation bubble due to streamline curvature induced by bubble blockage. Changes in the blockage, measured by the displacement thickness, which exceeded 20 cm at the maximum bubble thickness, caused convex streamline curvature at separation and at reattachment and

concave curvature over the central part of the bubble. The resulting static pressure field was calculated from measured total pressures and LV velocity data.

The inclusion of the normal static pressure changes, which were as large as 50 percent of the dynamic head between the test surface and the lower wall near the location of the maximum bubble thickness, was found to be very important. Integral properties were calculated three ways: (1) the classical definition based on the boundary layer edge velocity, (2) a pressure-based definition which calculated the retardation of the boundary layer relative to an equivalent inviscid field determined from the measured upstream total pressure and the local derived (from measurements) static pressure, and (3) the true definition (refs. 38 and 39) which was equivalent to the classical definition with the addition of correction terms to account for the normal static pressure gradient effects. These effects were especially evident at the location of the maximum bubble thickness where the shape factor, H, was calculated to be 16.1, 11.8, and 7.5 based upon the true, pressure-based, and classical definitions, respectively.

Because of the large streamline inclination angles trends in the turbulent shear stress measurements were not evident until the measurements obtained in a coordinate system orthogonal to the test surface were rotated into a coordinate system orthogonal to the local streamline direction. High values of the resulting streamwise shear stress, indicative of strong turbulence generation, were measured near the edge of the backflow region (i.e., near the locus of U = 0 points) over the forward half of the bubble. Downstream of the maximum bubble thickness, the peaks broadened, decayed, and moved away from the U = 0 line into the wake of the bubble.

Zone IIIA - Backflow Boundary Layer - The region at the base of the separation bubble is a highly unsteady laminar boundary layer having pseudo-turbulent characteristics. The backflow velocity profiles had a limited log-linear region with no wake component when plotted in law-of-the-wall coordinates. Skin friction coefficients derived from the law-of-the-wall plots (and corroborated by shear stress estimated from the normal velocity gradient at the wall) were approximately 100 percent higher than skin friction coefficients previously reported for intermittent backflow under open separation bubbles. The measured skin friction coefficient showed the $Re_{x'}^{-1/2}$ dependence (where x' is distance upstream from reattachment) typical of laminar boundary layers but was 400 percent higher than values anticipated for flat-plate zero-pressure-gradient boundary layers. Some of the increased shear stress is due to the favorable pressure gradient experienced by the backflow boundary layer as it moves upstream from the static pressure peak at reattachment. It is conjectured, however, that the majority of the increase can be attributed to the effect of low frequency (i.e., length scales on the

order of the bubble size) turbulence in the bubble which is typically 40 percent of the maximum backflow velocity.

Zone IV - Reattachment Zone - In this zone the reattaching flow impinges steeply onto the test surface causing a static pressure peak which drives the strong backflow within the separation bubble. The highly unsteady flow in this zone is characterized by random low frequency streamline flapping with large scale eddies being convected alternately upstream and downstream from the impingement point on the test surface. The forward flow fraction measured near the test surface, when plotted vs. non-dimensional distance from reattachment, matches the correlation of Westphal et al. (ref. 17) for reattaching backward-facing step flows. The appropriate length scale for closed separation bubble data is the distance from the maximum bubble thickness, $x_{\delta^*_{max}}$, to reattachment. In addition, skin friction correlated with forward flow fraction in Zone IV in the present study in the same manner as the backward-facing step data measured by Westphal et. al. (ref. 17).

Zone V - Redeveloping Near Wall Flow - This zone encompasses the near wall region downstream of reattachment where a new boundary layer begins to develop along the test surface. The boundary layer, which has high turbulence levels impressed upon it from the bubble wake, quickly develops a log-linear velocity profile near the wall and begins to merge with Zone VI, the relaxing outer shear layer, to obtain the wake-like structure of an equilibrium tur- bulent boundary layer.

Zone VI - Relaxing Outer Shear Layer - The free shear layer in this zone originated near the mean dividing streamline surrounding the bubble and was shed into the bubble wake. It contains relatively large length-scale, high intensity turbulence. This relaxing outer shear layer merges with the redeveloping near wall flow (Zone V) and begins an exchange of energy which eventually would lead to the development of an equilibrium turbulent profile given a sufficiently long test section. In the current study, law-of-the-wall plots of the merged boundary layer (Zones V and VI) contained negative wake components characteristics of reattaching flows. The data correlated well with the profiles of Chandrsuda and Bradshaw (ref. 18) when $x_{\delta^*_{max}} - x_R$ was used to non-dimensionalize the axial distance downstream from reattachment where x_R was the axial location at reattachment. It is estimated that 3.75 bubble lengths downstream of reattachment, which exceeded the test section length, would have been required to eliminate the negative wake.

Zone VII - Invariant Outer Flowfield - The flow in this zone is inviscid but rotational. Velocity profiles in this region are congruent over the axial extent of the bubble when static pressure variations associated with stream- line curvature are accounted for. In effect, the outer 80 percent of the

158

incident boundary layer is convected unaltered over the blockage associated with the inner viscously dominated bubble recirculation region. The identification of this feature of the velocity profile development appears to have important implications for the numerical modeling of the flow.

REFERENCES

1. Simpson, R. L., J. H. Strickland and P. W. Barr: Features of a
   Separating Turbulent Boundary Layer in the Vicinity of Separation, J.
   Fluid Mechanics, vol. 79, pt. 3, 1977, pp. 553-594.

2. Simpson, R. L., Y.-T. Chew and B. G. Shivaprasad: The Structure of a
   Separating Turbulent Boundary Layer. Part 1. Mean Flow and Reynolds
   Stresses, J. Fluid Mechanics, vol. 113, 1981, pp. 23-51.

3. Simpson, R. L., Y.-T. Chew and B. G. Shivaprasad: The Structure of a
   Separating Turbulent Boundary Layer. Part 2. Higher-Order Turbulence
   Results, J. Fluid Mechanics, vol. 113, 1981, pp. 53-73.

4. Shiloh, K., B. G. Shivaprasad and R. L. Simpson: The Structure of a
   Separating Turbulent Boundary Layer. Part 3. Transverse Velocity
   Measurements, J. Fluid Mechanics, vol. 113, 1981, pp. 75-90.

5. Perry, A. E., and B. D. Fairlie: A Study of Turbulent Boundary-Layer
   Separation and Reattachment, J. Fluid Mechanics, vol. 69, pt. 4, 1975,
   pp. 657-672.

6. Cutler, A. D. and J. P. Johnston: Adverse Pressure Gradient and
   Separating Turbulent Boundary-Layer Flows: The Effect of Disequilibrium
   in Initial Conditions, Rept. MD-46, Thermo-Sciences Div., Mechanical
   Engineering Dept., Stanford University, October 1984.

7. Kline, S. J., J. H. Ferziger, and J. P. Johnston: Opinion - The Calcu-
   lation of Turbulent Shear Flows: Status and Ten-Year Outlook, Trans.
   ASME, J. Fluids Eng., vol. 100, 1978, pp. 3-5.

8. Simpson, R. L.: REVIEW - A Review of Some Phenomena in Turbulent Flow
   Separation, Trans. ASME, J. of Fluids Engineering, vol. 103, December
   1981, pp. 520-533.

9. Simpson, R. L.: Summary Report on the Colloquium on Flow Separation,
   Project SQUID Rept. SMU-3-PU, 1979.

10. Mueller, T. J.: On Separation, Reattachment, and Redevelopment of
    Turbulent Boundary Layers, Ph.D. Thesis, Dept. of Mechanical Engineering,
    University of Illinois, 1961.

REFERENCES (Cont'd)

11. Bradshaw, P. and F. Y. F. Wong: The Reattachment and Relaxation of a Turbulent Shear Layer, J. Fluid Mechanics, vol. 52, pt. 1, 1972, pp. 113-135.

12. Eaton, J. K. and J. P. Johnston: A Review of Research on Subsonic Turbulent Flow Reattachment, AIAA J., vol. 19, no. 9, September 1981, pp. 1093-1100.

13. Kim, J., S. J. Kline and J. P. Johnston: Investigation of a Reattaching Turbulent Shear Layer: Flow Over a Backward-Facing Step, Trans. ASME, J. of Fluids Eng., vol. 102, September 1980, pp. 302-308.

14. Driver, D. M. and H. L. Seegmiller: Features of a Reattaching Turbulent Shear Layer Subject to an Adverse Pressure Gradient, AIAA Paper 82-1029, June 1982.

15. Armaly, B. F., F. Durst and R. Schönung: Measurements and Predictions of Flow Downstream of a Two-Dimensional Single Backward-Facing Step, Report SFB80/ET/172, Sonderforschungsbereich, Univ. of Karlsruhe, 1980.

16. Pronchick, S. W. and S. J. Kline: An Experimental Investigation of the Structure of a Turbulent Reattaching Flow Behind a Backward-Facing Step, Rept. MD-42, Thermosciences Div., Mechanical Engineering Dept., Stanford University, June 1983.

17. Westphal, R. V., J. P. Johnston and J. K. Eaton: Experimental Study of Flow-Reattachment in a Single-Sided Sudden Expansion, NASA CR 3765, January 1984.

18. Chandrsuda, C. and P. Bradshaw: Turbulence Structure of Reattaching Mixing Layer, J. Fluid Mechanics, vol. 110, pp. 171-194, 1981.

19. Ota, T. and N. Kon: Heat Transfer in the Separated and Reattached Flow on a Blunt Flat Plate, Trans. ASME, J. of Heat Transfer, November 1974, pp. 459-462.

20. Ota, T.: An Axisymmetric Separated and Reattached Flow on a Longitudinal Blunt Circular Cylinder, J. of Applied Mechanics, June 1975, pp. 311-315.

21. Ota, T. and M. Itasaka: A Separated and Reattached Flow on a Blunt Flat Plate, Trans. ASME, J. of Fluids Engineering, March 1976, pp. 79-86.

22. Mueller, T. J. and J. M. Robertson: A Study of Mean Motion and Turbulence Downstream of a Roughness Element, Developments in Theoretical and Applied Mechanics, vol. 1, 1963, pp. 326-340.

23. Sandborn, V. A., and S. J. Kline: Flow Models in Boundary-Layer Stall Inception, Trans. ASME, J. of Basic Engineering, September 1961, pp. 317-327.

24. Simpson, R. L.: Some Features of Two Dimensional Separated Flows, AIAA Paper 85-0178, January, 1985.

25. Smith P. D., R. C. Hastings and B. R. Williams: Calculation and Measurement of Separated Turbulent Boundary Layers, RAE Technical Memorandum Aero 1955, October 1982, (Paper presented at Euromech 148 Two-Dimensional Separated Flows, Bochum, W. Germany, 13-15, October 1981).

26. Simpson, R. L.: A Model for the Backflow Mean Velocity Profiles, AIAA Journal, vol. 21, no. 1, January 1983, pp. 142-143.

27. Simpson, R. L., B. G. Shivaprasad and Y.-T. Chew: The Structure of a Separating Turbulent Boundary Layer. Part 4. Effects of Periodic Free-Stream Unsteadiness, J. Fluid Mechanics, vol. 127, 1983, pp. 219-261.

28. Blair, M. F., D. A. Bailey, and R. H. Schlinker: Development of a Large-Scale Wind Tunnel for the Simulation of Turbomachinery Airfoil Boundary Layers, Trans. ASME, J. of Engineering for Power, vol. 103, 1981, pp. 678-687.

29. Landgrebe, A. J.: An Analytical and Experimental Investigation of Helicopter Rotor Hover Performance and Wake Geometry Characteristics, USAAMRDL Technical Report 71-24, June 1971.

30. Coles, D. E.: The Turbulent Boundary Layer in a Compressible Fluid, Rand Corp. Rept. R-403-PR, September 1962.

31. Klebanoff, P. S.: Characteristics of Turbulence in a Boundary Layer with Zero Pressure Gradient, NACA Rep. No. 1247, 1955.

32. Eaton, J. K. and J. P. Johnston: Low-frequency Unsteadiness of a Reattaching Turbulent Shear Layer, in Turbulent Shear Flows 3; International Symposium, 3rd, Davis, CA., Sept. 9-11, 1981, Springer-Verlag, Berlin, 1982, pp. 162-170.

REFERENCES (Cont'd)

33. Cherry, N. J., R. Hillier, and M. E. M. P. Latour: Unsteady Measurements in a Separated and Reattaching Flow, J. Fluid Mechanics, vol. 144, 1984, pp. 13-46.

34. Mabey, D. G.: Pressure Fluctuations Caused by Separated Bubble Flows at Subsonic Speeds, RAE Technical Report 71160 ref. Aero 3204, August 1971.

35. Schlichting, H.: Boundary Layer Theory. Fourth ed. McGraw-Hill, Inc., 1962.

36. Paterson, R. W. and H. D. Weingold: Experimental Investigation of a Simulated Compressor Trailing-Edge Flowfield, AIAA J., vol. 23, no. 5, May 1985, pp. 768-775.

37. Patrick, W. P.: Error Analysis for Benchmark Fluid Dynamic Experiments, Part I: Error Analysis Methodology and the Quantification of Laser Velocimeter Error Sources, United Technologies Research Center Rept. R85-151772, 1985.

38. Kiock, R.: Evaluation of Boundary Layer Measurements in Two-Dimensional Compressible Subsonic Flow with a Pressure Gradient across the Boundary Layer, European Space Agency Technical Translation, ESA-TT-810, July 1983.

39. Kooi, J. W.: Influence of Free-Stream Mach Number on Transonic Shock-Wave Boundary-Layer Interaction, Rept. No. NLR MP 78013 U, National Aerospace Laboratory, Amsterdam, The Netherlands, May 23, 1978.

40. So, R. M. C., and G. L. Mellor: Experiment on Convex Curvature Effects in Turbulent Boundary Layers, J. Fluid Mechanics, vol. 60, no. 1, 1973, pp. 43-62.

41. Mayle, R. E., F. C. Kopper, M. F. Blair, and D. A. Bailey: Effect of Streamline Curvature on Film Cooling, ASME Paper No. 76-GT-96, March 1976.

42. Swafford, T. W.: Analytical Approximation of Two-Dimensional Separated Turbulent Boundary-Layer Velocity Profiles, AIAA J., vol. 21, no. 6, June 1983, pp. 923-926.

REFERENCES (Cont'd)

43. White, F. W.: Viscous Fluid Flow, McGraw-Hill Book Co., N. Y., 1974.

44. Alber, I. E., Bacon, J. W., Masson, B. S., and D. J. Collins: An Experimental Investigation of Turbulent Transonic Viscous-Inviscid Interactions, AIAA J., vol. 11, May 1973, pp. 620-627.

45. Coles, D.: The Law of the Wake in the Turbulent Boundary Layer, J. Fluid Mechanics, vol. 1, 1956. pp. 191-226.

46. Clauser, F. H.: The Turbulent Boundary Layer, in Advances in Applied Mechanics, vol. IV, Academic Press, N. Y., 1956, pp. 1-51.

47. Kline, S. J., M. V. Morkovin, G. Sovran, D. J. Cockrell, eds: Proceedings, Computation of Turbulent Boundary Layers - 1968 AFOSR-IFP-Stanford Conference, vol. 1, Thermosciences Div., Dept. of Mech. Eng., Stanford Univ., 1968.

48. Kline, S. J. and P. W. Runstadler: Some Preliminary Visual Studies of the Wall Layers of Turbulent Boundary Layers, Trans. ASME, Ser. E: J. Applied Mechanics, vol. 26, 1959, pp. 166-170.

49. Sandborn, V. A. and C. Y. Liu: On Turbulent Boundary-Layer Separation, J. Fluid Mechanics, vol. 32, pt. 2, 1968, pp. 293-304.

50. Kline, S. J., J. G. Bardina, and R. C. Strawn: Correlation of the Detachment of Two-Dimensional Turbulent Boundary Layers, AIAA J., vol. 21, no. 1, January 1983, pp. 68-73.

51. Sandborn, V. A.: An Equation for the Mean Velocity Distribution of Boundary Layers, NASA Memo 2-5-59E, 1959.

52. Kline, S. J., A. V. Lisin, and B. A. Waitman: Preliminary Experimental Investigation of Effect of Free-Stream Turbulence on Turbulent Boundary-Layer Growth, NASA TN D-368, March 1960.

53. Wagner, J.: Personal Communication, United Technologies Research Center, 1985.

54. Dyban, Y. P., E. Y. Epik, and T. T. Suprun: Characteristics of the Laminar Boundary Layer in the Presence of Elevated Free-Stream Turbulence, Fluid Mechanics - Soviet Research, vol. 5, no. 4, July-Aug. 1976, pp. 30-36.

REFERENCES (Cont'd)

55. Simpson, R. L., B. Chehroudi, and B. G. Shivaprasad: Pointwise and
    Scanning Laser Anemometer Measurements in Steady and Unsteady Separated
    Turbulent Boundary Layers, Proceedings of the International Symposium on
    Applications of Laser - Doppler Anemometry to Fluid Mechanics, Paper
    11.3, Lisbon, Portugal, July 5-7, 1982.

56. Abernathy, R. B. and J. W. Thompson: Handbook-Uncertainty in Gas Turbine
    Measurements. AEDC-TR-73-5, 1973.

57. Paterson, R. W.: Turbofan Forced Mixer-Nozzle Internal Flowfield, I - A
    Benchmark Experimental Study. NASA CR-3492, April 1982.

58. Goldstein, S.: A Note on the Measurement of Total Head and Static
    Pressure in a Turbulent Stream, Proc. Roy. Soc. (London), vol. 155, 1936,
    p. 570.

59. Bryer, D. W. and R. C. Pankhurst: Pressure-Probe Methods for Determining
    Wind Speed and Flow Direction. National Physical Laboratory,
    H. M. Stationery Office, London, 1971.

60. Jorgenson, F. E.: Directional Sensitivity of Wire and Fiber-Film Probes
    - An Experimental Study. DISA Information, no. 11, May 1971, pp. 31-37.

TABLE I TRAVERSE MEASUREMENT STATIONS ON TEST SURFACE

STATION NO.	x (in.)	x (cm)
ref	−61.50	−156.2
0	−9.50	−24.1
1	1.00	2.5
2	3.00	7.6
3	5.25	13.3
4	7.50	19.1
5	9.50	24.1
6	10.50	26.7
7	11.50	29.2
8	12.50	31.8
9	13.50	34.3
10	14.50	36.8
11	16.00	40.6
12	17.50	44.5
13	19.00	48.3
14	20.50	52.1
15	22.00	55.9
16	23.50	59.7
17	25.00	63.5
18	26.50	67.3
19	28.00	71.1
20	29.50	74.9
21	31.00	78.7
22	32.50	82.6
23	34.00	86.4
24	35.50	90.2
25	37.00	94.0
26	38.50	97.8
27	40.00	101.6
28	41.50	105.4
29	43.00	109.2
30	44.50	113.0
31	47.00	119.4
32	50.00	127.0
33	52.50	133.4
34	55.25	140.3
35	58.25	148.0

v (cm)	y/δ	U/U_{ref}	$\sqrt{\overline{u^2}}/U_{ref}$	γ_{P_U}	V/U_{ref}	$\sqrt{\overline{v^2}}/U_{ref}$	γ_{P_V}
STATION NO C6	x = 26.7 cm			z = 0 cm			
.635	.063	.496	.081	1	.004	.039	.535
1.27	.127	.567	.083	1	.013	.036	.625
1.91	.19	.629	.084	1	.022	.036	.718
2.54	.253	.686	.087	1	.03	.033	.815
3.18	.316	.75	.076	1	.04	.03	.904
3.81	.38	.8	.058	1	.058	.028	.99
5.08	.506	.872	.031	1	.072	.019	.99
6.35	.633	.901	.022	1	.082	.012	.99
7.62	.759	.919	.014	1	.096	.01	.99
8.89	.886	.931	.013	1	.1	.009	.99
10.16	1.01	.944	.012	1	.109	.01	.99
12.7	1.27	.979	.013	1	.122	.011	.99
15.24	1.52	1.014	.015	1	.134	.014	.99
17.78	1.77	1.026	.035	1			
20.32	2.03	.969	.046	1			

v (cm)	y/δ	U/U_{ref}	$\sqrt{\overline{u^2}}/U_{ref}$	γ_{P_U}	V/U_{ref}	$\sqrt{\overline{v^2}}/U_{ref}$	γ_{P_V}
STATION NO C8	x = 31.8 cm			z = 0 cm			
.064	.006	.254	.104	1			
.102	.009	.276	.102	1			
.152	.014	.294	.099	1			
.305	.028	.346	.111	1			
.508	.046	.376	.096	1			
.635	.058	.401	.103	1	.008	.044	.557
1.27	.116	.487	.09	1	.024	.044	.692
1.91	.174	.556	.09	1	.039	.042	.826
2.54	.231	.613	.091	1			
3.18	.289	.651	.085	1	.059	.036	.95:
3.81	.347	.705	.079	1	.069	.034	.978
5.08	.463	.783	.052	1	.091	.029	1
6.35	.579	.827	.038	1	.111	.025	1
7.62	.694	.861	.026	1	.128	.021	1
8.89	.81	.887	.018	1	.145	.019	1
10.16	.926	.904	.017	1	.167	.024	1
12.7	1.157	.94	.016	1	.192	.016	1
15.24	1.389	.975	.016	1			

v (cm)	y/δ	U/U_{ref}	$\sqrt{\overline{u^2}}/U_{ref}$	γ_{P_U}	V/U_{ref}	$\sqrt{\overline{v^2}}/U_{ref}$	γ_{P_V}
STATION NO C11	x = 40.6 cm			z = 0 cm			
.064	.005	.035	.128	.581			
.102	.007	.033	.124	.613			
.152	.011	.029	.137	.56			
.203	.015	.029	.138	.562			
.305	.022	.044	.146	.592			
.406	.03	.042	.148	.582			
.508	.037	.056	.155	.596			
.635	.047	.113	.167	.723	0	.055	.494
.762	.056	.116	.169	.738			
1.02	.075	.188	.167	.837			
1.27	.093	.234	.161	.91	.014	.059	.593
1.52	.112	.278	.158	.937			
1.91	.14	.288	.166	.943	.036	.063	.714
2.03	.15	.342	.151	.993			
2.54	.187	.392	.135	1	.052	.061	.788
3.05	.224	.434	.126	1			
3.18	.234	.447	.124	1	.076	.054	.912
3.56	.262	.495	.11	1			
3.81	.28	.502	.103	1	.096	.047	.982
4.06	.299	.512	.107	1			
4.57	.336	.555	.094	1			
5.08	.374	.578	.085	1	.135	.039	1
6.35	.467	.643	.077	1	.164	.032	1
7.62	.561	.709	.058	1	.194	.028	1
8.89	.654	.752	.042	1	.218	.022	1
10.16	.748	.783	.026	1	.241	.02	1
12.7	.935	.815	.016	1	.284	.015	1
15.24	1.12	.834	.014	1	.322	.013	1
17.78	1.31	.85	.014	1	.364	.014	1
20.32	1.5	.862	.014	1	.409		
22.86	1.68	.844	.028	1			

TABLE II MEAN VELOCITY, TURBULENCE, AND FLOW FRACTION
(INTERMITTENCY) DATA MEASURED WITH LASER VELOCIMETER

	STATION NO C13	x = 48.3 cm			z = 0 cm		
y (cm)	y/δ	U/U_{ref}	$\sqrt{\overline{u^2}}/U_{ref}$	γ_{P_U}	V/U_{ref}	$\sqrt{\overline{v^2}}/U_{ref}$	γ_{P_V}
.064	.004	-.039	.0796	.317			
.102	.006	-.064	.0755	.222			
.152	.009	-.07	.0828	.222			
.203	.011	-.059	.0862	.267			
.305	.017	-.06	.0887	.263			
.406	.023	-.07	.0913	.24			
.508	.029	-.054	.0955	.288			
.635	.036	-.075	.0938	.229	-.006	.046	.478
.762	.043	-.059	.0929	.297			
1.02	.057	-.045	.114	.328			
1.27	.072	-.026	.12	.408	-.005	.065	.508
1.52	.086	-.008	.116	.431			
1.91	.108	.008	.141	.48	-.003	.07	.51
2.03	.115	.011	.131	.473			
2.54	.144	.063	.177	.6	.011	.082	.586
3.05	.172	.107	.177	.682			
3.18	.18	.137	.195	.718	.027	.082	.627
3.56	.201	.172	.175	.816			
3.81	.216	.203	.203	.81	.043	.076	.711
4.06	.23	.229	.181	.888			
4.57	.259	.272	.171	.943			
5.08	.287	.331	.18	.949	.077	.075	.829
6.35	.359	.407	.162	1	.13	.067	.965
7.62	.431	.5	.124	1	.174	.057	1
8.89	.503	.566	.0941	1	.212	.048	1
10.16	.575	.619	.0798	1	.249	.035	1
12.7	.718	.684	.0508	1	.305	.023	1
15.24	.862	.727	.0246	1	.352	.019	1
17.78	1.01	.742	.018	1	.394	.018	1
20.32	1.15	.75	.0162	1	.435	.015	1
22.86	1.29	.759	.0153	1	.475	.016	1
25.4	1.44	.754			.532		

	STATION NO C14	x = 52.1 cm			z = 0 cm		
y (cm)	y/δ	U/U_{ref}	$\sqrt{\overline{u^2}}/U_{ref}$	γ_{P_U}	V/U_{ref}	$\sqrt{\overline{v^2}}/U_{ref}$	γ_{P_V}
.064	.003	-.036	.111	.308			
.102	.005	-.037	.121	.303			
.152	.008	-.047	.107	.269			
.203	.01	-.048	.106	.261			
.305	.016	-.056	.101	.239			
.508	.026	-.065	.097	.242			
.635	.033	-.089		.124	.001	.037	.537
.762	.039	-.082	.086	.177			
1.02	.052	-.079	.093	.211			
1.27	.066	-.082	.086	.208	.003	.052	.543
1.52	.079	-.059	.106	.281			
2.03	.105	-.033	.123	.362			
2.54	.131	-.022	.133	.416	.012	.065	.575
3.05	.157	.035	.15	.549			
3.56	.183	.07	.17	.615			
3.81	.197	.085	.184	.623	.023	.081	.607
4.06	.21	.102	.18	.666			
4.57	.236	.134	.184	.729			
5.08	.262	.19	.199	.8	.045	.078	.726
6.35	.328	.279	.191	.906	.082	.085	.825
7.62	.393	.36	.18	.981	.122	.08	.923
8.89	.459	.45	.148	1	.166	.07	.995
10.16	.524	.509	.116	1	.216	.059	1
12.7	.655	.594	.084	1	.29	.036	1
15.24	.786	.662	.054	1	.347	.026	1
17.78	.917	.691	.039	1	.394	.021	1
20.32	1.05	.695	.022	1	.433	.017	1
22.86	1.18	.694	.018	1	.484	.018	1
25.4	1.31	.694	.016	1			

TABLE II MEAN VELOCITY, TURBULENCE, AND FLOW FRACTION
(INTERMITTENCY) DATA MEASURED WITH LASER VELOCIMETER (CONT.)

STATION NO C15	x = 55.9 cm				z = 0 cm		
y (cm)	y/δ	U/U_{ref}	$\sqrt{u^2}/U_{ref}$	γ_{P_U}	V/U_{ref}	$\sqrt{v^2}/U_{ref}$	γ_{P_V}
.064	.003	-.049	.063	.249			
.102	.005	-.071	.063	.143			
.152	.007	-.079	.073	.157			
.203	.009	-.088	.069	.122			
.305	.014	-.095	.064	.086			
.508	.023	-.097	.069	.093			
.635	.029	-.098	.072	.083	0	.03	.502
.762	.034	-.106	.066	.071			
1.02	.046	-.099	.072	.116			
1.27	.057	-.111	.076	.109	.003	.044	.53
1.52	.069	-.1	.086	.149			
1.91	.086	-.094	.09	.173	.006	.05	.558
2.03	.091	-.091	.091	.179			
2.54	.114	-.072	.103	.257	.007	.053	.571
3.05	.137	-.055	.114	.29			
3.18	.143	-.055	.118	.297	.017	.065	.607
3.56	.16	-.025	.128	.375			
3.81	.171	-.012	.127	.44	.023	.07	.641
4.06	.183	.005	.144	.436			
4.57	.20	.019	.142	.492			
5.08	.229	.065	.173	.569	.037	.077	.688
6.35	.286	.164	.194	.769	.059	.081	.766
7.62	.343	.216	.209	.811	.085	.079	.849
8.89	.4	.32	.196	.931	.115	.083	.899
10.16	.457	.372	.17	.994	.149	.086	.944
12.7	.571	.486	.136	1	.229	.071	1
15.24	.686	.569	.085	1	.305	.046	1
17.78	.8	.615	.053	1	.361	.028	1
20.32	.914	.623	.036	1	.404	.022	1
22.86	1.03	.608	.024	1	.446	.019	1

STATION NO C16	x = 59.7 cm				z = 0 cm		
y (cm)	y/δ	U/U_{ref}	$\sqrt{u^2}/U_{ref}$	γ_{P_U}	V/U_{ref}	$\sqrt{v^2}/U_{ref}$	γ_{P_V}
.064	.003	-.066	.055	.122			
.102	.004	-.079	.059	.116			
.152	.006	-.097	.059	.076			
.203	.008	-.097	.063	.07			
.305	.012	-.107	.06	.045			
.508	.02	-.11	.064	.041			
.762	.031	-.117	.061	.031			
1.02	.041	-.119	.062	.036			
1.52	.061	-.126	.059	.019			
1.91	.077	-.104	.082	.139	.012	.045	.612
2.03	.082	-.117	.073	.071			
2.54	.102	-.093	.089	.155	.016	.053	.606
3.05	.122	-.088	.084	.18			
3.18	.128	-.057	.1	.246	.022	.056	.661
3.56	.143	-.091	.084	.14			
3.81	.153	-.045	.112	.292	.029	.06	.647
4.06	.163	-.051	.107	.305			
4.57	.184	-.049	.106	.305			
5.08	.204	.013	.138	.469	.048	.077	.726
6.35	.255	.081	.168	.642	.05	.077	.74
7.62	.306	.143	.177	.752	.068	.084	.761
8.89	.357	.192	.19	.802	.098	.087	.86
10.16	.408	.28	.17	.934	.121	.09	.898
12.7	.51	.359	.171	.977	.17	.083	.978
15.24	.612	.445	.141	1	.236	.076	1
17.78	.714	.538	.105	1	.3	.048	1
20.32	.816	.569	.067	1	.345	.035	1
22.86	.918	.558	.049	1	.374	.034	1
25.4	1.02	.525	.036	1			

TABLE II   MEAN VELOCITY, TURBULENCE, AND FLOW FRACTION
(INTERMITTENCY) DATA MEASURED WITH LASER VELOCIMETER (CONT.)

STATION NO C18	x = 67.3 cm				z = 0 cm		
y (cm)	y/δ	U/U_{ref}	$\sqrt{u^2}/U_{ref}$	γ_{P_U}	V/U_{ref}	$\sqrt{v^2}/U_{ref}$	γ_{P_V}
.064	.002	-.125	.058	.008			
.102	.003	-.132	.061	.002			
.152	.005	-.139	.063	0			
.203	.007	-.144	.061	0			
.305	.01	-.146	.059	0			
.508	.016	-.153	.062	0			
.635	.02	-.151	.047	0	-.005	.031	.538
.762	.024	-.151	.058	0			
1.02	.033	-.151	.058	0			
1.27	.041	-.154	.051	0	.008	.036	.571
1.52	.049	-.14	.063	.004			
1.91	.061	-.146	.057	0	.008	.04	.573
2.03	.065	-.144	.059	0			
2.54	.082	-.135	.059	.007	.01	.045	.586
3.05	.098	-.119	.063	.039			
3.18	.102	-.125	.066	.027	.014	.053	.596
3.56	.114	-.114	.065	.049			
3.81	.122	-.109	.051	.08	.012	.061	.579
4.06	.131	-.097	.072	.113			
4.57	.147	-.089	.071	.11			
5.08	.163	-.078	.059	.156	.022	.068	.607
6.35	.204	-.056	.069	.263	.032	.077	.637
7.62	.245	-.017	.078	.408	.036	.09	.676
8.89	.285	.014	.097	.494	.051	.099	.772
10.16	.326	.07	.118	.599	.065	.112	.712
12.7	.408	.189	.139	.823	.094	.126	.771
15.24	.489	.277	.153	.958	.132	.123	.866
17.78	.571	.366	.146	.964	.155	.113	.916
20.32	.653	.439	.131	1	.164	.083	.968
22.86	.734	.525	.09	1	.217	.059	1
25.4	.816	.544	.046	1	.203	.023	1
27.94	.897	.527	.032	1	.199	.019	1
30.48	.979	.502	.026	1	.2	.017	
33.02	1.06	.45	.019	1	.181	.014	

STATION NO C20	x = 74.9 cm				z = 0 cm		
y (cm)	y/δ	U/U_{ref}	$\sqrt{u^2}/U_{ref}$	γ_{P_U}	V/U_{ref}	$\sqrt{v^2}/U_{ref}$	γ_{P_V}
.064	.002	-.127	.06	.004			
.102	.003	-.152	.066	0			
.152	.005	-.169	.067	0			
.203	.006	-.171	.066	0			
.305	.009	-.182	.065	0			
.508	.015	-.188	.065	0			
.635	.019	-.192	.065	0	.001	.032	.521
.762	.023	-.184	.066	0			
1.02	.03	-.175	.067	0			
1.27	.038	-.177	.063	0	.002	.044	.532
1.52	.045	-.165	.063	0			
1.91	.056	-.164	.064	0	-.003	.05	.489
2.03	.06	-.154	.063	0			
2.54	.075	-.146	.063	0	-.001	.056	.509
3.05	.09	-.125	.067	.025			
3.18	.094	-.133	.069	.029	0	.055	.52
3.81	.113	-.119	.067	.049	.003	.057	.535
4.06	.12	-.113	.069	.057			
4.57	.135	-.106	.071	.092			
5.08	.15	-.106	.067	.072	.007	.058	.559
6.35	.188	-.064	.074	.21	.006	.061	.56
7.62	.226	-.054	.08	.257	.011	.063	.578
8.89	.263	-.021	.088	.397	.012	.072	.576
10.16	.301	.015	.101	.547	.012	.072	.582
12.7	.376	.101	.132	.747	.001	.077	.502
15.24	.451	.202	.148	.925	.009	.089	.558
17.78	.527	.286	.154	.987	.003	.096	.53
20.32	.602	.386	.139	1	.006	.093	.526
22.86	.677	.465	.116	1	.013	.09	.59
25.4	.752	.523	.082	1	.027	.068	.704
27.94	.828	.545	.047	1	.034	.04	.801
30.48	.903	.519	.028	1	.028		
33.02	.978	.49	.032	1	.032		

TABLE II MEAN VELOCITY, TURBULENCE, AND FLOW FRACTION
(INTERMITTENCY) DATA MEASURED WITH LASER VELOCIMETER (CONT.)

STATION NO. C22	x = 82.6 cm				z = 0 cm		
y (cm)	y/δ	U/U_{ref}	$\sqrt{\overline{u^2}}/U_{ref}$	γ_{P_U}	V/U_{ref}	$\sqrt{\overline{v^2}}/U_{ref}$	γ_{P_V}
.064	.002	-.19	.072	0			
.102	.003	-.188	.073	0			
.152	.005	-.192	.077	0			
.203	.006	-.199	.068	0			
.305	.009	-.199	.07	0			
.508	.016	-.192	.069	0			
.635	.02	-.202	.071	0	-.002	.04	.496
.762	.024	-.191	.071	0			
1.02	.031	-.18	.6?	0			
1.27	.039	-.188	.07	0	-.005	.051	.491
1.52	.047	-.161	.073	.005			
1.91	.059	-.158	.073	.004	-.014	.061	.436
2.03	.063	-.147	.071	.006			
2.54	.079	-.131	.071	.037	-.004	.066	.468
3.18	.098	-.125	.072	.051	-.019	.068	.39
3.81	.118	-.123	.076	.068	-.017	.073	.404
4.06	.126	-.103	.076	.106			
4.57	.142	-.093	.079	.147			
5.08	.157	-.098	.079	.121	-.022	.071	.379
6.35	.197	-.062	.082	.228	-.028	.077	.383
7.62	.236	-.031	.083	.374	-.034	.083	.35
8.89	.275	.0034	.086	.519	-.037	.088	.356
10.16	.314	.037	.088	.644	-.046	.089	.335
12.7	.393	.132	.1	.895	-.079	.105	.249
15.24	.472	.23	.108	.995	-.114	.108	.153
17.78	.55	.308	.114	1	-.132	.108	.107
20.32	.629	.399	.109	1	-.151	.108	.088
22.86	.708	.472	.097	1	-.157	.102	.044
25.4	.786	.523	.066	1	-.132	.072	.014
27.94	.865	.545	.039	1	-.133	.051	0
30.48	.943	.524	.027	1	-.087		
33.02	1.02	.503			-.074		

STATION NO. C24	x = 90.2 cm				z = 0 cm		
y (cm)	y/δ	U/U_{ref}	$\sqrt{\overline{u^2}}/U_{ref}$	γ_{P_U}	V/U_{ref}	$\sqrt{\overline{v^2}}/U_{ref}$	γ_{P_V}
.064	.002	-.178	.082	.007			
.102	.003	-.18	.083	.012			
.152	.005	-.186	.079	0			
.203	.007	-.189	.077	0			
.305	.01	-.182	.084	.007			
.508	.017	-.167	.079	.005			
.635	.022	-.173	.076	.004	-.014	.054	.418
.762	.026	-.163	.075	.006			
1.02	.035	-.152	.074	.019			
1.27	.043	-.148	.072	.009	-.018	.068	.416
1.52	.052	-.123	.073	.04			
1.91	.065	-.13	.077	.057	-.029	.075	.366
2.03	.069	-.099	.081	.14			
2.54	.087	-.106	.078	.086	-.039	.081	.334
3.05	.104	-.073	.085	.202			
3.18	.108	-.075	.076	.171	-.059	.085	.255
3.56	.121	-.066	.084	.241			
3.81	.13	-.067	.085	.242	-.066	.094	.239
4.06	.139	-.042	.087	.333			
4.57	.156	-.038	.087	.338			
5.08	.173	-.03	.084	.367	-.074	.095	.224
6.35	.217	.0012	.087	.5	-.088	.104	.207
7.62	.26	.034	.087	.657	-.081	.116	.271
8.89	.303	.095	.083	.861	-.12	.107	.136
10.16	.347	.126	.088	.91	-.142	.111	.1
12.7	.433	.217	.087	1	-.185	.11	.036
15.24	.52	.312	.082	1	-.225	.105	.001
17.78	.607	.427	.08	1	-.243	.085	0
20.32	.639	.523	.075	1	-.249	.067	0
22.86	.78	.57	.054	1	-.262	.042	0
25.4	.867	.538	.039	1	-.273	.049	0
27.94	.953	.52	.029	1	-.254	.032	0
30.48	1.04	.496	.022	1	-.239	.015	0

TABLE II   MEAN VELOCITY, TURBULENCE, AND FLOW FRACTION
(INTERMITTENCY) DATA MEASURED WITH LASER VELOCIMETER (CONT.)

	STATION NO C26	x = 97.8 cm			z = 0 cm		
y (cm)	y/δ	U/U_{ref}	$\sqrt{\overline{u^2}}/U_{ref}$	γ_{P_U}	V/U_{ref}	$\sqrt{\overline{v^2}}/U_{ref}$	γ_{P_V}
.064	.003	-.089	.086	.17			
.102	.005	-.096	.086	.144			
.152	.008	-.111	.084	.092			
.203	.011	-.106	.088	.12			
.305	.016	-.095	.089	.16			
.508	.027	-.088	.088	.174			
.635	.034	-.078	.077	.181	-.03	.063	.343
.762	.04	-.071	.085	.209			
1.02	.054	-.053	.086	.271			
1.27	.067	-.032	.087	.375	-.048	.079	.275
1.52	.081	-.019	.082	.434			
1.91	.101	-.008	.089	.459	-.082	.093	.22
2.03	.108	-.002	.091	.48			
2.54	.134	.022	.09	.583	-.098	.103	.193
3.05	.161	.041	.09	.647			
3.56	.188	.053	.098	.678			
4.06	.215	.07	.1	.734			
4.57	.242	.097	.097	.833	-.144	.113	
6.35	.336	.134	.094	.915	-.183	.117	.06
7.62	.403	.171	.096	.946	-.202	.112	.035
8.89	.47	.23	.086	1	-.225	.111	.019
10.16	.538	.285	.08	1	-.248	.105	0
12.7	.672	.371	.064	1	-.292	.089	0
15.24	.806	.443	.059	1	-.316	.074	0
17.78	.941	.505	.051	1	-.333	.059	0
20.32	1.08	.546	.042	1	-.346	.043	0
22.86	1.21	.555	.035	1	-.366	.03	0
25.4	1.34	.551	.027	1	-.371	.023	
27.94	1.48	.53	.022	1			

	STATION NO C28	x = 105.4 cm			z = 0 cm		
y (cm)	y/δ	U/U_{ref}	$\sqrt{\overline{u^2}}/U_{ref}$	γ_{P_U}	V/U_{ref}	$\sqrt{\overline{v^2}}/U_{ref}$	γ_{P_V}
.064	.003	.067	.097	.768			
.102	.005	.052	.092	.714			
.152	.008	.072	.091	.787			
.203	.01	.089	.096	.824			
.305	.015	.082	.09	.807			
.508	.025	.096	.087	.87			
.635	.032	.111	.095	.865	-.054	.071	.234
.762	.038	.127	.093	.918			
1.02	.051	.136	.091	.931			
1.27	.064	.15	.099	.928	-.086	.081	.152
1.52	.076	.161	.093	.963			
1.91	.095	.16	.1	.943	-.112	.1	.139
2.03	.102	.168	.096	.964			
2.54	.127	.178	.1	.973	-.133	.108	.121
3.05	.153	.219	.098	1			
3.18	.159	.208	.098	.992	-.153	.111	.102
3.56	.178	.245	.097	1			
3.81	.191	.232	.096	1	-.172	.117	.085
4.06	.204	.265	.087	1			
4.57	.229	.271	.099	1			
5.08	.254	.277	.091	1	-.206	.116	.043
6.35	.318	.319	.086	1	-.235	.11	.016
7.62	.382	.37	.073	1	-.244	.109	.006
8.89	.445	.405	.064	1	-.279	.09	0
10.16	.509	.445	.056	1	-.295	.088	0
12.7	.636	.516	.046	1	-.339	.064	0
15.24	.763	.568	.039	1	-.367	.041	0
17.78	.891	.594	.032	1	-.398	.03	0
20.32	1.02	.593	.028	1	-.409	.021	0
22.352	1.12	.592	.025	1			

TABLE II   MEAN VELOCITY, TURBULENCE, AND FLOW FRACTION
(INTERMITTENCY) DATA MEASURED WITH LASER VELOCIMETER (CONT.)

173

	STATION NO C30	x = 113.0 cm			z = 0 cm		
y (cm)	y/δ	U/U$_{ref}$	$\sqrt{u^2}$/U$_{ref}$	γ_{P_U}	V/U$_{ref}$	$\sqrt{v^2}$/U$_{ref}$	γ_{P_V}
.064	.004	.261	.093	1			
.102	.006	.281	.099	1			
.152	.009	.294	.095	1			
.203	.012	.31	.095	1			
.305	.019	.32	.093	1			
.508	.031	.333	.092	1			
.635	.039	.347	.087	1	-.059	.065	.202
1.02	.062	.352	.092	1			
1.27	.077	.367	.084	1	-.084	.087	.181
1.52	.093	.384	.084	1			
1.91	.116	.382	.088	1	-.113	.099	.146
2.54	.155	.401	.089	1	-.137	.104	.11
3.05	.185	.41	.085	1			
3.18	.193	.414	.086	1	-.158	.107	.082
3.81	.232	.416	.087	1	-.175	.11	.067
4.06	.247	.441	.083	1			
4.57	.278	.467	.079	1			
5.08	.309	.477	.076	1	-.198	.107	.039
6.35	.386	.494	.075	1	-.225	.101	.011
7.62	.464	.558	.061	1	-.244	.096	0
8.89	.541	.583	.06	1	-.268	.079	0
10.16	.618	.639	.042	1	-.3	.067	0
12.7	.773	.699	.028	1	-.371	.036	0
15.24	.927	.717	.022	1	-.411	.024	0
17.78	1.08	.747	.024	1	-.411		

	STATION NO C31	x = 119.4 cm			z = 0 cm		
y (cm)	y/δ	U/U$_{ref}$	$\sqrt{u^2}$/U$_{ref}$	γ_{P_U}	V/U$_{ref}$	$\sqrt{v^2}$/U$_{ref}$	γ_{P_V}
.064	.005	.421	.093	1			
.102	.008	.451	.09	1			
.152	.012	.455	.083	1			
.203	.016	.468	.085	1			
.305	.024	.477	.083	1			
.635	.051	.49	.077	1	-.056	.062	.194
.762	.061	.509	.08	1			
1.02	.081	.512	.08	1			
1.27	.101	.515	.083	1	-.096	.076	.129
1.91	.152	.521	.08	1	-.112	.091	.133
2.03	.162			1			
2.54	.202	.53	.083	1	-.12	.104	.139
3.05	.243			1			
3.18	.253	.539	.092	1	-.145	.103	.094
3.56	.283			1			
3.81	.304	.559	.083	1	-.154	.11	.104
4.06	.324	.596	.083	1			
4.57	.364	.621	.073	1			
6.35	.506	.641	.087	1	-.205	.087	.008
7.62	.607	.713	.075	1	-.212	.076	0
8.89	.709	.786	.031	1	-.255	.054	0
10.16	.81	.822	.025	1	-.274	.042	0
12.7	1.01	.891	.023	1	-.288		
13.97	1.11	.926	.023	1			

TABLE II MEAN VELOCITY, TURBULENCE, AND FLOW FRACTION
(INTERMITTENCY) DATA MEASURED WITH LASER VELOCIMETER (CONT.)

STATION NO __C34__   x = __140.3__ cm   z = __0__ cm

y (cm)	y/δ	U/U_{ref}	$\sqrt{\overline{u^2}}/U_{ref}$	γ_{P_U}	V/U_{ref}	$\sqrt{\overline{v^2}}/U_{ref}$	γ_{P_V}
.127	.01	.579	.1				
.203	.016	.614	.103	1			
.305	.024	.643	.102	1			
.406	.032	.659	.1				
.508	.04	.667	.097	1			
.635	.05	.675	.095	1	-.028	.051	.268
.762	.06	.68	.092	1			
1.02	.08	.683	.092	1			
1.27	.1	.689	.089	1	-.035	.059	.277
1.52	.12	.689	.089	1			
1.91	.15			1	-.048	.069	.28
2.03	.16	.691	.089		-.049		
2.54	.2	.692	.093	1	-.053	.081	.253
3.05	.24	.692	.097		-.061		
3.18	.25			1		.081	.231
3.56	.28	.699	.103		-.06		
3.81	.3			1	-.058	.082	.234
4.06	.32	.696	.106		-.058		
4.57	.36	.698	.109		-.058		
5.08	.4	.708	.11	1	-.058	.079	.217
6.35	.5	.722	.107	1	-.057	.064	.172
7.62	.6	.752	.111	1	-.049	.031	.073
8.89	.7	.781	.098	1	-.029	.031	.163
10.16	.8	.809	.085	1	-.02	.027	.217
11.43	.9			1	-.012	.024	.288
12.7	1	.841	.047	1			
13.97	1.1	.847	.042				

STATION NO __E6__   x = __26.7__ cm   z = __-15.24__ cm

y (cm)	y/δ	U/U_{ref}	$\sqrt{\overline{u^2}}/U_{ref}$	γ_{P_U}	V/U_{ref}	$\sqrt{\overline{v^2}}/U_{ref}$	γ_{P_V}
.635	.063	.476	.082	1	.003	.036	.517
1.27	.127	.558	.078	1	.014	.038	.631
1.91	.19	.611	.08	1	.02	.036	.697
2.54	.253	.654	.085	1	.041	.036	.869
3.18	.316	.701	.083	1	.049	.033	.931
3.81	.38	.758	.069	1	.059	.03	.985
5.08	.506	.83	.05	1	.076	.025	1
6.35	.633	.896	.024	1	.093	.021	1
7.62	.759	.92	.014	1	.103	.017	1
8.89	.886	.936	.011	1	.113	.013	1
10.16	1.01	.95	.012	1	.121	.012	1
12.7	1.27	.981	.013	1	.134	.013	1
15.24	1.52	1.011	.022	1	.129	.013	1
17.78	1.77	1.013	.038	1	.145	.015	1
20.32	2.03	.973	.052	1			

TABLE II MEAN VELOCITY, TURBULENCE, AND FLOW FRACTION
(INTERMITTENCY) DATA MEASURED WITH LASER VELOCIMETER (CONT.)

STATION NO E11		x = 40.6 cm			z = -15.24 cm		
y (cm)	y/δ	U/U_{ref}	$\sqrt{u^2}/U_{ref}$	γ_{P_U}	V/U_{ref}	$\sqrt{v^2}/U_{ref}$	γ_{P_V}
.064	.005	.053	.103	.688			
.102	.008	.058	.11	.694			
.152	.011	.074	.122	.713			
.203	.015	.077	.125	.699			
.305	.023	.091	.119	.761			
.406	.030	.117	.137	.777			
.508	.038	.119	.137	.801			
.635	.048	.151	.15	.813	.029	.086	.604
.762	.057	.172	.157	.836			
1.02	.076	.236	.148	.925			
1.27	.095	.296	.139	.989	.031	.073	.656
1.52	.114	.304	.137	.992			
1.91	.143	.34	.135	1	.064	.081	.797
2.03	.152	.39	.123	1			
2.54	.191	.442	.103	1	.07	.061	.875
3.05	.229	.445	.111	1			
3.18	.238	.442	.104	1	.089	.053	.958
3.56	.267	.499	.094	1			
3.81	.286	.493	.097	1	.105	.048	.996
4.06	.305	.517	.09	1			
4.57	.343	.547	.086	1			
5.08	.381	.579	.087	1	.14	.04	1
6.35	.476	.638	.075	1	.168	.035	1
7.62	.572	.689	.063	1	.192	.032	1
8.89	.667	.736	.048	1	.215	.029	1
10.16	.762	.771	.035	1	.234	.024	1
12.7	.953	.813	.02	1	.276	.019	1
15.24	1.14	.832	.018	1	.313	.017	1
17.78	1.33	.847	.013	1	.353	.017	1
20.32	1.52	.857	.012	1	.377	.015	1
22.86	1.71	.858	.019	1			

STATION NO E18		x = 67.3 cm			z = -15.24 cm		
y (cm)	y/δ	U/U_{ref}	$\sqrt{u^2}/U_{ref}$	γ_{P_U}	V/U_{ref}	$\sqrt{v^2}/U_{ref}$	γ_{P_V}
.635	.022	-.142	.061	0	.007	.028	.606
1.27	.044	-.135	.063	.014	.014	.039	.651
1.91	.065	-.128	.068	.031	.014	.042	.446
2.54	.087	-.119	.07	.055	.012	.042	.61
3.18	.109	-.094	.069	.096	.019	.053	.636
3.81	.131	-.089	.07	.121	.017	.058	.616
5.08	.174	-.049	.094	.306	.02	.06	.636
6.35	.218	-.032	.097	.371	.03	.064	.664
7.62	.262	.011	.123	.461	.033	.067	.671
8.89	.305	.077	.141	.65	.042	.073	.696
10.16	.349	.138	.173	.749	.048	.073	.715
12.7	.436	.23	.176	.921	.086	.075	.817
15.24	.523	.358	.149	1	.111	.074	.911
17.78	.61	.434	.107	1	.16	.067	.983
20.32	.697	.5	.081	1	.184	.048	1
22.86	.785	.545	.056	1	.21	.032	1
25.4	.872	.548	.028	1	.211	.024	1
27.94	.959	.524	.023	1	.201	.018	1
30.48	1.05	.488	.02	1	.185	.015	1

STATION NO E31		x = 119.4 cm			z = -15.24 cm		
y (cm)	y/δ	U/U_{ref}	$\sqrt{u^2}/U_{ref}$	γ_{P_U}	V/U_{ref}	$\sqrt{v^2}/U_{ref}$	γ_{P_V}
.635	.051	.486	.07	1	-.046	.06	.25
1.27	.101	.517	.071	1	-.082	.075	.15
1.91	.152	.533	.078	1	-.118	.078	.084
2.54	.202	.561	.078	1	-.142	.084	.058
3.18	.253	.581	.075	1	-.163	.079	.015
3.81	.304	.609	.072	1	-.178	.081	.01
5.08	.405	.662	.064	1	-.205	.07	0
6.35	.506	.714	.051	1	-.224	.063	0
7.62	.607	.764	.035	1	-.235	.053	0
8.89	.709	.803	.027	1	-.247	.043	0
10.16	.81	.838	.024	1	-.26	.036	0
11.43	.911	.858					
12.7	1.01	.899					
13.97	1.11	.93					
15.24	1.22	.956					

TABLE II MEAN VELOCITY, TURBULENCE, AND FLOW FRACTION (INTERMITTENCY) DATA MEASURED WITH LASER VELOCIMETER (CONT.)

176

	STATION NO W6	x = 26.7 cm			z = 15.24 cm		
y (cm)	y/δ	U/U_{ref}	$\sqrt{\overline{u^2}}/U_{ref}$	γ_{P_U}	V/U_{ref}	$\sqrt{\overline{v^2}}/U_{ref}$	γ_{P_V}
.635	.063	.462	.084	1	.008	.038	.578
1.27	.127	.545	.075	1	.019	.038	.671
1.91	.19	.603	.076	1	.028	.037	.755
2.54	.253	.656	.079	1	.036	.036	.834
3.18	.316	.716	.074	1	.046	.034	.914
3.81	.38	.743	.073	1	.054	.029	.975
5.08	.506	.829	.047	1	.083	.025	1
6.35	.633	.872	.034	1	.096	.019	1
7.62	.759	.892	.025	1	.109	.016	1
8.89	.886	.929	.015	1	.121	.014	1
10.16	1.01	.953	.011	1	.126	.014	1
12.7	1.27	.977	.014	1	.122	.012	1
15.24	1.52	1.018	.015	1	.132	.014	1
17.78	1.77	1.023	.036	1			
20.32	2.03	.967	.052	1			

	STATION NO W11	x = 40.6 cm			z = 15.24 cm		
y (cm)	y/δ	U/U_{ref}	$\sqrt{\overline{u^2}}/U_{ref}$	γ_{P_U}	V/U_{ref}	$\sqrt{\overline{v^2}}/U_{ref}$	γ_{P_V}
.064	.004	.012	.101	.532			
.102	.007	.005	.107	.515			
.152	.011	-.009	.109	.473			
.203	.151	.031	.127	.563			
.305	.023	-.034	.127	.433			
.406	.03	-.011	.119	.477			
.508	.038	.017	.129	.544			
.635	.047	.064	.14	.652	.095	.13	.757
.762	.056	.089	.14	.724			
1.02	.075	.116	.153	.762			
1.27	.094	.161	.162	.824	.083	.113	.77
1.52	.113	.227	.155	.907			
1.91	.141	.255	.16	.931	.107	.109	.865
2.03	.151	.269	.163	.937			
2.54	.188	.336	.14	1	.075	.07	.868
3.05	.226	.349	.148	1			
3.18	.235	.403	.123	1	.095	.061	.945
3.56	.264			1			
3.81	.282	.458	.103	1	.114	.055	.989
4.06	.301			1			
4.57	.339			1			
5.08	.377	.592	.0827	1	.152	.047	1
6.35	.471	.656	.0704	1	.179	.037	1
7.62	.565	.701	.059	1	.208	.033	1
8.89	.659	.741	.046	1	.232	.027	1
10.16	.753			1			1
12.7	.942	.791	.0254	1	.295	.019	1
15.24	1.13	.821	.0239	1	.333	.017	1
17.78	1.32	.84	.0161	1			
20.32	1.51	.85	.0169	1			
22.86	1.7	.813	.0366	1			

TABLE II MEAN VELOCITY, TURBULENCE, AND FLOW FRACTION
(INTERMITTENCY) DATA MEASURED WITH LASER VELOCIMETER (CONT.)

177

STATION NO W18		x = 67.3 cm			z = 15.24 cm		
y (cm)	y/δ	U/U_{ref}	$\sqrt{u^2}/U_{ref}$	γ_{P_U}	V/U_{ref}	$\sqrt{v^2}/U_{ref}$	γ_{P_V}
.635	.019	-.151	.059	0	.004	.03	.568
1.27	.039	-.152	.056	0	.005	.034	.569
1.91	.058	-.14	.055	0	.008	.038	.58
2.54	.078	-.133	.056	0	.009	.04	.608
3.18	.097	-.111	.06	.033	.008	.047	.56
3.81	.116	-.105	.065	.058	.015	.049	.633
5.08	.155	-.076	.068	.139	.021	.05	.677
6.35	.194	-.053	.081	.263	.025	.056	.688
7.62	.233	-.016	.101	.401	.034	.059	.713
8.89	.272	.023	.117	.529	.044	.067	.727
10.16	.311	.062	.145	.603	.047	.074	.743
12.7	.388	.162	.162	.819	.078	.081	.81
15.24	.466	.283	.175	.939	.116	.083	.896
17.78	.543	.384	.147	1	.137	.075	.958
20.32	.621	.475	.105	1	.167	.072	.989
22.86	.699	.512	.08	1	.197	.051	1
25.4	.776	.529	.049	1	.2	.032	1
27.94	.854	.515	.033	1			
30.48	.932						

STATION NO W31		x = 119.4 cm			z = 15.24 cm		
y (cm)	y/δ	U/U_{ref}	$\sqrt{u^2}/U_{ref}$	γ_{P_U}	V/U_{ref}	$\sqrt{v^2}/U_{ref}$	γ_{P_V}
.635	.049	.514		1	.049	.059	.226
1.27	.097	.54		1	.086	.075	.153
1.91	.146	.557		1	.128	.084	.078
2.54	.195	.566		1	.158	.093	.059
3.18	.243	.585		1	.182	.095	.045
3.81	.292	.602		1	.196	.091	.02
5.08	.389	.634	.076	1	.228	.083	0
6.35	.486	.69	.062	1	.248	.069	0
7.62	.584	.743	.039	1	.269	.058	0
8.89	.681	.784	.03	1	.281	.046	0
10.16	.778	.818	.027	1	.294	.036	0
12.7	.973	.892	.023	1			
13.97	1.07	.925	.022	1			

TABLE II MEAN VELOCITY, TURBULENCE, AND FLOW FRACTION
(INTERMITTENCY) DATA MEASURED WITH LASER VELOCIMETER (CONCLUDED)

178

STATION NO. C6 $x = 26.7$ cm $z = 0$ cm

y.cm	y/δ	U/U_{ref}	γ_{P_U}	$\sqrt{u^2}/U_{ref}$	V/U_{ref}	γ_{P_V}	$\sqrt{v^2}/U_{ref}$	$\overline{uv}/U^2_{ref}$ ×10²	$S\overline{uv}/U^2_{ref}$ ×10²	$\overline{\alpha\beta}/U^2_{ref}$ ×10²	$S\overline{\alpha\beta}/U^2_{ref}$ ×10²
0.635	0.063	0.496	1.000	0.081	0.004	0.535	0.039	-0.0990	0.0145	-0.1031	0.0145
1.270	0.127	0.567	1.000	0.083	0.013	0.625	0.036	-0.1050	0.0125	-0.1175	0.0126
1.905	0.190	0.629	1.000	0.084	0.022	0.718	0.036	-0.0680	0.0099	-0.0876	0.0101
2.540	0.253	0.686	1.000	0.087	0.030	0.815	0.033	-0.0720	0.0008	-0.1017	0.0030
3.175	0.316	0.750	1.000	0.076	0.040	0.904	0.030	-0.0390	0.0051	-0.0390	0.0051
3.810	0.380	0.800	1.000	0.058	0.058	0.990	0.028	-0.0250	0.0040	-0.0432	0.0044
5.080	0.506	0.872	1.000	0.031	0.072	0.990	0.019	-0.0070	0.0036	-0.0118	0.0036
6.350	0.633	0.901	1.000	0.022	0.082	0.990	0.012	-0.0170	0.0013	-0.0198	0.0014
7.620	0.759	0.919	1.000	0.014	0.096	0.990	0.010	-0.0030	0.0009	-0.0039	0.0009
8.890	0.886	0.931	1.000	0.013	0.100	0.990	0.009	-0.0060	0.0010	-0.0068	0.0010
10.160	1.013	0.944	1.000	0.012	0.109	0.990	0.010	-0.0010	0.0012	-0.0015	0.0012
12.700	1.266	0.979	1.000	0.013	0.122	0.990	0.011	-0.0090	0.0012	-0.0093	0.0012
15.240	1.519	1.016	1.000	0.015	0.134	0.990	0.014	-0.0100	0.0013	-0.0100	0.0013
17.780	1.772	1.026	1.000	0.035				-0.0020	0.0027	-0.0020	0.0027

STATION NO. C8 $x = 31.8$ cm $z = 0$ cm

y.cm	y/δ	U/U_{ref}	γ_{P_U}	$\sqrt{u^2}/U_{ref}$	V/U_{ref}	γ_{P_V}	$\sqrt{v^2}/U_{ref}$	$\overline{uv}/U^2_{ref}$ ×10²	$S\overline{uv}/U^2_{ref}$ ×10²	$\overline{\alpha\beta}/U^2_{ref}$ ×10²	$S\overline{\alpha\beta}/U^2_{ref}$ ×10²
0.635	0.058	0.401	1.000	0.103	0.008	0.557	0.044	-0.0890	0.0226	-0.1064	0.0226
1.270	0.116	0.487	1.000	0.090	0.024	0.692	0.044	-0.0460	0.0183	-0.0759	0.0184
1.905	0.174	0.556	1.000	0.090	0.039	0.826	0.042	-0.0300	0.0126	-0.0739	0.0133
2.540	0.231	0.613	1.000	0.091				-0.0350	0.0099	-0.1127	0.0118
3.175	0.289	0.651	1.000	0.085	0.059	0.958	0.036	-0.0770	0.0073	-0.1295	0.0089
3.810	0.347	0.705	1.000	0.079	0.069	0.778	0.034	-0.0550	0.0079	-0.1037	0.0092
5.080	0.463	0.783	1.000	0.052	0.091	1.000	0.029	-0.0100	0.0048	-0.0313	0.0053
6.350	0.579	0.827	1.000	0.038	0.111	1.000	0.025	-0.0200	0.0031	-0.0302	0.0033
7.620	0.694	0.861	1.000	0.026	0.128	1.000	0.021	-0.0130	0.0014	-0.0159	0.0016
8.890	0.810	0.887	1.000	0.018	0.145	1.000	0.019	-0.0110	0.0013	-0.0098	0.0013
10.160	0.926	0.904	1.000	0.017	0.167	1.000	0.024	-0.0100	0.0012	-0.0041	0.0014
12.700	1.157	0.940	1.000	0.016	0.192	1.000	0.016	-0.0070	0.0011	-0.0064	0.0011
15.240	1.389	0.975	1.000	0.016				-0.0090	0.0012	-0.0090	0.0012

STATION NO. C11 $x = 40.6$ cm $z = 0$ cm

y.cm	y/δ	U/U_{ref}	γ_{P_U}	$\sqrt{u^2}/U_{ref}$	V/U_{ref}	γ_{P_V}	$\sqrt{v^2}/U_{ref}$	$\overline{uv}/U^2_{ref}$ ×10²	$S\overline{uv}/U^2_{ref}$ ×10²	$\overline{\alpha\beta}/U^2_{ref}$ ×10²	$S\overline{\alpha\beta}/U^2_{ref}$ ×10²
0.635	0.047	0.113	0.723	0.167	.000	0.494	0.055	-0.1130	0.0271	-0.1364	0.0272
1.270	0.093	0.234	0.910	0.161	0.014	0.593	0.059	0.0160	0.0399	-0.1585	0.0428
2.540	0.187	0.392	1.000	0.135	0.052	0.788	0.061	-0.0110	0.0443	-0.2003	0.0448
3.175	0.234	0.447	1.000	0.124	0.076	0.912	0.054	0.0490	0.0295	-0.1599	0.0346
3.810	0.280	0.502	1.000	0.103	0.096	0.982	0.047	0.0300	0.0251	-0.1274	0.0282
5.080	0.374	0.578	1.000	0.085	0.135	1.000	0.039	-0.0040	0.0157	-0.1295	0.0189
6.350	0.467	0.643	1.000	0.077	0.164	1.000	0.032	0.0140	0.0113	-0.1056	0.0151
7.620	0.561	0.709	1.000	0.058	0.194	1.000	0.028	0.0500	0.0063	-0.0225	0.0090
8.890	0.654	0.752	1.000	0.042	0.218	1.000	0.022	-0.0120	0.0041	-0.0444	0.0049
10.160	0.748	0.783	1.000	0.026	0.241	1.000	0.020	-0.0110	0.0022	-0.0169	0.0023
12.700	0.935	0.815	1.000	0.016	0.284	1.000	0.015	-0.0020	0.0014	-0.0025	0.0013
15.240	1.121	0.834	1.000	0.014	0.322	1.000	0.013	-0.0070	0.0013	-0.0061	0.0011
17.780	1.308	0.850	1.000	0.014	0.364	1.000	0.014	-0.0010	0.0014	-0.0007	0.0012
20.320	1.495	0.862	1.000	0.014	0.409			-0.0030	0.0008	-0.0030	0.0008

TABLE III REYNOLDS STRESS DATA MEASURED WITH LASER VELOCIMETER

STATION NO. __C13__   x = __18.3__ cm   z = __0__ cm

y,cm	y/δ	U/Uref	γ_PU	√(u²)/Uref	V/Uref	γ_PV	√(v²)/Uref	$\overline{uv}/U^2_{ref}$ x10²	$S\overline{uv}/U^2_{ref}$ x10²	$\overline{\alpha\beta}/U^2_{ref}$ x10²	$S\overline{\alpha\beta}/U^2_{ref}$ x10²
0.635	0.036	-0.075	0.229	0.094	-0.006	0.478	0.046	0.0100	0.0151	-0.0418	0.0159
1.270	0.072	-0.026	0.408	0.120	-0.005	0.508	0.065	-0.0190	0.0217	-0.1929	0.0279
1.905	0.108	0.008	0.480	0.141	-0.003	0.510	0.070	0.0160	0.0291	-0.7068	0.0652
2.540	0.144	0.063	0.600	0.177	-0.011	0.586	0.082	-0.0930	0.0396	-0.5113	0.0564
3.175	0.180	0.137	0.718	0.195	0.027	0.627	0.082	-0.0780	0.0472	-0.6557	0.0714
3.810	0.216	0.203	0.810	0.203	0.043	0.711	0.076	-0.0650	0.0435	-0.7815	0.0784
5.080	0.287	0.331	0.949	0.180	0.077	0.829	0.075	-0.0650	0.0376	-0.6527	0.0660
6.350	0.359	0.407	1.000	0.162	0.130	0.966	0.067	0.0010	0.0325	-0.6305	0.0652
7.620	0.431	0.500	1.000	0.124	0.174	1.000	0.057	0.1560	0.0271	-0.2542	0.0446
8.890	0.503	0.566	1.000	0.094	0.212	1.000	0.048	0.1000	0.0282	-0.1403	0.0319
10.160	0.575	0.619	1.000	0.080	0.249	1.000	0.035	0.0980	0.0192	-0.1077	0.0234
12.700	0.718	0.684	1.000	0.051	0.305	1.000	0.023	-0.0080	0.0056	-0.0818	0.0079
15.240	0.862	0.727	1.000	0.025	0.352	1.000	0.019	-0.0040	0.0016	-0.0121	0.0020
17.780	1.006	0.742	1.000	0.018	0.394	1.000	0.018	0.0040	0.0011	0.0022	0.0013
20.320	1.149	0.750	1.000	0.016	0.435	1.000	0.015	0.0030	0.0010	-0.0001	0.0011
22.860	1.293	0.759	1.000	0.015	0.475	1.000	0.016	-0.0030	0.0009	-0.0003	0.0011
25.400	1.437	0.754			0.532			0.0000	0.0008	0.0000	0.0008

STATION NO __C15__   x = __55.9__ cm   z = __0__ cm

y,cm	y/δ	U/Uref	γ_PU	√(u²)/Uref	V/Uref	γ_PV	√(v²)/Uref	$\overline{uv}/U^2_{ref}$ x10²	$S\overline{uv}/U^2_{ref}$ x10²	$\overline{\alpha\beta}/U^2_{ref}$ x10²	$S\overline{\alpha\beta}/U^2_{ref}$ x10²
0.635	0.029	-0.098	0.083	0.072	000	0.502	0.030	0.0340	0.0079	0.0350	0.0079
1.270	0.057	-0.111	0.109	0.076	0.003	0.530	0.044	0.0070	0.0100	0.0163	0.0101
1.905	0.086	-0.094	0.173	0.090	0.006	0.558	0.050	-0.0380	0.0136	-0.0013	0.0141
2.540	0.114	-0.072	0.257	0.103	0.007	0.571	0.053	-0.0780	0.0174	0.0000	0.0190
3.175	0.143	-0.055	0.297	0.118	0.017	0.607	0.065	-0.0040	0.0229	0.2808	0.0355
3.810	0.171	-0.012	0.440	0.127	0.023	0.641	0.070	-0.0330	0.0212	0.4893	0.0780
5.080	0.229	0.065	0.569	0.173	0.037	0.688	0.077	0.0220	0.0320	-0.9950	0.0933
6.350	0.286	0.164	0.769	0.194	0.059	0.766	0.081	0.0450	0.0430	-0.9442	0.0985
7.620	0.343	0.216	0.811	0.209	0.085	0.849	0.079	0.1810	0.0450	-1.1401	0.1230
8.890	0.400	0.320	0.931	0.196	0.115	0.899	0.083	0.2710	0.0649	-0.7918	0.1109
10.160	0.457	0.372	0.994	0.170	0.149	0.944	0.086	0.2730	0.0600	-0.5466	0.0912
12.700	0.571	0.486	1.000	0.136	0.229	1.000	0.071	0.2460	0.0428	-0.3632	0.0646
15.240	0.686	0.569	1.000	0.085	0.305	1.000	0.046	0.2390	0.0348	-0.0808	0.0356
17.780	0.800	0.615	1.000	0.053	0.361	1.000	0.028	0.0870	0.0105	-0.0460	0.0132
20.320	0.914	0.623	1.000	0.036	0.404	1.000	0.022	0.0070	0.0036	-0.0343	0.0046
22.860	1.029	0.608	1.000	0.024	0.446	1.000	0.019	0.0100	0.0028	-0.0073	0.0025

STATION NO __C18__   x = __67.3__ cm   z = __0__ cm

y,cm	y/δ	U/Uref	γ_PU	√(u²)/Uref	V/Uref	γ_PV	√(v²)/Uref	$\overline{uv}/U^2_{ref}$ x10²	$S\overline{uv}/U^2_{ref}$ x10²	$\overline{\alpha\beta}/U^2_{ref}$ x10²	$S\overline{\alpha\beta}/U^2_{ref}$ x10²
0.635	0.020	-0.151	0.000	0.047	-0.005	0.538	0.031	-0.0060	0.0069	-0.0041	0.0069
1.270	0.041	-0.154	0.000	0.051	0.008	0.571	0.036	-0.0290	0.0071	-0.0244	0.0072
1.905	0.061	-0.146	0.000	0.057	0.008	0.573	0.040	-0.0570	0.0087	-0.0494	0.0087
2.540	0.082	-0.135	0.007	0.059	0.010	0.586	0.045	-0.0500	0.0095	-0.0390	0.0096
3.175	0.102	-0.125	0.027	0.066	0.014	0.596	0.053	-0.0820	0.0101	-0.0635	0.0105
3.810	0.122	-0.109	0.080	0.051	0.012	0.579	0.061	-0.0620	0.0073	-0.0725	0.0077
5.080	0.163	-0.078	0.156	0.059	0.022	0.607	0.068	-0.0820	0.0093	-0.0968	0.0108
6.350	0.204	-0.056	0.263	0.069	0.032	0.637	0.077	-0.0550	0.0123	-0.0802	0.0189
7.620	0.245	-0.017	0.408	0.078	0.036	0.676	0.090	-0.1270	0.0161	0.0009	0.0498
8.890	0.285	0.014	0.494	0.097	0.051	0.772	0.099	-0.0210	0.0293	0.0281	0.0334
10.160	0.326	0.076	0.599	0.118	0.065	0.712	0.112	0.0660	0.0404	-0.0541	0.0582
12.700	0.408	0.189	0.823	0.139	0.094	0.771	0.126	0.1680	0.0539	0.0185	0.0657
15.240	0.489	0.277	0.958	0.153	0.132	0.866	0.123	0.4180	0.0850	0.0618	0.0895
17.780	0.571	0.366	0.964	0.146	0.155	0.916	0.113	0.4280	0.0759	0.0744	0.0806
20.320	0.653	0.439	1.000	0.131	0.164	0.968	0.083	0.5040	0.0560	0.0494	0.0656
22.860	0.734	0.525	1.000	0.090	0.217	1.000	0.059	0.2280	0.0268	0.0175	0.0311
25.400	0.816	0.544	1.000	0.046	0.203	1.000	0.023	0.0790	0.0048	0.0076	0.0077
27.940	0.897	0.527	1.000	0.032	0.199	1.000	0.019	0.0330	0.0023	0.0028	0.0036
30.480	0.979	0.502	1.000	0.026	0.200		0.017	0.0190	0.0016	0.0006	0.0024

TABLE III REYNOLDS STRESS DATA MEASURED WITH LASER VELOCIMETER (CONT.)

STATION NO. __C20__   x = __74.9__ cm   z = __0__ cm

y,cm	y/δ	U/U_{ref}	γ_{P_U}	$\sqrt{u^2}/U_{ref}$	V/U_{ref}	γ_{P_V}	$\sqrt{v^2}/U_{ref}$	$\overline{uv}/U^2_{ref}$ $\times10^2$	$S^{\overline{uv}}/U^2_{ref}$ $\times10^2$	$\overline{\alpha\beta}/U^2_{ref}$ $\times10^2$	$S^{\overline{\alpha\beta}}/U^2_{ref}$ $\times10^2$
0.635	0.019	-0.192	0.000	0.065	0.001	0.521	0.032	-0.0330	0.0081	-0.0308	0.0081
1.270	0.038	-0.177	0.000	0.063	0.002	0.532	0.044	-0.0590	0.0097	-0.0567	0.0097
1.905	0.056	-0.164	0.000	0.064	-0.003	0.489	0.050	-0.0550	0.0100	-0.0576	0.0100
2.540	0.075	-0.146	0.000	0.063	-0.001	0.509	0.056	-0.1150	0.0120	-0.1156	0.0120
3.175	0.094	-0.133	0.029	0.069	.000	0.520	0.055	-0.1010	0.0119	-0.1013	0.0119
3.810	0.113	-0.119	0.049	0.067	0.003	0.535	0.057	-0.0980	0.0125	-0.0947	0.0125
5.080	0.150	-0.106	0.072	0.067	0.007	0.559	0.058	-0.1360	0.0140	-0.1270	0.0141
6.350	0.188	-0.064	0.210	0.074	0.006	0.560	0.061	-0.1240	0.0145	-0.1057	0.0148
7.620	0.226	-0.054	0.257	0.080	0.011	0.578	0.063	-0.1890	0.0188	-0.1256	0.0201
8.890	0.263	-0.021	0.397	0.088	0.012	0.576	0.072	-0.1970	0.0208	0.0116	0.0319
11.160	0.301	0.015	0.547	0.101	0.012	0.582	0.072	-0.2180	0.0237	-0.2917	0.0386
12.700	0.376	0.101	0.747	0.132	0.001	0.502	0.077	-0.0950	0.0338	-0.4112	0.0462
15.240	0.451	0.202	0.925	0.148	0.009	0.558	0.089	-0.0730	0.0366	-0.3134	0.0449
17.780	0.527	0.286	0.987	0.154	0.003	0.530	0.096	0.2190	0.0311	0.0675	0.0358
20.320	0.602	0.386	1.000	0.139	0.006	0.526	0.093	0.2880	0.0221	0.2355	0.0231
22.860	0.677	0.465	1.000	0.116	0.013	0.590	0.090	0.1330	0.0092	0.1032	0.0108
25.400	0.752	0.523	1.000	0.082	0.027	0.704	0.068	-0.0260	0.0036	-0.0365	0.0045
27.940	0.828	0.545	1.000	0.047	0.034	0.801	0.040	-0.0040	0.0020	-0.0078	0.0022
30.480	0.903	0.519	1.000	0.028	0.028			-0.0130	0.0017	-0.0130	0.0017
33.020	0.978	0.490	1.000	0.032	0.032			-0.0090	0.0010	-0.0090	0.0010

STATION NO. __C22__   x = __74.9__ cm   z = __0__ cm

y,cm	y/δ	U/U_{ref}	γ_{P_U}	$\sqrt{u^2}/U_{ref}$	V/U_{ref}	γ_{P_V}	$\sqrt{v^2}/U_{ref}$	$\overline{uv}/U^2_{ref}$ $\times10^2$	$S^{\overline{uv}}/U^2_{ref}$ $\times10^2$	$\overline{\alpha\beta}/U^2_{ref}$ $\times10^2$	$S^{\overline{\alpha\beta}}/U^2_{ref}$ $\times10^2$
0.635	0.020	-0.202	0.000	0.071	-0.002	0.496	0.040	-0.0610	0.0113	-0.0639	0.0113
1.270	0.039	-0.188	0.000	0.070	-0.005	0.491	0.051	-0.0970	0.0124	-0.1025	0.0124
1.905	0.059	-0.158	0.004	0.073	-0.014	0.436	0.061	-0.1070	0.0142	-0.1193	0.0145
2.540	0.079	-0.131	0.037	0.071	-0.004	0.468	0.066	-0.1410	0.0158	-0.1423	0.0158
3.175	0.098	-0.125	0.051	0.072	-0.019	0.390	0.068	-0.1830	0.0168	-0.1832	0.0173
3.810	0.118	-0.123	0.068	0.076	-0.017	0.404	0.073	-0.1690	0.0171	-0.1686	0.0178
5.080	0.157	-0.098	0.121	0.079	-0.022	0.379	0.071	-0.1980	0.0190	-0.2046	0.0202
6.350	0.197	-0.062	0.228	0.082	-0.028	0.383	0.077	-0.1990	0.0193	-0.1618	0.0254
7.620	0.236	-0.031	0.374	0.083	-0.034	0.350	0.083	-0.2580	0.0219	0.0205	0.0440
8.890	0.275	0.003	0.519	0.086	-0.037	0.356	0.088	-0.3830	0.0279	0.3736	0.1212
10.160	0.314	0.037	0.644	0.088	-0.046	0.335	0.089	-0.3540	0.0280	0.0643	0.0634
12.700	0.393	0.132	0.895	0.100	-0.079	0.249	0.105	-0.4030	0.0336	-0.2368	0.0501
15.240	0.472	0.230	0.995	0.108	-0.114	0.153	0.108	-0.2050	0.0249	-0.1241	0.0447
17.780	0.550	0.308	1.000	0.114	-0.132	0.107	0.108	0.1260	0.0238	0.1351	0.0327
20.320	0.629	0.399	1.000	0.109	-0.151	0.088	0.108	0.2620	0.0198	0.2036	0.0361
22.860	0.708	0.472	1.000	0.097	-0.157	0.044	0.102	0.1210	0.0106	0.0671	0.0279
25.400	0.786	0.523	1.000	0.066	-0.132	0.014	0.072	0.0070	0.0045	-0.0135	0.0108
27.940	0.865	0.545	1.000	0.039	-0.133	0.000	0.051	0.0020	0.0024	-0.0230	0.0050
30.480	0.943	0.524	1.000	0.027	-0.087			-0.0120	0.0020	0.0003	0.0021
33.020	1.022	0.503			-0.074			-0.0020	0.0012	-0.0019	0.0012

TABLE III REYNOLDS STRESS DATA MEASURED WITH LASER VELOCIMETER (CONT.)

STATION NO C24   x = 90.2 cm   z = 0 cm

y,cm	y/δ	U/U_{ref}	γ_{P_U}	$\sqrt{\overline{u^2}}/U_{ref}$	V/U_{ref}	γ_{P_V}	$\sqrt{\overline{v^2}}/U_{ref}$	$\overline{uv}/U^2_{ref}$ $\times 10^2$	$S^{\overline{uv}}/U^2_{ref}$ $\times 10^2$	$\overline{\alpha\beta}/U^2_{ref}$ $\times 10^2$	$S^{\overline{\alpha\beta}}/U^2_{ref}$ $\times 10^2$
0.635	0.022	-0.173	0.004	0.076	-0.014	0.418	0.054	-0.0530	0.0147	-0.0749	0.0149
1.270	0.043	-0.148	0.009	0.072	-0.018	0.416	0.068	-0.1150	0.0173	-0.1184	0.0174
1.905	0.065	-0.130	0.057	0.077	-0.029	0.366	0.075	-0.1900	0.0198	-0.1781	0.0210
2.540	0.087	-0.106	0.086	0.078	-0.039	0.334	0.081	-0.1720	0.0225	-0.1163	0.8255
3.175	0.108	-0.075	0.171	0.076	-0.059	0.255	0.085	-0.3030	0.0264	0.0005	0.0420
3.810	0.130	-0.067	0.242	0.085	-0.066	0.239	0.094	-0.3500	0.0283	0.0735	0.0557
5.080	0.173	-0.030	0.367	0.084	-0.074	0.224	0.095	-0.4250	0.0326	0.3727	0.0772
6.350	0.217	0.001	0.500	0.087	-0.088	0.207	0.104	-0.5510	0.0386	0.5462	1.5843
7.620	0.260	0.034	0.657	0.087	-0.081	0.271	0.116	-0.5760	0.0399	0.1931	0.1882
8.890	0.303	0.095	0.861	0.083	-0.120	0.136	0.107	-0.6640	0.0495	-0.0715	0.1172
10.160	0.347	0.126	0.910	0.088	-0.142	0.100	0.111	-0.6120	0.0456	-0.1583	0.0993
12.700	0.433	0.217	1.000	0.087	-0.185	0.036	0.110	-0.3440	0.0388	-0.2790	0.0546
15.240	0.520	0.312	1.000	0.082	-0.225	0.001	0.105	-0.1230	0.0192	-0.2430	0.0388
17.780	0.607	0.427	1.000	0.080	-0.243	0.000	0.085	0.0860	0.0261	-0.0031	0.0304
20.320	0.639	0.523	1.000	0.075	-0.249	0.000	0.067	0.1800	0.0187	0.1366	0.0236
22.860	0.780	0.570	1.000	0.054	-0.262	0.000	0.042	0.0850	0.0079	0.0952	0.0102
25.400	0.867	0.538	1.000	0.039	-0.273	0.000	0.049	0.0050	0.0035	-0.0324	0.0077
27.940	0.953	0.520	1.000	0.029	-0.254	0.000	0.032	-0.0170	0.0021	-0.0177	0.0035
30.480	1.040	0.496	1.000	0.022	-0.239	0.000	0.015	-0.0180	0.0017	-0.0010	0.0021

STATION NO C26   x = 97.8 cm   z = 0 cm

y,cm	y/δ	U/U_{ref}	γ_{P_U}	$\sqrt{\overline{u^2}}/U_{ref}$	V/U_{ref}	γ_{P_V}	$\sqrt{\overline{v^2}}/U_{ref}$	$\overline{uv}/U^2_{ref}$ $\times 10^2$	$S^{\overline{uv}}/U^2_{ref}$ $\times 10^2$	$\overline{\alpha\beta}/U^2_{ref}$ $\times 10^2$	$S^{\overline{\alpha\beta}}/U^2_{ref}$ $\times 10^2$
0.635	0.034	-0.078	0.181	0.077	-0.030	0.343	0.063	-0.1340	0.0191	-0.1652	0.0205
1.270	0.067	-0.032	0.375	0.087	-0.048	0.275	0.079	-0.2720	0.0246	0.0461	0.0600
1.905	0.101	-0.008	0.459	0.089	-0.082	0.220	0.093	-0.3310	0.0295	0.3317	0.0473
2.540	0.134	0.022	0.583	0.090	-0.098	0.193	0.103	-0.4240	0.0338	0.3802	0.2279
3.175								-0.6350	0.0428	0.5359	0.1501
3.810								-0.7550	0.0494	0.6311	0.1774
5.080								-0.8580	0.0529	0.4700	0.1678
6.350	0.336	0.134	0.915	0.094	-0.183	0.060	0.117	-0.9000	0.0541	0.0418	0.1665
7.620	0.403	0.171	0.946	0.096	-0.202	0.035	0.112	-0.7640	0.0472	-0.0410	0.1242
8.890	0.470	0.230	1.000	0.086	-0.225	0.019	0.111	-0.5960	0.0400	-0.2595	0.0846
10.160	0.538	0.285	1.000	0.080	-0.248	0.000	0.105	-0.4000	0.0333	-0.2848	0.0558
12.700	0.672	0.371	1.000	0.064	-0.292	0.000	0.089	-0.2660	0.0292	-0.2481	0.0348
15.240	0.806	0.443	1.000	0.059	-0.316	0.000	0.074	-0.1000	0.0217	-0.1269	0.0211
17.780	0.941	0.505	1.000	0.051	-0.333	0.000	0.059	-0.0160	0.0205	-0.0467	0.0148
20.320	1.075	0.546	1.000	0.042	-0.346	0.000	0.043	-0.0070	0.0096	-0.0068	0.0083
22.860	1.210	0.555	1.000	0.035	-0.366	0.000	0.030	-0.0390	0.0043	-0.0024	0.0060
25.400	1.344	0.551	1.000	0.027	-0.371		0.023	-0.0230	0.0024	-0.0230	0.0024

TABLE III REYNOLDS STRESS DATA MEASURED WITH LASER VELOCIMETER (CONT.)

STATION NO __C28__   x = __105.4__ cm   z = __0__ cm

y.cm	y/δ	U/U_ref	γ_{P_U}	$\sqrt{u^2}/U_{ref}$	V/U_ref	γ_{P_V}	$\sqrt{v^2}/U_{ref}$	$\overline{uv}/U^2_{ref}$ x10²	$s\overline{uv}/U^2_{ref}$ x10²	$\overline{\alpha\beta}/U^2_{ref}$ x10²	$s\overline{\alpha\beta}/U^2_{ref}$ x10²
0.635	0.032	0.111	0.865	0.095	-0.054	0.234	0.071	-0.2110	0.0221	0.0248	0.0335
1.270	0.064	0.150	0.928	0.099	-0.086	0.152	0.081	-0.4440	0.0330	-0.0852	0.0487
1.905	0.095	0.160	0.943	0.100	-0.112	0.139	0.100	-0.4740	0.0359	-0.1628	0.0580
2.540	0.127	0.178	0.973	0.100	-0.133	0.121	0.108	-0.7280	0.0454	-0.2832	0.0791
3.175	0.159	0.208	0.992	0.098	-0.153	0.102	0.111	-0.7980	0.0489	-0.3679	0.0819
3.810	0.191	0.232	1.000	0.096	-0.172	0.085	0.117	-0.3390	0.0528	-0.3138	0.0566
5.080	0.254	0.277	1.000	0.091	-0.206	0.043	0.116	0.0750	0.0616	-0.2262	0.0521
6.350	0.318	0.319	1.000	0.086	-0.235	0.016	0.110	0.3980	0.0660	-0.1073	0.0621
7.620	0.382	0.370	1.000	0.073	-0.244	0.006	0.109	0.3810	0.0587	-0.1508	0.0589
8.890	0.445	0.405	1.000	0.064	-0.279	0.000	0.090	0.3770	0.0514	-0.0531	0.0485
10.160	0.509	0.445	1.000	0.056	-0.295	0.000	0.088	0.1460	0.0372	-0.1553	0.0335
12.700	0.636	0.516	1.000	0.046	-0.339	0.000	0.064	-0.0180	0.0277	-0.0980	0.0173
15.240	0.763	0.568	1.000	0.039	-0.367	0.000	0.041	0.0250	0.0118	0.0030	0.0083
17.780	0.891	0.594	1.000	0.032	-0.398	0.000	0.030	-0.1290	0.0129	-0.0441	0.0119
20.320	1.018	0.593	1.000	0.028	-0.409	0.000	0.021	-0.1460	0.0117	-0.0368	0.0131

STATION NO __C30__   x = __113.0__ cm   z = __0__ cm

y.cm	y/δ	U/U_ref	γ_{P_U}	$\sqrt{u^2}/U_{ref}$	V/U_ref	γ_{P_V}	$\sqrt{v^2}/U_{ref}$	$\overline{uv}/U^2_{ref}$ x10²	$s\overline{uv}/U^2_{ref}$ x10²	$\overline{\alpha\beta}/U^2_{ref}$ x10²	$s\overline{\alpha\beta}/U^2_{ref}$ x10²
0.635	0.039	0.347	1.000	0.087	-0.059	0.202	0.065	-0.2370	0.0253	-0.1682	0.0260
1.270	0.077	0.367	1.000	0.084	-0.084	0.181	0.087	-0.2870	0.0274	-0.2697	0.0285
1.905	0.116	0.382	1.000	0.088	-0.113	0.146	0.099	-0.3690	0.0290	-0.3657	0.0325
2.540	0.155	0.401	1.000	0.089	-0.137	0.110	0.104	-0.5070	0.0353	-0.4890	0.0388
3.175	0.193	0.414	1.000	0.086	-0.158	0.082	0.107	-0.4800	0.0378	-0.4933	0.0407
3.810	0.232	0.416	1.000	0.087	-0.175	0.067	0.110	-0.5780	0.0388	-0.5666	0.0438
5.080	0.309	0.477	1.000	0.076	-0.198	0.039	0.107	-0.5880	0.0378	-0.6066	0.0411
6.350	0.386	0.494	1.000	0.075	-0.225	0.011	0.101	-0.5230	0.0330	-0.5156	0.0376
7.620	0.464	0.558	1.000	0.061	-0.244	0.000	0.096	-0.4900	0.0294	-0.5277	0.0322
8.890	0.541	0.583	1.000	0.060	-0.268	0.000	0.079	-0.2950	0.0195	-0.2722	0.0226
10.160	0.618	0.639	1.000	0.042	-0.300	0.000	0.067	-0.1280	0.0113	-0.1863	0.0137
12.700	0.773	0.699	1.000	0.028	-0.371	0.000	0.036	0.0120	0.0043	-0.0146	0.0049
15.240	0.927	0.717	1.000	0.022	-0.411	0.000	0.024	0.0090	0.0030	0.0006	0.0026

STATION NO __C31__   x = __119.4__ cm   z = __0__ cm

y.cm	y/δ	U/U_ref	γ_{P_U}	$\sqrt{u^2}/U_{ref}$	V/U_ref	γ_{P_V}	$\sqrt{v^2}/U_{ref}$	$\overline{uv}/U^2_{ref}$ x10²	$s\overline{uv}/U^2_{ref}$ x10²	$\overline{\alpha\beta}/U^2_{ref}$ x10²	$s\overline{\alpha\beta}/U^2_{ref}$ x10²
0.635	0.051	0.490	1.000	0.077	-0.056	0.194	0.062	-0.1960	0.0208	-0.1676	0.0210
1.270	0.101	0.515	1.000	0.083	-0.096	0.129	0.076	-0.2600	0.0235	-0.2225	0.0244
1.905	0.152	0.521	1.000	0.080	-0.112	0.133	0.091	-0.3820	0.0285	-0.3870	0.0293
2.540	0.202	0.530	1.000	0.083	-0.120	0.139	0.104	-0.5190	0.0350	-0.5529	0.0359
3.175	0.253	0.539	1.000	0.092	-0.145	0.094	0.103	-0.4760	0.0328	-0.4655	0.0357
3.810	0.304	0.559	1.000	0.083	-0.154	0.104	0.110	-0.5910	0.0371	-0.6411	0.0389
5.080							0.087	-0.5200	0.0309	-0.4519	0.0282
6.350	0.506	0.641	1.000	0.087	-0.205	0.008	0.076	-0.5030	0.0281	-0.4101	0.0321
7.620	0.607	0.713	1.000	0.075	-0.212	0.000	0.054	-0.3300	0.0186	-0.2892	0.0211
8.890	0.709	0.786	1.000	0.031	-0.255	0.000	0.042	-0.1430	0.0125	-0.1732	0.0114
10.160	0.810	0.822	1.000	0.025	-0.274	0.000		-0.0320	0.0035	-0.0597	0.0046
12.700	1.012	0.891	1.000	0.023	-0.288			-0.0110	0.0021	0.0066	0.0022
13.970	1.113	0.926	1.000	0.023				0.0000	0.0000	0.0000	0.0000

TABLE III REYNOLDS STRESS DATA MEASURED WITH LASER VELOCIMETER (CONCLUDED)

STATION NO. C3 x = 11.3 cm z = 0.0 cm $(P_w - P_{w_{ref}})/Q_{ref} = .077$

y, cm	y/δ	P/Q_ref	(p - P_w)/Q_ref	η_p
0	.0022	.077		
.022	.0048	.261		
.047	.0074	.321		
.072	.0100	.345	.08	
.098	.0126	.363	.072	
.123	.0152	.378	.061	
.149	.0204	.389	.069	
.199	.0296	.417		
.290	.0386	.431	.067	
.377	.0516	.503		
.504	.0650	.531		
.635	.0780	.551	.053	
.762	.1041	.593		
1.02	.1301	.622	.01	
1.27	.1561	.649	.002	
1.52	.1821	.679	.014	
1.78	.2081	.7	.037	
2.03	.2341	.723	.04	
2.29	.2601	.745		
2.54	.3122	.773	.027	
3.05	.3642	.795		
3.56	.3902	.816		
3.81	.5203	.887	.01	
5.08	.6504	.938		
6.35	.7804	.974		
7.62	.9105	.991	.31	
8.89	1.041	.995		
10.2	1.106	.996		
10.8	1.171	.997		
11.4	1.236	.999		
12.1	1.301	.999		
13.0	1.431	1.001		
14.6	1.496	1.002		
15.5	1.561	1.002		
16.5	1.691	1.002		
17.8	1.756	.992		
18.4	1.821	.956		
19.1	1.886	.881		
19.7	1.951	.787		
20.3	2.016	.668		
21.0	2.081	.496		
	2.146			

STATION NO. C2 x = 7.6 cm z = 0.0 cm $(P_w - P_{w_{ref}})/Q_{ref} = .051$

y, cm	y/δ	P/Q_ref	(p - P_w)/Q_ref	η_p
0	.0028	.051		
.027	.0033	.206		
.032	.0038	.232		
.037	.0043	.261		
.042	.0049	.273		
.047	.0062	.304		
.060	.0075	.32	.048	
.072	.0088	.342		
.098	.0101	.344	.047	
.110	.0114	.355		
.123	.0127	.36		
.149	.0154	.376	.031	
.174	.0180	.389	.041	
.199	.0206	.402		
.225	.0232	.413		
.250	.0259	.425	.043	
.301	.0311	.442		
.352	.0364	.46		
.403	.0416	.477	.012	
.453	.0469	.491		
.504	.0521	.5	-.035	
.635	.0656	.53	-.041	
.762	.0788	.556		
.889	.0919	.575	-.026	
1.02	.1050	.594		
1.27	.1181	.612	-.005	
1.52	.1313	.627	.005	
1.78	.1576	.657		
2.03	.1838	.703	.01	
2.29	.2100	.735		
2.54	.2363	.757	.004	
3.05	.2625	.787		
3.56	.3150	.81	.006	
4.45	.3938	.823		
5.08	.4594	.89	.015	
5.72	.5251	.917		
6.99	.5907	.938		
7.62	.6563	.958		
8.26	.7220	.971		
8.89	.7876	.98		
9.53	.8532	.985		
10.2	.9189	.989		
10.8	.9845	.992		
11.4	1.050	.993		
12.1	1.116	.994		
12.7	1.181	.993		
13.3	1.247	.994		
14.0	1.313	.995		
14.6	1.378	.996		
15.2	1.444	.997		
15.9	1.510	.998		
16.5	1.575	.999		
17.1	1.641	.989		
17.8	1.706	.951		
18.4	1.772	.886		
19.1	1.838	.797		
19.7	1.903	.682		
20.3	1.969	.544		
21.0	2.035	.474		
21.2	2.100	.371		
	2.166			
	2.187			

STATION NO. C1 x = 2.54 cm z = 0.0 cm $(P_w - P_{w_{ref}})/Q_{ref} = .041$

y, cm	y/δ	P/Q_ref	(p - P_w)/Q_ref	η_p
0	.0022	.041		
.022	.0047	.246		
.047	.0072	.314		
.072	.0098	.336	.027	
.098	.0123	.357		
.123	.0149	.372	.017	
.149	.0199	.387		
.290	.0239	.409	.017	
.377	.0377	.428	.019	
.504	.0502	.469	.029	
.635	.0504	.502		
.762	.0635	.532	.026	
1.02	.0762	.556		
1.27	.1017	.595	.01	
1.52	.1271	.63		
1.78	.1525	.662	-.029	
2.03	.1779	.689	-.035	
2.29	.2033	.711	-.016	
2.54	.2287	.736	-.012	
3.05	.2541	.755	.017	
3.56	.3050	.78	.018	
3.81	.3558	.803		
5.08	.3812	.827	.02	
6.35	.5083	.89		
7.62	.6353	.94	.016	
8.89	.7624	.972		
10.2	.8895	.985	.055	
11.4	1.037	.99		
12.1	1.164	.992		
12.7	1.207	.992		
13.3	1.271	.993		
14.6	1.334	.996		
15.5	1.461	.997		
16.5	1.525	.999		
17.1	1.588	.999		
17.8	1.652	.999		
18.4	1.715	.951		
19.1	1.779	.906		
19.7	1.842	.879		
20.3	1.951	.782		
21.0	1.970	.661		
	2.033	.473		
	2.097			

STATION NO. C0 x = 24.1 cm z = 0.0 cm $(P_w - P_{w_{ref}})/Q_{ref} = .000$

y, cm	y/δ	P/Q_ref	(p - P_w)/Q_ref	η_p
0	.0017	.021		
.013	.0026	.129		
.020	.0033	.142		
.025	.0043	.197		
.033	.0050	.23		
.038	.0060	.253		
.046	.0066	.274		
.051	.0083	.289		
.064	.0100	.306		
.076	.0116	.326		
.089	.0133	.336		
.102	.0165	.354		
.127	.0198	.355		
.152	.0232	.363		
.178	.0265	.382		
.203	.0298	.396		
.229	.0331	.411		
.254	.0397	.424		
.305	.0463	.457		
.356	.0529	.477		
.406	.0595	.495		
.457	.0662	.508		
.508	.0827	.517		
.635	.0992	.553		
.762	.1158	.577		
.889	.1323	.604		
1.02	.1489	.625		
1.14	.1654	.643		
1.27	.1985	.657		
1.52	.2316	.692		
1.78	.2646	.717		
2.03	.2976	.742		
2.29	.3306	.786		
2.54	.3968	.825		
3.05	.4631	.871		
3.56	.5954	.898		
4.45	.6616	.92		
5.08	.7443	.941		
6.35	.8270	.963		
7.62	.9097	.982		
8.89	.9924	.994		
10.2	1.075	1.002		
10.8	1.240	1.006		
11.4	1.323	1.009		
12.1	1.406	1.011		
13.0	1.489	1.009		
14.6	1.571	1.006		
15.5	1.654	1.009		
16.5	1.737	1.01		
17.8	1.819	1.01		
18.4	1.902	1.012		
19.1	1.985	1.01		
19.7	2.067	.986		
20.1	2.150	.871		
20.4	2.233	.845		
20.7	2.316	.749		
20.8	2.382	.706		
21.0	2.447	.657		
	2.530	.602		
	2.547	.571		
	2.613	.533		
	2.645	.491		
	2.663	.431		
	2.696	.344		
	2.713	.196		
	2.729			
	2.737			

TABLE IV   PRESSURE TRAVERSE DATA   (MEASURED TOTAL PRESSURES AND INFERRED STATIC PRESSURES)

STATION NO. C4 x = 19.1 cm z = 0.0 cm $(\varphi_w - p_{w_{ref}})/Q_{ref} =$

y, cm	y/δ	$(\varphi - p_w)/Q_{ref}$	P/Q_ref	η_p
.022	.0023		.119	
.047	.0051		.249	
.072	.0078		.314	
.098	.0106		.344	
.123	.0134		.36	
.149	.0161		.371	
.199	.0216		.384	
.250	.0271		.41	
.377	.0409		.428	
.504	.0547		.47	
.635	.0689		.498	
.762	.0826		.528	
1.02	.1102		.546	
1.27	.1377		.581	
1.52	.1652		.62	
2.03	.2203		.647	
2.54	.2754		.693	
3.05	.3305		.738	
3.56	.3856		.767	
4.06	.4406		.793	
4.57	.4957		.815	
5.08	.5508		.845	
5.72	.6197		.867	
6.35	.6885		.894	
6.99	.7574		.922	
7.62	.8262		.942	
8.26	.8951		.957	
8.95	.9639		.97	
9.53	1.033		.98	
10.2	1.102		.987	
10.8	1.170		.988	
11.4	1.239		.99	
12.1	1.308		.992	

STATION NO. C5 x = 24.1 cm z = 0.0 cm $(\varphi_w - p_{w_{ref}})/Q_{ref} = .181$

y, cm	y/δ	$(\varphi - p_w)/Q_{ref}$	P/Q_ref	η_p
0	0		.181	
.022	.0022		.268	
.047	.0047		.303	
.072	.0073		.332	
.098	.0099		.356	
.123	.0124		.367	
.149	.0150		.379	
.199	.0201		.404	
.250	.0253		.421	
.377	.0381		.456	
.504	.0509		.489	
.635	.0641		.51	
.762	.0769		.528	
1.02	.1026	.179	.569	1
1.27	.1282	.196	.601	1
1.52	.1539		.626	
2.03	.2052	.165	.681	1
2.54	.2565	.152	.721	1
3.05	.3078		.752	
3.56	.3591		.778	
4.06	.4104		.801	
4.57	.4617	.072	.828	1
5.08	.5510	.066	.859	1
5.72	.5771	.072	.888	1
6.35	.6412	.073	.914	1
6.99	.7053	.061	.935	1
7.62	.7694	.04	.952	1
8.26	.8335		.971	
8.89	.8977		.979	
9.53	.9618		.989	
10.2	1.026		.994	
10.8	1.090		.996	
11.4	1.154		.998	
12.1	1.218		.998	

STATION NO. C6 x = 26.7 cm z = 0.0 cm $(\varphi_w - p_{w_{ref}})/Q_{ref} = .222$

y, cm	y/δ	$(\varphi - p_w)/Q_{ref}$	P/Q_ref	η_p
.022	0		.222	
.047	.0022		.29	
.072	.0047		.327	
.098	.0072		.352	
.123	.0097		.37	
.149	.0123		.381	
.199	.0148		.396	
.250	.0199		.413	
.377	.0249		.445	
.504	.0376		.472	
.635	.0503	.213	.497	1
.762	.0633		.511	
1.02	.0759		.556	
1.27	.1013	.213	.586	1
1.52	.1266		.613	
1.78	.1519		.633	
2.03	.1772		.659	
2.29	.2025		.67	
2.54	.2278	.178	.686	1
3.05	.2532		.712	
3.56	.3038	.178	.803	1
3.81	.3797	.158	.825	1
6.35	.4063	.139	.928	1
7.55	.6329	.144	.95	1
8.89	.7595	.152	.99	1
10.2	.8861		1.004	
10.8	1.013		1.004	
11.4	1.076	.127	1.005	1
12.1	1.203		1.006	
12.7	1.266		1.007	
13.0	1.329		1.008	
14.0	1.392	.067	1.007	1
14.6	1.456		1.008	
15.2	1.519		1.008	
15.9	1.582		1.008	
16.5	1.646		1.009	
17.1	1.709	-.02	1.01	1
18.4	1.835		.99	
19.1	1.962		.936	
19.7	2.025		.845	
20.3	2.063		.728	
21.0	2.104		.568	
21.2	2.114		.418	

STATION NO. C7 x = 29.2 cm z = 0.0 cm $(\varphi_w - p_{w_{ref}})/Q_{ref} =$

y, cm	y/δ	$(\varphi - p_w)/Q_{ref}$	P/Q_ref	η_p
0	0		.265	
.022	.0020		.321	
.047	.0043		.33	
.072	.0066		.36	
.098	.0089		.37	
.123	.0112		.377	
.149	.0135		.38	
.199	.0182		.393	
.250	.0228		.409	
.377	.0344		.439	
.504	.0459		.457	
.635	.0579		.483	
.762	.0694		.507	
1.02	.0926		.554	
1.27	.1157		.588	
1.52	.1389		.607	
1.78	.1620		.637	
2.03	.1851		.661	
2.29	.2083		.676	
2.54	.2314		.705	
3.05	.2777		.718	
3.56	.3240		.739	
3.81	.3471		.788	
5.08	.4629		.858	
5.72	.5286		.915	
6.35	.5943		.956	
7.42	.8100		.98	
8.89	.9257		1.001	
10.2	.9836		1.004	
10.8	1.041		1.005	
11.4	1.099		1.005	
12.1	1.157		1.004	
12.7	1.215		1.005	
13.3	1.273		1.006	
14.0	1.331		1.006	
14.6	1.389		1.007	
15.2	1.446		1.009	
16.5	1.504		1.01	
17.1	1.562		1.004	
18.4	1.620		.975	
19.1	1.678		.904	
19.7	1.736		.803	
20.3	1.794		.672	
21.6	1.851		.372	

TABLE IV PRESSURE TRAVERSE DATA (MEASURED TOTAL PRESSURES AND INFERRED STATIC PRESSURES) (CONT.)

STATION NO. C8   x = 31.8 cm   z = 0.0 cm $(P_w - P_{w_{rel}})/Q_{rel}$ = .306

y, cm	y/δ	P/Q_rel	(P-P_w)/Q_rel	γ_p
0	0	.306		
.022	.0020	.342		
.047	.0043	.362		
.072	.0066	.375		
.098	.0089	.381		
.123	.0112	.383		
.149	.0152	.391		
.199	.0182	.403		
.250	.0228	.411		
.377	.0344	.435		
.504	.0459	.454	.314	1
.635	.0579	.475		1
.762	.0694	.497	.321	1
1.02	.0926	.529		
1.27	.1157	.559		
1.52	.1389	.59		
1.78	.1620	.619		
2.03	.1852	.637	.278	1
2.29	.2083	.651		1
2.54	.2315	.679	.225	1
3.05	.2778	.702	.211	1
3.56	.3472	.779	.193	1
3.81	.4051	.814	.177	1
4.45	.4630	.846	.158	1
5.08	.5787	.907		
6.35	.6644	.951		
7.62	.8136	.984		
8.89	.9259	1.003		1
10.4	.9638	1.002	.092	
11.7	1.100	1.012		1
12.1	1.157	1.014		1
13.3	1.215	1.012		1
14.6	1.273	1.013		1
15.2	1.331	1.013		1
15.9	1.389	1.015	.055	1
16.5	1.447	1.015		1
17.1	1.505	1.017		
17.8	1.563	1.009		1
18.4	1.620	.982		
19.7	1.736	.908		
20.3	1.794	.824	-.054	1
21.6	1.852	.708		
22.2	1.910	.544		
	1.968			
	2.025			

STATION NO. C9   x = 34.3 cm   z = 0.0 cm $(P_w - P_{w_{rel}})/Q_{rel}$ = .34

y, cm	y/δ	P/Q_rel	(P-P_w)/Q_rel	γ_p
0	0	.34		
.022	.0019	.349		
.047	.0042	.36		
.072	.0064	.367		
.098	.0087	.374		
.123	.0110	.38		
.149	.0132	.383		
.199	.0178	.386		
.250	.0223	.389		
.377	.0336	.411		
.504	.0449	.428	.34	
.635	.0565	.443		
.762	.0679	.456	.349	
1.02	.0905	.489		
1.27	.1131	.523		
1.52	.1357	.546		
1.78	.1583	.571		
2.03	.1810	.604	.332	
2.29	.2036	.628		
2.54	.2262	.641	.314	
3.05	.2714	.678	.279	
3.56	.3167	.705	.257	
3.81	.3393	.744	.24	
4.45	.4524	.824	.229	
5.08	.5089	.855	.221	
5.72	.5655	.883		
6.35	.6786	.934		
7.62	.7917	.982		
8.89	.9043	.992	.169	
10.2	.9618	.999		
10.4	1.018	1.004		
11.7	1.074	1.007		
12.1	1.131	1.008		
13.0	1.188	1.008	.11	
14.0	1.244	1.008		
14.6	1.301	1.009		
15.2	1.357	1.008		
15.9	1.414	1.009		
16.5	1.470	1.009		
17.1	1.527	1.007		
17.8	1.583	1.007	.023	
18.4	1.640	1.007		
19.1	1.696	1.006		
19.7	1.753	.992		
20.3	1.810	.944		
21.6	1.866	.871		
22.2	1.923	.782		
22.9	1.979	.677		
23.5	2.036	.549		
	2.092			

STATION NO. C10   x = 36.8 cm   z = 0.0 cm $(P_w - P_{w_{rel}})/Q_{rel}$ =

y, cm	y/δ	P/Q_rel	(P-P_w)/Q_rel	γ_p
0	0	.365		
.022	.0018	.376		
.047	.0039	.381		
.072	.0059	.385		
.098	.0080	.388		
.123	.0101	.39		
.149	.0122	.391		
.199	.0164	.391		
.250	.0206	.398		
.377	.0414	.416		
.504	.0636	.442		
.635	.0835	.464		
.762	.1044	.492		
1.02	.1253	.511		
1.27	.1461	.541		
1.52	.1670	.562		
1.78	.1879	.586		
2.03	.2088	.61		
2.29	.2505	.651		
2.54	.2923	.682		
3.05	.3340	.715		
3.56	.3758	.755		
4.06	.4175	.787		
4.57	.4697	.818		
5.08	.5219	.847		
5.72	.5741	.878		
6.35	.6263	.924		
6.99	.6785	.943		
7.62	.7307	.963		
8.26	.7829	.985		
8.89	.8873	.994		
10.2	.9395	.998		
10.4	.9916	1.002		
11.4	1.044	1.005		
12.7	1.148	1.004		
13.3				
14.0				

STATION NO. C11   x = 40.6 cm   z = 0.0 cm $(P_w - P_{w_{rel}})/Q_{rel}$ = .38

y, cm	y/δ	P/Q_rel	(P-P_w)/Q_rel	γ_p
0	0	.38		
.022	.0016	.386		
.047	.0035	.376		
.072	.0053	.391		
.098	.0072	.389		
.123	.0091	.393		
.149	.0109	.393		
.199	.0147	.394		.723
.250	.0184	.397		.738
.304	.0278	.405	.392	.837
.635	.0371	.406		.91
.762	.0467	.42		.937
1.02	.0561	.436	.381	
1.27	.0748	.447		.993
1.52	.0935	.47		1
1.78	.1121	.482	.361	1
2.03	.1308	.515		1
2.29	.1495	.523		1
2.54	.1682	.568	.35	1
3.05	.1869	.605	.338	1
3.56	.2243	.651		1
4.06	.2617	.677	.292	1
4.57	.2991	.715	.269	1
5.08	.3364	.754	.244	1
5.72	.3738	.794		1
6.35	.4206	.824	.22	1
6.99	.4673	.851	.173	1
7.62	.5140	.877		1
8.26	.5607	.903	.119	1
8.89	.6075	.941		1
10.2	.6542	.972	.085	1
10.4	.7477	.99		
11.7	.8411	1.003		
12.1	.9346	1.001		
14.0	.99	1.001		
15.5	1.121	1.001		
16.5	1.215	.993		
19.1	1.308	.912		
20.3	1.402	.759		
21.6	1.495	.538		
24.1	1.589			
26.7	1.682			
	1.776			
	1.869			
	1.963			

TABLE IV   PRESSURE TRAVERSE DATA   (MEASURED TOTAL PRESSURES AND INFERRED STATIC PRESSURES) (CONT.)

186

STATION NO. C15   x = 55.9 cm   z = 0.0 cm

$(P_w - P_{wref})/Q_{ref} = .419$

y, cm	y/δ	P/Q_ref	(P - P_w)/Q_ref	γp
0	0	.419		
.047	.0021	.421		.857
.072	.0033	.426		
.098	.0044	.427		.843
.123	.0055	.428		.878
.149	.0067	.429		
.199	.0090	.431		.907
.250	.0113	.431		.929
.304	.0170	.428		.884
.395	.0227	.431		.891
.762	.0235	.43	.421	.851
1.02	.0343	.43		
1.27	.0457	.424	.418	.821
1.52	.0571	.422		
1.78	.0686	.42		
2.03	.0914	.417		
2.29	.1029	.414	.415	.71
2.54	.1143	.422		.375
3.05	.1371	.429		.466
3.56	.16	.436		.517
4.06	.1829	.448	.43	.569
4.57	.2057	.465	.435	
5.08	.2286	.477	.442	
5.72	.2571	.496	.427	.769
6.35	.2857	.531	.423	.811
6.99	.3143	.543		
7.62	.3429	.561		.931
8.26	.3714	.584		
8.89	.4	.606	.426	.994
9.53	.4286	.646		
10.2	.4571	.68		
10.8	.4857	.724	.419	
11.4	.5143	.755		
12.1	.5714	.799		
12.7	.6286	.837	.416	1
13.3	.6571	.862		
14.0	.6857	.872		
14.6	.7143	.912	.429	
15.2	.7429	.925		
15.9	.7714	.941		
16.5	.8286	.962	.441	1
17.1	.8571	.973		
17.8	.8857	.98		
18.4	.9143	.995		1
19.1	.9429	1.004		
19.7	.9714	1.008		
20.3		1.009		1
21.0	1.029	1.01		
21.6	1.057	1.011		
22.2	1.086	1.013		1
22.9	1.114	1.015		
23.5	1.171	1.014		
24.1	1.2	1.013		
24.8	1.229	1.011		
25.4	1.257	1.011		
26.0	1.286	1.013		
26.7	1.314	1.012		
27.3	1.343	.991		
27.9	1.371	.777		
28.6	1.4			

STATION NO. C14   x = 52.1 cm   z = 0.0 cm

$(P_w - P_{wref})/Q_{ref} = .414$

y, cm	y/δ	P/Q_ref	(P - P_w)/Q_ref	γp
0	0	.414		
.022	.0011	.414		
.047	.0024	.419		.697
.098	.0037	.423		
.123	.0057	.421		.731
.149	.0079	.425		.739
.199	.0103	.425		
.250	.0129	.424		
.377	.0195	.423		.758
.504	.0260	.425	.413	.876
.635	.0328	.421		.823
.762	.0393	.424	.411	.789
1.02	.0524	.418		.792
1.27	.0655	.419		.719
1.52	.0786	.417		
1.78	.0917	.411	.406	.638
2.03	.1048	.407		
2.29	.1180	.416		.46
2.54	.1311	.424		.549
3.05	.1573	.432	.419	.615
3.56	.1835	.445		.666
4.06	.2097	.457		.729
4.57	.2359	.486	.429	.8
5.08	.2621	.513		
5.72	.2949	.554	.426	.906
6.35	.3277	.594		
6.99	.3604	.629		
7.62	.3932	.661	.396	.981
8.26	.4260	.699		
8.89	.4587	.732	.394	
9.53	.4915	.765		
10.2	.5242	.794		1
10.8	.5570	.831	.395	
11.4	.5898	.856		
12.1	.6225	.9		
12.7	.6553	.926	.37	1
13.3	.7208	.944		
14.0	.7536	.96		
14.6	.7864	.972	.348	1
15.2	.8191	.979		
15.9	.8519	.989		
16.5	.8847	.995	.331	1
17.1	.9174	1.003		
17.8	.9502	1.002		
18.4	.9830	1.002	.289	1
19.1	1.016	1		
19.7	1.081	.999		
20.3	1.114	.995		
21.0	1.180	.986		
21.6	1.213	.969		
22.2	1.245	.943		
22.9	1.278	.915		
23.5	1.343	.886		
24.1	1.409	.853		
24.8	1.474	.824		
25.4	1.507	.79		
26.0	1.540	.761		
26.7	1.606	.738		
27.3	1.638	.726		
27.9	1.671	.668		
28.6	1.704			

STATION NO. C13   x = 48.3 cm   z = 0.0 cm

$(P_w - P_{wref})/Q_{ref} = .409$

y, cm	y/δ	P/Q_ref	(P - P_w)/Q_ref	γp
0	0	.409		
.022	.0012	.414		
.047	.0027	.415		.778
.072	.0041	.416		
.098	.0055	.415		.778
.123	.0070	.418		.733
.149	.0084	.418		
.199	.0113	.418		
.250	.0142	.416		.712
.304	.0205	.416	.41	.771
.635	.0285	.414		.703
.762	.0359	.412	.409	.672
1.02	.0431	.41		.639
1.27	.0575	.406		.569
1.52	.0718	.406		
1.78	.0862	.413	.422	.473
2.03	.1006	.42		
2.29	.1149	.426		.679
2.54	.1293	.435		.682
3.05	.1437	.45	.397	.816
3.56	.1724	.478		.888
4.06	.2011	.496		.943
4.57	.2299	.513	.405	.962
5.08	.2586	.549		
5.72	.2874	.587	.367	.998
6.35	.3233	.615		
6.99	.3592	.647		
7.62	.4310	.687	.369	1
8.26	.4670	.734		
8.89	.5029	.763	.357	
9.53	.5388	.802		
10.2	.5748	.839		1
10.8	.6106	.866	.353	
11.4	.6466	.886		
12.1	.6825	.934		
12.7	.7543	.949	.326	1
13.3	.7902	.967		
14.0	.8262	.978		
14.6	.8621	.989	.299	1
15.2	.8980	.994		
15.9	.9339	1.004		
16.5	.9698	1.008	.256	1
17.1	1.006	1.008		
17.8	1.042	1.007		
18.4	1.078	1.008	.206	1
19.1	1.114	1.008		
19.7	1.185	1.007		
20.3	1.221	1.006		
21.0	1.257	1.009	.152	
21.6	1.293	1.005		
22.2	1.329	1.003		
22.9	1.365	.993		
23.5	1.437	.947		
24.1	1.473	.886		
24.8	1.509	.853		
25.4	1.545	.812		
26.0	1.580	.725		
26.7	1.616	.61		
27.3	1.652			
27.9	1.688			
28.6	1.724			
29.2	1.760			

STATION NO. C12   x = 44.5 cm   z = 0.0 cm

$(P_w - P_{wref})/Q_{ref} = .4$

y, cm	y/δ	P/Q_ref	(P - P_w)/Q_ref	γp
0	0	.4		
.098	.0067	.403		
.123	.0085	.406		
.149	.0102	.406		
.199	.0137	.406		
.250	.0172	.406		
.504	.0347	.401		
.762	.0524	.402		
1.02	.0698	.411		
1.27	.0873	.412		
1.52	.1048	.429		
1.78	.1222	.437		
2.03	.1397	.451		
2.29	.1572	.458		
2.54	.1746	.489		
3.05	.2095	.512		
3.56	.2445	.54		
4.06	.2794	.589		
4.57	.3143	.609		
5.08	.3492	.661		
5.72	.3929	.696		
6.35	.4365	.737		
6.99	.4802	.771		
7.62	.5238	.808		
8.26	.5675	.846		
8.89	.6111	.869		
9.53	.6548	.895		
10.2	.6984	.917		
10.8	.7421	.936		
11.4	.7858	.951		
12.1	.8294	.965		
12.7	.8731	.974		
13.3	.9167	.983		
14.0	.9604	.992		
14.6	1.004	.995		
15.2	1.048	.995		
15.9	1.135	.996		

TABLE IV   PRESSURE TRAVERSE DATA   (MEASURED TOTAL PRESSURES AND INFERRED STATIC PRESSURES) (CONT.)

STATION NO. C19   x = 71.1 cm   z = 0.0 cm $(P_0 - P_{w_{rel}})/Q_{rel} = .418$

y, cm	y/δ	P_0/Q_{rel}	$(p - P_{w_{rel}})/Q_{rel}$	η_p
0	0			
.047	.0015	.418		
.072	.0023	.423		
.098	.0031	.43		
.123	.0039	.435		
.149	.0046	.438		
.174	.0054	.441		
.199	.0062	.441		
.250	.0078	.442		
.377	.0118	.447	.416	
.504	.0158	.446		
.635	.0199	.451	.418	
.762	.0238	.444		
1.02	.0318	.447	.422	
1.27	.0477	.445		
1.52	.0556	.443	.42	
1.78	.0636	.442		
2.03	.0794	.442	.417	
2.29	.0953	.441	.425	
2.54	.1112	.437		
2.79	.1271	.434		
3.05	.1430	.431	.417	
3.30	.1589	.427		
3.56	.1748	.425		
3.81	.1906	.421		
4.06	.2065	.418		
4.32	.2224	.416	.426	
4.57	.2383	.413		
4.83	.2542	.412		
5.08	.2780	.412		
5.33	.3019	.413		
5.59	.3098	.411		
5.84	.3257	.411	.44	
6.35	.3337	.416		
6.86	.3575	.42		
7.37	.3773	.424	.468	
7.87	.3972	.436		
8.38	.4171	.45		
8.89	.4369	.459	.514	
9.40	.4568	.469		
9.91	.4766	.488		
10.2	.4965	.505	.522	
10.7	.5164	.524		
11.2	.5362	.538	.58	
12.4	.5559	.559		
12.7	.5958	.385		
13.2	.6157	.602	.649	
14.6	.6355	.692		
15.2	.6752	.716	.713	
16.5	.6950	.77		
17.8	.7150	.789	.764	
19.1	.7547	.82		
20.3	.7745	.864		
21.6	.7944	.884		
22.9	.8143	.907		
24.1	.8341	.925		
25.4	.8540	.943		
26.7	.8738	.957		
27.9	.8937	.97		
29.2	.9136	.978		
30.5	.9334	.987		
31.8	.9533	.994		
33.0	.9731	.999		
34.3	.9930	1.004		
35.6	1.013	1.003		
36.8	1.053	1.007		
37.5	1.072	1.006		
38.7	1.092	1.006		
	1.112	1.007		
	1.132	1.007		
	1.152	1.007		
	1.172	1.007		
	1.192	1.007		
	1.211	.987		

STATION NO. C18   x = 67.3 cm   z = 0.0 cm $(P_0 - P_{w_{rel}})/Q_{rel} = .417$

y, cm	y/δ	P_0/Q_{rel}	$(p - P_{w_{rel}})/Q_{rel}$	η_p
0	0			
.047	.0015	.417		
.072	.0023	.423		.998
.098	.0031	.428		1
.123	.0040	.431		1
.149	.0048	.433	.417	1
.199	.0064	.435		1
.250	.0080	.436		1
.377	.0121	.439	.416	.996
.504	.0161	.441		1
.635	.0204	.44		.993
.762	.0245	.439	.412	.961
1.02	.0326	.437		.951
1.27	.0408	.435		.92
1.52	.0489	.432	.415	.887
1.78	.0571	.432		.89
2.03	.0653	.43		.844
2.29	.0734	.428	.413	
2.54	.0816	.427		
2.79	.0897	.425		
3.05	.0979	.422		.737
3.30	.1060	.42		
3.56	.1142	.42		
3.81	.1223	.419	.41	.408
4.06	.1305	.418		
4.32	.1387	.417		
4.57	.1468	.416		
4.83	.1550	.415	.422	.494
5.08	.1631	.415		
5.33	.1713	.413	.42	.599
5.84	.1876	.412		
6.10	.1958	.412	.441	.823
6.35	.2039	.413		
6.60	.2121	.419		
7.11	.2284	.425	.46	.958
7.37	.2447	.43		
7.62	.2529	.436	.488	.964
7.87	.2610	.457		
8.13	.2773	.471	.522	
8.38	.2855	.486		1
8.64	.3059	.498		
8.89	.3263	.516	.59	1
9.53	.3467	.554		
10.2	.3670	.573	.661	1
11.4	.3874	.62		
12.1	.4078	.646	.699	1
12.7	.4282	.677		
13.7	.4486	.699	.76	1
14.6	.4690	.723		
15.2	.4894	.77		
16.5	.5098	.798		
17.1	.5302	.833		
18.4	.5506	.882		
19.1	.5914	.91		
20.3	.6117	.926		
21.6	.6321	.945		
22.9	.6733	.965		
24.1	.6937	.978		
26.7	.7753	.99		
27.9	.8157	.991		
28.6	.8564	.994		
29.2	.8768	.995		
30.5	.8972	.994		
31.8	.9176	.994		
32.4	.9380	.994		
33.0	.9584	.996		
34.3	.9788	.997		
35.6	1.060			
36.8	1.081			
	1.101			
	1.122			
	1.142			
	1.162			
	1.183			

STATION NO. C17   x = 63.5 cm   z = 0.0 cm $(P_0 - P_{w_{rel}})/Q_{rel} = .413$

y, cm	y/δ	P_0/Q_{rel}	$(p - P_{w_{rel}})/Q_{rel}$	η_p
0	0			
.047	.0016	.413		
.072	.0025	.423		
.098	.0034	.426		
.123	.0043	.43		
.149	.0052	.431		
.199	.0069	.433		
.250	.0087	.433		
.377	.0131	.436		
.504	.0175	.437		
.635	.0265	.438		
.762	.0355	.437		
1.02	.0451	.437		
1.27	.0529	.434		
1.52	.0618	.432		
1.78	.0706	.432	.409	
2.03	.0794	.431		
2.29	.0882	.429		
2.54	.0971	.428	.42	
2.79	.1059	.426		
3.05	.1147	.424		
3.30	.1235	.422	.421	
3.56	.1324	.422		
3.81	.1412	.418		
4.06	.1500	.417		
4.32	.1588	.417		
4.57	.1677	.414		
4.83	.1765	.412		
5.08	.1853	.411		
5.33	.1941	.41		
5.59	.2030	.408		
5.84	.2118	.41	.413	
6.10	.2206	.411		
6.35	.2294	.412		
6.60	.2481	.416		
6.86	.2559	.418	.415	
7.11	.2647	.423		
7.37	.2736	.424	.409	
7.62	.2824	.433		
7.87	.2868	.449		
8.13	.3089	.462		
8.26	.3309	.475		
8.89	.3530	.486		
9.53	.3861	.501		
10.2	.4081	.53		
11.1	.4302	.549		
12.4	.4523	.572		
13.7	.4964	.599		
14.9	.5184	.649		
16.2	.5405	.67		
17.5	.5626	.695		
18.7	.5846	.75		
19.4	.6067	.781		
20.6	.6288	.812		
21.9	.6508	.858		
23.2	.6729	.88		
24.4	.6949	.889		
25.7	.7170	.919		
26.9	.7611	.934		
28.3	.7831	.946		
28.9	.8055	.968		
30.2	.8273	.984		
31.4	.8494	.991		
32.1	.8714	.996		
33.0	.8935	.997		
34.3	.9376	.998		
35.2	.9597	.999		
35.6	1.004	1.001		
	1.070	1.002		
	1.092	.998		
	1.114			
	1.136			
	1.158			
	1.180			
	1.202			
	1.238			

STATION NO. C16   x = 59.7 cm   z = 0.0 cm $(P_0 - P_{w_{rel}})/Q_{rel} = .422$

y, cm	y/δ	P_0/Q_{rel}	$(p - P_{w_{rel}})/Q_{rel}$	η_p
0	0	.422		
.047	.0019	.43		
.072	.0029	.434		
.098	.0049	.434		
.123	.0060	.436		
.149	.0080	.437		
.199	.0101	.438		
.250	.0152	.439		
.377	.0203	.44		
.504	.0255	.441		
.635	.0306	.442		
.762	.0408	.44	.424	.884
1.02	.0510	.44		.924
1.27	.0612	.438		.93
1.52	.0714	.436	.424	
1.78	.0816	.433		.959
2.03	.1020	.432		.906
2.29	.1124	.43	.418	.969
2.54	.1327	.429		.964
2.79	.1429	.428		.981
3.05	.1531	.427	.425	
3.30	.1633	.424		.929
3.56	.1735	.419	.423	
3.81	.1837	.419		.89
4.06	.1939	.421	.422	.82
4.32	.2041	.423		
4.57	.2143	.424	.411	.86
4.83	.2245	.425		.708
5.08	.2296	.432		.695
5.33	.2551	.439	.451	
5.59	.2806	.448		.695
5.84	.3061	.458		
6.35	.3316	.468	.472	.469
6.99	.3571	.489		
7.62	.3827	.504	.455	.642
8.26	.4082	.526		.752
8.89	.4337	.576		.802
9.53	.4592	.579	.487	
10.4	.4847	.609		.934
11.4	.5102	.638		
12.7	.5357	.661	.526	
13.4	.5867	.698		.977
14.6	.6122	.726		
15.2	.6633	.772		
16.5	.6888	.809		1
17.8	.7143	.835		
19.1	.7398	.863		
19.7	.7653	.887		1
20.3	.7908	.902		
21.6	.8163	.929		
22.9	.8418	.944		1
23.5	.8673	.958		
24.1	.8929	.97		
25.4	.9184	.977		
26.7	.9439	.987		
27.9	.9694	.992		
28.6	.9949	.998		
29.8	1.020	1.003		
30.5	1.046	1.005		
31.8	1.071	1.001		
31.4	1.097	1.004		
32.1	1.122	1.001		
33.7	1.148	.996		
	1.173	.987		
	1.199	.992		
	1.224			
	1.250			
	1.301	1.013		
	1.352	1.01		

TABLE IV PRESSURE TRAVERSE DATA (MEASURED TOTAL PRESSURES AND INFERRED STATIC PRESSURES) (CONT.)

C-3

STATION NO. C20 x = 74.9 cm z = 0.0 cm

$(p_w - p_{w_{ref}})/Q_{ref} = .418$

y, cm	y/δ	P/Q_ref	$(p-p_{w_{ref}})/Q_{ref}$	η_p
0		.418		
.022	.0006	.424		
.047	.0014	.436		
.072	.0021	.44		
.098	.0029	.442		
.123	.0036	.445		
.149	.0044	.449		
.199	.0059	.447		
.250	.0074	.45		
.377	.0149	.453		1
.504	.0226	.45		
.762	.0301	.453		1
1.02	.0376	.445		1
1.27	.0451	.443		1
1.52	.0527	.444		1
1.78	.0602	.44		1
2.03	.0677	.438		
2.29	.0752	.437		1
2.54	.0903	.435	.415	.975
3.05	.1054	.433		.945
3.56	.1204	.427	.417	.937
4.06	.1354	.425		.928
4.57	.1505	.423	.419	
5.08	.1693	.419	.423	.79
5.72	.1881	.416	.421	
6.35	.2069	.414	.42	.743
6.99	.2257	.41		
7.62	.2445	.403	.428	.603
8.26	.2634	.405		
8.89	.2822	.408	.421	.547
9.53	.3010	.409		
9.91	.3085	.411		
10.4	.3160	.413	.437	.747
10.7	.3236	.414		
10.9	.3311	.417		
11.2	.3461	.418	.468	.925
11.7	.3536	.425		
12.2	.3612	.43	.499	.987
12.4	.3687	.431		
12.7	.3762	.437		1
13.3	.3950	.448	.547	1
14.6	.4138	.457		
15.2	.4327	.478	.6	1
15.9	.4515	.495		
16.5	.4703	.517	.647	1
17.1	.5079	.53		
18.4	.5267	.55	.72	1
19.7	.5455	.607		
20.3	.5831	.624	.763	1
21.6	.6020	.676		
22.2	.6208	.708		
22.9	.6396	.732		
23.5	.6584	.763		
24.4	.6772	.791		
25.4	.6960	.821		
26.7	.7148	.874		
27.9	.7524	.889		
29.2	.7713	.909		
30.5	.8089	.931		
31.8	.8277	.946		
33.7	.8465	.963		
34.3	.8653	.975		
35.6	.8841	.984		
38.1	.9029	.991		
38.7	.9217	.998		
	.9406	1.002		
	.9594	1.005		
	.9782	1.006		
	.9970	1.009		
	1.016	1.01		
	1.035	1.012		
	1.053	1.015		
	1.072	1.012		
	1.091	1.012		
	1.110	1.01		
	1.129			
	1.147			

STATION NO. C21 x = 78.7 cm z = 0.0 cm

$(p_w - p_{w_{ref}})/Q_{ref} =$

y, cm	y/δ	P/Q_ref	$(p-p_{w_{ref}})/Q_{ref}$	η_p
0		.418		
.022	.0007	.443		
.047	.0015	.441		
.072	.0023	.443		
.098	.0031	.444		
.123	.0039	.447		
.149	.0046	.45		
.199	.0062	.451		
.250	.0078	.452		
.377	.0118	.453		
.504	.0158	.451		
.635	.0199	.452		
.762	.0238	.446		
1.02	.0277	.443		
1.27	.0393	.443		
1.52	.0536	.437		
1.78	.0636	.437		
2.03	.0715	.434		
2.29	.0954	.426		
2.54	.1113	.423		
3.05	.1272	.42		
3.56	.1431	.417		
4.06	.1590	.413		
4.57	.1788	.412		
5.08	.1987	.408		
5.72	.2186	.407		
6.35	.2384	.403		
6.99	.2583	.402		
7.62	.2782	.401		
8.26	.2980	.404		
8.89	.3179	.405		
9.53	.3378	.407		
10.2	.3576	.41		
10.4	.3775	.416		
10.8	.3874	.424		
11.4	.4173	.434		
11.7	.4371	.443		
12.2	.4570	.456		
12.7	.4769	.477		
14.6	.4967	.496		
15.2	.5166	.512		
15.9	.5365	.533		
16.5	.5564	.558		
17.1	.5762	.583		
18.4	.5961	.605		
19.7	.6160	.628		
20.3	.6358	.664		
21.6	.6557	.691		
22.9	.6954	.725		
23.5	.7153	.749		
24.8	.7352	.772		
26.0	.7550	.812		
26.7	.7749	.848		
27.9	.7948	.862		
28.6	.8145	.881		
29.2	.8543	.908		
30.5	.8741	.928		
31.8	.8941	.96		
32.4	.9140	.972		
33.0	.9339	.98		
34.3	.9736	.994		
34.9	.9935	.998		
35.6	1.013	1.001		
39.4	1.033	1.003		
40.0	1.053	1.002		
40.6	1.073	1.002		
	1.093	1.003		
	1.113	1.002		
	1.133	1.003		
	1.232	1.003		
	1.272	1.005		

STATION NO. C22 x = 82.6 cm z = 0.0 cm

$(p_w - p_{w_{ref}})/Q_{ref} = .423$

y, cm	y/δ	P/Q_ref	$(p-p_{w_{ref}})/Q_{ref}$	η_p
0		.423		
.047	.0015	.427		
.072	.0022	.44		
.098	.0030	.45		
.123	.0038	.453		
.149	.0046	.455		
.199	.0062	.457		1
.250	.0077	.458		
.377	.0117	.46		1
.504	.0156	.456		1
.635	.0197	.453	.417	1
.762	.0236	.452		1
1.02	.0314	.447	.415	1
1.27	.0393	.445		.995
1.52	.0472	.442		.994
1.78	.0550	.437	.424	.963
2.03	.0629	.433		.951
2.29	.0946	.428		.93
2.54	.1101	.422	.418	.894
3.05	.1258	.42	.423	.853
3.56	.1415	.418	.422	.879
4.06	.1572	.415		
4.57	.1769	.41	.423	.772
5.08	.1965	.41		
5.72	.2162	.407	.428	.626
6.35	.2358	.407		
6.99	.2555	.404		.481
7.62	.2752	.404		
8.26	.2948	.404	.403	.644
8.89	.3145	.406		
9.53	.3341	.41		
10.2	.3538	.426		
10.8	.3931	.428	.436	.895
11.4	.4127	.434		
12.1	.4324	.442	.464	.965
12.7	.4520	.455		
13.3	.4914	.477	.518	1
14.6	.5110	.503		
15.2	.5307	.535	.593	1
15.9	.5503	.567		
17.1	.5700	.58	.644	1
17.8	.6093	.623		
19.1	.6486	.646	.711	1
20.3	.6682	.672		
21.0	.6879	.708	.745	1
21.6	.7075	.749		
22.2	.7272	.766		
22.9	.7469	.794		
23.5	.7665	.831		
24.8	.7862	.852		
25.4	.8058	.902		
26.0	.8255	.927		
26.7	.8451	.947		
27.3	.8648	.959		
27.9	.8844	.974		
28.6	.9041	.881		
29.2	.9237	.989		
30.5	.9434	.993		
31.1	.9631	1.001		
32.4	.002	1.003		
33.0	1.022	1.004		
34.3	1.042	1.007		
34.9	1.061	1.005		
35.6	1.081	1.006		
36.8	1.101	1.001		
37.5	1.120	1.006		
38.1	1.160	1.008		
	1.179	1.007		

STATION NO. C23 x = 86.4 cm z = 0.0 cm

$(p_w - p_{w_{ref}})/Q_{ref} =$

y, cm	y/δ	P/Q_ref	$(p-p_{w_{ref}})/Q_{ref}$	η_p
0	.0007	.433		
.022	.0015	.445		
.047	.0023	.457		
.072	.0031	.466		
.098	.0039	.471		
.123	.0047	.472		
.149	.0063	.472		
.199	.0079	.473		
.250	.0118	.47		
.377	.0158	.467		
.504	.0199	.464		
.635	.0239	.459		
.762	.0319	.458		
1.02	.0399	.45		
1.27	.0478	.448		
1.52	.0558	.442		
1.78	.0638	.438		
2.03	.0718	.434		
2.29	.0797	.434		
2.54	.0957	.432		
3.05	.1116	.429		
3.56	.1276	.426		
4.06	.1435	.424		
4.57	.1595	.42		
5.08	.1794	.418		
5.72	.1994	.414		
6.35	.2193	.411		
6.99	.2392	.41		
7.62	.2592	.406		
8.26	.2990	.423		
10.2	.3389	.435		
12.1	.3788	.449		
13.3	.4187	.458		
14.0	.4386	.473		
14.6	.4585	.487		
15.2	.4785	.502		
15.9	.5183	.521		
17.3	.5383	.544		
18.4	.5582	.568		
19.1	.5781	.289		
19.7	.5980	.617		
20.3	.6180	.648		
21.0	.6379	.705		
21.6	.6578	.705		
22.2	.6778	.765		
23.1	.7376	.804		
23.5	.7576	.83		
24.8	.7775	.861		
26.0	.8174	.891		
26.7	.8373	.913		
27.3	.8772	.952		
28.6	.8971	.965		
29.2	.9171	.978		
29.8	.9370	.985		
31.1	.9569	.993		
31.8	.9769	1.003		
32.4	.9968	1.005		
33.7	1.017	1.006		
34.9	1.057	1.01		
35.2	1.077	1.011		
35.6	1.096	1.009		
36.2	1.116	1.012		
37.5	1.136	1.013		
38.1	1.156	1.013		
	1.176	1.011		
	1.196	1.001		

TABLE IV PRESSURE TRAVERSE DATA (MEASURED TOTAL PRESSURES AND INFERRED STATIC PRESSURES) (CONT.)

TABLE IV — PRESSURE TRAVERSE DATA (MEASURED TOTAL PRESSURES AND INFERRED STATIC PRESSURES) (CONT.)

STATION NO. C24 x = 90.2 cm z = 0.0 cm
$(p_w - p_{wrel})/Q_{rel} = .448$

y, cm	y/δ	P/Q_rel	(p − p_w)/Q_rel	ηp
.022	0	.448		
.047	.0007	.457		
.072	.0016	.465		
.098	.0025	.477		
.123	.0033	.475		
.149	.0042	.478		
.199	.0051	.48		.988
.250	.0068	.475		
.301	.0085	.48	.437	
.504	.0129	.474		1
.635	.0172	.471		1
.762	.0217	.467	.422	
1.02	.0260	.467		
1.27	.0347	.454	.429	.995
1.52	.0433	.45		.996
1.78	.0520	.446		.994
2.03	.0693	.445	.419	.981
2.29	.0780	.442		.991
2.54	.0867	.434	.407	.96
3.05	.1213	.43	.411	.86
3.56	.1386	.426	.402	
4.06	.1560	.425	.403	.841
4.57	.1733	.419		.798
5.08	.1950	.413	.397	.759
5.72	.2166	.419		.667
6.35	.2383	.419	.411	.662
6.99	.2600	.419	.42	.633
7.62	.2816	.425		.5
8.26	.3033	.439	.437	
8.89	.3220	.431		.657
9.53	.3466	.451	.479	.861
10.2	.3683	.46		.91
10.8	.3899	.478	.592	
11.4	.4116	.502		1
12.1	.4333	.514	.66	
12.7	.4549	.532		1
13.3	.4766	.558	.698	
14.0	.4983	.582		1
14.6	.5199	.605		
15.2	.5416	.625		
15.8	.5633	.652		
16.5	.5849	.687		
17.1	.6066	.722		
17.8	.6282	.749		
18.4	.6499	.789		
19.1	.6716	.816		
19.7	.6932	.871		
20.3	.7166	.896		
21.0	.7382	.925		
21.6	.7599	.943		
22.2	.8016	.963		
22.9	.8232	.987		
23.5	.8449	.995		
24.1	.8666	.999		
24.8	.8882	1.004		
25.4	.9099	1.002		
26.0	.9315	1.003		
26.7	.9532	1.003		
27.3	.9749	1.005		
27.9	.9965	1.003		
28.6	1.018	1.003		
29.2	1.040	1.001		
29.8	1.062	1.001		
30.5	1.083	.992		
31.1	1.105			
31.8	1.127			
32.4	1.148			
33.0	1.170			
33.7	1.192			
34.3	1.213			

STATION NO. C25 x = 94.0 cm z = 0.0 cm

y, cm	y/δ	P/Q_rel	(p − p_w)/Q_rel	ηp
.022	0	.466		
.047	.0008	.473		
.072	.0018	.479		
.098	.0028	.485		
.123	.0038	.487		
.149	.0048	.485		
.199	.0058	.485		
.250	.0078	.493		
.301	.0097	.488		
.504	.0147	.484		
.635	.0196	.48		
.762	.0247	.479		
1.02	.0297	.473		
1.27	.0395	.473		
1.52	.0494	.462		
1.78	.0593	.456		
2.03	.0692	.452		
2.29	.0791	.449		
2.54	.0890	.444		
3.05	.0988	.443		
3.56	.1186	.443		
4.06	.1384	.436		
4.57	.1581	.435		
5.08	.1779	.43		
5.72	.1977	.43		
6.35	.2224	.432		
6.99	.2471	.433		
7.62	.2718	.436		
8.26	.2965	.441		
8.89	.3212	.454		
9.53	.3460	.454		
10.2	.3707	.478		
10.8	.3954	.486		
11.4	.4201	.505		
12.1	.4448	.522		
12.7	.4695	.538		
13.3	.4942	.559		
14.0	.5189	.582		
14.6	.5436	.61		
15.2	.5684	.632		
15.8	.5931	.661		
16.5	.6178	.687		
17.1	.6425	.721		
17.8	.6672	.748		
18.4	.6919	.772		
19.1	.7166	.805		
19.7	.7413	.91		
20.3	.7907	.947		
21.0	.8402	.972		
21.6	.8896	.987		
22.2	.9390	.994		
22.9	.9884			
23.5	1.038			

STATION NO. C26 x = 97.8 cm z = 0.0 cm
$(p_w - p_{wrel})/Q_{rel} = .485$

y, cm	y/δ	P/Q_rel	(p − p_w)/Q_rel	ηp
.022	0	.485		
.047	.0011	.487		
.072	.0025	.492		
.098	.0038	.496		
.123	.0052	.497		
.149	.0079	.495		
.199	.0106	.493		
.250	.0132	.493		
.301	.0168	.488		
.504	.0200	.484		
.635	.0267	.48	.481	.856
.762	.0336	.478		.819
1.02	.0403	.471	.484	.729
1.27	.0538	.466		.625
1.52	.0672	.461		.566
1.78	.0806	.458		
2.03	.0941	.455	.48	.52
2.29	.1075	.451		.417
2.54	.1210	.448		.677
3.05	.1344	.446		
3.56	.1613	.447	.42	.764
4.06	.1882	.448		
4.57	.2151	.45		
5.08	.2419	.453	.412	.915
5.72	.2688	.457	.407	.946
6.35	.3024	.464		
6.99	.3360	.474		1
7.62	.3636	.477	.397	
8.26	.3968	.488		
8.89	.4250	.5	.382	1
9.53	.4534	.513		
10.2	.4760	.531	.387	
10.8	.5040	.546		1
11.4	.5376	.566	.418	
12.1	.5712	.61		1
12.7	.6048	.634	.471	
13.3	.6384	.663		1
14.0	.6720	.691	.518	
14.6	.7056	.714		1
15.2	.7392	.748	.545	
15.8	.7728	.783		1
16.5	.8065	.808	.563	
17.1	.8401	.838		1
17.8	.8737	.865		
18.4	.9073	.893		
19.1	.9409	.914		
19.7	.9745	.936		
20.3	1.008	.952		
21.0	1.042	.962		
21.6	1.075	.972		
22.2	1.109	.986		
22.9	1.142	.991		
23.5	1.176	1		
24.1	1.210	.999		
24.8	1.243	1.003		
25.4	1.277			
	1.344			

STATION NO. C27 x = 101.6 cm z = 0.0 cm
$(p_w - p_{wrel})/Q_{rel} = .512$

y, cm	y/δ	P/Q_rel	(p − p_w)/Q_rel	ηp
0	0	.512		
.022	.0010	.509		
.047	.0021	.509		
.072	.0032	.507		
.098	.0044	.506		
.123	.0055	.502		
.149	.0066	.5		
.199	.0112	.491		
.377	.0168	.489	.469	
.504	.0225	.485		
.635	.0283	.48	.451	
.762	.0340	.476	.443	
1.02	.0453	.471		
1.27	.0567	.478	.446	
1.52	.0680	.482	.454	
1.78	.1133	.481	.461	
2.03	.1360	.482	.475	
2.54	.1587	.49	.468	
3.05	.1813	.498		
3.56	.2040	.524		
4.06	.2267	.533		
4.57	.2850	.55	.438	
5.08	.3117	.569		
5.72	.3400	.582	.402	
6.35	.3684	.61		
6.99	.3967	.627	.393	
7.62	.4250	.654		
8.26	.4534	.677	.436	
8.89	.4817	.735		
9.53	.5100	.791	.427	
10.2	.5384	.821		
10.8	.5667	.855		
11.4	.5950	.874		
12.1	.6234	.899		
12.7	.6517	.939		
13.3	.6800	.955		
14.0	.7084	.967		
14.6	.7367	.981		
15.2	.7650	.987		
15.9	.7934	.992		
16.5	.8217	.999		
17.1	.8501	1.001		
18.4	.8784	.99		
19.1	.9067	1.001		
19.7	.9351	1.001		
20.3	.9634	.992		
21.0	1.020	1.001		
21.6	1.077	.991		
22.2	1.133	1.003	.493	

STATION NO. C28 x = 105.4 cm z = 0.0 cm
$(p_w - p_{wrel})/Q_{rel} = .527$

y, cm	y/δ	P/Q_rel	(p − p_w)/Q_rel	ηp
0	0	.527	.467	.978
2.54	.1272	.516	.454	1
3.18	.1590	.52	.444	1
3.81	.1903	.527	.424	1
5.08	.2545	.543	.418	1
6.35	.3181	.575	.41	1
7.62	.3817	.612	.409	1
8.89	.4453	.651	.41	1
10.2	.5089	.695	.429	1
11.4	.5709	.81	.453	1
12.7	.6361	.91	.47	1
15.8	.7634	.979	.482	
17.8	.8906	.999		
20.3	1.018			

STATION NO. C29 x = 109.2 cm z = 0.0 cm
$(P_w - P_{w_{rel}})/Q_{rel} =$

y, cm	y/δ	P/Q_rel	$(P-P_w)/Q_{rel}$	γ_p
0	0	.521		
.022	.0012	.524		
.047	.0027	.532		
.072	.0041	.538		
.098	.0056	.543		
.123	.0070	.544		
.149	.0085	.546		
.199	.0114	.545		
.250	.0143	.546		
.377	.0215	.547		
.504	.0288	.548		
.635	.0362	.544		
.762	.0435	.542		
1.02	.0580	.537		
1.27	.0725	.537		
1.52	.0870	.536		
1.78	.1015	.547		
2.03	.1160	.552		
2.54	.1450	.561		
3.05	.1740	.564		
3.56	.2030	.573		
4.06	.2320	.59		
4.57	.2609	.601		
5.08	.2899	.622		
5.72	.3262	.64		
6.35	.3624	.667		
6.99	.3987	.695		
7.62	.4349	.717		
8.26	.4712	.748		
8.89	.5074	.78		
9.53	.5436	.804		
10.4	.5799	.846		
11.4	.6151	.864		
12.7	.6886	.892		
13.0	.7248	.915		
14.0	.7611	.952		
15.2	.7973	.966		
16.5	.8336	.985		
17.8	.8698	.994		
19.1	.9061	.995		
19.7	.9423	.999		
20.3	.9785	1.000		
21.6	1.051	.999		
22.2	1.268	.991		

STATION NO. C30 x = 113.0 cm z = 0.0 cm
$(P_w - P_{w_{rel}})/Q_{rel} = .494$

y, cm	y/δ	P/Q_rel	$(P-P_w)/Q_{rel}$	γ_p
0	0	.494		
.022	.0013	.524		
.047	.0029	.559		
.072	.0044	.564		
.098	.0060	.574		
.123	.0075	.579		
.149	.0090	.58		
.199	.0121	.587		
.250	.0152	.587		
.377	.0230	.588		
.504	.0307	.594		
.635	.0386	.59	.47	1
.762	.0464	.588		
1.02	.0618	.598	.458	1
1.27	.0773	.597		1
1.52	.0927	.6		
1.78	.1082	.599		1
2.03	.1236	.598	.418	1
2.29	.1391	.599		1
2.54	.1546	.598		1
3.05	.1855	.598		1
3.56	.2164	.612	.381	1
4.06	.2473	.624		1
4.57	.2782	.647	.394	1
5.08	.3091	.665		1
5.72	.3478	.689	.38	1
6.35	.3864	.719		1
6.99	.4250	.775	.384	1
7.62	.4637	.785		1
8.26	.5023	.819	.359	1
8.89	.5410	.857		
9.53	.6182	.868		
10.4	.6369	.912	.33	1
11.4	.6955	.936		
12.1	.7342	.955		
12.7	.7728	.968		
13.3	.8114	.978	.306	1
14.0	.8501	.985		
14.6	.8887	.989		
15.2	.9274	.992	.346	1
16.5	.9660	.993		
17.1	1.005	.992		
17.8	1.043	.996		
18.4	1.082			
	1.121			

STATION NO. C31 x = 119.4 cm z = 0.0 cm
$(P_w - P_{w_{rel}})/Q_{rel} = .41$

y, cm	y/δ	P/Q_rel	$(P-P_w)/Q_{rel}$	γ_p
0	0	.41		
.022	.0017	.487		
.047	.0038	.558		
.072	.0059	.58		
.098	.0080	.595		
.123	.0100	.598		
.149	.0120	.601		
.174	.0162	.61		
.199	.0203	.613		
.250	.0306	.62		
.377	.0408	.622	.38	1
.504	.0514	.623		1
.635	.0617	.626	.347	1
.762	.0823	.624		1
1.02	.1029	.621		1
1.27	.1235	.618		1
1.52	.1440	.626		1
1.78	.1646	.626	.335	1
2.03	.1852	.621		1
2.29	.2058	.63		1
2.54	.2469	.624		1
3.05	.2881	.622		1
3.56	.3292	.629	.279	1
4.06	.3704	.637		1
4.57	.4115	.656	.289	1
5.08	.4630	.684		1
5.72	.5144	.747	.246	1
6.35	.5573	.812		
6.99	.6087	.834	.2	1
7.62	.6587	.854		
8.26	.7202	.887	.191	1
8.89	.7716	.919		
9.53	.8230	.946		
10.4	.8745	.968	.113	1
11.4	.9259	.978		
12.1	.9774	.991		1
12.7	1.029	.996		1
13.3	1.080	.998		
14.0	1.132			
14.6	1.183	.997		
15.2	1.235	.908		
15.9	1.286			

STATION NO. C33 x = 133.4 cm z = 0.0 cm
$(P_w - P_{w_{rel}})/Q_{rel} = .277$

y, cm	y/δ	P/Q_rel	$(P-P_w)/Q_{rel}$	γ_p
0	0	.277		
.022	.0017	.434		
.047	.0036	.532		
.072	.0055	.573		
.098	.0075	.593		
.123	.0094	.62		
.149	.0114	.632		
.174	.0133	.643		
.199	.0152	.651		
.250	.0191	.658		
.377	.0288	.687		
.504	.0385	.696	.269	
.635	.0485	.707		
.762	.0583	.711	.257	
1.02	.0777	.714		
1.27	.0971	.706		
1.52	.1165	.709	.235	
1.78	.1359	.705		
2.03	.1553	.701		
2.29	.1748	.706		
2.54	.1942	.69		
3.05	.2330	.691	.196	
3.56	.2718	.694		
4.06	.3107	.702	.201	
4.57	.3495	.718	.2	
5.08	.3883	.752		
5.72	.4854	.784		
6.35	.5340	.819		
6.99	.5825	.851	.209	
7.62	.6311	.868		
8.26	.6796	.913	.219	
8.89	.7282	.936		
9.53	.7767	.96		
10.2	.8252	.973	.212	
10.8	.8738	.988		
11.4	.9223	.981		
12.1	.9709	1.001		
12.7	1.019	.985		
13.3	1.068	.973		
14.0	1.117	.476		
14.6	1.165			
15.2				

TABLE IV PRESSURE TRAVERSE DATA (MEASURED TOTAL PRESSURES AN INFERRED STATIC PRESSURES) (CONT.)

191

STATION NO. E11   x = 40.6 cm   z = -15.24cm $(p_w - p_{w_{ref}})/Q_{ref} = .378$

y, cm	y/δ	P/Q_ref	(p-p_w)/Q_ref	η_p
0	0	.378	.378	
.047	.0035	.382		
.123	.0092	.381		
.250	.0188	.381		
.377	.0283	.385		
.504	.0378	.389		
.635	.0476	.391		
.762	.0572	.395	.367	.801
1.02	.0762	.412		.813
1.27	.0953	.427	.359	.836
1.52	.1143	.441		.925
2.54	.1524	.479		.989
3.18	.1905	.52	.346	.992
3.81	.2381	.575	.369	1
4.45	.2858	.638	.377	1
5.08	.3334	.675		1
5.72	.3810	.715	.372	1
6.35	.4287	.76		1
8.89	.4763	.796	.379	1
10.2	.5715	.853	.335	1
11.4	.6668	.907	.317	1
12.7	.7620	.948	.281	1
14.0	.8573	.974		1
15.2	.9526	.991	.235	1
16.5	1.048	1.002		1
17.8	1.143	1.001	.174	1
19.1	1.238	1		1
20.3	1.334	1.001	.123	1
21.6	1.429	1.001		1
22.9	1.524	1	.219	1
24.1	1.619	.98		
25.4	1.715	.888		
26.7	1.810	.75		
	1.905	.573		
	2.000			

STATION NO. E2   x = 5.1 cm   z = -15.24cm $(p_w - p_{w_{ref}})/Q_{ref} = .045$

y, cm	y/δ	P/Q_ref	(p-p_w)/Q_ref	η_p
0	0	.045	.045	
.022	.0024	.199		
.032	.0035	.214		
.037	.0040	.248		
.042	.0046	.267		
.047	.0051	.279		
.060	.0065	.289		
.072	.0079	.306		
.085	.0093	.319		
.098	.0107	.332		
.110	.0120	.341		
.123	.0134	.352		
.149	.0162	.359		
.174	.0190	.375		
.199	.0217	.388		
.225	.0245	.398		
.250	.0273	.411		
.301	.0328	.422		
.352	.0384	.437	.031	
.377	.0411	.458		
.403	.0439	.479		
.504	.0550	.488		
.635	.0693	.501	.027	
.762	.0831	.524		
.889	.0970	.551		
1.08	.1108	.571	.016	
1.14	.1247	.591		
1.27	.1385	.608		
1.52	.1662	.623	.004	
1.78	.1939	.68		
1.91	.2078	.704		
2.03	.2216	.729	-.034	
2.29	.2493	.752		
2.54	.2770	.776	-.058	
3.05	.3324	.804		
3.56	.3463	.816	-.062	
3.81	.3878	.852		
4.45	.4155	.887	-.037	
5.08	.4648	.915		
5.72	.5540	.943	-.014	
6.35	.6623	.974		
6.99	.7695	.988	-.006	
7.62	.8518	.99		
8.89	.9003	.994	-.008	
9.53	.9695	.993		
10.2	1.039	.994		
10.4	1.108	.994	-.02	
11.1	1.177	.995		
12.1	1.247	.994		
13.3	1.316	.995	-.02	
14.6	1.454	.997		
15.9	1.593	.998		
16.5	1.662	.998	-.043	
17.8	1.731	.98		
18.4	1.801	.939		
19.1	1.870	.867		
19.7	1.939	.778		
20.3	2.008	.688		
21.0	2.078	.581		
21.1	2.147	.406		
	2.216	.33		
	2.285			
	2.301			

STATION NO. C35   x = 148.0 cm   z = 0.0 cm $(p_w - p_{w_{ref}})/Q_{ref} = .257$

y, cm	y/δ	P/Q_ref	(p-p_w)/Q_ref	η_p
0	0	.257		
.022	.0016	.431		
.047	.0035	.525		
.072	.0054	.552		
.098	.0074	.576		
.123	.0093	.597		
.149	.0113	.611		
.199	.0151	.637		
.250	.0190	.664		
.377	.0286	.695	.294	
.504	.0382	.71		
.635	.0482	.732	.296	
.762	.0578	.742		
1.02	.0771	.748		
1.27	.0963	.753	.278	
1.52	.1156	.754		
1.78	.1348	.75	.252	
2.03	.1541	.743	.219	
2.29	.1734	.749		
2.54	.1926	.744	.187	
3.05	.2312	.741		
3.56	.2697	.722	.163	
3.81	.2890	.727		
4.45	.3371	.725	.183	
5.08	.3853	.725		
5.72	.4334	.738	.163	
6.35	.4816	.762		
7.62	.5779	.782		
8.89	.6742	.814	.194	
9.53	.7224	.842		
10.2	.7706	.859	.203	
11.4	.8187	.88		
12.1	.8669	.908		
12.7	.9150	.935		
14.0	.9632	.949		
14.2	1.011	.965		
14.5	1.060	.97		
14.7	1.079	.976		
15.0	1.098	.968		
15.2	1.137	.936		
	1.156	.634		

STATION NO. C34   x = 140.3 cm   z = 0.0 cm $(p_w - p_{w_{ref}})/Q_{ref} = .26$

y, cm	y/δ	P/Q_ref	(p-p_w)/Q_ref	η_p
0	0	.26		
.022	.0017	.499		
.047	.0037	.555		
.072	.0057	.588		
.098	.0077	.604		
.123	.0097	.618		
.199	.0157	.659		1
.250	.0197	.673		1
.377	.0297	.708	.271	
.504	.0397	.716		1
.635	.05	.729	.26	1
.762	.06	.733		1
1.02	.08	.74		1
1.27	.1	.737	.245	
1.52	.12	.738		
1.78	.14	.738		
2.03	.16	.731	.232	
2.29	.18	.727	.248	
2.54	.2	.727	.254	
3.05	.24	.718	.265	
3.56	.28	.723	.27	
4.06	.32	.726		
4.57	.36	.735		1
5.08	.4	.745		1
5.72	.45	.772		1
6.35	.5	.792	.279	1
7.62	.6	.821		
8.26	.65	.856		
8.89	.7	.876		
9.53	.75	.9		
10.2	.8	.928		
10.8	.85	.95		
11.4	.9	.967		
12.1	.95	.986		
12.7	.99	.99		
13.3	1.05	.997		
14.0	1.1	.997		
14.6	1.15	.915		
15.2	1.2	.527		

TABLE IV PRESSURE TRAVERSE DATA (MEASURED TOTAL PRESSURES AND INFERRED STATIC PRESSURES) (CONT.)

STATION NO. E31   x = 119.4 cm   z = -15.24 cm

$(P_w - P_{w_{ref}})/Q_{ref} = .392$

y, cm	y/δ	P/Q_ref	(p - p_wref)/Q_ref	η_p
0	0	.392		
.047	.0037	.48		
.123	.0098	.547		
.250	.0199	.593		
.377	.0301	.603		
.504	.0402	.607		
.635	.0506	.61		
.762	.0607	.612	.372	1
1.02	.0810	.618		
1.27	.1012	.612	.346	1
1.52	.1215	.62		
2.03	.1619	.619	.317	1
2.54	.2024	.624	.304	1
3.18	.2530	.652	.278	1
3.81	.3036	.667	.25	1
4.45	.3543	.681		
5.08	.4049	.709	.244	1
5.72	.4555	.73	.223	1
6.35	.5061	.765	.202	1
7.62	.6073	.803	.18	1
8.89	.7085	.862	.025	1
10.2	.8097	.929		
11.4	.9109	.971		
12.7	1.012	.989		
14.0	1.013	.995		
15.2	1.215	.987		

STATION NO. E24   x = 90.2 cm   z = -15.24 cm

$(P_w - P_{w_{ref}})/Q_{ref} =$

y, cm	y/δ	P/Q_ref	(p - p_wref)/Q_ref	η_p
0	0	.45		
.047	.0017	.465		
.123	.0044	.473		
.250	.0090	.473		
.377	.0136	.472		
.635	.0229	.465		
1.27	.0458	.456		
2.03	.0734	.449		
2.54	.0917	.444		
3.18	.1146	.44		
5.08	.1375	.434		
5.72	.1834	.428		
6.35	.2063	.425		
6.99	.2292	.426		
7.62	.2522	.426		
8.26	.2751	.432		
8.89	.2980	.432		
9.53	.3209	.439		
10.2	.3438	.444		
12.7	.4585	.453		
15.2	.5502	.463		
17.8	.6418	.508		
20.3	.7335	.718		
22.9	.8252	.828		
25.4	.9169	.917		
27.9	1.009	.97		
30.5	1.100	.987		
33.0	1.192	.991		
35.6	1.284	.986		
		.971		

STATION NO. E18   x = 67.3 cm   z = -15.24 cm

$(P_w - P_{w_{ref}})/Q_{ref} = .409$

y, cm	y/δ	P/Q_ref	(p - p_wref)/Q_ref	η_p
0	0	.409		
.047	.0016	.418		
.123	.0042	.424		
.250	.0086	.427		
.377	.0129	.429		
.504	.0173	.432		
.635	.0218	.43	.41	1
.762	.0262	.428		
1.02	.0349	.427	.409	.986
1.27	.0436	.427	.413	.945
1.52	.0523	.427	.414	.904
2.03	.0872	.423	.413	.879
3.18	.1090	.421		
3.81	.1308	.414	.411	.694
4.45	.1744	.416		
5.08	.1962	.406	.402	.629
5.72	.2180	.404		
6.35	.2398	.408	.411	.461
7.62	.2616	.412		
8.26	.2833	.418	.415	.65
8.89	.3051	.423		
9.53	.3269	.423	.421	.749
10.2	.3487	.432		
11.4	.3705	.442		
12.7	.3923	.475	.447	.921
14.0	.4359	.507		
15.2	.4795	.541	.439	1
16.5	.5231	.581		
17.8	.5667	.641	.484	1
19.1	.6103	.7		
20.3	.6539	.753	.517	1
21.6	.6975	.804		
22.9	.7411	.88	.543	1
24.1	.7847	.932		
25.4	.8282	.954	.603	1
26.7	.8718	.972		
27.9	.9154	.984	.666	1
29.2	.9590	.993		
30.5	1.003	.998	.723	1
31.8	1.046	.997		
33.0	1.090	.996		
34.3	1.133	.997		
35.6	1.177	.994		
36.8	1.221	.995		
37.6	1.264	.995		
	1.290	.986		

STATION NO. E14   x = 52.1 cm   z = -15.24 cm

$(P_w - P_{w_{ref}})/Q_{ref} =$

y, cm	y/δ	P/Q_ref	(p - p_wref)/Q_ref	η_p
.022	.0011	.404		
.027	.0014			
.032	.0016			
.037	.0019			
.042	.0022			
.047	.0024	.405		
.060	.0031			
.072	.0037			
.085	.0044			
.098	.0050			
.110	.0057			
.123	.0063			
.149	.0076	.409		
.174	.0089			
.199	.0102			
.225	.0116			
.250	.0129	.411		
.301	.0155			
.352	.0181			
.377	.0194	.412		
.403	.0207			
.453	.0233			
.504	.0259	.407		
.762	.0392			
.889	.0457			
1.02	.0522	.407		
1.14	.0588			
1.27	.0653	.4		
1.52	.0784			
1.78	.0914			
1.91	.0979	.392		
2.03	.1045			
2.29	.1175			
2.54	.1306			
2.79	.1567	.412		
3.56	.1828			
3.81	.1959	.458		
4.45	.2285			
5.08	.2612	.523		
5.72	.2938	.583		
6.35	.3265	.66		
6.99	.3591	.735		
7.62	.3918	.797		
8.26	.4244	.848		
8.89	.4571			
9.53	.4897	.931		
10.2	.5224			
10.8	.5550			
11.4	.5877			
12.1	.6203	.98		
12.7	.6530			
13.3	.6856			
14.0	.7183			
14.6	.7509			
15.2	.7836			
15.9	.8162	.997		
16.5	.8489			
17.1	.8815			
17.8	.9142			
18.4	.9468			
19.1	.9795	.988		
19.7	1.012			
20.3	1.045			
21.0	1.077			
21.6	1.085	.992		
22.9	1.012			
24.1	1.175			
25.4	1.241	.996		
26.7	1.306			
27.9	1.371			
	1.437			

TABLE IV   PRESSURE TRAVERSE DATA (MEASURED TOTAL PRESSURES AND INFERRED STATIC PRESSURES) (CONT.)

STATION NO. E34   x = 140.3 cm   z = 15.24 cm

$(P_w - P_{w_{ref}})/Q_{ref} = .25$

y, cm	y/δ	P/Q_ref	(P-P_w)/Q_ref	γp
0	0	.25		
.022	.0019			
.027	.0023			
.032	.0028			
.037	.0032			
.042	.0036			
.047	.0041	.485		
.060	.0052			
.072	.0063			
.085	.0074			
.098	.0085			
.110	.0096	.575		
.123	.0107			
.149	.0129			
.174	.0151			
.199	.0173			
.225	.0195	.651		
.250	.0217			
.301	.0261			
.352	.0305			
.377	.0327	.685		
.403	.0349			
.453	.0393			
.504	.0437			
.635	.0550	.697	.191	
.762	.0660	.718		
.889	.0770	.724		
1.02	.0880	.725		
1.14	.0990			
1.27	.1120	.73	.185	
1.52	.1320	.733		
1.78	.1540			
2.03	.1760	.739	.181	
2.29	.1980			
2.54	.2200	.734	.167	
3.05	.2640			
3.18	.2750			
3.56	.3080	.715		
3.81	.3300			
4.45	.3850	.713	.129	
5.08	.4400	.728		
5.72	.4950	.749		
6.35	.5501	.782		
6.99	.6051	.798		
7.62	.6601	.846	.125	
8.26	.7151	.898		
8.89	.7701			
9.53	.8251	.934	.175	
10.2	.8801	.955		
10.8	.9351		.193	
11.4	.9901	.962	.201	
12.1	1.045			
12.7	1.100	.963		
13.3	1.155			
14.0	1.210	.546		
14.6	1.265			
15.2	1.320			

STATION NO. V2   x = 7.6 cm   z = 15.24 cm

$(P_w - P_{w_{ref}})/Q_{ref} = .052$

y, cm	y/δ	P/Q_ref	(P-P_w)/Q_ref	γp
.022	.0023	.052	.045	
.027	.0029	.196		
.032	.0034	.218		
.037	.0039	.246		
.042	.0045	.259		
.047	.0050	.274		
.060	.0064	.283		
.072	.0077	.301		
.085	.0091	.314		
.098	.0105	.322		
.110	.0118	.334		
.123		.34		
.149	.0159	.356		
.174	.0186	.374		
.199	.0213	.386		
.225	.0241	.399		
.250	.0268	.411		
.301	.0322	.432	.042	
.352	.0377	.449		
.403	.0431	.459	.043	
.453	.0485	.471		
.504	.0540	.486		
.635	.0680	.51	.032	
.762	.0816	.534		
.889	.0952	.555	-.005	
1.02	.1088	.576	-.021	
1.14	.1223	.592	-.015	
1.27	.1359	.61	-.003	
1.52	.1631	.627	.004	
1.78	.1903	.663	.008	
2.03	.2175	.696		
2.29	.2447	.712	.007	
2.54	.2719	.736		
3.05	.3263	.753	-.006	
3.56	.3806	.789		
4.45	.4738	.809	-.065	
5.08	.5438	.84		
5.72	.6117	.908		
6.35	.6797	.935		
6.99	.7477	.955		
7.62	.8157	.969		
8.26	.8836	.979		
8.89	.9516	.984		
9.53	1.020	.989		
10.2	1.088	.99		
10.8	1.156	.993		
11.4	1.223	.995		
12.1	1.291	.995		
12.7	1.359	.995		
13.3	1.427	.995		
14.0	1.495	.997		
15.2	1.563	.996		
15.9	1.631	.997		
16.5	1.699	.985		
17.1	1.767	.943		
17.8	1.835	.875		
18.4	1.903	.788		
19.1	1.971	.699		
19.7	2.039	.599		
20.3	2.107	.431		
21.2	2.175	.327		
	2.243			
	2.267			

STATION NO. V11   x = 40.6 cm   z = 15.24 cm

$(P_w - P_{w_{ref}})/Q_{ref} = .381$

y, cm	y/δ	P/Q_ref	(P-P_w)/Q_ref	γp
0	0	.381		
.047	.0035	.385		
.123	.0091	.384		
.250	.0185	.386		
.377	.0280	.387		
.504	.0374	.391		
.635	.0471	.39		
.762	.0565	.392		
1.27	.0753	.404	.377	.544
1.52	.1130	.419		.629
1.78	.1507	.428	.386	.724
2.03	.1883	.463		.731
2.54	.2354	.552	.383	.907
3.18	.2825	.586	.379	.937
4.45	.3296	.642	.363	1
4.45	.3766	.682	.308	1
5.08	.4237	.727		1
5.72	.4708	.766	.304	1
6.35	.5650	.835	.301	1
7.62	.6591	.892	.289	1
8.89	.7533	.935		1
10.2	.8475	.968	.275	1
11.4	.9416	.989		1
12.7	1.036	.995	.211	
14.0	1.130	.999		
15.2	1.224	.999		
16.5	1.318	.998		
17.8	1.412	.998		
19.1	1.507	.996		
20.3	1.601	.99		
21.6	1.695	.877		
22.9	1.789	.864		
24.1	1.883	.723		
25.4	1.977	.496		
26.7				

STATION NO. V14   x = 52.1 cm   z = 15.24 cm

$(P_w - P_{w_{ref}})/Q_{ref} =$

y, cm	y/δ	P/Q_ref	(P-P_w)/Q_ref	γp
0	0		.406	
.022	.0011			
.027	.0014			
.032	.0016			
.037	.0019			
.042	.0021		.41	
.047	.0024			
.060	.0030			
.072	.0037			
.085	.0043			
.098	.0050		.412	
.110	.0056			
.123	.0063			
.149	.0075			
.174	.0088			
.225	.0101		.41	
.250	.0127			
.301	.0153		.411	
.352	.0178			
.377	.0191		.413	
.403	.0204			
.453	.0230			
.504	.0256		.407	
.635	.0322			
.762	.0387		.403	
.889	.0451			
1.02	.0515		.4	
1.14	.0580			
1.27	.0644		.403	
1.52	.0773		.413	
1.78	.0902		.445	
2.03	.0966		.485	
2.54	.1031		.531	
3.18	.1160		.601	
3.45	.1289		.663	
4.08	.1546		.733	
4.45	.1611		.801	
5.08	.1804		.907	
5.72	.2233		.964	
6.35	.2577		.989	
6.99	.2899		.988	
7.62	.3222		.941	
8.26	.3544		.820	
8.89	.3866		.673	
9.53	.4188		.571	
10.2	.4510			
10.8	.4832			
11.4	.5155			
12.1	.5477			
12.7	.5799			
13.3	.6121			
14.0	.6443			
14.6	.6765			
15.2	.7088			
15.9	.7410			
16.5	.7732			
17.1	.8054			
17.8	.8376			
18.4	.8698			
19.1	.9021			
19.7	.9343			
20.3	.9665			
21.0	.9987			
21.6	1.031			
22.2	1.063			
24.1	1.074			
25.4	1.095			
26.7	1.204			
27.9	1.259			
29.2	1.353			
30.5	1.482			
31.8	1.611			
33.0	1.675			

TABLE IV   PRESSURE TRAVERSE DATA   (MEASURED TOTAL PRESSURES AND INFERRED STATIC PRESSURES) (CONT.)

STATION NO. W34 x = 140.3 z = 15.24 cm $(P_w - P_{w_{ref}})/Q_{ref}$ = .258

y, cm	y/δ	P/Q_ref	(P-P_w)/Q_ref	η_p
0	0	.258		
.022	.0018			
.027	.0022			
.032	.0026			
.037	.0030			
.042	.0035			
.047	.0039	.484		
.060	.0049			
.072	.0060			
.085	.0070			
.098	.0081	.568		
.110	.0091			
.123	.0102			
.149	.0123			
.174	.0143			
.199	.0164	.654		
.225	.0185			
.250	.0206			
.301	.0248	.695		
.352	.0290			
.403	.0331			
.453	.0374	.719	.227	
.504	.0416	.723		
.635	.0524	.738		
.762	.0628			
.889	.0733	.734	.226	
1.02	.0838			
1.14	.0942	.742		
1.27	.1047	.742	.222	
1.52	.1257			
1.78	.1466	.746	.209	
1.91	.1571			
2.03	.1675	.743	.196	
2.29	.1885			
2.54	.2094	.741	.18	
3.05	.2513			
3.18	.2618	.742	.16	
3.56	.2932	.75		
3.81	.3141	.784	.147	
4.45	.3665	.806	.173	
5.08	.4188			
5.72	.4712			
6.35	.5236			
6.99	.5759			
7.62	.6283	.855		
8.26	.6806			
8.89	.7330	.896		
9.53	.7853			
10.2	.8377	.938	.2	
10.8	.8901			
11.4	.9424	.96		
12.1	.9948			
12.7	1.047	.975	.22	

STATION NO. W31 x = 119.4 z = 15.24 cm $(P_w - P_{w_{ref}})/Q_{ref}$ = .422

y, cm	y/δ	P/Q_ref	(P-P_w)/Q_ref	η_p
0	0	.404		
.047	.0036	.537		
.123	.0094	.565		
.250	.0192	.6		
.377	.0289	.614		
.504	.0386	.623	.36	1
.635	.0486	.626		
.762	.0584	.625		
1.02	.0778	.627		
1.27	.0973	.629	.328	1
1.52	.1167	.63		
2.03	.1556	.652		
2.54	.1946	.656	.305	1
3.18	.2432	.676	.28	1
3.81	.2918	.693	.274	1
4.45	.3405	.718		
5.08	.3891	.74	.264	1
5.72	.4377	.768		
6.35	.4864	.831	.231	1
7.62	.5837	.881	.207	1
8.89	.6809	.944	.197	1
10.2	.7782	.975	.188	1
11.4	.8755	.989		
12.7	.9728	.987	.108	1
14.0	1.070	.977	.025	
15.2	1.167			

STATION NO. W24 x = 90.2 z = 15.24 cm $(P_w - P_{w_{ref}})/Q_{ref}$ =

y, cm	y/δ	P/Q_ref	(P-P_w)/Q_ref	η_p
0	0	.447		
.022	.0007			
.027	.0009			
.032	.0011			
.037	.0012			
.042	.0014	.465		
.047	.0016			
.060	.0020			
.072	.0024			
.085	.0029			
.098	.0033	.471		
.110	.0037			
.123	.0041			
.149	.0050			
.174	.0059			
.199	.0067	.476		
.225	.0076			
.250	.0084			
.301	.0101	.475		
.352	.0118			
.403	.0135			
.453	.0153	.468		
.504	.0170			
.635	.0214			
.762	.0256	.455		
.889	.0299			
1.02	.0342			
1.14	.0385	.448		
1.27	.0427			
1.52	.0513	.44		
1.78	.0598	.436		
1.91	.0641			
2.03	.0684	.433		
2.29	.0769			
2.54	.0855	.427		
3.05	.1026	.42		
3.18	.1197	.417		
3.56	.1282	.419		
3.81	.1496	.418		
4.45	.1710	.423		
5.08	.1923	.425		
5.72	.2137	.432		
6.35	.2351	.442		
6.99	.2564			
7.62	.2778	.461		
8.26	.2992			
8.89	.3205			
9.53	.3419	.514		
10.2	.3633			
10.8	.3846			
11.4	.4060	.598		
12.1	.4274			
12.7	.4488			
13.3	.4701	.711		
14.0	.4915			
14.6	.5129			
15.2	.5342	.816		
15.9	.5556	.922		
16.5	.5983	.969		
17.1	.6197	.985		
17.8	.6411	.986		
18.4	.6624			
19.1	.6838	.961		
19.7	.7052			
20.3	.7127			
21.0	.7266			
21.6	.7693			
22.9	.8120			
24.1	.8548			
25.4	.8975			
26.7	.9403			
27.9	.9830			
29.2	1.026			
30.5	1.111			
31.8	1.197			
33.0				
34.3				
35.6				

STATION NO. W18 x = 67.3 z = 15.24 cm $(P_w - P_{w_{ref}})/Q_{ref}$ = .411

y, cm	y/δ	P/Q_ref	(P-P_w)/Q_ref	η_p
0	0	.411		
.047	.0014	.423		
.123	.0038	.427		
.250	.0076	.43		
.377	.0115	.432		
.504	.0154	.433		
.635	.0194	.434	.41	1
.762	.0233	.435		
1.02	.0311	.431		
1.27	.0388	.43	.408	1
1.52	.0466	.429		
2.03	.0621	.427	.409	1
2.54	.0776	.423	.411	.967
3.18	.0970	.42	.409	.942
3.81	.1165	.417		
4.45	.1359	.416	.41	.861
5.08	.1553	.41		
5.72	.1747	.408	.405	.737
6.35	.1941	.405		
6.99	.2135	.401	.404	.599
7.62	.2329	.405		
8.26	.2523	.404	.405	.529
8.89	.2717	.407		
9.53	.2911	.41	.408	.603
10.2	.3106	.417		
11.4	.3494	.424	.39	.819
12.7	.3882	.449		
14.0	.4270	.465	.351	.939
15.2	.4658	.491		
16.5	.5047	.534	.357	
19.1	.5435	.587		
20.3	.5823	.636	.377	1
21.6	.6211	.684		
22.9	.6540	.75	.441	1
24.1	.6929	.854		
25.4	.7764	.915	.533	1
26.7	.8540	.946		
27.9	.8929	.969	.632	1
29.2	.9317	.984		
30.5	.9705	.993	.722	
31.8	.985	.997		
33.0	1.009	.994		
34.3	1.048	.996		
35.6	1.087	.995		
36.8	1.126	.908		
37.3	1.141			

TABLE IV PRESSURE TRAVERSE DATA (MEASURED TOTAL PRESSURES AND INFERRED STATIC PRESSURES) (CONCLUDED)

195

STATION NO C1 $x = 2.54$ cm $z = 0$ cm			
y, cm	y/δ	U_{eff}/U_{ref}	u_{eff}/U_{ref}
.127	.013	.587	.072
.203	.020	.626	.071
.305	.030	.656	.072
.406	.041	.678	.073
.508	.051	.695	.072
.635	.064	.709	.072
.762	.076	.728	.07
1.02	.102	.756	.067
1.27	.127	.777	.064
1.52	.152	.795	.062
2.03	.203	.831	.055
2.54	.254	.863	.051
3.05	.305	.891	.045
3.56	.356	.914	.039
4.06	.407	.935	.034
4.57	.457	.95	.028
5.08	.508	.962	.021
6.35	.635	.978	.011
7.62	.762	.98	.008
8.89	.889	.984	.007
10.16	1.02	.986	.007
12.7	1.27	.986	.006
15.24	1.52	.99	.007
17.78	1.78	.967	.036
20.07	2.01	.804	.06

STATION NO C2 $x = 7.6$ cm $z = 0$ cm			
y, cm	y/δ	U_{eff}/U_{ref}	u_{eff}/U_{ref}
.127	.013	.559	.074
.203	.021	.596	.074
.305	.032	.642	.074
.406	.042	.662	.074
.508	.053	.685	.073
.635	.066	.699	.073
.762	.079	.716	.072
1.02	.105	.74	.07
1.27	.131	.764	.067
1.52	.158	.785	.064
2.03	.210	.828	.057
2.54	.263	.862	.052
3.05	.315	.885	.047
3.56	.368	.916	.041
4.06	.420	.937	.035
4.57	.473	.951	.029
5.08	.525	.965	.023
6.35	.656	.982	.012
7.62	.788	.988	.008
8.89	.919	.99	.01
10.16	1.05	.991	.007
12.7	1.31	.995	.007
15.24	1.58	1.001	.007
17.78	1.84	.987	.031
19.939	2.06	.836	.058

STATION NO C3 $x = 13.3$ cm $z = 0$ cm			
y, cm	y/δ	U_{eff}/U_{ref}	u_{eff}/U_{ref}
.127	.013	.546	.075
.203	.021	.587	.074
.305	.031	.623	.074
.406	.042	.646	.074
.508	.052	.659	.074
.635	.065	.68	.073
.762	.078	.696	.072
1.02	.104	.722	.069
1.27	.130	.745	.067
1.52	.156	.766	.065
2.03	.208	.801	.059
2.54	.260	.832	.052
3.05	.312	.862	.047
3.56	.364	.886	.042
4.06	.416	.909	.036
4.57	.468	.928	.031
5.08	.520	.941	.024
6.35	.650	.961	.012
7.62	.780	.968	.009
8.89	.911	.973	.008
10.16	1.04	.977	.007
12.7	1.30	.985	.007
15.24	1.56	.996	.007
17.78	1.82	.981	.031
20.07	2.06	.826	.058

STATION NO C5 $x = 24.1$ cm $z = 0$ cm			
y, cm	y/δ	U_{eff}/U_{ref}	u_{eff}/U_{ref}
.127	.013	.434	.083
.203	.021	.478	.085
.305	.031	.506	.086
.406	.041	.541	.085
.508	.051	.562	.086
.635	.064	.582	.085
.762	.077	.602	.083
1.02	.103	.631	.079
1.27	.128	.66	.079
1.52	.154	.679	.073
2.03	.205	.72	.068
2.54	.256	.754	.062
3.05	.308	.789	.055
3.56	.359	.818	.049
4.06	.410	.844	.042
4.57	.462	.867	.036
5.08	.513	.887	.03
6.35	.641	.921	.018
7.62	.769	.938	.01
8.89	.898	.951	.008
10.16	1.03	.964	.008
12.7	1.28	.992	.008
15.24	1.54	1.026	.009
17.78	1.80	1.073	.033
20.07	2.03	.954	.055

STATION NO C6 $x = 26.7$ cm $z = 0$ cm			
y, cm	y/δ	U_{eff}/U_{ref}	u_{eff}/U_{ref}
.127	.013	.409	.086
.203	.020	.427	.089
.305	.030	.464	.09
.406	.041	.491	.09
.508	.051	.517	.089
.635	.063	.533	.089
.762	.076	.552	.087
1.02	.101	.588	.083
1.27	.127	.611	.08
1.52	.152	.634	.077
2.03	.203	.676	.07
2.54	.253	.713	.065
3.05	.304	.746	.059
3.56	.355	.778	.052
4.06	.405	.803	.045
4.57	.456	.825	.039
5.08	.507	.847	.033
6.35	.634	.888	.02
7.62	.760	.907	.012
8.89	.887	.923	.007
10.16	1.01	.938	.008
12.7	1.27	.97	.007
15.24	1.52	1.014	.008
17.78	1.77	1.096	.019
20.32	2.03	1.018	.055

$YP_U = 1.0$

STATION NO C8 $x = 31.8$ cm $z = 0$ cm			
y, cm	y/δ	U_{eff}/U_{ref}	u_{eff}/U_{ref}
.203	.019	.316	.101
.305	.028	.333	.108
.406	.037	.36	.11
.508	.046	.378	.113
.635	.058	.404	.112
.762	.070	.438	.11
1.02	.093	.474	.106
1.27	.116	.504	.103
1.52	.139	.535	.097
2.03	.185	.584	.089
2.54	.232	.632	.081
3.05	.278	.659	.075
3.56	.324	.705	.066
4.06	.371	.737	.059
4.57	.417	.761	.052
5.08	.463	.789	.045
6.35	.579	.837	.028
7.62	.695	.864	.017
8.89	.811	.889	.011
10.16	.927	.914	.007
12.7	1.16	.93	.008
15.24	1.39	.979	.008
17.78	1.62	1.035	.008
20.32	1.85	1.053	.041

$YP_U = 1.0$

TABLE V   HOT-FILM TRAVERSE DATA

STATION NO. C9 x = 34.3 cm z = 0 cm

y, cm	y/δ	U_{eff}/U_{ref}	u_{eff}/u_{ref}
.127	.011	.196	.093
.203	.018	.217	.101
.305	.027	.249	.11
.406	.036	.27	.111
.508	.045	.29	.114
.635	.057	.318	.118
.762	.068	.341	.119
1.02	.090	.382	.123
1.27	.113	.417	.118
1.52	.136	.455	.113
2.03	.181	.507	.102
2.54	.226	.556	.091
3.05	.271	.601	.081
3.56	.317	.637	.074
4.06	.362	.675	.066
4.57	.407	.71	.06
5.08	.452	.738	.052
6.35	.565	.791	.036
7.62	.679	.833	.021
8.89	.792	.859	.011
10.16	.905	.878	.008
12.7	1.13	.916	.007
15.24	1.36	.948	.007
17.78	1.58	.992	.007
20.32	1.81	1.018	.026
22.86	2.04	.886	.052

STATION NO. C11 x = 40.6 cm z = 0 cm

y, cm	y/δ	U_{eff}/U_{ref}	u_{eff}/u_{ref}
.127	.010	.117	.063
.203	.015	.126	.067
.305	.023	.136	.072
.406	.030	.147	.078
.508	.038	.152	.082
.635	.048	.166	.09
.762	.057	.177	.095
1.02	.076	.201	.108
1.27	.095	.235	.114
1.52	.114	.261	.125
2.03	.152	.323	.133
2.54	.191	.378	.138
3.05	.229	.441	.129
3.56	.267	.486	.122
4.06	.305	.524	.103
4.57	.343	.57	.103
5.08	.381	.611	.09
6.35	.476	.684	.07
7.62	.572	.742	.05
8.89	.667	.798	.034
10.16	.762	.824	.026
12.7	.953	.866	.008
15.24	1.14	.893	.007
17.78	1.33	.921	.006
20.32	1.52	.948	.007
22.86	1.71	.967	.02
25.4	1.91	.857	.045

$y_{P_U} < 1.0$ ↑ $y_{P_U} = 1.0$ ↓

STATION NO. C13 x = 48.3 cm z = 0 cm

y, cm	y/δ	U_{eff}/U_{ref}	u_{eff}/u_{ref}
.127	.007	-.097*	.049*
.203	.012	-.109*	.054*
.305	.017	-.112*	.054*
.406	.023	-.122*	.057*
.508	.029	-.122*	.055*
.635	.036	-.123*	.056*
.762	.043	-.129*	.055*
1.02	.058	-.132*	.058*
1.27	.072	-.136*	.059*
1.52	.086	-.141*	.063*
2.03	.115	-.153*	.072*
2.54	.144	-.169*	.082*
3.05	.173	-.192*	.093*
3.56	.201	-.217*	.103*
4.06	.230	-.25 *	.112*
4.57	.259	-.284*	.119*
5.08	.288	-.315*	.119*
		-.358	.143
6.35	.359	-.386*	.119*
		-.467	.136
7.62	.431	-.46 *	.115*
		-.554	.121
8.89	.503	-.527*	.106*
		-.629	.099
10.16	.575	-.582*	.106*
		-.7	.071
12.7	.719	-.785	.026
15.24	.863	-.818	.011
17.78	1.01	-.839	.009
20.32	1.15	-.864	.009
22.86	1.29	-.895	.008
25.4	1.44	-.935	.009
27.94	1.58	-.969	.028
30.48	1.73	-.902	.04

$y_{P_U} < 1.0$ ↑ $y_{P_U} = 1.0$ ↓

STATION NO. C14 x = 52.1 cm z = 0 cm

y, cm	y/δ	U_{eff}/U_{ref}	u_{eff}/u_{ref}
.127	.007	-.094*	.05 *
.203	.010	-.105*	.052*
.305	.016	-.113*	.053*
.406	.021	-.115*	.051*
.508	.026	-.12 *	.053*
.635	.033	-.126*	.054*
.762	.039	-.13 *	.054*
1.02	.052	-.131*	.055*
1.27	.066	-.133*	.057*
1.52	.079	-.136*	.057*
2.03	.105	-.139*	.042*
2.54	.131	-.146*	.066*
3.05	.157	-.157*	.074*
3.56	.184	-.169*	.083*
4.06	.210	-.184*	.09 *
4.57	.236	-.214*	.1 *
5.08	.262	-.228*	.109*
		-.263	.133
6.35	.328	-.29 *	.119*
		-.338	.15
7.62	.393	-.367*	.122*
		-.427	.148
8.89	.459	-.43 *	.123*
		-.515	.141
10.16	.525	-.494*	.114*
		-.599	.123
12.7	.656	-.728	.072
15.24	.787	-.804	.029
17.78	.918	-.827	.017
20.32	1.05	-.843	.012
22.86	1.18	-.863	.012
25.4	1.31	-.903	.012
27.94	1.44	-.981	.011
30.48	1.73	-.902	.04

$y_{P_U} < 1.0$ ↑ $y_{P_U} = 1.0$ ↓

STATION NO. C15 x = 55.9 cm z = 0 cm

y, cm	y/δ	U_{eff}/U_{ref}	u_{eff}/u_{ref}
.127	.006	-.102*	.052*
.203	.009	-.11 *	.054*
.305	.014	-.12 *	.056*
.406	.018	-.124*	.057*
.508	.023	-.129*	.057*
.635	.029	-.132*	.057*
.762	.034	-.136*	.058*
1.02	.046	-.14 *	.058*
1.27	.057	-.141*	.059*
1.52	.069	-.142*	.058*
2.03	.091	-.145*	.06 *
2.54	.114	-.147*	.06 *
3.05	.137	-.146*	.063*
3.56	.160	-.148*	.066*
4.06	.183	-.155*	.074*
4.57	.206	-.164*	.079*
5.08	.228	-.179*	.088*
		-.198	.106
6.35	.286	-.22 *	.109*
		-.238	.13
7.62	.343	-.275*	.123*
		-.301	.145
8.89	.400	-.336*	.128*
		-.373	.154
10.16	.457	-.398*	.13 *
		-.444	.155
12.7	.571	-.608	.13
15.24	.685	-.724	.083
17.78	.800	-.78	.043
20.32	.914	-.796	.028
22.86	1.03	-.803	.012
25.4	1.14	-.803	.012
27.94	1.26	-.806	.011
30.48	1.37	-.895	.013

$y_{P_U} < 1.0$ ↑ $y_{P_U} = 1.0$ ↓

STATION NO. C16 x = 59.7 cm z = 0 cm

y, cm	y/δ	U_{eff}/U_{ref}	u_{eff}/u_{ref}
.127	.005	-.109*	.054*
.203	.008	-.12 *	.057*
.305	.012	-.126*	.057*
.406	.016	-.131*	.056*
.508	.020	-.135*	.058*
.635	.026	-.14 *	.058*
.762	.031	-.143*	.059*
1.02	.041	-.15 *	.059*
1.27	.051	-.15 *	.059*
1.52	.061	-.15 *	.058*
2.03	.082	-.148*	.059*
2.54	.102	-.147*	.059*
3.05	.122	-.146*	.061*
3.56	.143	-.146*	.062*
4.06	.163	-.144*	.063*
4.57	.184	-.147*	.067*
5.08	.204	-.15 *	.071*
		-.146	.075
6.35	.255	-.173*	.087*
		-.18	.094
7.62	.306	-.204*	.105*
		-.22	.115
8.89	.357	-.245*	.119*
		-.277	.136
10.16	.408	-.314*	.131*
		-.338	.148
12.7	.510	-.463	.15
15.24	.612	-.585	.129
17.78	.714	-.674	.084
20.32	.816	-.715	.046
22.86	.918	-.706	.025
25.4	1.02	-.67	.02
27.94	1.12	-.61	.015
30.48	1.22	-.514	.014
33.02	1.33	-.427	.015

$y_{P_U} < 1.0$ ↑ $y_{P_U} = 1.0$ ↓

*DATA OBTAINED FROM HOT-FILM PROBE ROTATED 180 DEGREES

TABLE V HOT-FILM TRAVERSE DATA (Cont'd)

86-4-82-3

STATION NO. C17	x = 63.5 cm	z = 0 cm	
y cm	y/δ	U_{eff}/U_{ref}	u_{eff}/U_{ref}
.127	.004	-.106*	.051*
.203	.007	-.121*	.056*
.305	.011	-.132*	.058*
.406	.014	-.138*	.058*
.508	.018	-.14 *	.058*
.635	.022	-.152*	.056*
.762	.026	-.148*	.061*
1.02	.035	-.154*	.059*
1.27	.044	-.155*	.057*
1.52	.053	-.159*	.058*
2.03	.071	-.152*	.058*
2.54	.088	-.149*	.06 *
3.05	.106	-.144*	.056*
3.56	.124	-.146*	.059*
4.06	.141	-.14 *	.058*
4.57	.159	-.139*	.06 *
5.08	.176	-.139*	.061*
		.131	.062
6.35	.221	-.14 *	.066*
		.141	.071
7.62	.265	-.163*	.082*
		.163	.087
8.89	.309	-.191*	.099*
		.191	.105
10.16	.353	-.228*	.112*
		.238	.123
12.7	.441	.347	.151
15.24	.529	.448	.152
17.78	.618	.553	.142
20.32	.706	.551	.102
22.86	.794	.636	.058
25.4	.882	.661	.04
27.94	.971	.639	.02
30.48	1.06	.59	.015
33.02	1.15	.535	.015

STATION NO. C18	x = 67.3 cm	z = 0 cm	
y cm	y/δ	U_{eff}/U_{ref}	u_{eff}/U_{ref}
.127	.004	-.136*	.062*
.203	.007	-.15 *	.065*
.305	.010	-.164*	.067*
.406	.013	-.171*	.067*
.508	.016	-.175*	.068*
.635	.020	-.177*	.067*
.762	.024	-.18 *	.068*
1.02	.033	-.186*	.067*
1.27	.041	-.185*	.066*
1.52	.049	-.184*	.064*
2.03	.065	-.178*	.066*
2.54	.082	-.171*	.065*
3.05	.098	-.167*	.065*
3.56	.114	-.164*	.066*
4.06	.131	-.158*	.066*
4.57	.147	-.155*	.066*
5.08	.163	-.148*	.063*
		.135	.06
6.35	.204	-.144*	.065*
		.135	.063
7.62	.245	-.147*	.068*
		.144	.073
8.89	.286	-.159*	.078*
		.159	.086
10.16	.326	-.177*	.092*
		.184	.104
12.7	.408	.275	.139
15.24	.489	.375	.157
17.78	.571	.477	.154
20.32	.653	.569	.137
22.86	.734	.626	.1
25.4	.816	.639	.054
27.94	.897	.61	.036
30.48	.979	.566	.031
33.02	1.06	.53	.029

(Annotations on C18: arrow up, $Y_{P_U} < 1.0$, arrow down, $Y_{P_U} = 1.0$)

STATION NO. C19	x = 71.1 cm	z = 0 cm	
y cm	y/δ	U_{eff}/U_{ref}	u_{eff}/U_{ref}
.127	.004	-.154*	.063*
.203	.006	-.166*	.066*
.305	.010	-.17 *	.068*
.406	.013	-.18 *	.067*
.508	.016	-.186*	.069*
.635	.020	-.187*	.067*
.762	.024	-.184*	.066*
1.02	.032	-.188*	.065*
1.27	.040	-.18 *	.062*
1.52	.048	-.183*	.066*
2.03	.064	-.178*	.064*
2.54	.079	-.175*	.064*
3.05	.095	-.166*	.064*
3.56	.111	-.163*	.064*
4.06	.127	-.158*	.063*
4.57	.143	-.153*	.067*
5.08	.159	-.148*	.064*
		.139	.061
6.35	.199	-.143*	.065*
		.136	.061
7.62	.238	-.137*	.062*
		.134	.063
8.89	.278	-.141*	.064*
		.144	.07
10.16	.318	-.152*	.074*
		.16	.083
12.7	.397	.211	.11
15.24	.477	.302	.144
17.78	.556	.407	.151
20.32	.636	.495	.143
22.86	.715	.581	.11
25.4	.794	.611	.064
27.94	.874	.594	.032
30.48	.953	.55	.024
33.02	1.03	.505	.019

STATION NO. C20	x = 74.9 cm	z = 0 cm	
y cm	y/δ	U_{eff}/U_{ref}	u_{eff}/U_{ref}
.127	.004	-.157*	.067*
.203	.006	-.184*	.07 *
.305	.009	-.189*	.069*
.406	.012	-.197*	.071*
.508	.015	-.201*	.071*
.635	.019	-.202*	.069*
.762	.023	-.202*	.07 *
1.02	.030	-.207*	.068*
1.27	.038	-.205*	.069*
1.52	.045	-.2 *	.068*
2.03	.060	-.19 *	.069*
2.54	.075	-.184*	.067*
3.05	.090	-.181*	.068*
3.56	.105	-.173*	.068*
4.06	.120	-.167*	.071*
4.57	.135	-.164*	.069*
5.08	.151	-.156*	.067*
		.151	.067
6.35	.188	-.15 *	.066*
		.147	.066
7.62	.226	-.145*	.068*
		.141	.065
8.89	.263	-.142*	.065*
		.141	.068
10.16	.301	-.145*	.067*
		.147	.072
12.7	.376	.174	.098
15.24	.452	.25	.134
17.78	.527	.35	.148
20.32	.602	.46	.145
22.86	.677	.564	.115
25.4	.753	.612	.074
27.94	.828	.617	.041
30.48	.903	.588	.032
33.02	.978	.548	.029

(Annotations on C20: arrow up, $Y_{P_U} < 1.0$, arrow down, $Y_{P_U} = 1.0$)

STATION NO. C21	x = 78.7 cm	z = 0 cm	
y cm	y/δ	U_{eff}/U_{ref}	u_{eff}/U_{ref}
.127	.004	-.186*	.074*
.203	.006	-.203*	.076*
.305	.010	-.212*	.075*
.406	.013	-.218*	.077*
.508	.016	-.222*	.076*
.635	.020	-.224*	.074*
.762	.024	-.224*	.074*
1.02	.032	-.221*	.072*
1.27	.040	-.219*	.073*
1.52	.048	-.213*	.073*
2.03	.064	-.208*	.073*
2.54	.079	-.202*	.073*
3.05	.095	-.192*	.073*
3.56	.111	-.186*	.073*
4.06	.127	-.184*	.075*
4.57	.143	-.179*	.075*
5.08	.159	-.172*	.074*
		.155	.068
6.35	.199	-.166*	.074*
		.152	.069
7.62	.238	-.157*	.072*
		.143	.065
8.89	.278	-.153*	.071*
		.142	.064
10.16	.318	-.148*	.069*
		.145	.069
12.7	.397	.164	.084
15.24	.477	.227	.115
17.78	.556	.345	.133
20.32	.636	.45	.127
22.86	.715	.549	.102
25.4	.795	.609	.06
27.94	.874	.604	.028
30.48	.954	.567	.022
33.02	1.03	.53	.02

STATION NO. C22	x = 82.6 cm	z = 0 cm	
y cm	y/δ	U_{eff}/U_{ref}	u_{eff}/U_{ref}
.127	.004	-.204*	.079*
.203	.006	-.218*	.081*
.305	.009	-.227*	.08 *
.406	.013	-.232*	.079*
.508	.016	-.231*	.078*
.635	.020	-.232*	.077*
.762	.024	-.23 *	.076*
1.02	.031	-.228*	.074*
1.27	.039	-.228*	.075*
1.52	.047	-.222*	.075*
2.03	.063	-.213*	.074*
2.54	.079	-.204*	.075*
3.05	.094	-.199*	.076*
3.56	.110	-.194*	.077*
4.06	.126	-.187*	.077*
4.57	.142	-.182*	.077*
5.08	.157	-.179*	.077*
		.165	.073
6.35	.197	-.169*	.076*
		.158	.072
7.62	.236	-.165*	.075*
		.152	.07
8.89	.275	-.156*	.111*
		.145	.067
10.16	.314	-.151*	.071*
		.144	.068
12.7	.393	.163	.083
15.24	.472	.232	.107
17.78	.550	.36	.122
20.32	.629	.466	.113
22.86	.708	.571	.089
25.4	.786	.623	.05
27.94	.865	.408	.027
30.48	.943	.568	.02
33.02	1.02	.528	.019

(Annotations on C22: arrow up, $Y_{P_U} < 1.0$, arrow down, $Y_{P_U} = 1.0$)

*DATA OBTAINED FROM HOT-FILM PROBE ROTATED 180 DEGREES

TABLE V   HOT-FILM TRAVERSE DATA   (Cont'd)

STATION NO. C23 x = 86.4 cm z = 0 cm

y, cm	y/δ	Ueff/Uref	ueff/Uref
.127	.004	-.22 *	.082*
.203	.006	-.223*	.082*
.305	.010	-.232*	.081*
.406	.013	-.226*	.077*
.508	.016	-.227*	.078*
.635	.020	-.23 *	.074*
.762	.024	-.223*	.074*
1.02	.032	-.218*	.072*
1.27	.040	-.219*	.075*
1.52	.048	-.214*	.072*
2.03	.064	-.201*	.073*
2.54	.080	-.198*	.072*
3.05	.096	-.195*	.076*
3.56	.112	-.183*	.076*
4.06	.128	-.183*	.075*
4.57	.144	-.184*	.077*
5.08	.159	-.174*	.077*
	.169		.075
6.35	.199	-.171*	.074*
	.164		.075
7.62	.239	-.161*	.075*
	.156		.071
8.89	.279	-.153*	.073*
	.154		.072
10.16	.319	-.147*	.072*
	.151		.071
12.7	.399	.176	.087
15.24	.478	.267	.108
17.78	.558	.395	.111
20.32	.638	.516	.096
22.86	.718	.612	.069
25.4	.797	.642	.035
27.94	.877	.613	.024
30.48	.957	.569	.022
33.02	1.04	.519	.018

STATION NO. C24 x = 90.2 cm z = 0 cm

y, cm	y/δ	Ueff/Uref	ueff/Uref
.127	.004	-.218*	.085*
.203	.007	-.225*	.084*
.305	.010	-.232*	.083*
.406	.014	-.228*	.081*
.508	.017	-.23 *	.081*
.635	.022	-.228*	.081*
.762	.026	-.22 *	.078*
1.02	.035	-.225*	.078*
1.27	.043	-.216*	.076*
1.52	.052	-.212*	.076*
2.03	.069	-.208*	.077*
2.54	.087	-.201*	.078*
3.05	.104	-.198*	.079*
3.56	.121	-.193*	.079*
4.06	.139	-.19 *	.079*
4.57	.156	-.183*	.079*
5.08	.173	-.182*	.079*
	.179		.081
6.35	.217	-.172*	.078*
	.179		.084
7.62	.260	-.166*	.078*
	.165		.079
8.89	.303	-.162*	.079*
	.166		.082
10.16	.347	-.162*	.079*
	.17		.083
12.7	.433	.222	.103
15.24	.520	.356	.116
17.78	.607	.48	.103
20.32	.693	.607	.078
22.86	.780	.672	.044
25.4	.867	.669	.026
27.94	.953	.635	.022
30.48	1.04	.594	.02
33.02	1.13	.546	.018

(Data obtained from hot-film probe rotated 180 degrees; $Y_{P_U} < 1.0$ and $Y_{P_U} = 1.0$ regions indicated)

STATION NO. C25 x = 94.0 cm z = 0 cm

y, cm	y/δ	Ueff/Uref	ueff/Uref
.127	.005	-.206*	.086*
	.195		.084
.203	.008	-.217*	.091*
	.201		.081
.305	.012	-.215*	.083*
	.199		.078
.406	.016	-.215*	.081*
	.178		.077
.508	.020	-.213*	.08 *
	.194		.076
.635	.025	-.215*	.08 *
	.197		.075
.762	.030	-.21 *	.079*
	.195		.074
1.02	.040	-.205*	.077*
	.195		.074
1.27	.049	-.203*	.076*
	.194		.073
1.52	.059	-.199*	.077*
	.189		.074
2.03	.079	-.195*	.078*
	.193		.074
2.54	.099	-.2 *	.081*
	.189		.075
3.05	.119	-.197*	.082*
	.191		.079
3.56	.138	-.194*	.083*
	.189		.081
4.06	.158	-.193*	.084*
	.187		.08
4.57	.178	-.191*	.084*
	.185		.08
5.08	.198	-.186*	.084*
	.183		.082
6.35	.247	-.186*	.089*
	.182		.084
7.62	.297	-.18 *	.089*
	.182		.086
8.89	.346	-.187*	.095*
	.188		.091
10.16	.395	-.201*	.104*
	.209		.104
12.7	.494	.31	.122
15.24	.593	.439	.112
17.78	.692	.573	.091
20.32	.791	.672	.056
22.86	.890	.704	.029
25.4	.988	.683	.023
27.94	1.09	.454	.021
30.48	1.19	.42	.019

STATION NO. C26 x = 97.8 cm z = 0 cm

y, cm	y/δ	Ueff/Uref	ueff/Uref
.127	.005	.163	.074
.203	.008	.167	.073
.305	.013	.168	.069
.406	.017	.168	.069
.508	.021	.17	.068
.635	.026	.169	.067
.762	.032	.17	.068
1.02	.042	.174	.068
1.27	.053	.176	.07
1.52	.064	.177	.071
2.03	.085	.182	.075
2.54	.106	.186	.079
3.05	.127	.188	.082
3.56	.148	.19	.086
4.06	.170	.191	.088
4.57	.191	.193	.09
5.08	.212	.195	.093
6.35	.265	.204	.102
7.62	.318	.217	.109
8.89	.371	.249	.124
10.16	.424	.289	.132
12.7	.530	.419	.132
15.24	.636	.567	.103
17.78	.742	.69	.07
20.32	.848	.744	.033
22.86	.954	.743	.025
25.4	1.06	.724	.021
27.94	1.17	.703	.02

($Y_{P_U} < 1.0$ and $Y_{P_U} = 1.0$ regions indicated)

STATION NO. C28 x = 105.4 cm z = 0 cm

y, cm	y/δ	Ueff/Uref	ueff/Uref
.127	.006	.118	.056
.203	.010	.124	.058
.305	.015	.13	.059
.406	.020	.137	.061
.508	.025	.14	.061
.635	.032	.146	.064
.762	.038	.151	.066
1.02	.051	.164	.072
1.27	.064	.169	.076
1.52	.076	.179	.081
2.03	.102	.191	.089
2.54	.127	.203	.095
3.05	.153	.214	.103
3.56	.178	.223	.109
4.06	.204	.232	.114
4.57	.229	.239	.117
5.08	.254	.251	.123
6.35	.318	.281	.135
7.62	.382	.329	.142
8.89	.445	.391	.143
10.16	.509	.463	.137
12.7	.636	.629	.095
15.24	.763	.73	.053
17.78	.890	.771	.028
20.32	1.02	.77	.023
22.86	1.14	.763	.02

($Y_{P_U} < 1.0$ and $Y_{P_U} = 1.0$ regions indicated)

STATION NO. C30 x = 113.0 cm z = 0 cm

y, cm	y/δ	Ueff/Uref	ueff/Uref
.127	.008	.268	.095
.203	.012	.283	.097
.305	.019	.295	.095
.406	.025	.301	.094
.508	.031	.308	.095
.635	.039	.316	.095
.762	.046	.322	.095
1.02	.062	.336	.097
1.27	.077	.344	.1
1.52	.093	.351	.102
2.03	.124	.366	.108
2.54	.155	.38	.111
3.05	.186	.391	.118
3.56	.216	.405	.122
4.06	.247	.415	.125
4.57	.278	.431	.128
5.08	.309	.449	.132
6.35	.387	.493	.137
7.62	.464	.568	.133
8.89	.541	.649	.114
10.16	.619	.724	.086
12.7	.773	.822	.037
15.24	.928	.855	.028
17.78	1.08	.863	.026

($Y_{P_U} = 1.0$ region indicated)

*DATA OBTAINED FROM HOT-FILM PROBE ROTATED 180 DEGREES

TABLE V HOT-FILM TRAVERSE DATA (Cont'd)

STATION NO. E2 x = 7.6 cm z = -15.24 cm

y, cm	y/δ	U_{eff}/U_{ref}	u_{eff}/U_{ref}
.127	.014	.578	.073
.203	.022	.61	.074
.305	.033	.643	.074
.406	.044	.665	.074
.508	.055	.685	.073
.635	.069	.702	.072
.762	.083	.719	.071
1.02	.111	.746	.069
1.27	.139	.772	.066
1.52	.166	.793	.063
2.03	.222	.831	.056
2.54	.277	.865	.051
3.05	.332	.897	.046
3.56	.388	.923	.04
4.06	.443	.946	.033
4.57	.499	.962	.027
5.08	.554	.974	.021
6.35	.693	.989	.011
7.62	.831	.993	.009
8.89	.970	.997	.012
10.16	1.11	1.001	.007
12.7	1.39	1.006	.007
15.24	1.66	1.009	.007
17.78	1.94	.991	.038
20.07	2.19	.811	.06

STATION NO. E6 x = 26.7 cm z = -15.24 cm (γP_U = 1.0)

y, cm	y/δ	U_{eff}/U_{ref}	u_{eff}/U_{ref}
.127	.013	.359	.088
.203	.020	.4	.092
.305	.030	.432	.094
.406	.041	.463	.094
.508	.051	.48	.094
.635	.063	.51	.093
.762	.076	.532	.092
1.02	.101	.569	.086
1.27	.127	.594	.083
1.52	.152	.619	.08
2.03	.203	.661	.073
2.54	.253	.698	.068
3.05	.304	.732	.063
3.56	.355	.764	.057
4.06	.405	.792	.051
4.57	.456	.815	.045
5.08	.507	.836	.039
6.35	.634	.884	.028
7.62	.760	.916	.017
8.89	.887	.935	.011
10.16	1.01	.95	.009
12.7	1.27	.984	.008
15.24	1.52	1.036	.009
17.78	1.77	1.093	.017
20.07	2.00	1.049	.052

STATION NO. E11 x = 40.6 cm z = -15.24 cm (γP_U < 1.0; γP_U = 1.0)

y, cm	y/δ	U_{eff}/U_{ref}	u_{eff}/U_{ref}
.127	.010	.111	.055
.203	.015	.118	.059
.305	.023	.125	.062
.406	.030	.13	.064
.508	.038	.139	.071
.635	.048	.149	.078
.762	.057	.162	.085
1.02	.076	.183	.098
1.27	.095	.209	.109
1.52	.114	.232	.118
2.03	.152	.286	.131
2.54	.191	.343	.135
3.05	.229	.392	.134
3.57	.267	.443	.126
4.06	.305	.47	.12
4.57	.343	.533	.106
5.08	.381	.568	.098
6.35	.476	.651	.072
7.62	.572	.715	.053
8.89	.667	.765	.038
10.16	.762	.805	.023
12.7	.953	.847	.008
15.24	1.14	.875	.007
17.78	1.33	.904	.006
20.32	1.52	.933	.007
22.86	1.71	.947	.019
25.4	1.91	.832	.044

STATION NO. E18 x = 67.3 cm z = -15.24 cm (γP_U < 1.0; γP_U = 1.0)

y, cm	y/δ	U_{eff}/U_{ref}	u_{eff}/U_{ref}
.127	.004	-.13*	.062*
.203	.007	-.139*	.062*
.305	.010	-.149*	.063*
.406	.014	-.157*	.065*
.508	.017	-.162*	.066*
.635	.022	-.163*	.065*
.762	.026	-.166*	.065*
1.02	.035	-.167*	.065*
1.27	.044	-.167*	.064*
1.52	.052	-.166*	.063*
2.03	.070	-.162*	.064*
2.54	.087	-.156*	.064*
3.05	.105	-.148*	.063*
3.56	.122	-.143*	.064*
4.06	.140	-.138*	.063*
4.57	.157	-.133*	.061*
5.08	.174	-.129*	.061*
		.122	.057
6.35	.218	-.126*	.06*
		.123	.06
7.62	.262	-.13*	.065*
		.131	.066
8.89	.305	-.146*	.073*
		.147	.079
10.16	.349	-.167*	.09*
		.175	.099
12.7	.436	.239	.151
15.24	.523	.338	.151
17.78	.611	.434	.156
20.32	.698	.519	.145
22.86	.785	.597	.108
25.4	.872	.623	.064
27.94	.959	.604	.035
30.48	1.05	.561	.029
33.02	1.13	.521	.018

STATION NO. E24 x = 90.2 cm z = -15.24 cm

y, cm	y/δ	U_{eff}/U_{ref}	u_{eff}/U_{ref}
.127	.005	-.201*	.087*
.203	.007	-.214*	.086*
.305	.011	-.166*	.085*
.406	.015	-.22*	.084*
.508	.018	-.217*	.082*
.635	.023	-.215*	.08*
.762	.028	-.21*	.079*
1.02	.037	-.205*	.077*
1.27	.046	-.197*	.074*
1.52	.055	-.192*	.074*
2.03	.073	-.181*	.073*
2.54	.092	-.173*	.071*
3.05	.110	-.168*	.071*
3.56	.128	-.16*	.07*
4.06	.147	-.161*	.072*
4.57	.165	-.156*	.072*
5.08	.183	-.155*	.073*
		.116	.073
6.35	.229	-.152*	.075*
		.155	.077
7.62	.275	-.166*	.086*
		.168	.085
8.89	.321	-.184*	.091*
		.189	.093
10.16	.367	-.21*	.096*
		.226	.101
12.7	.458	.307	.107
15.24	.550	.411	.101
17.78	.642	.513	.089
20.32	.734	.61	.071
22.86	.825	.67	.042
25.4	.917	.669	.026
27.94	1.01	.642	.022
30.48	1.10	.612	.02
33.02	1.19	.547	.018

STATION NO. E28 x = 105.4 cm z = -15.24 cm

y, cm	y/δ	U_{eff}/U_{ref}	u_{eff}/U_{ref}
.127	.006	.121	.058
.203	.010	.13	.059
.305	.015	.138	.063
.406	.020	.142	.062
.508	.025	.149	.066
.635	.032	.157	.068
.762	.038	.165	.072
1.02	.051	.177	.078
1.27	.064	.188	.083
1.52	.076	.203	.091
2.03	.102	.225	.098
2.54	.127	.244	.109
3.05	.153	.267	.112
3.56	.178	.285	.118
4.06	.204	.308	.123
4.57	.229	.333	.127
5.08	.254	.359	.129
6.35	.318	.426	.129
7.62	.382	.478	.123
8.89	.445	.546	.107
10.16	.509	.604	.091
12.7	.636	.698	.059
15.24	.763	.752	.031
17.78	.890	.765	.021
20.32	1.02	.76	.017
22.86	1.14	.752	.017

*DATA OBTAINED FROM HOT-FILM PROBE ROTATED 180 DEGREES

TABLE V   HOT-FILM TRAVERSE DATA   (Cont'd)

86-4-82-6

STATION NO. __E31__ x = __119.4__ cm z = __-15.24__ cm

y, cm	y/δ	u_{eff}/U_{ref}	u'_{eff}/U_{ref}
.127	.010	.452	.094
.203	.017	.469	.095
.305	.025	.479	.091
.406	.033	.49	.09
.508	.042	.491	.09
.635	.052	.497	.089
.762	.062	.506	.089
1.02	.083	.513	.09
1.27	.104	.519	.092
1.52	.125	.53	.094
2.03	.166	.544	.096
2.54	.208	.568	.098
3.05	.249	.587	.1
3.56	.291	.603	.103
4.06	.333	.624	.1
4.57	.374	.648	.098
5.08	.416	.67	.094
6.35	.520	.725	.079
7.62	.624	.781	.056
8.89	.728	.823	.039
10.16	.832	.859	.028
12.7	1.04	.928	.021
14.224	1.16	.987	.022

$YP_U = 1.0$

STATION NO. __E34__ x = __140.3__ cm z = __-15.24__ cm

y, cm	y/δ	u_{eff}/U_{ref}	u'_{eff}/U_{ref}
.127	.011	.616	.096
.203	.018	.665	.098
.305	.026	.696	.097
.406	.035	.708	.096
.508	.044	.719	.091
.635	.055	.726	.089
.762	.066	.727	.088
1.02	.088	.735	.085
1.27	.110	.738	.085
1.52	.132	.743	.085
2.03	.176	.747	.087
2.54	.220	.753	.09
3.05	.264	.764	.092
3.56	.308	.769	.092
4.06	.352	.778	.093
4.57	.396	.79	.092
5.08	.440	.799	.09
6.35	.550	.831	.076
7.62	.660	.849	.066
8.89	.770	.863	.05
10.16	.880	.871	.035
12.7	1.10	.877	.023
13.97	1.21	.873	.024

STATION NO. __V2__ x = __7.6__ cm z = __15.24__ cm

y, cm	y/δ	u_{eff}/U_{ref}	u'_{eff}/U_{ref}
.127	.014	.547	.075
.203	.022	.585	.075
.305	.033	.622	.075
.406	.044	.646	.074
.508	.054	.667	.074
.635	.068	.684	.073
.762	.082	.703	.072
1.02	.109	.729	.07
1.27	.136	.753	.067
1.52	.163	.774	.064
2.03	.218	.812	.058
2.54	.272	.839	.054
3.05	.326	.868	.049
3.56	.381	.891	.044
4.06	.435	.912	.039
4.57	.489	.934	.035
5.08	.544	.949	.029
6.35	.680	.975	.018
7.62	.816	.986	.009
8.89	.952	.991	.008
10.16	1.09	.991	.008
12.7	1.36	.994	.007
15.24	1.63	1.001	.007
17.78	1.90	1.004	.029
19.94	2.13	.993	.059

STATION NO. __V6__ x = __26.7__ cm z = __15.24__ cm

y, cm	y/δ	u_{eff}/U_{ref}	u'_{eff}/U_{ref}
.127	.013	.397	.084
.203	.020	.429	.089
.305	.030	.464	.091
.406	.041	.49	.09
.508	.051	.512	.09
.635	.063	.534	.087
.762	.076	.555	.087
1.02	.101	.591	.083
1.27	.127	.616	.081
1.52	.152	.64	.076
2.03	.203	.686	.071
2.54	.253	.729	.064
3.05	.304	.761	.059
3.56	.355	.795	.052
4.06	.405	.823	.044
4.57	.456	.847	.038
5.08	.507	.867	.032
6.35	.634	.906	.019
7.62	.760	.924	.012
8.89	.887	.943	.009
10.16	1.01	.959	.009
12.7	1.27	.992	.008
15.24	1.52	1.057	.01
17.78	1.77	1.102	.017
20.07	2.00	1.035	.056

$YP_U = 1.0$

STATION NO. __V11__ x = __40.6__ cm z = __15.24__ cm

y, cm	y/δ	u_{eff}/U_{ref}	u'_{eff}/U_{ref}
.127	.009	.108	.055
.203	.015	.116	.058
.305	.023	.127	.063
.406	.030	.134	.068
.508	.038	.144	.073
.635	.047	.154	.08
.762	.057	.168	.088
1.02	.075	.19	.1
1.27	.094	.223	.113
1.52	.113	.25	.122
2.03	.151	.309	.131
2.54	.188	.359	.135
3.05	.226	.424	.128
3.56	.264	.474	.119
4.06	.301	.523	.109
4.57	.339	.558	.105
5.08	.377	.603	.088
6.35	.471	.69	.064
7.62	.565	.755	.044
8.89	.659	.799	.026
10.16	.753	.827	.014
12.7	.942	.86	.009
15.24	1.13	.891	.009
17.78	1.32	.921	.008
20.32	1.51	.948	.008
22.86	1.70	.958	.022
25.4	1.88	.83	.044

$YP_U < 1.0$; $YP_U = 1.0$

STATION NO. __V18__ x = __67.3__ cm z = __15.24__ cm

y, cm	y/δ	u_{eff}/U_{ref}	u'_{eff}/U_{ref}
.127	.004	-.138*	.061*
.203	.006	-.152*	.064*
.305	.009	-.16*	.063*
.406	.012	-.165*	.065*
.508	.016	-.171*	.065*
.635	.019	-.17 *	.065*
.762	.023	-.169*	.063*
1.02	.031	-.173*	.062*
1.27	.039	-.17 *	.06 *
1.52	.047	-.174*	.064*
2.03	.062	-.147*	.062*
2.54	.078	-.16 *	.063*
3.05	.093	-.155*	.063*
3.56	.109	-.15 *	.065*
4.06	.124	-.147*	.063*
4.57	.140	-.142*	.061*
5.08	.155	-.14 *	.065*
		.125	.059
6.35	.194	-.131*	.061*
		.127	.042
7.62	.233	-.134*	.063*
		.13	.065
8.89	.272	-.145*	.071*
		147	.079
10.16	.311	-.167*	.088*
		.17	.094
12.7	.388	.256	.131
15.24	.466	.364	.153
17.78	.544	.46	.153
20.32	.621	.563	.133
22.86	.699	.63	.085
25.4	.777	.632	.045
27.94	.854	.597	.026
30.48	.932	.548	.02
33.02	1.01	.509	.015

$YP_U < 1.0$; $YP_U = 1.0$

*DATA OBTAINED FROM HOT-FILM PROBE ROTATED 180 DEGREES

TABLE V   HOT-FILM TRAVERSE DATA   (Cont'd)

STATION NO. W24   x = 90.2 cm z = 15.24 cm

y, cm	y/δ	u_{eff}/u_{ref}	u_{eff}/u_{ref}
.127	.004	-.196*	.082*
.203	.007	-.204*	.081*
.305	.010	-.206*	.08 *
.406	.014	-.208*	.08 *
.508	.017	-.207*	.076*
.635	.021	-.208*	.075*
.762	.026	-.202*	.073*
1.02	.034	-.198*	.073*
1.27	.043	-.193*	.072*
1.52	.051	-.189*	.07 *
2.03	.068	-.181*	.069*
2.54	.085	-.178*	.07 *
3.05	.103	-.173*	.07 *
3.56	.120	-.17 *	.07 *
4.06	.137	-.168*	.071*
4.57	.154	-.165*	.072*
5.08	.171	-.162*	.073*
		.161	.072
6.35	.214	-.159*	.076*
		.159	.077
7.62	.256	-.16 *	.08 *
		.166	.083
8.89	.299	-.172*	.088*
		.181	.091
10.16	.342	-.192*	.094*
		.21	.1
12.7	.427	.282	.111
15.24	.513	.401	.109
17.78	.598	.521	.094
20.32	.684	.612	.07
22.86	.769	.665	.039
25.4	.855	.664	.024
27.94	.940	.633	.022
30.48	1.03	.592	.018
33.02	1.11	.549	.017

STATION NO. W28   x = 105.4 cm z = 15.24 cm

y, cm	y/δ	u_{eff}/u_{ref}	u_{eff}/u_{ref}
.127	.006	.128	.059
.203	.010	.135	.062
.305	.015	.143	.064
.406	.020	.15	.065
.508	.025	.155	.067
.635	.032	.161	.07
.762	.038	.169	.072
1.02	.051	.178	.077
1.27	.064	.191	.081
1.52	.076	.203	.087
2.03	.102	.225	.097
2.54	.127	.243	.104
3.05	.153	.259	.111
3.56	.178	.278	.117
4.06	.204	.3	.122
4.57	.229	.318	.128
5.08	.254	.341	.131
6.35	.318	.385	.132
7.62	.382	.45	.127
8.89	.445	.515	.117
10.16	.509	.583	.103
12.7	.636	.696	.065
15.24	.763	.75	.03
17.78	.890	.761	.022
20.32	1.02	.758	.019
22.86	1.14	.751	.017

STATION NO. W31   x = 117.4 cm z = 15.24 cm

y, cm	y/δ	u_{eff}/u_{ref}	u_{eff}/u_{ref}
.127	.010	.446	.095
.203	.017	.462	.095
.305	.025	.472	.094
.406	.033	.483	.091
.508	.042	.487	.089
.635	.052	.494	.09
.762	.063	.502	.09
1.02	.084	.51	.09
1.27	.105	.516	.092
1.52	.125	.527	.094
2.03	.167	.54	.099
2.54	.209	.559	.102
3.05	.251	.575	.106
3.56	.293	.589	.107
4.06	.334	.611	.107
4.57	.376	.635	.107
5.08	.418	.66	.103
6.35	.523	.707	.093
7.62	.627	.775	.071
8.89	.732	.825	.048
10.16	.834	.865	.032
12.7	1.05	.945	.024
14.22	1.17	1.006	.023

(annotation: $Y_{P_U} = 1.0$)

STATION NO. W34   x = 140.3 cm z = 15.24 cm

y, cm	y/δ	u_{eff}/u_{ref}	u_{eff}/u_{ref}
.127	.010	.614	.099
.203	.017	.641	.1
.305	.025	.673	.099
.406	.034	.69	.097
.508	.042	.697	.094
.635	.052	.704	.092
.762	.063	.707	.091
1.02	.084	.712	.088
1.27	.105	.718	.088
1.52	.126	.719	.089
2.03	.168	.725	.091
2.54	.209	.731	.094
3.05	.251	.736	.096
3.56	.293	.745	.099
4.06	.335	.754	.101
4.57	.377	.764	.1
5.08	.419	.774	.099
6.35	.524	.798	.092
7.62	.628	.826	.078
8.89	.733	.847	.061
10.16	.838	.859	.045
12.7	1.05	.869	.026
13.97	1.15	.87	.025

*DATA OBTAINED FROM HOT-FILM PROBE ROTATED 180 DEGREES

TABLE V   HOT-FILM TRAVERSE DATA   (Cont'd)

86-4-82-8

TABLE VI

STREAMLINE COORDINATES DETERMINED FROM LASER VELOCIMETER MEAN VELOCITY DATA

STREAMLINE NO.	X LOCATION																
	26.7	31.8	40.6	48.3	52.1	55.9	59.7	67.3	74.9	82.6	90.2	97.8	105.4	113.0	119.4	140.3	(cm)
	10.5	12.5	16.0	19.0	20.5	22.0	23.5	26.5	29.5	32.5	35.5	38.5	41.5	44.5	47.0	55.25	(in.)
1	0.00	0.00	0.00	3.10	4.62	6.99	8.94	14.35	16.99	15.95	11.76	4.37	0.00	0.00	0.00	0.00	
2	1.27	1.55	2.77	5.56	7.14	9.37	11.20	16.54	19.08	18.16	14.45	8.66	3.84	1.85	1.32	1.07	
3	2.54	2.95	4.45	7.49	9.19	11.43	13.54	18.82	21.26	20.45	16.89	11.51	6.65	3.86	2.90	2.26	
4	3.81	4.32	6.05	9.25	11.05	13.46	15.77	21.03	23.39	22.61	19.08	14.07	9.17	5.89	4.55	3.61	
5	5.08	5.69	7.65	10.97	12.95	15.44	17.93	23.19	25.53	24.77	21.18	16.48	11.51	7.92	6.22	5.13	
6	6.35	7.06	9.17	12.70	14.73	17.35	19.96	25.30	27.64	26.92	23.24	18.75	13.72	9.83	7.87	6.68	
7	7.62	8.41	10.67	14.35	16.48	19.23	22.02	27.46	29.82	29.08	25.32	20.90	15.80	11.58	9.37	8.23	
8	8.89	9.73	12.14	15.98	18.21	21.13	24.16	29.72	32.11	31.32	27.53	23.04	17.83	13.31	10.80	9.73	
9	10.16	11.02	13.59	17.60	19.94			32.16			29.87	25.20	19.84	14.99	12.17	11.18	

Y-COORDINATE (cm)

TABLE VII
BACKFLOW BOUNDARY LAYER PARAMETERS

STATION NO.	x, cm	N, cm	U_N/U_{ref}	NU_τ/ν	C_f'	Re_θ	$C_f Re_\theta$	H
25	94.0	0.097	0.156	—	0.0221	38	0.84	1.98
24	90.2	0.15	0.191	—	0.0163	57	0.93	1.90
23	86.4	0.25	0.210	—	0.0149	62	0.92	1.87
22	82.6	0.50	0.202	—	0.0090	125	1.13	1.70
21	78.7	0.63	0.194	60	0.0124	111	1.38	1.59
20	74.9	0.50	0.192	125	0.0105	124	1.30	1.61
19	71.1	0.51	0.178	110	0.0081	184	1.49	1.60
18	67.3	0.76	0.154	155	0.0076	174	1.32	1.54
17	63.5	0.76	0.139	147	0.0074	158	1.17	1.55
16	59.7	0.76	0.126	132	0.0059	174	1.03	1.48

PARAMETERS FOR			240	0.00590	425	2.51	1.535
TURBULENT BOUNDARY LAYER			500	0.00426	1150	4.88	1.445
UNDER CONSTANT PRESSURE			1000	0.00340	2650	8.94	1.390
COLES (REF. 30)			2000	0.00290	5650	16.36	1.350

85−8−36−3

APPENDIX A

LASER VELOCIMETRY SYSTEM

A.1 System Description

The LV system (fig. 3-8) consisted of a 2W argon-ion laser, a backscatter optical system employing a Bragg cell and a 3.75X beam expander, a TSI 1990B counter type signal processor, a PDP 11/10 computer for on-line data reduction, and a 7.8 MB hard disk with integral 8 in floppy disk backup for data storage (and subsequent off-line data reduction). Traversing capability was achieved by mounting the laser and optical system on a lathe bed. All system components are commercially available.

The LV was operated in a dual beam or "fringe" mode in which light from the intersection of two incident beams is heterodyned to detect the Doppler shift from an injected seed particle moving, at the local, instantaneous fluid velocity. In this mode, the LV measures the velocity component in the plane of the incident beams that is perpendicular to the bisector of the beams. The effective shape of the resultant measurement volume is an ellipsoid with major axis in the direction of the bisector of the beams. Sketch A (p. 21) shows these features and the theoretical measurement volume dimensions assuming that the ellipsoidal surface is defined by the locus of points where Doppler signal amplitude is $1/e^2$ of its centerline value. No direct measurement of the effective measurement volume size was made; it can be effected by signal amplitude and the signal processor threshold level setting. To obtain maximum resolution, the major axis was aligned in the spanwise direction. Resolution of the LV system was quite high when compared to the relevant dimensions of the experiment. The minor axis of the measuring ellipsoid, d_m, was 1/850 of the inlet boundary layer thickness and the major axis was 1/560 of the test section width.

A.2 Optical System

The optical system, used a 3.75X beam expander, a relatively wide angle lens (κ = 4.9 deg), and 152 mm dia optics to produce a sufficiently high signal/noise ratio (SNR) to permit measurements to be made in the backscatter mode. The SNR was enhanced by a factor of 45 compared to an equivalent optical package using standard 50 mm dia optics without a beam expander. Focal length (762 mm) of the transmitting and collecting lens was set by the transverse dimensions of the test section. A 10 MHz Bragg shift was used to eliminate directional ambiguity and to provide 360 deg acceptance angle for all particle velocities. The 10 MHz Bragg shift was accomplished by upshifting the frequency of one incident beam by 40 MHz and downshifting the collected Doppler signal by 30 MHz.

A.3 Signal Processor

The TS1 1990B counter-type signal processor featured user selectable measurement modes, fringe count $\left(N_f = 2^N, \; N = 1 \text{ to } 7\right)$, validation accuracy (1% to 20% in 9 increments), input gain, and large amplitude signal rejection level (i.e. large particle discriminator). Four measurement modes were available: (1) continuous mode (CONT) in which a measurement is made each time the minimum number of cycles is satisfied; (2) single measurement per burst mode (SM/B); (3) total burst count mode (TBC) in which the number of cycles in the burst are the Doppler frequency of the first N_f cycles are measured; (4) total burst mode (TBM) in which the duration of the burst and number of cycles in the burst are measured. The CONT mode was used for all measurements reported herein and the SM/B mode was used at selected points for redundancy. The CONT mode was chosen to minimize individual realization bias errors (see discussion below). Note also the CONT mode data is a superset of SM/B data because CONT data can be processed using the measured time between data points as a discriminator to eliminate multiply counted samples per burst to yield SM/B data.

A.4 Data Processing and Storage

The time period and the time between samples for each CONT sample obtained in this test program has been stored and retained on floppy disks to permit future additional processing.

After trial-and-error testing the 32 fringe count setting was found to yield an optimal combination of high data rate and "clean" histograms having minimal spurious data points in the tails. In this setting data validation is performed by making a 5/8 comparison between the time period for 20 cycles and the time period for 32 cycles. Validation accuracy was chosen to be 2% which permitted signals from seed particles following turbulence fluctuations up to approximately 25 kHz to be accepted. The signal gain and large amplitude signal rejection level were adjusted to reject 10 to 25% of the Doppler bursts to eliminate particle by biasing.

Based upon the uncertainty analysis in Appendix C and the large turbulence levels generated by the separation bubble, 2000 samples were acquired per data point to generate velocity histograms for mean velocity and turbulence intensity measurements. For Reynolds stress measurements the previously measured local turbulence intensity was used to determine whether 2000, 4000, or 8000 samples per data point were required to obtain the desired accuracy. Additional details concerning LV data processing are given in Appendix C.

A.5 Seeding System

Titanium dioxide powder having a nominal particle size of 1.0 μm was dispersed into the tunnel airstream to provide highly reflective light scattering centers for LV measurements using a fluidized bed seeding system driven by a low pressure dry air supply. A mixture of titanium dioxide powder and Cab-o-Sil, a silicon deaglomerating agent, were fluidized in the seeder to produce a densely seeded airstream which was directed to the tunnel. The seed was injected into the tunnel just downstream of the aftermost turbulence suppression screen using a cylindrical seeder probe, shown in figure A-1, which was designed to minimize the disturbance to the tunnel airstream. A similarly configured probe, designated the "zero-wake seeder" has been developed independently by Simpson (ref. 55). In principle, the flowrate through the seeder is adjusted until the momentum of the seeded air injected into the base region of the cylinder equals the cylinder drag and eliminates the wake deficit. Optimal seeder probe operation was achieved using a dry air supply pressure of 7 psi. Residual turbulence in the seeder wake was reduced by the 4 to 1 tunnel contraction. Total pressure probing revealed no discernible wake deficit at the test section inlet during seeder operation. Similarly, hot-wire measurement showed no difference in freestream turbulence level at the test section inlet during seeder operation compared to the clean tunnel operation with the seeder probe out of the tunnel. As expected, the turbulence level was increased when the probe was in the flow but not operating.

The seeder probe produced a seed cloud having an approximately circular cross-section with a 12.7 cm dia at the test section inlet. During LV traversing upstream of separation the seeder probe was frequently repositioned to center the measuring volume within the seed cloud. Traverses downstream of separation required infrequent probe repositioning because of the rapid diffusion of the seed cloud within the separated flow. For off-centerline traverses the seeder probe was moved to an off-centerline location.
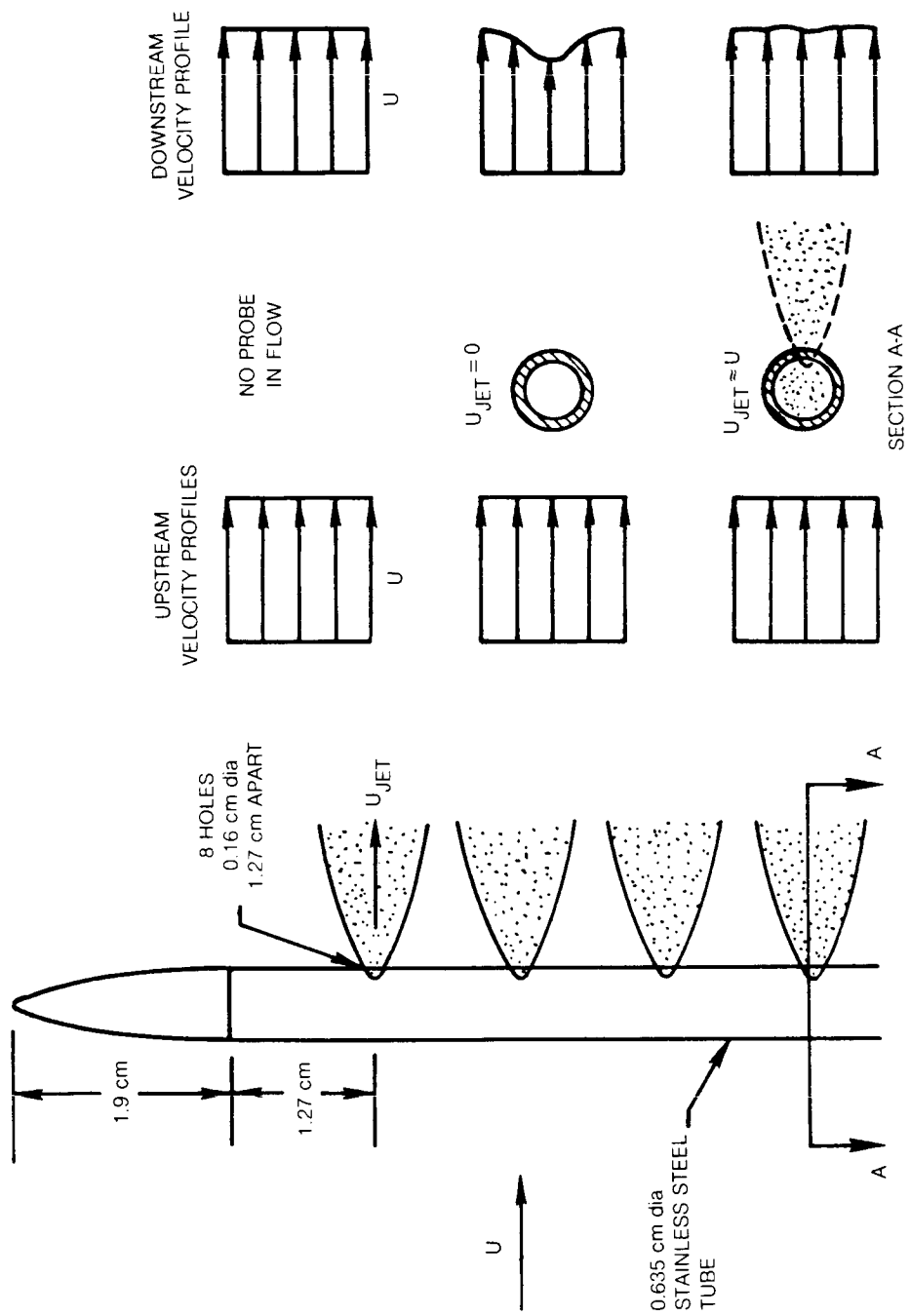
Figure A-1 Zero-Wake Seeding Probe

APPENDIX B

LASER VELOCIMETER DATA REDUCTION EQUATIONS

Figure B-1 below shows the four laser beam orientations used to extract axial and transverse velocity data with a vertical traverse of the LV measurement volume. $\tilde{\mathrm{U}}_1$, $\tilde{\mathrm{U}}_2$, $\tilde{\mathrm{U}}_3$, and $\tilde{\mathrm{U}}_4$ represent the magnitudes of the instantaneous velocity in the directions indicated by the sketch during a validated particle count. Velocities $\tilde{\mathrm{U}}_1$ and $\tilde{\mathrm{U}}_2$ were used to measure the axial and transverse velocity fields respectively. Velocities $\tilde{\mathrm{U}}_3$ and $\tilde{\mathrm{U}}_4$ were used primarily to determine the Reynolds stress $(\overline{uv})$ and secondarily to provide redundant axial and transverse mean velocity measurements. The angle ξ was a small 5 deg laser beam inclination angle required to obtain transverse velocity and Reynolds stress measurements near the test surface. The angles α_3 and α_4 were set at 45 deg for Reynolds stress measurements.

The desired axial and transverse velocities are related to the measured velocities by the following equations:

$$\tilde{\mathrm{U}}_1 = \tilde{\mathrm{U}} \tag{B1}$$

$$\tilde{\mathrm{U}}_2 = \tilde{\mathrm{V}}\cos\xi + \tilde{\mathrm{W}}\sin\xi \tag{B2}$$

$$\tilde{\mathrm{U}}_3 = \tilde{\mathrm{U}}\cos\alpha_3 - \tilde{\mathrm{V}}\sin\alpha_3\cos\xi - \tilde{\mathrm{W}}\sin\xi \tag{B3}$$

$$\tilde{\mathrm{U}}_4 = \tilde{\mathrm{U}}\cos\alpha_4 - \tilde{\mathrm{V}}\sin\alpha_4\cos\xi + \tilde{\mathrm{W}}\sin\xi \tag{B4}$$

Taking each velocity, $\tilde{\mathrm{U}}$, as the sum of a mean, U, and a fluctuating part, u(t), yields the mean velocity eqs. (B5) through (B8)

$$U = U_1 \tag{B5}$$

$$V = \frac{U_2}{\cos\xi} - W\tan\xi \tag{B6}$$

$$U = \frac{U_3 \sin\alpha_4 - U_4 \sin\alpha_3}{\cos\alpha_3 \sin\alpha_4 - \sin\alpha_3 \cos\alpha_4} + W \frac{\sin\xi \left(\sin\alpha_3 + \sin\alpha_4\right)}{\cos\alpha_3 \sin\alpha_4 - \sin\alpha_3 \cos\alpha_4} \qquad (B7)$$

$$V = \frac{U_4 \cos\alpha_3 - U_3 \cos\alpha_4}{\cos\xi\left(\cos\alpha_3 \sin\alpha_4 - \sin\alpha_3 \cos\alpha_4\right)} - W \frac{\tan\xi\left(\cos\alpha_3 + \cos\alpha_4\right)}{\cos\alpha_3 \sin\alpha_4 - \sin\alpha_3 \cos\alpha_4} \qquad (B8)$$

The measurement of U and V are redundant because eqs. (B5) and (B6) are independent from eqs. (B7) and (B8).

Evaluating eqs. (B7) and (B8) for α_3 = +45 deg and α_4 = -45 deg yields considerably simplified eqs. (B9) and (B10).

$$U = \frac{\sqrt{2}}{2} \left(U_3 + U_4\right) \qquad (B9)$$

$$V = \frac{\sqrt{2}}{2\cos\xi} \left(U_3 - U_4\right) - \sqrt{2}\, W\tan\xi \qquad (B10)$$

Squaring, time averaging, and subtracting the mean flow equations yields equations for the axial and transverse turbulence intensities.

$$\overline{u^2} = \overline{u_1^2} \qquad (B11)$$

$$\overline{v^2} = \frac{\overline{u_2^2}}{\cos^2\xi} - 2\,\overline{vw}\tan\xi - \overline{w^2}\tan^2\xi \qquad (B12)$$

and the Reynolds stress

$$\overline{uv} = \frac{1}{2\cos\xi}\left(\overline{u_4^2} - \overline{u_3^2}\right) - \sqrt{2}\,\overline{uw}\tan\xi \qquad (B13)$$

after setting α_3 = +45 deg and α_4 = -45 deg.

In evaluating equations (B6) and (B10-13) only the first terms on the right hand side were used. The additional correction terms, which contained

unmeasured spanwise velocity components, were very small because of the two-dimensionality of the flow ($W \simeq 0$) and the small inclination angle ($\xi = 5$ deg). Away from the immediate vicinity of the wall ($\xi = 0$) the correction terms disappeared.
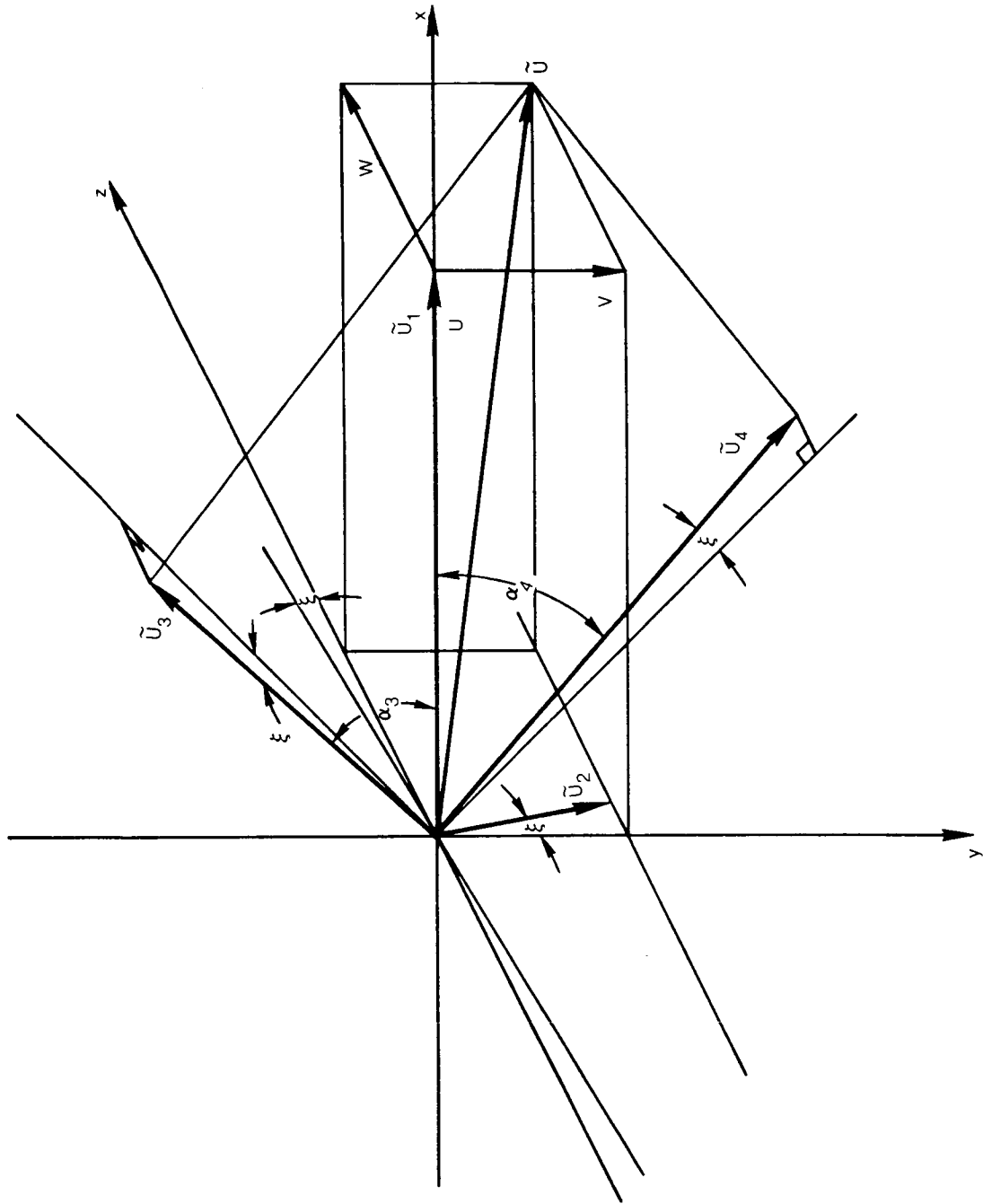
Figure B-1 LV Measurement Geometry

APPENDIX C

LV ERROR ANALYSIS

A procedure for quantifying LV measurement errors has been developed
(ref. 37) in conjunction with the present study as part of UTRC's independent
research activities in gas dynamics. This uncertainty analysis includes the
consideration of fixed (bias) and precision (random) errors and the methods
for calculating the propagation of measurement errors through the system.
Errors in the LV measurement system have been categorized as: (1) data
processing errors, (2) laser beam geometrical errors, (3) processor errors,
and (4) errors associated with seeding. Data processing errors arise from
averaging a finite number of data samples per data point. Processor errors
are the clock synchronization error, the quantizing error, the threshold limit
error, the pedestal removal filter error, and the electronic noise induced
errors. Laser beam geometrical errors include positioning uncertainty of the
probe volume, angular sensitivity of the probe volume, fringe spacing uncer-
tainty, and beam orientation errors, as well as, limitations imposed by a
finite-sized probe volume. Seeding errors include flow distortion caused by
seed injection, errors associated with the arrival rate of seed passing
through the probe volume (individual realization bias), and particle lag
errors in accelerating (or decelerating) flowfields.

In this Appendix the error analysis presented in reference 37 will be
summarized briefly. The error analysis methodology including the definition
of terms, the determination of measurement uncertainty, and the propagation of
measurement errors will be explained. Then, each error source will be
described briefly. Finally, values of the precision and bias errors for the
current experiment will be calculated and combined to determine estimates of
the total uncertainty of LV measurements throughout the flowfield.

C.1   Error Analysis Methodology

C.1.1 Definition of Terms

An error is the difference between the measurement and the true value of
the parameter being measured. Uncertainty is the maximum error which reason-
ably might be expected in a parameter which is measured or which is computed
from measured data. Measurement errors are of two types, random (or preci-
sion) errors and fixed (or bias) errors.

Random errors occur because of variations in repeated measurements of the
same parameter. The precision index, S, is an estimate of the random (or
precision) error. For N measurements $(X_1, X_2, \ldots, X_i, \ldots X_N)$ of the
parameter X the precision index is defined as

$$S = \sqrt{\frac{\displaystyle\sum_{i=1}^{N} (X_i - \bar{X})^2}{N - 1}} \qquad\qquad (C-1)$$

where $\bar{X}$, the mean of the measured values, is defined as

$$\bar{X} = \frac{1}{N} \sum_{i=1}^{N} X_i \qquad\qquad (C-2)$$

Bias is the fixed or systematic error. In repeated measurements, each measurement has the same bias, as illustrated in figure C-1. Examples of bias errors encountered in LV measurements are laser beam geometrical errors, process errors, and errors associated with seeding.

C.1.2 Determination of Measurement Uncertainty

The uncertainty is determined by combining the precision and bias errors in the following manner:

$$U = \pm (B + t_{95} S) \qquad\qquad (C-3)$$

where B is the bias limit and t_{95} is the 95th percentile point for the two-tailed Student's "t" distribution (ref. 56). When the bias limit is non-symmetric, upper ($U^+ = B^+ + t_{95} S$) and lower ($U^- = B^- - t_{95} S$) uncertainty limits are calculated. The t_{95} value is a function of the number of degrees of freedom used in calculating S as shown in Table C-1. In a sample, the number of degrees of freedom is the size of the sample. For a statistic calculated from the sample the number of degrees of freedom is reduced by one for every estimated parameter used in calculating the statistic. For example, the mean, $\bar{X}$, calculated from the sample (eq. (C-2)) has N degrees of freedom and the precision index, S, calculated from the mean (eq. (C-1)) has N-1 degrees of freedom.

C.1.3 Propagation of Measurement Error

Although only the uncertainty parameters, U, need be presented with the data, the bias and precision values are required to determine the propagation of the measurement error. The proper method for combining elemental measurement uncertainty values is to determine the root-sum-square values of the elemental bias limits and the elemental precision indices separately using a
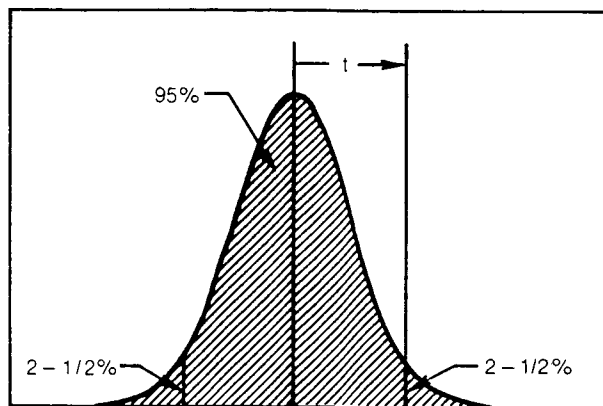
DEGREES OF FREEDOM	"t"	DEGREES OF FREEDOM	"t"
1	12.706	17	2.110
2	4.303	18	2.101
3	3.182	19	2.093
4	2.776	20	2.086
5	2.572	21	2.080
6	2.447	22	2.074
7	2.365	23	2.069
8	2.306	24	2.064
9	2.262	25	2.060
10	2.228	26	2.056
11	2.201	27	2.052
12	2.179	28	2.048
13	2.160	29	2.045
14	2.145	30	2.042
15	2.131		
16	2.120		
		31 OR MORE USE 2.0	

Table C-1 Two-Tailed Student's "t" Table

84-8-1-55

Taylor series expansion of the function being calculated from the elemental measurements. For example, the streamwise Reynolds stress, $\overline{\alpha\beta}$, is determined from measured values of the Reynolds stress, axial and transverse turbulence components, and the flow angle

$$\overline{\alpha\beta} = \overline{uv}\,(\cos^2\phi - \sin^2\phi) + (\overline{v^2} - \overline{u^2})\,\sin\phi\,\cos\phi \tag{C-4}$$

The precision index for the streamwise Reynolds stress, $S^{\overline{\alpha\beta}}$, can be determined as

$$S^{\overline{\alpha\beta}} = \left\{ \left[\frac{\partial(\overline{\alpha\beta})}{\partial(\overline{uv})}\,S^{\overline{uv}} \right]^2 + \left[\frac{\partial(\overline{\alpha\beta})}{\partial(\overline{v^2})}\,S^{\overline{v^2}} \right]^2 + \left[\frac{\partial(\overline{\alpha\beta})}{\partial(\overline{u^2})}\,S^{\overline{u^2}} \right]^2 + \left[\frac{\partial(\overline{\alpha\beta})}{\partial\phi}\,S^\phi \right]^2 \right\}^{1/2} \tag{C-5}$$

Performing the indicated differentiation yields

$$S^{\overline{\alpha\beta}} = \left\{ \left[(\cos^2\phi - \sin^2\phi)\,S^{\overline{uv}} \right]^2 + \sin^2\phi\,\cos^2\phi \left[\left(S^{\overline{u^2}}\right)^2 + \left(S^{\overline{v^2}}\right)^2 \right] \right.$$
$$\left. + \left[(\overline{v^2} - \overline{u^2})\,(\cos^2\phi - \sin^2\phi) - 4\overline{uv}\,\sin\phi\,\cos\phi \right]^2 \, \left(S^\phi\right)^2 \right\}^{1/2} \tag{C-6}$$

Similarly, the bias limit of the calculated streamwise Reynolds stress, $B^{\overline{\alpha\beta}}$, is propagated from the bias limits of the measured variables.

$$B^{\overline{\alpha\beta}} = \left\{ \left[\frac{\partial(\overline{\alpha\beta})}{\partial(\overline{uv})}\,B^{\overline{uv}} \right]^2 + \left[\frac{\partial(\overline{\alpha\beta})}{\partial(\overline{v^2})}\,B^{\overline{v^2}} \right]^2 + \left[\frac{\partial(\overline{\alpha\beta})}{\partial\overline{u^2}}\,B^{\overline{u^2}} \right]^2 + \left[\frac{\partial(\overline{\alpha\beta})}{\partial\phi}\,B^\phi \right]^2 \right\}^{1/2} \tag{C-7}$$

To propagate nonsymmetrical bias limits, the bias limit portion of the analysis must be completed for both the upper and the lower limits. The uncertainty in the calculated value of U is then determined by combining the bias and precision indices as shown in eq. (C-3).

C.2   Data Processing (Precision) Errors

Data processing errors are precision errors which arise from averaging a finite number of data samples per data point. In general, the precision error for any finite number of measurements of a fixed quantity can be calculated using eqs. (C-1) and (C-2). However, in LV velocity measurements, the velocity being measured does not remain constant during the sampling period but fluctuates due to turbulence. Thus, for LV measurements, equations (C-1) and (C-2) can be written in the form

$$S = \sqrt{\frac{\sum\limits_{i=1}^{N} (U_i - U)^2}{N-1}} \qquad (C-8)$$

$$U = \frac{1}{N} \sum\limits_{i=1}^{N} U_i \qquad (C-9)$$

where U_i is the velocity of the ith sample and U is the sample mean velocity which is an unbiased estimate of U_p, the population mean velocity. The precision (or random) error calculated by eq. (C-8) is an estimate of the rms turbulence level of the flow being sampled. In the limit of an infinite number of samples, S becomes an exact measurement of the turbulence level. For a finite number of samples both the indicated rms turbulence level calculated in eq. (C-8) and the mean sample velocity calculated in eq. (C-9) will deviate from the true turbulence level and mean velocity of the flowfield by precision errors S^ζ and S^U respectively.

C.2.1   Precision Errors in Turbulence Measurements

Since the mean square turbulence velocity has a Chi-squared distribution (ref. 57) S^ζ can be obtained from tables by entering the number of degrees of freedom, N-1. For a large sample size, however, the inconvenient tables are unnecessary since

$$\frac{S^\zeta}{\zeta} = \frac{1}{\sqrt{2N}} \qquad N > 50 \qquad (C-10)$$

Values of the precision error in turbulence measurement are calculated for various sample sizes typical of LV measurements in Table C-2. In the present study 2000 samples were taken to acquire each turbulence measurement. Thus, the precision error in the measurement of the turbulence component is ± 1.58 percent of the turbulence magnitude.

TABLE C-2.   PRECISION ERROR IN TURBULENCE
MEASUREMENT, S^ζ/ζ

N	S^ζ/ζ
500	.0316
1000	.0224
2000	.0158
4000	.0112
8000	.0079

C.2.2 Precision Errors in Mean Velocity Measurements

Relative to mean velocity measurements, the sampling distribution of U is normal about U_p as a mean with a standard deviation $u_p/\sqrt{N}$. Thus, the precision error in the mean velocity measurement can be estimated as

$$\frac{S^U}{U_p} = \frac{\zeta}{\sqrt{N}}$$

(C-11)

which is a function of the turbulence level. U_p and ζ are unknown but can be approximated by the measured quantities U and $\sqrt{u^2}/U$. Values of the precision error in mean velocity measurement for turbulence levels and sampling sizes typical of LV measurements are given in Table C-3. Note that both the

TABLE C-3.   PRECISION ERRORS IN MEAN VELOCITY
MEASUREMENT, $\dfrac{S^U}{U_{ref}} \times 10^2$

N	$\dfrac{\sqrt{u^2}}{U_{ref}} \times 100$			
	1%	5%	15%	25%
500	.045	.224	.671	1.118
1000	.032	.158	.474	.791
2000	.022	.112	.335	.559
4000	.016	.079	.237	.395
8000	.011	.056	.168	.280

precision error and the turbulence level have been normalized by U_{ref} to avoid extreme local turbulence levels which occur in regions of the flow where $U \simeq 0$. Since 2000 samples were acquired to obtain each mean velocity measurement, the precision error in mean velocity varies from $\pm$ 0.02% in regions of low turbulence intensity $\left(\sqrt{\overline{u^2}}/U_{ref} = 0.01 \right)$ to $\pm$ 0.56% in regions of high turbulence $\left(\sqrt{\overline{u^2}}/U_{ref} = 0.25 \right)$.

The precision error in Reynolds stress measurements obtained with a one-component LV system can be shown to be (ref. 37)

$$S_1^{\overline{uv}} = \sqrt{2} \; \zeta \; S^{\zeta} \qquad\qquad (C-12)$$

The precision error in the streamwise shear stress component, $\overline{\alpha\beta}$, can then be calculated using eq. (C-6). Calculated values of the precision error in the Reynolds stress and the streamwise shear stress measurements for each data point are presented in Table III.

C.3 Bias Errors

C.3.1 Laser Beam Geometrical Errors

C.3.1.1 Finite Probe Volume Bias (PVB)

Finite probe volume bias occurs because LV measurements represent a spatial average of the velocity throughout the probe volume rather than at a point in space. This bias error tends to increase the turbulence measurement and may increase or decrease the mean velocity measurement depending on the velocity gradients within the probe volume.

C.3.1.2 Beam Location Bias (BLB)

Beam location bias is caused by the uncertainty in positioning the probe volume within the test section. It can be calculated as the product of the estimated velocity or turbulence gradients and the positional uncertainty in the direction of the gradient.

C.3.1.3 Beam Orientation Bias (BOB)

Two types of bias errors arise from beam orientation errors. The first type, B_ε, which effects all measurements, is caused by misalignment of the laser beams relative to the rig axis. The second type, B_{45}, is caused by the uncertainty in setting $\pm$ 45 degree beam orientation during shear stress measurements.

C.3.1.4 Fringe Spacing Uncertainty (FSB)

This bias is due to the uncertainty in the fringe spacing caused by the error, $\Delta\kappa$, in setting the angle, κ, between the intersecting laser beams.

C.3.1.5 Negative Velocity Beam (NVB)

The laser velocimeter measures the relative speed between the seed particles in the flow and the fringes in the measurement volume. If the fringe pattern is stationary the LV system cannot discriminate between seed particles traveling in the positive or negative directions. The LV processor thus rectifies the velocity signal in the same manner as a hot-wire. Consequently, in flow fields containing regions or periods of flow reversal the ensemble-averaged velocity will be biased high and the turbulence level will be biased low. When a Bragg shift is used to move the fringes in the negative direction at a velocity greater than the maximum negative velocity, NVB is eliminated.

C.3.1.6 Incomplete Signal Bias (ISB)

Incomplete signal bias is caused by the angular sensitivity of the measurement volume. The probability that a seed particle passing through the measurement volume will cross the minimum number of fringes required to register a valid velocity sample decreases as the angle between the seed particle velocity vector and the normal to the fringe plane increases. Bragg shifting can be used, however, to achieve near isotropic response to eliminate ISB.

C.3.1.7 Frequency Broadening Bias (FBB)

Frequency broadening bias occurs when the laser beams do not intersect at the beam waists, where the wavefronts are plane, but elsewhere where the wavefronts have a finite radius of curvature. The resulting measurement volume has spatial variations in the fringe spacing. In a properly designed and aligned LV system the beams will intersect at the beam waists and frequency broadening will be eliminated.

C.3.2 Processor Bias Errors

C.3.2.1 Comparison Accuracy Biases (CAB)

Comparison accuracy biases occur in flows in which individual particle velocity changes within the probe volume normal to the fringe pattern are significant. When changes in velocity occur within the probe volume, the comparator on the LV processor may reject valid signals causing a bias. Two types of comparison accuracy biases are particle acceleration bias (PAB) which

can occur in strong acceleration or deceleration fields and comparator toler-
ance bias (CTB) which can occur in highly turbulent flows due to changes in
flow direction within the probe volume and/or particle velocity changes
induced by swirling turbulent eddies.

C.3.2.2 Clock Synchronization Error (CSB)

The clock synchronization error is the bias caused by the mismatch
between the randomly occurring Doppler burst and the start of the clock cycle
in the processor. The uncertainty ranges from 0 to -1 clock pulse with all
values in between being equally probable.

C.3.2.3 Quantizing Error (QB)

The quantizing error is the bias arising from the determination of the
frequency of the analog Doppler signal using the digital reference clock in
the processor. The quantized time interval determined by the clock is
accurate to within ±1 clock pulse with all values in between being equally
probable.

C.3.2.4 Threshold Limit Error (TLB)

The threshold limit error is the bias caused by the use of a non-zero
volt Schmitt trigger in the processor to digitize the Doppler burst. The
processor used in the current study used a true-zero-crossing detector which
eliminated this bias.

C.3.2.5 Electronic Noise Induced Error (ENB)

The electronic noise induced error is the bias which occurs at low
signal-to-noise ratios (SNR) when electronic noise mixed with the Doppler
signal causes incorrect LV measurements. This bias can be significantly
reduced by data validation circuitry within the processor and by operating at
SNR > 5.

C.3.2.6 Pedestal Filter Removal Error (PFB)

This error is caused by the improper setting of the cutoff frequency of
the high-pass pedestal removal filter. If the cutoff frequency is set too
high, the Doppler burst caused by a low velocity particle will be distorted by
the filter or even dropped out causing the velocity estimate from the LV
processor to become biased high. If the cutoff frequency is at too low, some
high velocity bursts will pass through the filter with residual pedestals
causing a biased velocity estimate of the distorted frequency packet.

C.3.3 Seeding Bias Errors

C.3.3.1 Flow Distortion Bias (FDB)

Flow distortion bias occurs when the mean flowfield is distorted by the seed injection process. Small seed particles, which have been sized to follow the flow, cannot be dispersed across the tunnel cross section except by natural diffusion. They cannot be projected across flow streamlines but instead must be convected with the seed injection jet.

C.3.3.2 Particle Lag Bias (PLB)

The accuracy of LV flow velocity measurements is limited by the ability of the seed particles, which reflect the laser light, to move at the same velocity as the surrounding fluid. When the seed particles are too large to accurately follow rapid oscillations in the flowfield, particle lag bias occurs.

C.3.3.3 Individual Realization Bias (IRB)

If the seed particles are distributed uniformly in space the number of particles passing through a unit volume in the flowfield varies directly with the particle velocity. High velocity regions of the flow contribute more LV samples per unit time than low velocity regions. In a shear layer or in turbulent flow the LV probe volume will span a region of the flow having both high and low flow velocities. In such cases the ensemble average velocity will be larger than the time-mean velocity of the flow because of the increased number of high velocity samples in the ensemble. A detailed discussion of this individual realization bias and correction schemes to reduce it are presented in reference 37.

C.3.3.4 Bragg Bias (BB)

When the LV processor is operated in a continuous sampling mode while a Bragg shift is used to move the fringe pattern, slower particles will be multiply sampled more often than faster particles because they spend more time in the probe volume. This effect has been termed Bragg bias and it partially offsets individual realization bias.

C.4 Determination of Total Uncertainty

Before the uncertainty of LV measurements could be evaluated using the equations and graphs given in reference 37, the parameter values listed in Table C-4 were estimated. These parameter values included probe volume dimensions, processor settings, seed particle characteristics, estimates of the

TABLE C-4
PARAMETER VALUES USED IN LV ERROR ANALYSIS

FLOW PARAMETERS:

U_{max} = 27.4 m/sec, V_{max} = 12.2 m/sec, $W = 0$, $\phi = 30$ deg

$$\left.\frac{\Delta U}{\Delta x}\right|_{max} = 100/sec, \quad \left.\frac{\Delta U}{\Delta y}\right|_{max} = 1920/sec, \quad \frac{\Delta U}{\Delta z} = 0$$

$$\left.\frac{\Delta V}{\Delta x}\right|_{max} = 200/sec, \quad \left.\frac{\Delta V}{\Delta y}\right|_{max} = 100/sec, \quad \frac{\Delta V}{\Delta z} = 0$$

$$\frac{\Delta W}{\Delta x} = \frac{\Delta W}{\Delta y} = \frac{\Delta W}{\Delta z} = 0$$

$$\left.\frac{1}{\zeta}\frac{\partial \zeta_x}{\partial x}\right|_{max} = 55/m \quad \left.\frac{1}{\zeta}\frac{\partial \zeta_y}{\partial x}\right|_{max} = 25/m \quad \left.\frac{1}{\zeta}\frac{\partial \zeta_z}{\partial x}\right|_{max} = 45/m$$

$$\left.\frac{1}{\zeta}\frac{\partial \zeta_x}{\partial y}\right|_{max} = 160/m \quad \left.\frac{1}{\zeta}\frac{\partial \zeta_y}{\partial y}\right|_{max} = 32/m \quad \left.\frac{1}{\zeta}\frac{\partial \zeta_z}{\partial y}\right|_{max} = 1/m$$

$$\frac{1}{\zeta}\frac{\partial \zeta_x}{\partial z} = \frac{1}{\zeta}\frac{\partial \zeta_y}{\partial z} = \frac{1}{\zeta}\frac{\partial \zeta_z}{\partial z} = 0$$

BEAM GEOMETRY:

$M = 32$, $N_f = 44$, $f_B = 10.16$ MHz, SNR = 40

$d_m = 133 \mu m$, $\ell_m = 1.6$ mm, $d_f = 3 \mu m$

$\Delta x = \pm 2$ mm, $\Delta y = \pm .025$ mm, $\Delta z = \pm 1$ mm, $\Delta \phi = \pm .25$ deg

$\kappa = 4.9$ deg, $\Delta \kappa = \pm .01$ deg

PROCESSOR PARAMETERS: $f_c = 500$ MHz, COMP = 0.02, N = 2000

SEED PARAMETERS: SEED MATERIAL, TiO_2: $d_p = 1 \mu m$

maximum mean flow and turbulence gradients in each of the three coordinate directions, and uncertainties in laser beam positioning, orientation, and intersection angle. Each of the precision and bias errors discussed in the previous sections has been evaluated to determine estimates for the total uncertainty of LV measurements of U, V, $\sqrt{\overline{u^2}}$, and $\sqrt{\overline{v^2}}$. The uncertainties for U and $\sqrt{\overline{u^2}}$ measurements have been estimated for regions of the flowfield having moderate ($\sqrt{\overline{u^2}}/U_{ref} = 0.05$) and high ($\sqrt{\overline{u^2}}/U_{ref} = 0.20$) axial turbulence levels. The uncertainties for V and $\sqrt{\overline{v^2}}$ measurements have been estimated for regions of the flowfield having an intermediate transverse turbulence level ($\sqrt{\overline{v^2}}/U_{ref} = 0.10$). Values for each error source and the total uncertainties are listed in Table C-5.

When evaluating the uncertainties several biases were assumed to be negligible. They are the pedestal removal filter error (PFB), the threshold limit error (TLB), the finite probe volume bias (PVB), particle acceleration bias (PAB), negative velocity bias (NVB), frequency broadening bias (FBB), and flow distortion bias (FDB). The negligible values for these biases follow respectively from the following assumptions: the pedestal removal filter has been set correctly, the processor has a true-zero-crossing detector, the probe volume is small compared to any spatial velocity gradients in the flowfield (PVB and PAB), Bragg shifting was used in regions of reversed flow, the laser beams intersected at the beam waists, and the zero-wake seeder probe caused negligible flowfield distortion at the measurement location.

As shown in Table C-5, none of the processor bias errors exceeds $^{+.06}_{-.01}$ percent. For mean velocity measurements beam geometry biases are also very low, the highest being the ± 0.7% bias due to uncertainty in probe volume location (BLB). The combined effect of seed bias errors on the mean velocity uncertainty is also very small. Particle lag bias, estimated from figure 8 in reference 37, is approximately 0.1 percent in both U and V components. The individual realization bias in the U component measurement would have been large ($^{+0.040}_{-0}$) in regions of high turbulence level ($\sqrt{\overline{u^2}}/U_{ref} = 0.20$) but it was offset by Bragg bias because the processor was operated in the continuous sampling mode. Thus, the total bias from all sources is ± 0.0080 and $^{+0.013}_{-0.0087}$ for U and V measurements, respectively. When combined with the precision error estimated for 2000 sample measurements, the uncertainty in LV measurements of U is ± 0.010 and ± 0.017 in regions of moderate ($\sqrt{\overline{u^2}}/U_{ref} = 0.05$) and high ($\sqrt{\overline{u^2}}/U_{ref} = 0.20$) turbulence, respectively. The estimated uncertainty in the transverse velocity is $^{+0.016}_{-0.012}$ in regions of intermediate transverse turbulence ($\sqrt{\overline{v^2}}/U_{ref} = 0.10$). This uncertainty value means that 19 out of every 20 mean velocity measurements will be within these quoted accuracies as noted above in Section C.1.2.

TABLE C-5

ESTIMATED BIAS ERRORS, PRECISION ERRORS, AND UNCERTAINTIES OF LV MEASUREMENTS

PROCESSOR BIAS ERRORS	$U(\frac{\sqrt{\overline{u'^2}}}{U_{ref}} = 0.20)$	$U(\frac{\sqrt{\overline{u'^2}}}{U_{ref}} = 0.05)$	$V(\frac{\sqrt{\overline{u'^2}}}{U_{ref}} = 0.10)$	$\frac{\sqrt{\overline{u'^2}}}{U_{ref}} = 0.20$	$\frac{\sqrt{\overline{u'^2}}}{U_{ref}} = 0.05$	$\frac{\sqrt{\overline{u'^2}}}{U_{ref}} = 0.10$
1. PARTICLE ACCELERATION BIAS (PAB)	0	0	0	0	0	0
2. COMPARATOR TOLERANCE BIAS (CTB)	0	0	0	0	0	0
3. CLOCK SYNCHRONIZATION ERROR (CSB)	+0.00064 / -0	<0.01%	+0.00030 / -0	+0.00058 / -0	+0.00060 / -0	+0.00046 / -0
4. QUANTIZING ERROR (QB)	<0.01%	<0.01%	<0.01%	<0.01%	<0.01%	<0.01%
5. THRESHOLD LIMIT ERROR (TLB)	0	<0.01%	0	0	0	0
6. ELECTRONIC NOISE INDUCED ERROR (ENB)	<0.01%	<0.01%	<0.01%	<0.01%	<0.01%	<0.01%
7. PEDESTAL FILTER REMOVAL ERROR (PFB)	0	0	0	0	0	0
PROCESSOR BIAS (PB)	+0.00064 / -0	<0.01%	+0.0003 / -0	+0.0006 / -0	+0.0006 / -0	+0.0005 / -0
BEAM GEOMETRY BIAS ERRORS						
1. FINITE PROBE VOLUME BIAS (PVB)	0	0	0	0	0	0
2. BEAM LOCATION BIAS (BLB)	±0.0075	±0.0075	±0.0073	±0.0551	±0.0551	±0.025
3. BEAM ORIENTATION BIAS (BOB)	±0.0019	±0.0019	±0.0044	±0.0035	±0.0035	±0.0052
4. FRINGE SPACING (UNCERTAINTY (FSB)	±0.0020	±0.0020	±0.00089	±0.0020	±0.0020	±0.0020
5. NEGATIVE VELOCITY BIAS (NVB)	0	0	0	0	0	0
6. INCOMPLETE SIGNAL BIAS (ISB)	0	0	0	0	0	0
7. FREQUENCY BROADENING BIAS (FBB)	0	0	0	0	0	0
BEAM GEOMETRY BIAS (BGB)	±0.0008	±0.0008	±0.0086	±0.0552	±0.0552	±0.0256
SEEDING BIAS ERRORS						
1. FLOW DISTORTION BIAS (FDB)	0	0	0	0	0	0
2. PARTICLE LAG BIAS (PLB)	±0.0008	±0.0008	+0.0013	0	0	0
3. INDIVIDUAL REALIZATION BIAS (IRB)	+0.040 / -0	+0.0025 / -0	+0.010 / -0	+0 / -0.050	+0 / -0.005	+0 / -0.010
4. BRAGG BIAS (BB)	+0 / -0.040	-0 / -0.0025	0	0	0	0
SEEDING BIAS (SB)	±0.0008	±0.0008	+0.010 / -0.0013	+0 / -0.050	+0 / -0.005	+0 / -0.010
TOTAL BIAS (B)	±0.0080	±0.0080	+0.013 / -0.0087	+0.0552 / -0.0745	+0.0552 / -0.0554	+0.0362 / -0.0275
PRECISION ERROR	±0.00447	±0.00112	±0.00158	±0.0158	±0.0158	±0.0158
TOTAL UNCERTAINTY (U)	±0.0169	±0.0102	+0.0162 / -0.0119	+0.087 / -0.106	+0.087 / -0.087	+0.068 / -0.059

For turbulence measurements, the bias errors are expressed as a fraction of the maximum turbulence intensity $\left(\zeta_{max} = 0.25 \ U_{ref}\right)$. Beam geometry biases are small except for the beam location bias which is estimated to be $\pm$ .055 and $\pm$ .025 for measurements of axial and transverse turbulence components, respectively. This is a worst-case estimate, assuming the maximum positioning uncertainty occurs at the location of the maximum turbulence gradient. The effect of particle lag on turbulence measurements is negligible since the 1.0 μm dia. TiO_2 seed particles can track at 2500 Hz sinusoidal oscillation to an accuracy better than 1% and most of the energy in the turbulence spectrum was in the 0-100 Hz band (fig. 4-15). The individual realization bias is estimated to be as high as $^{+0}_{-0.050}$ for axial turbulence component measurements in the high turbulence $\left(\sqrt{\overline{u^2}}/U_{ref} = 0.20\right)$ environment but throughout most of the flowfield IRB is less than 1%. It is assumed that Bragg bias did not effect the turbulence measurements.

When combined with the precision error ($\pm$ 0.0158) estimated for a 2000 sample measurement, the uncertainty in the measurement of the axial turbulence component is $\pm$ 0.087 and $^{+0.087}_{-0.106}$ in regions of moderate and high turbulence levels, respectively. The estimated uncertainty in the transverse turbulence component measurement is $^{+0.068}_{-0.059}$ in regions of intermediate transverse turbulence level. As noted above, these uncertainty estimates are expressed as fractions of the maximum turbulence intensity $\left(\zeta_{max} = 0.25 \ U_{ref}\right)$ and are worst-case estimates.
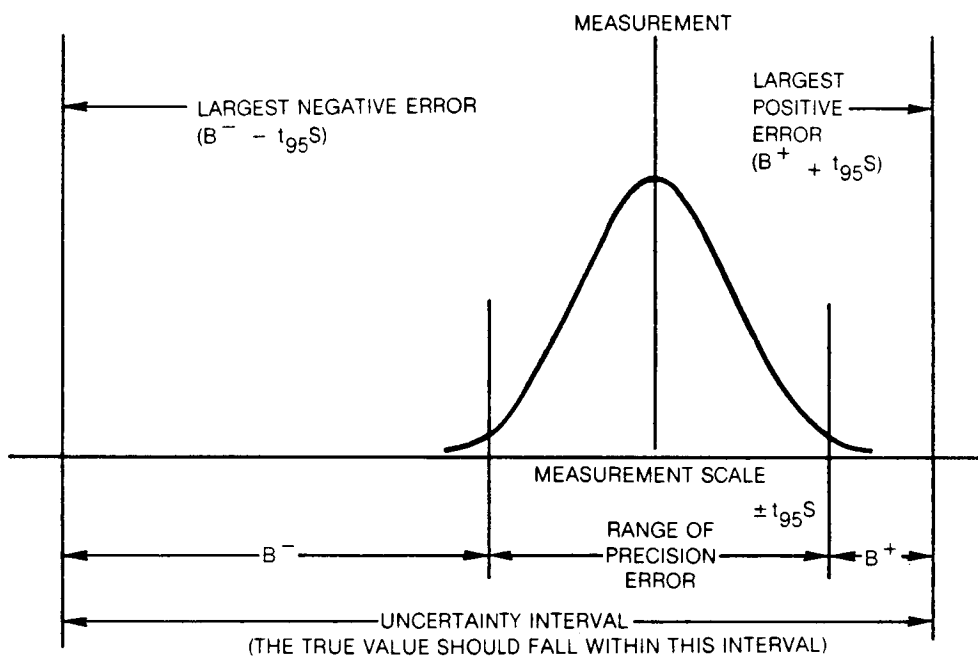
Fig. C-1 Measurement Uncertainty, Nonsymmetrical Bias

APPENDIX D

ERROR ESTIMATES FOR TOTAL PRESSURE AND HOT-FILM MEASUREMENTS

D.1 Accuracy of Total Pressure Measurements

The accuracy of the total pressure measurements is dependent on several factors including the accuracy of the pressure transducers, the angular sensitivity of the pitot probes, and the effect of turbulence on the pitot reading. Each of these factors will be discussed below.

D.1.1 Transducer Calibrations

Pressure transducers were calibrated to an accuracy of $\pm$ 0.0005 Q_{ref} with a micromanometer (fig. 3-9) at the beginning of each test day. Transducer output voltages were zeroed prior to each traverse to compensate for thermal drift. Zeroes were also checked after each traverse to ensure that drift during the traverse did not exceed $\pm$ 0.002 Q_{ref} otherwise the data was retaken.

D.1.2 Angular Sensitivity of Probes

The total pressure probes were calibrated for angular sensitivity in pitch and yaw over a $\pm$ 30 deg. range at three dynamic pressures: Q_{ref}, 0.45 Q_{ref}, and 0.09 Q_{ref}. The boundary layer probes were accurate to within 1% of the dynamic head pressure over $\pm$ 7 deg. relative to the normal to the probe shaft. The aspirated kielhead probes were accurate to within 0.005 Q_{ref} over $\pm$ 26 deg. relative to the normal to the face of the probe. The angular sensitivity of all probes used in the current study were essentially uneffected by flow speed over the range tested.

Since the boundary layer probes were only used to obtain data near the test surface (y < 2 cm) where the mean flow inclination angle was within the $\pm$ 7 deg. acceptance angle range of the probe, the angular sensitivity bias error in boundary layer pitot measurements is less than $^{+0}_{-0.01}$ Q_{ref} except near separation and reattachment. In those regions, the mean flow inclination angles exceeded the probe acceptance angle and frequent flow reversals added to measurement uncertainty. The angular sensitivity bias error in kielhead measurements is better than $^{+0}_{-0.005}$ Q_{ref} throughout the flowfield because of the large acceptance angle of the aspirated kielhead probe and because the probe was bent when necessary prior to traversing to optimize its alignment with the mean flow direction known beforehand from smoke flow visualization (see figure 4-6).

D.1.3 Effect of Turbulence on Pitot Readings

The instantaneous total pressure at a point in the flowfield can be
expressed as

$$\tilde{P} = p + \frac{1}{2} \rho \; (\tilde{U}^2 + \tilde{V}^2 + \tilde{W}^2) \qquad\qquad \text{(D-1)}$$

where $\tilde{U}$, $\tilde{V}$, and $\tilde{W}$ are the magnitudes of the instantaneous velocities in the
axial, transverse, and spanwise directions, respectively. These instantaneous
velocities can be assumed to be comprised of a time-mean component plus a
sinusoidally oscillating unsteady component

$$\tilde{U} = U + 2u \sin \omega t \qquad\qquad \text{(D-2a)}$$

$$\tilde{V} = V + 2v \sin \omega t \qquad\qquad \text{(D-2b)}$$

$$\tilde{W} = W + 2w \sin \omega t \qquad\qquad \text{(D-2c)}$$

Substituting eqs. (D-2) into eq. (D-1) and time averaging yields

$$P = p + \frac{1}{2} \rho \; (U^2 + V^2 + W^2 + \overline{u^2} + \overline{v^2} + \overline{w^2}) \qquad\qquad \text{(D-3)}$$

Thus, when a pitot tube is used in a turbulent stream its reading can
exceed the total pressure corresponding to the mean flow by an amount propor-
tional to the mean kinetic pressure of the turbulent velocity fluctuations,
$1/2 \; \rho \; (\overline{u^2} + \overline{v^2} + \overline{w^2})$. Goldstein (ref. 58) suggested that the pitot reading
should be corrected by the entire turbulent kinetic pressure. However, the
magnitude of any correction should depend on the scale as well as the inten-
sity of the turbulence fluctuations (ref. 59).

In the current study, the turbulence scale is large compared to the
diameter of the pitot probes employed. The flow approaches the probe at
randomly varying inclination angles due to turbulence fluctuations. Such
inclination angles can be quite large for turbulence intensities at which the
mean kinetic pressure, ΔP_t, is significant as shown in Table D-1. For
example, at a 7.5 percent turbulence level having a mean kinetic pressure of
$0.0169 \; Q_{ref}$, the flow angle occasionally exceeds the ± 30 deg. acceptance of

TABLE D-1. MAXIMUM FLOW ANGLES INDUCED BY TURBULENT FLUCTUATIONS

$$\left(U = .5 \ U_{ref}, \ V = W = 0, \ \sqrt{\overline{u^2}} = \sqrt{\overline{v^2}} = \sqrt{\overline{w^2}}\right)$$

$\dfrac{\sqrt{\overline{u^2}}}{U_{ref}}$	$\dfrac{\Delta P_t}{Q_{ref}}$	ϕ_{max} (deg)
0	0	0
.025	.0019	±8.9
.050	.0075	±19.5
.075	.0169	±31.2
.100	.030	±43.3
.125	.047	±54.7

the aspirated kielhead probes. At such large inclination angles the pitot probe would read low causing the time-averaged pitot reading to exceed the total pressure corresponding to the static pressure and the mean flow by an amount which is less than the mean kinetic pressure of the turbulent velocity fluctuations.

Since a rigorous procedure is not presently available, the total pressure data tabulated in Table IV have not been corrected for the effect of the turbulent kinetic pressure. However, it is the author's opinion that such a correction would be much less than the magnitude of the mean kinetic pressure.

D.1.4 Estimate of Total Pressure Accuracy

The accuracy of the total pressure measurement varied throughout the flowfield. In the freestream and near the test surface (except near separation and reattachment) overall accuracy was better than ± 0.01 Q_{ref}. In other parts of the flowfield measurements were less accurate but high turbulence levels and flow reversals preclude a quantitative estimate of the error.

D.2 Accuracy of Hot-Film Measurements

In many flow experiments the accuracy of hot-film measurements can be easily quantified and is limited only by the accuracy of the calibration, the linearizer settings, and the sensitivity of the sensor to moderate flow

angularity. In the current study flow reversals, high turbulence levels, and extreme flow angularity combine to limit the accuracy of the hot-film measurements. Each of these factors will be discussed in this section.

D.2.1 Probe Calibration and Linearization

Hot-film probes were calibrated in a 3.8 cm dia low turbulence calibration jet. The probes were aligned such that the sensor was perpendicular to the jet axis and the tips of the needle supports were parallel to the jet axis. Mean velocity and bridge output voltage were recorded for 20 jet speeds ranging from 0.01 Q_{ref} to 1.20 Q_{ref}. The mean response equation for each sensor was assumed to conform to a modified King's law in the following form

$$E^2 = A + B\ U_{jet}^{0.45} \tag{D-4}$$

where E is the bridge output voltage.

The calibration data was then used to calculate coefficients for a fourth-order polynomial linearizer. Maximum deviation of the calibration data from the linearized fit was 2.5%. To account for hot-film aging and day-to-day tunnel temperature changes, a single point in-place calibration was conducted at the start of each test shift to ensure that a 10 volt linearizer output corresponded to 100 ft/sec (30.48 m/sec). This was accomplished by positioning the probe within the test section at a specific location (x = 7.6 cm, y = 10.2 cm, z = 0) where the streamwise velocity was known to equal 0.9925 U_{ref} and adjusting the linearizer span accordingly.

D.2.2 Effect of Turbulence and Flow Angle Variations on Hot-Film Measurements

Jörgensen (ref. 60) has shown that the effective cooling velocity of a hot-film/wire sensor can be expressed as

$$U_{eff}^2 = \tilde{U}_N^2 + h^2\ \tilde{U}_B^2 + k^2\ \tilde{U}_T^2 \tag{D-5}$$

where $\tilde{U}_N$, $\tilde{U}_B$, and $\tilde{U}_T$ are the normal, binormal, and tangential components of the instantaneous velocity vector as shown in the sketch. These velocity components correspond to the instantaneous axial, $\tilde{U}$, transverse, $\tilde{V}$, and spanwise, $\tilde{W}$, velocity components in the test section. Thus, the effective cooling velocity can be written as

232

$$\tilde{U}_{eff}^2 = \tilde{U}_2 + h^2 \tilde{v}^2 + k^2 \tilde{w}^2 \qquad \text{(D-6)}$$

SUPPORT NEEDLES

HOT-FILM SENSOR
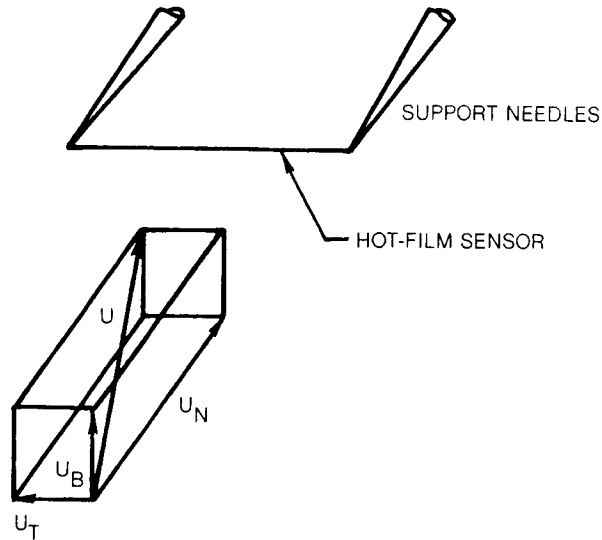
The coefficients h and k are functions of the probe geometry and should be determined from calibration. Typical values for h and k are 1.05 and 0.18, respectively (ref. 60). Replacing the instantaneous velocity components in eq. (D-6) with the time-mean and fluctuating velocity components (eqs. D-2) and time averaging yields the following expression for the effective cooling velocity

$$U_{eff} = \sqrt{\left[(U + u)^2 + h^2 (V + v)^2 \right]^{1/2}} \qquad \text{(D-7)}$$

assuming k^2 is small and $W \simeq 0$. After expanding the rhs of eqs. (D-7) with a binomial expansion and performing the indicated time average, the bias in single-sensor hot-film measurements of axial velocity due to transverse velocity and axial and transverse turbulence can be estimated.

$$\frac{\Delta U_{eff}}{U} = 1 + \frac{h^2(V^2 + \overline{v^2})}{2 U^2} \qquad \text{(D-8)}$$

A comparison of hot-film and LV data acquired at Station 18 (x = 67.3 cm) is shown in figure D-1 to indicate the magnitude of this bias error in the present study. Data at Station 18 was chosen for illustration because it is the location of the maximum bias error. Except near the wall, the difference between the hot-film data and U/U_{ref} measured with the LV is approximately 0.1

U_{ref}. The hot-film data also measures approximately 0.05 U_{ref} higher than the streamwise velocity component, $\sqrt{U^2 + V^2}/U_{ref}$. However, the U_{eff} profile calculated from LV data using eq. (D-7) approximates the hot-film data, thus verifying the magnitude of the bias error given in eq. (D-8).

D.2.3 Effect of Flow Reversals on Hot-Film Output

Since a single-component hot-film probe cannot distinguish the direction of the effective cooling velocity, the bridge output voltage is always positive, even in regions or periods of reversed flow. This rectification of the velocity signal can cause the measured time-averaged effective cooling velocity to be significantly larger than the streamwise mean velocity and the indicated turbulence level to be lower than actual when flow reversals occur during the averaging period (see Section D.3 below.)

D.3 Comparison of Hot-Film, LV, and Pitot Data Near Separation

LV and hot-film measurements of the mean streamwise velocity and turbulence profiles at Station 11 (x = 40.6 cm) near separation are plotted in figure D-2. In addition, the mean streamwise velocity profile calculated from total pressure measurements assuming constant static pressures across the traverse is plotted for comparison. Several aspects of these profiles are interesting.

Near the wall, where the forward flow fraction, γ_{P_U}, is approximately 0.5, the mean velocity measured with the LV approaches zero as y approaches zero. However, the pitot and hot-film data approach a constant positive value. This positive value occurs because the hot-film probe and, to a lesser extent, the pitot probe are directionally insensitive and tend to rectify the velocity fluctuations causing the time-averaged velocity to have a positive bias. Signal rectification also effects the turbulence measurements made with the hot-film in regions of the flow where $\gamma_{P_U} < 1.0$. Near the wall, the turbulence measured with the hot-film is half the LV measurement because the peak-to-peak oscillation sensed by the hot-film are half the actual value because of signal rectification. Near the freestream, where the turbulence levels are low, LV and hot-film mean velocity and turbulence measurements are nearly identical. The mean velocity inferred from pitot readings in significantly lower than actual, however, because of the negative transverse pressure gradient near separation.

DATA OBTAINED AT STATION 18, $x = 67.3$ cm, $z = 0$

□ HOT-FILM DATA

♭ LV DATA, $\dfrac{U}{U_{ref}}$

♂ LV DATA, $\left(\dfrac{U^2 + V^2}{U_{ref}^2}\right)^{1/2}$

♂ LV DATA, $\left[\left(\dfrac{U^2 + \overline{u^2}}{U_{ref}^2}\right) + 1.1 \left(\dfrac{V^2 + \overline{v^2}}{U_{ref}^2}\right)\right]^{1/2}$
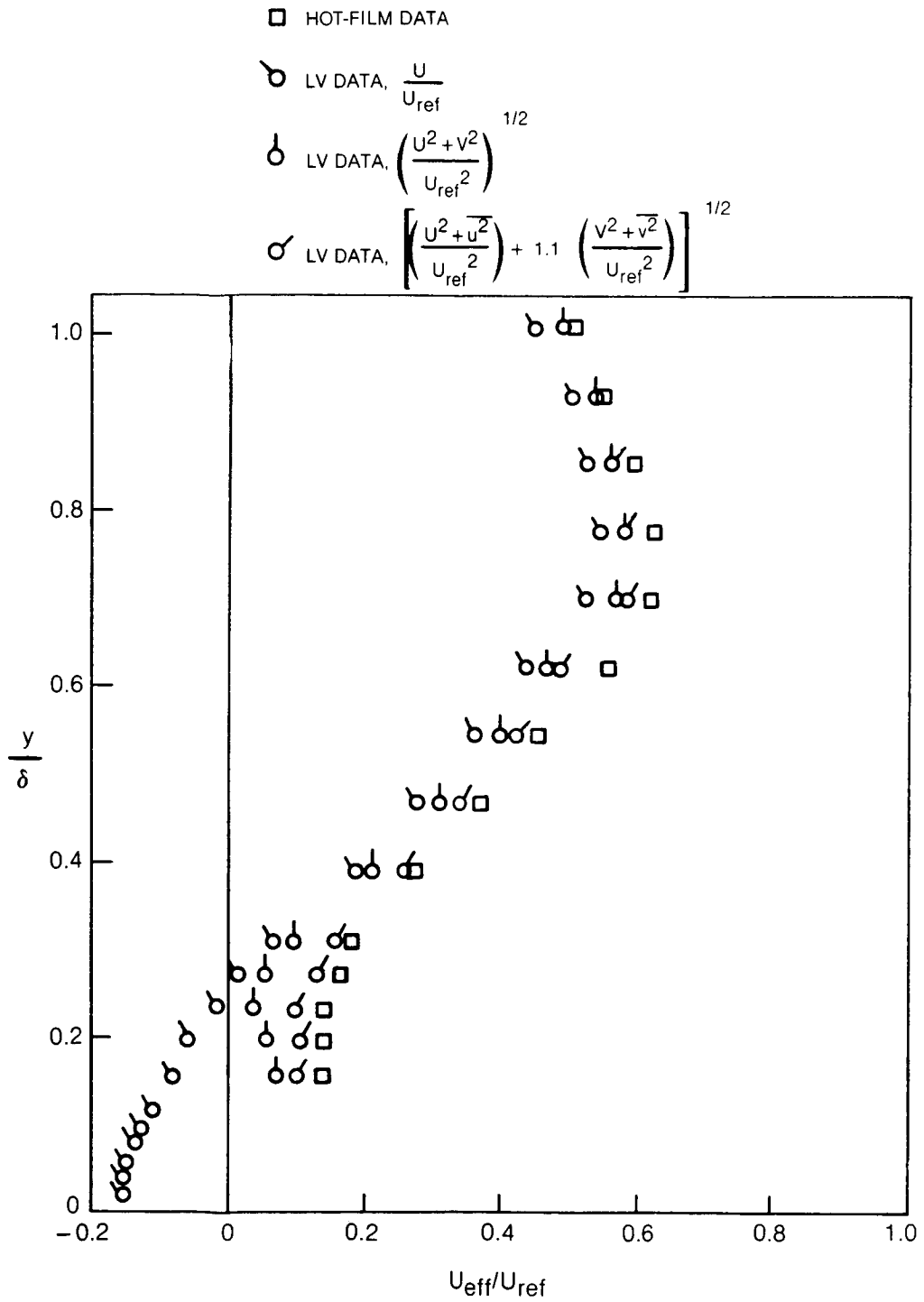
Figure D-1 Comparison of Hot-Film and LV Data

85—8—36—10

DATA OBTAINED AT STATION 11, x = 40.6 cm, z = 0
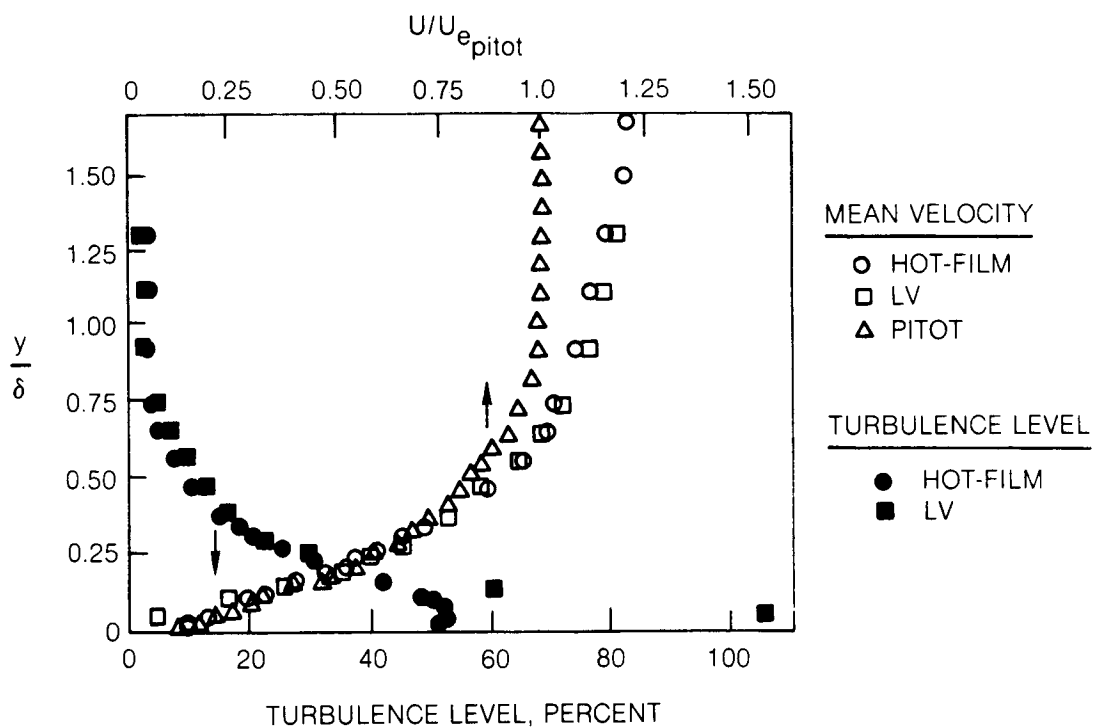
Figure D-2 Comparison of Hot-Film, LV, and Pitot Data Near Separation

E-3254

85-8-36-8

1. Report No.	2. Government Accession No.	3. Recipient's Catalog No.
NASA CR-4052		

4. Title and Subtitle		5. Report Date
Flowfield Measurements in a Separated and Reattached Flat Plate Turbulent Boundary Layer		March 1987
		6. Performing Organization Code

7. Author(s)	8. Performing Organization Report No.
William P. Patrick	None (E-3254)
	10. Work Unit No.
	535-05-01

9. Performing Organization Name and Address	11. Contract or Grant No.
United Technologies Research Center Experimental Gas Dynamics Group East Hartford, Connecticut 06108	NAS3-22770
	13. Type of Report and Period Covered

12. Sponsoring Agency Name and Address	Contractor Report Final
National Aeronautics and Space Administration Lewis Research Center Cleveland, Ohio 44135	14. Sponsoring Agency Code

15. Supplementary Notes

Project Manager, Thomas F. Gelder, Propulsion Systems Division.

16. Abstract

The separation and reattachment of a large-scale, two-dimensional turbulent boundary layer at low subsonic speed on a flat plate has been studied experimentally. The separation bubble was 55 cm long and had a maximum bubble thickness, measured to the height of the mean dividing streamline, of 17 cm, which was twice the thickness of the inlet boundary layer. A combination of laser velocimetry, hot-wire anemometry, pneumatic probing techniques, and flow visualization were used as diagnostics. Principal findings were that an outer inviscid rotational flow was defined which essentially convected over the blockage associated with the inner, viscously dominated bubble recirculation region. A strong backflow region in which the flow moved upstream 100 percent of the time was measured near the test surface over the central 35 percent of the bubble. A laminar backflow boundary layer having pseudo-turbulent characteristics including a log-linear velocity profile was generated under the highly turbulent backflow. Velocity profile shapes in the reversed flow region matched a previously developed universal backflow profile at the upstream edge of the separation region but not in the steady backflow region downstream. A smoke flow visualization movie and hot-film measurements revealed low frequency nonperiodic flapping at reattachment. However, forward flow fraction data at reattachment and mean velocity profiles in the redeveloping boundary layer downstream of reattachment correlated with backward-facing step data when the axial dimension was scaled by the distance from the maximum bubble thickness to reattachment.

17. Key Words (Suggested by Author(s))	18. Distribution Statement
Separation bubble; Turbulent separation, Reattachment; LV error analysis	Unclassified - unlimited STAR Category 34

19. Security Classif. (of this report)	20. Security Classif. (of this page)	21. No. of pages	22. Price*
Unclassified	Unclassified	245	A11